



# Eulerian modeling of aerosol dynamics

From nucleation to deposition

---

Edo Frederix

# EULERIAN MODELING OF AEROSOL DYNAMICS

EDO FREDERIX

*Leden van de promotiecommissie:*

Prof. dr. P.M.G. Apers *Voorzitter en secretaris*

Prof. dr. ir. B.J. Geurts *Promotor*

Prof. dr. J.G.M. Kuerten *Universiteit Twente*

Dr. ir. R. Hagmeijer *Universiteit Twente*

Prof. dr. ir. B. Koren *Technische Universiteit Eindhoven*

Prof. dr. A.E.P. Veldman *Rijksuniversiteit Groningen*

Prof. dr. W. Hofmann *University of Salzburg*

Dr. A.K. Kuczaj *Philip Morris International R&D*



INSTITUTE FOR NANOTECHNOLOGY



ISBN: 978-90-365-4228-9

DOI: 10.3990/1.9789036542289

The research presented in this work was carried out at the chair of Multiscale Modeling and Simulation of the Department of Applied Mathematics, University of Twente, Drienerlolaan 5, 7522 NB, The Netherlands.

The research presented in this work was funded by Philip Morris Products S.A. (part of Philip Morris International group of companies).

Copyright © 2016, E.M.A. Frederix, Enschede, The Netherlands.

# EULERIAN MODELING OF AEROSOL DYNAMICS

PROEFSCHRIFT

ter verkrijging van  
de graad van doctor aan de Universiteit Twente,  
op gezag van de rector magnificus,  
prof. dr. H. Brinksma,  
volgens besluit van het College voor Promoties  
in het openbaar te verdedigen  
op vrijdag 11 november 2016 om 12.45 uur

door

EDOARDO MARIA AUGUSTINUS FREDERIX

geboren op 6 augustus 1986  
te Ubachsberg, Nederland

*Dit proefschrift is goedgekeurd door de promotor:*

Prof. dr. ir. B.J. Geurts

## ACKNOWLEDGMENTS

*In a capitalist society, all human relationships are voluntary. Men are free to cooperate or not, to deal with one another or not, as their own individual judgments, convictions and interests dictate. — Ayn Rand*

Hoping that this is the basis of our interaction, I would like to thank the following people who have, in one way or another, helped in the realization of this thesis.

I want to thank my advisor and promotor Bernard Geurts. He taught me to consider my work in terms of the bigger picture, and to always ask the question: *wat is het springende punt?* Also, I thank Bernard for the many hours he spent discussing and reading my work, which improved its quality dramatically.

I owe many thanks to Arkadiusz Kuczaj and Markus Nordlund from Philip Morris International who, while sailing the turbulent waters of lake Neuchâtel, steered clear of trouble and navigated my research project in a direction where it could flourish to have meaning in both Twente and Switzerland. I enjoyed my many visits to them in hospitable Neuchâtel which gave me the valuable opportunity to see the other side of the story: industry.

In Twente I worked closely together with colleagues and friends Paolo Cifani, Gijs Kooij and Milos Stanic who I also want to thank. Within an easygoing setting and with a shared sense of humor we drew together to help in solving each other's problems in work. Often unable to solve them, off the clock many glasses were raised while forgetting about those problems. I also want to thank Matthias Brauns for often joining us in that effort, and for many interesting discussions. A special *grazie* must go to Paolo & Daniela and their family who welcomed me twice to their Italian home in beautiful Cocullo.

My project in Twente started around the time of Prof. Arthur Veldman's retirement. Fortunately, his retirement did not seem to change anything to his engagement with science, and I was very lucky to have many helpful discussions with him on my work, and to listen to fascinating science stories from 'back in the day' when computers were crunching punch cards. I am very grateful to Arthur for this.

A welcome distraction from work in Twente was the Pi Hard futsal team, which, it is safe to say, dominated the university employee competition in its glorious heyday. Otherwise, there were the sometimes fierce lunch table discussions giving food for stomach and thought. In the evening I often played pub quiz; a fun time with friends but often with a disastrous score. Nevertheless, I want to thank everyone who participated in these and other fun distractions, in particular: Bettina, Bijoy, Elena, Felix (who I also thank for welcoming me twice to his Austrian home), Gjerrit, Hil, Ivana, Kamiel, Koen, Laura, Marjo, Michaela, Michel, Nastya, Ove, Shavarsh, Sjoerd and Wilbert.

Finally, a word of thanks must go to secretaries Linda and Marielle for their quality support in fixing broken laptops, booking flights and arranging everything else.

A Ph.D. project comes and goes but some things remain forever:

I want to thank my good friends Jonthe and Michiel with whom I not only annually celebrate *Vastelaovend in Limburg* as part of *V.V. Ummer Fes* but also made an unforgettable trip to Brazil to attend the legendary Spain – Netherlands 2014 World Cup football match. I would also like to thank the guys from my hometown group of friends *Neemes*, among them Kai and Paul, blessed with a brilliant yet for bystanders incomprehensible *Ubachsbergian* sense of humor.

From my bachelor and master time at the Eindhoven University of Technology I have inherited a friendship with five guys, forming a group dubbed *The B-boys*. This band of brothers is annually renewed with an exhausting but indispensable holiday trip, the essence of which is accurately captured in two words: *bakken rammen*. I want to thank Bram, Giel, Jeroen, Olaf and Tom for this unique friendship and hopefully persisting tradition.

A final word of thanks goes to my parents Jeanny and Peter and my two brothers Pascal and Remi. There are no other people who know me better and have shaped me more than they have, and I want to thank them for their sincere involved interest in me. *Dier weete waal wat ich bedoel wa.*

Edo Frederix, Enschede, November 2016.

# CONTENTS

ACKNOWLEDGMENTS	v
1 INTRODUCTION	1
2 A COMPRESSIBLE INTERNALLY MIXED EULERIAN AEROSOL MODEL	9
2.1 Introduction	9
2.2 A compressible gas-liquid mixture description	10
2.3 Transport equations	13
2.4 The droplet size distribution	15
2.5 The sectional formulation of the droplet size distribution	17
2.6 Summary	18
3 THE COMPRESSIBLE PISO ALGORITHM FOR AEROSOL DYNAMICS	21
3.1 Introduction	21
3.2 OpenFOAM finite volume discrete formulation	23
3.3 The modified PISO algorithm	27
4 HOMOGENEOUS AEROSOL NUCLEATION AND CONDENSATION	33
4.1 Introduction	33
4.2 Homogeneous aerosol nucleation and condensation	36
4.3 Characteristics-based method for aerosol dynamics	38
4.4 Analytical test cases	43
4.5 Homogeneous nucleation and condensation	51
4.6 Conclusions	56
5 AEROSOL FORMATION AND TRANSPORT	59
5.1 Introduction	59
5.2 Extension of the CBSM to a spatially varying setting	61
5.3 Aerosol formation and transport in a lid-driven cavity flow	66
5.4 Aerosol nucleation in a double-mixing tee	75

5.5 Conclusions	81
<b>6 NON-ISOKINETIC AEROSOL SAMPLING</b>	<b>83</b>
6.1 Introduction	84
6.2 Eulerian droplet drift model	86
6.3 A sectional method retaining mass fractions and liquid mass	91
6.4 Aspiration efficiency of a thin-walled sampler	96
6.5 Conclusions	105
6.A Implication of the chosen Z-equation expansion	107
6.B Unity preservation of the discrete mass fraction equations	107
<b>7 INERTIAL AND DIFFUSIONAL AEROSOL DEPOSITION</b>	<b>109</b>
7.1 Introduction	109
7.2 Extension of the model with drift, diffusion and deposition	112
7.3 Bent pipe aerosol deposition validation	120
7.4 Conclusions	132
<b>8 AEROSOL DEPOSITION IN HUMAN LUNGS</b>	<b>135</b>
8.1 Introduction	135
8.2 Validation against lung cast deposition experiments	139
8.3 Size-dependent deposition in the human upper airways	149
8.4 Conclusions	152
<b>9 CONCLUSION</b>	<b>155</b>
<b>BIBLIOGRAPHY</b>	<b>i</b>
<b>SUMMARY</b>	<b>xv</b>
<b>SAMENVATTING</b>	<b>xvii</b>
<b>ABOUT THE AUTHOR</b>	<b>xxi</b>
<b>LIST OF PUBLICATIONS</b>	<b>xxiii</b>

# CHAPTER 1

## INTRODUCTION

Aerosols are all around us. Naturally, they appear as clouds, dust, fog or haze and more strikingly as desert sand storms or even as Saharan dust traveling from Africa to South America fertilizing the Amazon rainforest [1]. People often use aerosols as a way to transport material, for example, as sprays for cosmetic products, sprays inside the combustion chamber of an engine, tobacco smoke or drug delivery with a nebulizer. All these illustrations of aerosols have in common that they can be generally defined as *suspensions of small particles in gases*, as stated by Friedlander in *Smoke, Dust, and Haze: Fundamentals of Aerosol Dynamics* [2]. The word ‘particles’ may refer to both liquids and solids. The word ‘suspension’ implies that the particulate phase is carried by the gas phase, as if ‘suspended’ in it. Friedlander’s definition is general. The properties of a sand–air mixture are quite different from those of smoke emitted by a camp fire, while both instances can be classified as aerosols. However, to conceptualize both as mixtures consisting of a dispersed and carrier phase, i.e., to distinguish between two components rather than to consider the mixture as a whole, is helpful in understanding their dynamics. This statement poses two questions: what are those dynamics and how can they be understood? Identifying an answer to these questions inevitably raises another, more specific to this thesis: can we *model* the *aerosol dynamics*? The main objective of this thesis is to formulate answers to these questions and to develop techniques for the simulation of the aerosol properties as they evolve with time.

We distinguish two types of aerosol dynamics: aerosol evolution and transport. We define aerosol evolution as mechanisms contributing to changes in an aerosol without the necessity of macroscopic physical motion of the particulate phase. In this thesis we will discuss the following aerosol-evolving mechanisms:

- *Nucleation*. In a mixture consisting only of vapors one or more of the chemical components may be in a supersaturated state, meaning that the partial pressure is larger than the equilibrium vapor pressure with respect to the mixture. It is energetically favorable for the vapor molecules to reorganize into the liquid phase. If the supersaturation is sufficiently high, the energy barrier associated with the formation of droplet surface can be overcome, leading to droplet nucleation. A supersaturated state is usually achieved by cooling or expansion. For example, in a cold environment humid exhaled air may form a cloud, or at high altitudes where both temperature and pressure are low, contrails consisting

of water crystals can be formed by airplanes.

- *Condensation and evaporation.* Once the particulate phase is formed it is easier for vapor molecules to change phase and condense onto the already existing surface. This process is driven by the saturation level of the vapor, as well as by the mobility of vapor molecules with respect to the mixture. If the vapor becomes undersaturated the aerosol droplets may start to evaporate and disappear.
- *Congulation and break-up.* Even though at the macroscopic scale an aerosol mixture may appear as quiescent, at the microscopic scale there is always some motion. In dense aerosols the particles may hit each other. Associated with these collision events there is a probability with which the two particles become one; they coagulate. Conversely, there is also a probability that a particle is scattered into multiple particles, i.e., the particle breaks up.

All these aerosol-evolving mechanisms are governed by physics which take place at the scale of the particulate phase, which in case of nucleation is equivalent to the molecular scale. Making the distinction between the particulate and carrier phase is essential in understanding the evolution of an aerosol.

Aerosol transport, the second aspect of aerosol dynamics, is related to physical motion of the particulate phase of an aerosol. We consider the following mechanisms:

- *Drift.* Generally, particles have different properties than the carrier gas, e.g., density or viscosity. In a point-particle formulation, this may lead to motion of the particulate phase which deviates from that of the carrier gas. This motion can be induced by inertia, e.g., when droplets carry too much momentum to adapt sufficiently quickly to local accelerations felt by the carrier gas. This is often the case in flow around or inside geometries inducing curvature of the flow. Another mechanism driving aerosol drift is gravitational settling.
- *Diffusion.* Aerosol particles are constantly being bombarded by carrier gas molecules due to their thermal motion. These molecules may transfer momentum, causing a random so-called Brownian motion of the particle. When particles are sufficiently small, this Brownian motion leads to diffusion of droplets. From a macroscopic point of view this diffusion acts like ‘regular’ molecular diffusion; one can define a net diffusive flux which is proportional to the gradient of particle concentration. Since the random particle motion is induced by molecule-to-particle momentum transfer, it is clear that small particles are more sensitive to this and generally exhibit larger fluctuations in their motion, making the aerosol quickly appear more diffuse.
- *Deposition.* When particles collide with a surface they may bounce or remain attached to this surface, depending on the properties of the surface, the particle and the velocity at impact. Aerosol deposition may take place. In most situations the carrier gas behaves according to a no-slip boundary condition at the surface.

This means that the velocity of the carrier gas at this surface is zero, implying that no gas molecules can cross the surface. If aerosol particles would follow exactly the streamlines of the carrier gas their motion would also stagnate at the surface, preventing deposition. However, aerosol drift and diffusion may induce a net transport of particles deviating from carrier streamlines. Therefore, both drift and diffusion are mechanisms enabling aerosol deposition and in that sense deposition can be viewed as a consequence of the dispersed character of an aerosol.

The physics enabling both drift and diffusion is related to the aerosol particle scales. In fact, both mechanisms exhibit a strong dependence on the typical particle size. For large Brownian motion the mass of the particle should be sufficiently small for collisions with molecules to have a significant impact. Conversely, for large aerosol drift the particle mass should be substantial such that its momentum causes an appreciable deviation of carrier gas streamlines. It becomes clear that retaining detailed information about the particulate phase is essential in understanding aerosol transport dynamics.

Having identified the main mechanisms contributing to the dynamics of an aerosol, we now turn to discussing the modeling aspect. When modeling an aerosol, we must keep track of the particulate phase and its dispersed character, as it was argued that aerosol dynamics is closely related to physics taking place on the particle scale. In fact, the size of a particle is an important parameter in the modeling of aerosol dynamics and should therefore be captured accurately. There are two main approaches to model an aerosol:

- *Lagrangian.* In the Lagrangian framework one keeps track of the aerosol particles by following them along their path. At a given time the positions of all particles in the domain of interest are known, as well as their properties such as velocity, temperature and size. Particles are modeled as point particles, assuming they are much smaller than other relevant length scales. Each particle adheres to a set of equations of motion, in which the rate of change of the particle properties is expressed. These equations are usually quite easy to derive and solve numerically. A drawback of the Lagrangian approach is that it is prone to become computationally expensive, in particular for aerosols with a large particle number density. Conversely, for dilute aerosols the Lagrangian method is more affordable, however, in such cases achieving statistically converged predictions of properties of interest may take too long.
- *Eulerian.* Alternatively and inseparably, the Eulerian approach proposes a continuous point of view. Rather than tracking individual particles, one is interested in properties of the aerosol at fixed points in space. These points represent the aerosol locally. This approach has the potential to reduce the computational cost of the aerosol model significantly, and is therefore a popular

method in many more realistic applications. A drawback of the Eulerian approach is that variables describing an aerosol mixture usually adhere to partial differential equations which are more complex and less intuitive to formulate than their Lagrangian counterparts. Also, if much physical detail is required in the description of the aerosol—detail which comes naturally in the Lagrangian approach—the problem can become too computationally expensive. For example, the droplet number concentration can be modeled as a function of time, space, particle size and particle velocity, supplying 8 dimensions to this function in a three-dimensional setting. This usually is beyond the reach of modern computers. However, if it is acceptable to reduce the aerosol model sufficiently, the Eulerian approach remains the method of choice to model dense aerosols.

In this thesis we will adopt the Eulerian approach to model aerosol dynamics. The main reason for this is its feasibility in realistic application. Inevitably, the model contains a number of assumptions which reduce its complexity significantly. The model along with all its underlying simplifications will be presented in Chp. 2. At the heart of the model stands the droplet size distribution. This distribution function carries the information of how many particles we have at time  $t$  and position  $\mathbf{x}$  having state  $\mathbf{s}$ . The state vector  $\mathbf{s}$  says something about the particle, e.g., its diameter, temperature, velocity or chemical composition. The complexity of  $\mathbf{s}$  will in fact be reduced to a single scalar variable  $s$ , as discussed in Chp. 2, to manage the complexity of our computational model. In this chapter too we will introduce the technique which is used to capture the size distribution numerically. The main idea of this technique is to split up  $s$  in a finite number of  $\mathcal{P}$  intervals. Each interval is then assigned a unique  $s$  which is representative for all particles within this interval. This reduces the dimensionality of the problem by one, but adds  $\mathcal{P} - 1$  additional functions, each adhering to its own governing equation. Following the formulation of the governing set of equations constituting the aerosol model, in Chp. 3 the complete numerical framework and method to find a solution will be presented. This work is mainly based on the compressible PISO (Pressure Implicit with Splitting of Operators) method together with the finite volume method to discretize our solution variables in time and space. The discussion of the model and numerical framework remains generic in the sense that no specific choices are made for the mechanisms that contribute to aerosol changes. Therefore, Chp. 2 and 3 act as a foundation for further development of models and methods including the previously discussed mechanisms for aerosol dynamics.

This further development of models and methods, as well as their application to simulation of aerosol dynamics in various settings is presented in this thesis in Chp. 4–8. These chapters will cover the following topics:

- *Aerosol nucleation and condensation.* In the Eulerian setting, nucleation and condensational growth can be modeled using a hyperbolic partial differential equation, where a convective term in  $s$ -space is responsible for particle growth.

In Chp. 4 we present the Characteristics Based Sectional Method (CBSM). This method implements the analytical solution for spatially homogeneous condensational growth using the method of characteristics, to find a solution of the evolution of a droplet size distribution function undergoing both droplet nucleation and condensation or evaporation. The method is based on the sectional formulation in which the droplet size distribution is discretized using  $\mathcal{P}$  intervals. A major benefit of this method is that no a priori assumptions are made on the shape or moments of the distribution, resulting in a method capable of predicting highly non-trivial evolution of droplet sizes. The method is validated against analytical solutions of aerosol particle nucleation and growth. A second advantage is that due to the use of the method of characteristics no time step restriction is required to ensure numerical stability of the condensational growth model. It is shown that the method is capable of handling settings in which droplets grow beyond several sections within one time step.

Continuing on the work presented in Chp. 4, in Chp. 5 the CBSM is extended to the spatially inhomogeneous setting. By making use of the fractional step method, the spatial contributions in the droplet size distribution transport equation can be separated from source terms, such that CBSM can be embedded in the computational framework presented in Chp. 2 and 3. This extension of CBSM is illustrated by simulation of aerosol formation and condensational growth in lid-driven cavity flow, where nucleation is induced by a forced cooling of a vapor present in the cavity by cooling its walls. The non-trivial formation of aerosol results from the interaction of both flow and cooling. Next, to show the feasibility of the method in a realistic setting, we simulate aerosol formation in a double-tee mixing chamber and study statistical properties of the produced aerosol.

- *Aerosol drift.* Until this point in the thesis it is assumed that droplets and carrier gas are transported by a single vector  $\mathbf{u}$ . In Chp. 6 the aerosol model is extended to include an additional transport term for aerosol particles, with respect to the motion of the carrier gas. This additional term is called the 'drift flux'. Special attention is paid to a consistent extension of the model; on both analytical and numerical level two consistency relations should be satisfied, by construction. These consistency relations ensure that mathematical choices in the model are upheld at all times also in the numerical implementation. For example, the total aerosol droplet mass as expressed by the droplet size distribution remains exactly equal to the total aerosol droplet mass as expressed by the concentration fields. Within this framework, we select a separate model for the Eulerian description of droplet motion, incorporating contributions such as a size-dependent drag or gravitational force exerted on a particle. Two models are chosen, one in which the droplet velocity is algebraically known due to a so-called 'local equilibrium assumption' and one in which the full PDE is

solved for the droplet velocity. Both models contain droplet drag and gravity. To validate the drift aspect of the aerosol model we present simulations of an aerosol sampler, in which droplet drift plays an important role. Due to large curvature of the flow around the sampler, large droplets are more prone to enter the sampler rather than small droplets, causing aerosol aspiration. This transforms a given ambient droplet size distribution into an apparent size distribution inside the sampler, making the sampled aerosol unrepresentative of the ambient one. Simulations of this setting are compared against experimental data and we find good agreement. This agreement encourages the use of our Eulerian model in settings in which droplet drift is important.

- *Inertial and diffusional aerosol deposition.* Building upon Chp. 6, in Chp. 7 we extend the drift model with aerosol diffusion. The diffusive particle flux is treated in a similarly consistent way as was done with the drift flux, satisfying the same consistency relations. The diffusive and drift fluxes are taken as mechanisms driving deposition at solid walls. Two numerical boundary treatments are introduced for the computation of the particle deposition velocity at the wall. One is based on a ‘zero-gradient’ approach, where particles may attain a wall-ward velocity near the wall that is approximated by their velocity at the cell center of the grid cells adjacent to the wall. The second boundary treatment relies on the analytical solution of the Lagrangian equation of motion of a particle near the wall, assuming that the wall-ward carrier velocity reduces linearly to the wall. We apply the model to simulation of aerosol droplet deposition in a bent pipe. We distinguish two deposition regimes: one in which droplets are sufficiently small to deposit due to diffusion and another where large droplets deposit due to drift. In both regimes we validate our predictions of the bent pipe deposition efficiency by making use of models and numerical or experimental data from literature. We find good agreement for both deposition regimes, establishing confidence in the Eulerian deposition modeling approach. The results for the bent pipe deposition show that, as a function of droplet diameter the deposition efficiency is overpredicted when adopting the zero-gradient boundary treatment on coarse computational meshes. This overprediction is adequately reduced by a Lagrangian sub-grid model boundary treatment.

Though the bent pipe geometry forms a well understood setting to allow for validation of deposition against an array of data published in literature, it is quite an abstract and academic problem. In Chp. 8 we show the feasibility of the methods developed in this thesis by application of the drift and diffusion-driven deposition model to simulation of aerosol flow in a realistic cast of the human upper airways. For this lung cast, consisting of several segments representing individual parts of the respiratory tract, experimental deposition data of a reasonably monodisperse glycerol aerosol is available for each segment. We compare our predictions against this data and find good agreement when

using a sufficiently wall-resolved mesh. Additionally, our simulations show non-trivial deposition patterns which are induced by the geometrical features of the cast, clearly demonstrating the added value of modeling and simulation. Moreover, we also show results of a lung cast exposed to a polydisperse aerosol spanning a size domain of 10 nm to 20  $\mu\text{m}$  in diameter. As well as in the bent pipe a diffusional and inertial deposition regime is uncovered, leading to a 'V-shape' deposition efficiency curve. We study the size-dependent deposition rates and surface-averaged deposition fluxes, for each generation of the lung cast.

The general approach taken in these chapters 4–8 is to develop or extend the aerosol model to include the required physics, and to validate the model against other data. Moreover, we study the sensitivity of the solution to numerical parameters such as typical mesh size, section size or time step. By doing so, one can establish an understanding of how a numerical method performs under certain conditions. In any case, a numerical scheme should be such that its solution converges to the real solution once the resolution of the discretization becomes sufficiently high. We demonstrate this by performing grid and time step refinement studies throughout. This and the level of agreement with experimental data, helps us to validate the developed numerical tools in order to model the discussed aerosol dynamics properly.



## CHAPTER 2

# A COMPRESSIBLE INTERNALLY MIXED EULERIAN AEROSOL MODEL

### ABSTRACT

In this chapter the compressible Eulerian aerosol model is discussed. First we discuss the main properties of the model. The model is: 1) Eulerian, 2) multi-species, 3) compressible, 4) internally mixed and 5) applicable to dilute aerosols. The internally mixed assumption implies that aerosol particles locally have a uniform composition, independent of their size. This assumption reduces the complexity of the model and makes the model computationally more feasible. Next, the macroscopic description of a multi-species mixture is presented, without detailing the particulate phase in terms of its dispersed character. We adopt a formulation in which vapors behave according to the ideal gas law while liquids behave incompressible. We introduce the relevant equations for the transport of phase and species-specific mass concentration. Finally, the particulate phase is described by the droplet size distribution. This distribution is a function of time, position and particle size, and is discretized in size space using the sectional formulation. In this formulation the size domain is split up in a number of adjoining intervals. For each interval a transport equation can be formulated, alongside those of the mass concentrations, to model aerosol dynamics.

### 2.1 INTRODUCTION

In this chapter a description of the adopted aerosol model will be given. This model features a combination of the following five properties:

- The description of the system is in the *Eulerian* context. Both carrier gas and dispersed droplets are described with respect to a fixed frame of reference  $(x, t)$  in space-time. This approach is discussed previously in the introduction, Chp. 1.
- The description is *multi-species*. Both the droplets and carrier gas may consist of one or more species or constituents. The multi-species formulation is general and the single-species formulation is merely a subset of this formulation.
- The model is *compressible*, meaning that density is allowed to change. Changes in density are not only flow-induced but may also be activated due to temperature

change or phase change. The compressible fluid framework is beneficial for obtaining general and accurate models as reliable constitutive relations can be formulated explicitly. For example, well-known models such as the ideal gas law can be readily implemented in the compressible formulation. The incompressible formulation can be viewed as a limit of the compressible one.

- The model is *internally mixed*. We use the ‘internally mixed’ concept as given by Friedlander [2], stating that the droplet’s chemical composition is locally independent of droplet size. In other words, the compositions at positions  $x$  and  $x'$  may differ from each other, but the collection of droplets at either  $x$  or  $x'$  has a uniform composition that is the same for all sizes of droplets found at these locations. The advantage of this approach is that it reduces the complexity of the problem significantly. Since composition is assumed to be no longer size dependent it can be locally described by a set of scalars. The number of required scalars to describe the chemical composition corresponds to the number of constituents times the number of chemical states (i.e., gaseous, liquid or solid) in which these constituents may be present.
- A *dilute aerosol* system is described in which both the mass and volume concentration of the droplet phase with respect to the total mixture is small. This allows for a number of approximations, as will be described later, simplifying the mathematical form of the model. With ‘small’ we mean that the fraction taken up by the droplets is smaller than about  $10^{-5}$  of the total volume. Most aerosol systems are sufficiently dilute to meet this requirement, for example, the total mass in a fog cloud consists only for 0.001% of water droplets [3] while a dense combustion plume is in terms of its volume 99.999% pure air [3].

In this chapter the model will be detailed. We first derive a general description of an aerosol mixture where the dispersed character of the droplet phase is not yet considered, Sec. 2.2. Next, the governing transport equations for the aerosol mixture are introduced, Sec. 2.3. In Sec. 2.4 the dispersed phase will be considered in terms of the droplet size distribution, for which a corresponding transport equation will be introduced as well. In Sec. 2.5, the ‘sectional’ formulation of the droplet size distribution will be introduced. A brief summary of the main points of this chapter is given in Sec. 2.6.

## 2.2 A COMPRESSIBLE GAS-LIQUID MIXTURE DESCRIPTION

We consider a small volume  $V \in \mathbb{R}^M$ , having units  $\text{m}^M$ , as schematically shown in Fig. 2.1 and take a ‘snapshot’ of this system at some moment in time. The volume  $V$  consists of a mixture of  $N$  vapors and  $N$  liquids. The liquids are concentrated in droplets. All droplets within  $V$ , as imposed by the internally mixed assumption, have the same chemical composition. With this we mean that the fraction of the number of

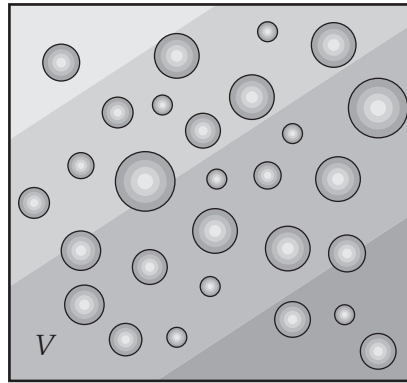


Figure 2.1: Schematic overview of a volume  $V$  containing an internally mixed multi-species droplet–gas aerosol mixture. Shades of gray symbolize the multi-species character of the model describing the mixture. In  $V$  all droplets have the same composition.

molecules of a particular species with respect to the total number of molecules inside a droplet is constant for all droplets in  $V$  and for all species. Since mass is directly proportional to the number of molecules weighed by their molecular masses, this property also holds for mass fractions.

The total mass inside  $V$  can be measured and is given by  $m$  in units of kg. We define the total mixture mass density as  $\rho = m/V$ . This mass density comprises both vapors and liquids. At the basis of our model stand the two  $\mathcal{N}$ -dimensional mass fraction vectors  $\mathbf{Y} \equiv (Y_1, Y_2, \dots, Y_{\mathcal{N}})$  and  $\mathbf{Z} \equiv (Z_1, Z_2, \dots, Z_{\mathcal{N}})$ ,  $Y_j \geq 0$ ,  $Z_j \geq 0$  with  $1 \leq j \leq \mathcal{N}$ , to describe the composition inside  $V$ , for vapors and liquids, respectively. They are defined as

$$\mathbf{Y} = \frac{\mathbf{m}^v}{m} \quad \text{and} \quad \mathbf{Z} = \frac{\mathbf{m}^\ell}{m}, \quad (2.1)$$

with  $\mathbf{m}^v \equiv (m_1^v, m_2^v, \dots, m_{\mathcal{N}}^v)$  the vector of per-species vapor masses (in units of kg) present in  $V$  and likewise  $\mathbf{m}^\ell \equiv (m_1^\ell, m_2^\ell, \dots, m_{\mathcal{N}}^\ell)$  for liquids, and naturally  $m_j^v > 0$  and  $m_j^\ell > 0$ . Since the vectors  $\mathbf{m}^v$  and  $\mathbf{m}^\ell$  describe all the mass present inside  $V$ , it must follow that the sum of their  $L^1$ -norms equals  $m$ . Therefore, using (2.1), we conclude that

$$|\mathbf{m}^v|_1 + |\mathbf{m}^\ell|_1 = m \quad \Rightarrow \quad Y + Z = 1, \quad (2.2)$$

with

$$Y \equiv |\mathbf{Y}|_1 \quad \text{and} \quad Z \equiv |\mathbf{Z}|_1 \quad (2.3)$$

and with the  $L^1$ -norm defined as

$$|\mathbf{a}|_1 = \sum_{k=1}^n |a_k|, \quad \mathbf{a} \equiv (a_1, a_2, \dots, a_n). \quad (2.4)$$

We use the  $L^1$ -norm as a compact notation for the summation of all elements of a vector, even though all those elements are non-negative. Eq. (2.2) is obvious considering that  $Y_j$  and  $Z_j$  are mass fractions. The products  $\rho\mathbf{Y}$  and  $\rho\mathbf{Z}$  give the vectors of vapor and liquid mass concentrations in  $V$  in units of  $\text{kg}/\text{m}^M$ , respectively.

Each *pure* constituent  $j$  has a mass density  $\varrho_j^v$  in the vapor phase and  $\varrho_j^\ell$  in the liquid phase\*. These densities of pure constituent are generally functions of temperature  $T$  and pressure  $p$  which arise in  $V$ . This implies  $\varrho_j^v \equiv \varrho_j^v(p, T)$  and  $\varrho_j^\ell \equiv \varrho_j^\ell(p, T)$  but this explicit notation is usually omitted for compactness. Moreover, we assume that these species mass densities are independent of the mixture's chemical composition, which is equivalent to stating that Amagat's law [4] holds. The quantities  $\varrho_j^v$  and  $\varrho_j^\ell$  are material properties of each component, which are grouped inside the  $N$ -dimensional vapor and liquid density-of-pure-constituent vectors  $\varrho^v$  and  $\varrho^\ell$ , respectively. We assume that the underlying dependencies on  $p$  and  $T$  for both types of densities are known. We can now relate this to the total mixture mass density  $\rho$ . Since  $m_j^v$  gives the total mass of  $j$ -species vapor in  $V$  then  $m_j^v/\varrho_j^v$  gives the partial volume in  $V$  consumed by  $j$  vapor. The same applies for liquid. Assuming that Amagat's law holds, i.e., all partial volumes add up to the total volume  $V$ , we find

$$V = \left| \frac{\mathbf{m}^v}{\varrho^v} \right|_1 + \left| \frac{\mathbf{m}^\ell}{\varrho^\ell} \right|_1. \quad (2.5)$$

Dividing this relation by  $m$  and using definition (2.1) gives

$$\rho = \left[ \frac{V}{m} \right]^{-1} = \left[ \left| \frac{\mathbf{Y}}{\varrho^v} \right|_1 + \left| \frac{\mathbf{Z}}{\varrho^\ell} \right|_1 \right]^{-1}. \quad (2.6)$$

This relation can be considered as a general *equation of state* (EOS) based on Amagat's law. It relates the mixture mass density  $\rho$  to the chemical composition as captured by  $\mathbf{Y}$  and  $\mathbf{Z}$ , pressure  $p$  and temperature  $T$ .

From this point on we will leave the general 'compressible' approach behind us and make a choice for the  $(p, T)$  dependence of  $\varrho_j^v$  and  $\varrho_j^\ell$ . We make the following two choices:

1. Vapors are compressible and assumed to adhere to the ideal gas law [5]. We can write

$$\varrho_j^v = \frac{p}{R_j T} = \chi_j^v(T)p, \quad (2.7)$$

with  $R_j$  the specific  $j$ -species gas constant and  $\chi_j^v(T) = (R_j T)^{-1}$  the 'compressibility ratio', which can be grouped in the vector  $\chi^v(T)$ . The ideal gas law shows a linear dependence on pressure and an inverse dependence on temperature.

---

\*We use the  $\varrho$  symbol to denote density of pure constituent, i.e., a property of a substance independent of the mixture.

2. Liquids are assumed to expand or contract in volume due to changes in temperature only, making fluids incompressible with respect to changes in pressure. This reduces  $\varrho_j^\ell$  to be only a function of  $T$ . We assume that this function is known a-priori. They are often reliably available in standard works such as [6].

These two choices reduce the general EOS to a specific EOS, which is obtained in the following form, after multiplying and dividing (2.6) by  $p$  and some rewriting:

$$\rho = \left[ \left| \frac{\mathbf{Y}}{\chi^v(T)} \right|_1 + p \left| \frac{\mathbf{Z}}{\varrho^\ell(T)} \right|_1 \right]^{-1} p \equiv \psi(p, T)p, \quad (2.8)$$

where we introduced the ‘mixture compressibility ratio’  $\psi(p, T)$ . It can be seen that for systems without liquid, i.e.,  $Z = 0$ , the mixture compressibility ratio reduces to a function dependent on temperature alone. In that case the total mixture density  $\rho$  has a linear dependence on pressure, in agreement with the ideal gas law incorporated for each of the species.

In general, aerosol-forming systems are spatially heterogeneous and may be unsteady. Extending to such situations is readily done by allowing the variables  $\rho$ ,  $T$ ,  $p$ ,  $\mathbf{Y}$  and  $\mathbf{Z}$  to be functions of  $(\mathbf{x}, t)$ . From here on this is implied, unless specified otherwise.

## 2.3 TRANSPORT EQUATIONS

Returning to Fig. 2.1, we can define a velocity vector  $\mathbf{u}$  as the velocity with which the complete mixture in  $V$  moves, assuming that droplets and vapors have the same velocity. In addition, we assume that only vapors may diffuse, although later, in Chp. 6 and beyond, we will relax these two restrictions somewhat. Mixture mass density  $\rho$  and momentum  $\rho\mathbf{u}$  adhere to the well-known continuity equation

$$\partial_t \rho + \nabla \cdot (\rho \mathbf{u}) = 0 \quad (2.9)$$

and Navier-Stokes equations

$$\partial_t(\rho \mathbf{u}) + \nabla \cdot (\rho \mathbf{u} \mathbf{u}) = -\nabla p - (\nabla \cdot \boldsymbol{\tau}), \quad (2.10)$$

with  $\partial_t$  the partial derivative with respect to time  $t$  and rate of strain tensor  $\boldsymbol{\tau}$ , given by

$$\boldsymbol{\tau} = -\mu \left[ \nabla \mathbf{u} + (\nabla \mathbf{u})^T \right] + \frac{2}{3} \mu (\nabla \cdot \mathbf{u}) \mathbf{I} \quad (2.11)$$

with identity tensor  $\mathbf{I}$  and molecular mixture viscosity  $\mu$ . For the transport of energy we introduce the temperature equation in the following form [5]:

$$c_p [\partial_t(\rho T) + \nabla \cdot (\rho \mathbf{u} T)] = \nabla \cdot (\kappa \nabla T) - (\boldsymbol{\tau} : \nabla \mathbf{u}) + D_t p, \quad (2.12)$$

with  $c_p$  the mixture heat capacity at constant pressure,  $\kappa$  the mixture heat conductivity and  $D_t \equiv \partial_t + \mathbf{u} \cdot \nabla$  the material derivative. This form of the energy equation is convenient as boundary conditions for temperature  $T$  can be readily implemented.

Next, we formulate the transport equations for individual species transport. Starting from (2.9) we introduce Eq. (2.2) (which is equal to unity) inside the two left-hand side terms. We can then expand this form into  $2\mathcal{N}$  equations for each species in either phase:

$$\partial_t(\rho Y_j) + \nabla \cdot (\rho \mathbf{u} Y_j) = -\nabla \cdot (\rho Y_j \mathbf{w}_j) - S_j \quad (2.13a)$$

$$\partial_t(\rho Z_j) + \nabla \cdot (\rho \mathbf{u} Z_j) = S_j, \quad (2.13b)$$

with  $j$ th species diffusive velocity  $\mathbf{w}_j$  and vapor-to-liquid mass transfer rate  $S_j$ . It is assumed that chemical reactions do not occur and that the diffusive velocity of liquid droplets is negligible. The expanded form (2.13) of the continuity equation is valid when the sum

$$\sum_j [\text{Eq. (2.13a)} + \text{Eq. (2.13b)}] = 0 \quad (2.14)$$

reduces to the continuity equation (2.9). The short-hand notation  $\sum_j$  is defined as

$$\sum_j \equiv \sum_{j=1}^{\mathcal{N}}. \quad (2.15)$$

Eq. (2.14) is only consistent with (2.9) if

$$\sum_j \nabla \cdot (\rho Y_j \mathbf{w}_j) = 0, \quad (2.16)$$

i.e., the net diffusive flux is zero. Following [7], we adopt ‘Hirschfelder-Curtiss approximated diffusion’, in which the species-specific diffusive velocity takes the shape

$$\mathbf{w}_j = -\frac{\mathbb{D}_j^v}{X_j} \nabla X_j + \mathbf{u}_c, \quad (2.17)$$

with  $\mathbb{D}_j^v$  the  $j$ th species vapor diffusion coefficient (see [7]), vapor mole fraction  $X_j$  with  $\mathbf{X} \equiv (X_1, X_2, \dots, X_{\mathcal{N}})$  and  $\mathbf{u}_c$  the species-independent correction velocity. This correction velocity gives a degree of freedom to impose (2.16). By inserting (2.17) into (2.16) an expression is found for  $\mathbf{u}_c$ , related to the vapor mole fraction gradients and vapor diffusion coefficients. Following [5], we can rewrite (2.17) in terms of  $\mathbf{Y}$ , i.e.,

$$\mathbf{w}_j = -\frac{\mathbb{D}_j^v}{Y_j} \nabla Y_j - \frac{\mathbb{D}_j^v}{Q} \nabla Q + \mathbf{u}_c \quad (2.18)$$

with  $Q$  the ‘molar mean molecular weight’ of the mixture (in units of kg/mole). Since

we only consider dilute aerosol mixtures with an abundant carrier gas,  $Q$  will vary only weakly in space. The gradient of  $Q$ , i.e.,  $\nabla Q$  in (2.18) becomes negligible so that we can approximate (2.18) as

$$\mathbf{w}_j \approx -\frac{\mathbb{D}_j^v}{Y_j} \nabla Y_j + \mathbf{u}_c. \quad (2.19)$$

The vapor-to-liquid source term  $S_j$  accounts for mass transport due to droplet nucleation, condensation or evaporation. For this moment  $S_j$  will be left as a ‘placeholder’, and will be detailed later in Chp. 4 and 5.

Concluding, in this section we have introduced the transport equations for total mixture mass  $\rho$ , Eq. (2.9), momentum density  $\rho\mathbf{u}$ , Eq. (2.10) and temperature  $T$ , Eq. (2.12). Also, we have derived the transport equations for mass concentration of species  $j$  in either phase, Eq. (2.13). These equations adhere to the continuity equation in view of the ‘unity division’ of mass fractions, Eq. (2.2).

## 2.4 THE DROPLET SIZE DISTRIBUTION

Until this point we have only considered the chemical composition of our aerosol mixture in terms of mass fraction vectors  $\mathbf{Y}$  and  $\mathbf{Z}$ . Referring once again to Fig. 2.1 we see that the liquid phase consists of spherical droplets, that these droplets do not necessarily have a unique size and that they have a uniform composition in view of the internally mixed assumption. To describe these additional features of the aerosol mixture, we introduce the *droplet size distribution*. Following Ramkrishna [8], we assume a continuous description of the droplet phase. Recalling that due to the internally mixed assumption the composition of droplets is independent of size at  $(\mathbf{x}, t)$ , we can introduce a new independent variable  $s \in \mathbb{R}$ , representing the size of a droplet, and a droplet size distribution function  $n(s, \mathbf{x}, t)$  defined such that  $n(s, \mathbf{x}, t)ds$  is the total number of droplets per unit of volume residing in the size range  $[s, s + ds]$ , at  $(\mathbf{x}, t)$ . In the remainder of this thesis we set the ‘size’  $s$  equal to the mass of a droplet, i.e.,  $s$  has unit kg. This choice gives  $n(s, \mathbf{x}, t)$  unit  $\text{kg}^{-1}\text{m}^{-3}$ . The chemical composition of each droplet is completely determined by  $\mathbf{Z}$  and is independent of  $s$ . Therewith, the composition is only dependent on time and location.

We assume that droplets are perfectly spherical. This means that the droplet mass is related to droplet diameter as

$$s = \frac{\rho^\ell \pi d^3}{6}, \quad (2.20)$$

with droplet diameter  $d$  and  $\rho^\ell$  the local liquid mixture mass density. The quantity  $\rho^\ell$  is a function of the droplet chemical composition as expressed by  $\mathbf{Z}$  and the liquid

density-of-pure-constituent vector  $\varrho^\ell$ . It is defined as

$$\rho^\ell = \frac{m^\ell}{V^\ell}, \quad (2.21)$$

i.e., the ratio of the total local liquid mass  $m^\ell$  and the total local liquid volume  $V^\ell$ . These two can be expressed as

$$m^\ell = \left| \mathbf{m}^\ell \right|_1 = \rho V Z \quad \text{and} \quad V^\ell = \rho V \left| \frac{\mathbf{Z}}{\varrho^\ell} \right|_1$$

such that we find

$$\rho^\ell = Z \left| \frac{\mathbf{Z}}{\varrho^\ell} \right|_1^{-1}. \quad (2.22)$$

By using  $\rho^\ell$  we can relate mass  $s$  to volumetric properties of the droplet, such as diameter, surface area or volume. Note that  $\rho^\ell$  is through its dependence on  $\mathbf{Z}$  generally a function of  $(\mathbf{x}, t)$ .

From a physical point of view the droplet size distribution  $n(s, \mathbf{x}, t)$  can be regarded as information about how many droplets we have of mass  $s$  at  $(\mathbf{x}, t)$ . From this interpretation it is then clear that  $n(s, \mathbf{x}, t)$  also tells us how much droplet *mass* is present in the system. On the other hand, this information is also carried by  $\mathbf{Z}$  and  $\rho$ ; the product  $\rho Z$  gives the total mass concentration of the droplet phase at  $(\mathbf{x}, t)$ . This means that  $n(s, \mathbf{x}, t)$  and  $\mathbf{Z}$  are related to each other as follows:

$$\rho Z = \int_0^\infty s n(s, \mathbf{x}, t) ds, \quad (2.23)$$

where the right-hand side of this relation represents the first moment of the size distribution. Within our model, this relation will show to be very useful in the derivation of consistent transport equations for droplet drift, diffusion and deposition, and will be frequently referred to in Chp. 6 and 7. We call this relation the aerosol *consistency relation*.

The droplet size distribution adheres to its own transport equation, which is often referred to as the General Dynamic Equation (GDE) [2]. It can be written as

$$\partial_t n(s, \mathbf{x}, t) + \nabla \cdot [\mathbf{u} n(s, \mathbf{x}, t)] = J(s, \mathbf{x}, t) \quad (2.24)$$

with right-hand side source term  $J(s, \mathbf{x}, t)$  containing both internal and external contributions. With ‘internal’ we mean changes that redistribute droplet mass in  $s$ -space without affecting the local mixture at the macroscopic scale, e.g., droplet coagulation or break-up. Internal changes do not have an effect on pressure or density; two droplets are assumed to occupy the same volume as when those two droplets are coagulated into one, and vice versa. More formally speaking, an internal contribution is not allowed to change the first moment of the size distribution, i.e., the total local

liquid mass concentration remains constant. All other contributions to  $J(s, \mathbf{x}, t)$  can be labeled as ‘external’, e.g., condensation, evaporation and nucleation. The exact form of  $J(s, \mathbf{x}, t)$  will be discussed in Chp. 4 and 5.

## 2.5 THE SECTIONAL FORMULATION OF THE DROPLET SIZE DISTRIBUTION

It is useful to introduce an approximate representation of  $n(s, \mathbf{x}, t)$  which has a dimensionality equal to that of other unknowns, such that conventional numerical methods can be used to solve (2.24), alongside the transport equations for  $\mathbf{u}$ ,  $T$ ,  $p$ , etc. For this we employ the *sectional method* (e.g., see [9, 10, 11]), also referred to as the *discrete population balance method*. We follow closely the approach taken by Kumar and Ramkrishna [10].

In the sectional formulation of the droplet size distribution  $n(s, \mathbf{x}, t)$  the size domain is divided into  $\mathcal{P}$  arbitrarily sized adjoining intervals. The  $i$ th section (with  $i = 1, 2, \dots, \mathcal{P}$ ) covers a part of the size domain limited by  $y_i \leq s < y_{i+1}$  with  $y_i$  the position of the interface between the  $(i - 1)$ th and  $i$ th section. The droplets which reside in the  $i$ th section are assigned to a representative size  $s_i$  with  $y_i \leq s_i < y_{i+1}$ , such that the complete size distribution may be approximated by

$$n(s, \mathbf{x}, t) \approx \sum_i N_i(\mathbf{x}, t) \delta(s - s_i), \quad (2.25)$$

with  $N_i(\mathbf{x}, t) \geq 0$  the total number of droplets per unit of volume in the  $i$ th section,  $\delta$  the Dirac delta function and  $\sum_i$  the short-hard notation of

$$\sum_i \equiv \sum_{i=1}^{\mathcal{P}}. \quad (2.26)$$

Conversely, we can write

$$N_i(\mathbf{x}, t) = \int_{y_i}^{y_{i+1}} n(s, \mathbf{x}, t) ds, \quad (2.27)$$

from which it can be readily seen that  $N_i$  represents the zeroth moment of the size distribution function in the  $i$ th section and has units  $\text{m}^{-3}$ .

Where the GDE (2.24) describes the rate of change of the complete droplet size distribution, we are now also interested in how the droplet number concentration within a section  $i$  changes. By taking the integral over the interval  $[y_i, y_{i+1}]$  of (2.24) and using definition (2.27), we find

$$\partial_t (\rho M_i) + \nabla \cdot (\rho \mathbf{u} M_i) = \mathcal{J}_{M_i} \quad (2.28)$$

where we define  $M_i$  as

$$M_i = \frac{N_i}{\rho}. \quad (2.29)$$

The introduction of  $M_i$  as a replacement of  $N_i$  will show to be numerically convenient, as the flux  $\rho\mathbf{u}$  in the second term of the left-hand side of (2.28), with which  $M_i$  is transported, is now the same flux with which  $\mathbf{Y}$ ,  $\mathbf{Z}$ ,  $T$  and  $\mathbf{u}$  are transported. This allows for consistent and conservative numerical schemes which by construction respect the aerosol consistency relation (2.23). In (2.28) we also have the right-hand side source term

$$\mathcal{J}_{M_i} = \int_{y_i}^{y_{i+1}} J(s, \mathbf{x}, t) \, ds. \quad (2.30)$$

The consistency relation (2.23) can also be written in terms of  $M_i$ . Replacing  $n(s, \mathbf{x}, t)$  by approximation (2.25) in (2.23) gives

$$Z = \sum_i s_i M_i. \quad (2.31)$$

## 2.6 SUMMARY

This chapter presented the aerosol modeling framework used throughout this thesis. The model is 1) Eulerian, 2) generally formulated in a multi-species context, 3) compressible, 4) internally mixed and 5) applicable to dilute (a liquid volume fraction below  $10^{-5}$ ) aerosol systems, see Sec. 2.1. The aerosol mixture is described by the  $\mathcal{N}$ -dimensional mass fraction vectors  $\mathbf{Y}$  and  $\mathbf{Z}$  which, by definition, adhere to the ‘division of unity’ (2.2). Based on Amagat’s law a general equation of state was derived, (2.6), which was reduced to Eq. (2.8) for the specific case of compressible vapors adhering to the ideal gas law and incompressible liquids. For the total mixture density  $\rho$ , momentum density  $\rho\mathbf{u}$  and temperature  $T$  we introduced the well-known continuity equation, (2.9), Navier-Stokes equations, (2.10) and energy equation, (2.12). The continuity equation was expanded in  $j$ -space to form a set of equations describing the evolution of each species mass concentration in either phase.

This global multi-phase and multi-species framework was then extended to include a notion of the dispersed character of the liquid phase, by means of the droplet size distribution  $n(s, \mathbf{x}, t)$ . In the internally mixed context, the droplet size distribution carries the information of ‘how many droplets we have with what size’, and is unaware of the composition of those droplets. From a physical point of view it could be shown that  $n(s, \mathbf{x}, t)$  is related to  $\mathbf{Z}$  through ‘consistency relation’ (2.23). The size distribution adhered to its own transport equation, i.e., the GDE, Eq. (2.24).

Finally, the size distribution function was approximated by a set of  $\mathcal{P}$  sectional droplet number concentration functions  $N_i$  which can be treated using conventional numerical methods to find an approximate solution to the governing equations. For clarity, the size distribution was approximated by a finite sum of Dirac delta functions,

Eq. (2.25), each delta function associated with a unique representative droplet size  $s_i$ . The introduction of  $M_i = N_i / \rho$  as a droplet number concentration belonging to size  $s_i$  lead to a sectional formulation of the GDE, Eq. (2.28).

In the following Chapter we address the issue of the numerical solution of the governing equations, thereby completing the computational model that is basic to the subsequent applied chapters.



## CHAPTER 3

# THE COMPRESSIBLE PISO ALGORITHM FOR AEROSOL DYNAMICS\*

### ABSTRACT

The Eulerian aerosol model which was formulated in the previous chapter describes the aerosol mixture in a compressible way. To find a solution to the set of governing equations we adopt the compressible PISO algorithm and extend it to include additional equations describing the evolution of the droplet size distribution. In this chapter a self-contained description will be given of our interpretation of the PISO algorithm, aimed at being readily implementable in OpenFOAM (Open source Field Operation and Manipulation). In some cases we deviate from the original formulation of the PISO algorithm [13]. For instance, we generalize the PISO algorithm to an iterative scheme, in order to have the ability to reduce the error introduced through splitting to an arbitrarily low level. These changes aside, the pressure equation remains at the heart of the algorithm. The pressure equation results from imposing the continuity equation on an implicit prediction of the velocity field. We base the face fluxes on the solution of the pressure equation for consistency, and to reduce ‘numerical checkerboarding’ (i.e., Rhie-Chow interpolation [14]). The purpose of this chapter is to act as a foundation for further application of the aerosol model to specific problems. The right-hand side ‘sources’ contributing to the previously discussed aerosol dynamics will be detailed in subsequent chapters. In the current chapter, these sources will be left as general placeholders.

### 3.1 INTRODUCTION

In the previous chapter a compressible Eulerian aerosol model was presented. This model is captured by six transport equations and a number of constitutive

---

\*Parts of this chapter are based on Frederix et al. [12]: Extension of the compressible PISO algorithm to single-species aerosol formation and transport. *International Journal of Multiphase Flow*, 74:184–194, 2015.

equations. We write these equations in the following form:

$$\partial_t \rho = -\nabla \cdot (\rho \mathbf{u}) \quad (3.1a)$$

$$\partial_t(\rho \mathbf{u}) = -\nabla \cdot (\rho \mathbf{u} \mathbf{u}) - \nabla p + \nabla \cdot (\mu \nabla \mathbf{u}) + \nabla \cdot (\mu \boldsymbol{\Gamma}) \quad (3.1b)$$

$$c_p \partial_t(\rho T) = -\nabla \cdot (\rho \mathbf{u} T) + \nabla \cdot (\kappa \nabla T) + D_t p + \mu(\nabla \mathbf{u} + \boldsymbol{\Gamma}) : \nabla \mathbf{u} \quad (3.1c)$$

$$\partial_t(\rho M_i) = -\nabla \cdot (\rho \mathbf{u} M_i) + \mathcal{J}_{M_i} \quad (3.1d)$$

$$\partial_t(\rho Y_j) = -\nabla \cdot (\rho \mathbf{u} Y_j) + \mathcal{J}_{Y_j} \quad (3.1e)$$

$$\partial_t(\rho Z_j) = -\nabla \cdot (\rho \mathbf{u} Z_j) + \mathcal{J}_{Z_j}, \quad (3.1f)$$

which correspond to (2.9), (2.10), (2.12), (2.28) and (2.13), and with  $\boldsymbol{\Gamma}$  defined as

$$\boldsymbol{\Gamma} = (\nabla \mathbf{u})^T - \frac{2}{3} \text{trace}\left[(\nabla \mathbf{u})^T\right] \mathbf{I}. \quad (3.2)$$

For notational compactness the scalar transport equations for  $Y_j$  and  $Z_j$  are written in terms of  $\mathcal{J}_{Y_j}$  and  $\mathcal{J}_{Z_j}$ , respectively, which are defined as

$$\mathcal{J}_{Y_j} = -\nabla \cdot (\rho Y_j \mathbf{w}_j) - S_j \quad \text{and} \quad \mathcal{J}_{Z_j} = S_j, \quad (3.3)$$

see Section 2.3. The sources  $\mathcal{J}_{Y_j}$ ,  $\mathcal{J}_{Z_j}$  and  $\mathcal{J}_{M_i}$  account for aerosol processes such as nucleation, condensation and coagulation, but are for the sake of compactness kept as ‘placeholder’ terms to be specified later. The case-dependent implementations of the sources will be specified in the next chapters according to the aerosol physics that are required to be captured.

In this chapter we propose a numerical algorithm for the solution of (3.1). The algorithm is mainly based on the compressible PISO algorithm due to Issa [13, 15, 16], in which the numerical solution for pressure and velocity is found in a segregated way. There is sufficient evidence to state that the PISO algorithm is computationally efficient, robust, accurate and versatile. Issa et al. [16] showed that PISO has better convergence properties than the SIMPLE algorithm, as well as a better stability for large time steps and requires a reduced computational effort. Bressloff [17] studied the application of PISO to a collocated grid and showed it to be suitable for low-Mach compressible and incompressible flow. Barton [18] assessed the performance of PISO-type algorithms for transient flows and found that PISO predicts accurate results and is robust. Wanik and Schnell [19] studied steady turbulent flow problems and concluded that PISO is computationally efficient and much more effective for time-accurate simulations than SIMPLE. This chapter presents the application of a modified PISO approach [13] within the framework of OpenFOAM to the extended problem of aerosol dynamics. OpenFOAM was recently successfully used for the modeling of compressible flows using the PISO algorithms at any Mach number, e.g., see [20] and [21]. While the PISO approach was formulated for combustion processes (e.g., [13], [22], [23], [24]) the application to the wide range of time and length scales

relevant to aerosol formation poses new challenges to the PISO framework that will be considered in Chp. 4 and 5.

OpenFOAM offers a C++ toolbox which can be used to develop numerical solvers. Although the current OpenFOAM versions contain ready-to-use solvers based on the PISO algorithm, we only use OpenFOAM as a low-level toolbox in which we implement our own solver. In fact, we consider OpenFOAM only as a ‘language’ in which a problem can be formulated and solved. By only relying on low-level OpenFOAM-functions the responsibility of the proper implementation of model and method remains with the user and allows the user to have full control over all the details of the model and the exact procedure of the method. Moreover, the portability of OpenFOAM makes it such that collaboration becomes efficient. In OpenFOAM the algorithm and modeling side is clearly separated from the application of the program. A solver contains the algorithm and main governing equations and relies on libraries specifying specific models. It uses standard classes and tools to formulate and solve systems of equations. It is written such that it is generic to any combination of simulation geometry, initial conditions and boundary conditions. Indeed, these three aspects of a simulation are separately specified in a ‘case’. This generic way of programming makes an implementation of model and method widely applicable to many different settings, and can be regarded as another benefit of using OpenFOAM.

The purpose of this chapter is to act as a documentation of our custom PISO implementation in OpenFOAM, and to act as a foundation for further application of the aerosol model to specific problems. These problems, containing the various types of aerosol dynamics as discussed in the introduction of this thesis, will be discussed in Chp. 4–7. The discussions presented there rely on the formulation of the underlying PISO algorithm in this chapter.

The layout of this chapter is as follows. In Section 3.2 the finite volume framework available in OpenFOAM is discussed, and all necessary notations and formulations of the transport equations will be introduced. Also, a detailed overview of the  $\theta$ -method [25] implementation in OpenFOAM is given. In Section 3.3 we discuss step by step our PISO algorithm extended for the simulation of aerosol dynamics.

## 3.2 OPENFOAM FINITE VOLUME DISCRETE FORMULATION

We discretize the set of governing equations (3.1) using a cell-centered collocated finite volume framework, in OpenFOAM. In the finite volume method we integrate each transport equation in physical space over a computational volume,  $V \in \mathbb{R}^M$ . This volume is enclosed by faces  $f \in \mathcal{F}$  and  $\mathcal{F}$  the set of faces enclosing  $V$ . By taking the integral over such a computational volume, applying Gauss’ theorem and dividing everything by  $V$ , we can approximate divergence terms as

$$\nabla \cdot (\mathbf{a}b) \approx \frac{1}{V} \sum_{f \in \mathcal{F}} (\mathbf{a}_f \cdot \mathbf{A}_f) b_f, \quad (3.4)$$

for a vector  $\mathbf{a}$  and transported variable  $b$ , where the subscript  $f$  denotes ‘at the face  $f$ ’ and  $\mathbf{A}_f$  is the outward (outward with respect to  $V$ ) normal vector at face  $f$ , with magnitude  $|\mathbf{A}_f| = A_f$  the surface area of face  $f$ . Solution variables are only computed at cell centers such that the subscript  $f$  implies that an interpolation scheme must be invoked. Eq. (3.4) suggests that to compute the approximate form of a divergence term, the scalar  $a_f \equiv \mathbf{a}_f \cdot \mathbf{A}_f$  must be computed at each face in  $\mathcal{F}$ . This scalar is called the flux and is usually readily available. Naturally, we could define the function  $\mathcal{D}(\mathbf{a}, b)$  as the discrete counterpart of the divergence operator acting on  $\mathbf{a}$  and  $b$ , performing the operation as expressed by the right-hand side of (3.4). However, it is more convenient to define a function which acts directly on the face fluxes of  $b$ , i.e.,  $a_f b_f$  for all  $f \in \mathcal{F}$ . In this way the construction of the flux is always visible and not ‘hidden’ inside the definition of  $\mathcal{D}$ . We introduce the following short-hand flux-based notation for discrete divergence terms:

$$\mathcal{D}(a_f b_f) = \frac{1}{V} \sum_{f \in \mathcal{F}} a_f b_f, \quad (3.5)$$

For the computation of cell-centered gradients, we can make a similar approximation. By taking the integral over the volume, applying the gradient theorem and dividing by volume  $V$ , we find

$$\nabla b \approx \mathbf{G}(b) = \frac{1}{V} \sum_{f \in \mathcal{F}} b_f \mathbf{A}_f, \quad (3.6)$$

for a variable  $b$ . Also, we introduce

$$G_f(b) = \nabla_f b \cdot \mathbf{A}_f \quad (3.7)$$

as the surface-normal component of the gradient of  $b$  at the face  $f$ , multiplied by the surface area of the face  $f$ . In the right-hand side,  $\nabla_f b$  is the gradient of  $b$  at that face, which is directly related to cell-centered values of  $b$  and face-to-cell-center distances using an adequate scheme, e.g., the second order central scheme. The form (3.7) is useful for Laplacians, in which the divergence is taken of a gradient. In the approximate form of a divergence term, as indicated by (3.4), we must evaluate its argument at  $\mathcal{F}$  and take the inner product with  $\mathbf{A}_f$ , the latter of which is achieved by (3.7).

For the discretization of the time derivatives we introduce the so-called  $\theta$ -scheme, see Morton and Mayers [25]. Let  $t = m\Delta t$  with  $m = 0, 1, 2, \dots$  the discrete time level. The right-hand sides of (3.1) must be evaluated at the current time level  $m$  and at the new time level  $m + 1$ , according to some  $\theta$ -based weighing. For  $\theta = 1$  the scheme reduces to ‘implicit Euler’ and for  $\theta = 0$  to ‘explicit Euler’. At  $\theta = \frac{1}{2}$  the scheme is the second order accurate Crank-Nicolson scheme.

Considering the computational volume  $V$ , we now write (3.1) in the following dis-

crete form, where, for notational compactness, we introduce the set  $\mathbf{X} = \{M_i, Y_j, Z_j\}$

$$\frac{\rho^{m+1}\mathbf{u}^{m+1} - \rho\mathbf{u}^m}{\Delta t} = \theta \mathbf{S}_{\mathbf{u}}^{m+1} + (1 - \theta) \mathbf{S}_{\mathbf{u}}^m \quad (3.8)$$

$$\frac{\rho^{m+1} - \rho^m}{\Delta t} = \theta S_{\rho}^{m+1} + (1 - \theta) S_{\rho}^m \quad (3.9)$$

$$c_p \frac{\rho^{m+1} T^{m+1} - \rho^m T^m}{\Delta t} = \theta S_T^{m+1} + (1 - \theta) S_T^m \quad (3.10)$$

$$\frac{\rho^{m+1} \mathbf{X}^{m+1} - \rho^m \mathbf{X}^m}{\Delta t} = \theta S_{\mathbf{X}}^{m+1} + (1 - \theta) S_{\mathbf{X}}^m + \mathcal{J}_{\mathbf{X}}^m, \quad (3.11)$$

with  $\Delta t$  the time step size and each right-hand side  $S$  consisting of the convection and diffusion transport terms and source terms  $\mathcal{J}$ . In the  $\mathbf{X}$  equations we keep the source terms  $\mathcal{J}_{\mathbf{X}}$  outside  $S_{\mathbf{X}}$  and explicit. This allows the  $\mathbf{X}$  equations to be solved in two separate stages using the fractional step method, integrating first the contributions of  $S_{\mathbf{X}}$  and then those of  $\mathcal{J}_{\mathbf{X}}$ . This allows for the implementation of different methods for the treatment of the source terms, as will be shown in Chp. 5.

The right-hand sides  $S_{\dots}^m$  and  $\mathbf{S}_{\mathbf{u}}^m$  can be directly related to the discretized approximations of the right-hand side terms in (3.1). However, the  $\theta$ -scheme is implemented in a particular way in OpenFOAM. Let  $a(\mathbf{x}, t)$  be some variable adhering to the equation

$$\partial_t a = F(a) \quad (3.12)$$

with a right-hand side term  $F(a)$ . Using the  $\theta$ -scheme this equation is discretized in time as

$$\frac{a^{m+1} - a^m}{\Delta t} = \theta F^{m+1}(a^{m+1}) + (1 - \theta) F^m(a^m) \quad (3.13)$$

to find the solution at  $t^{m+1}$ . Similarly, for the previous time step, the discrete form reads

$$\frac{a^m - a^{m-1}}{\Delta t} = \theta F^m(a^m) + (1 - \theta) F^{m-1}(a^{m-1}). \quad (3.14)$$

This relation can be rewritten to find an expression, based on previous evaluations of  $F$  and  $a$ , for  $F^m(a^m)$ :

$$F^m(a^m) = \frac{a^m - a^{m-1}}{\theta \Delta t} - \frac{(1 - \theta)}{\theta} F^{m-1}(a^{m-1}), \quad (3.15)$$

which can be used in (3.13). For the first time step  $F^{m-1}(a^{m-1})$  is unavailable and (3.15) cannot be evaluated. This problem is resolved by using the implicit Euler scheme for the first time step, i.e.,

$$\frac{a^{[1]} - a^{[0]}}{\Delta t} = F^{[1]}(a^{[1]}) \quad (3.16)$$

with superscript<sup>†</sup> [0] denoting the (initial) solution at  $t = 0$  and [1] that at  $t = \Delta t$ . For the second time level we use the  $\theta$ -scheme, i.e.,

$$\frac{a^{[2]} - a^{[1]}}{\Delta t} = \theta F^{[2]}(a^{[2]}) + (1 - \theta) F^{[1]}(a^{[1]}) \quad (3.17)$$

where  $F^{[1]}(a^{[1]})$  is directly available from (3.16). The third and subsequent time levels can be solved using (3.13) and (3.15). Quite interestingly, when inserting (3.15) into (3.13) by substituting  $F^m(a^m)$ , we find

$$\frac{a^{m+1} - \left(1 + \frac{(1-\theta)}{\theta}\right)a^m + \frac{(1-\theta)}{\theta}a^{m-1}}{\Delta t^2} = \frac{\theta F^{m+1}(a^{m+1}) - \frac{(1-\theta)^2}{\theta}F^{m-1}(a^{m-1})}{\Delta t} \quad (3.18)$$

It can be seen that setting  $\theta = \frac{1}{2}$  gives the second order-accurate discrete form of

$$\partial_{tt}a = \partial_t F(a), \quad (3.19)$$

which is equal to the derivative in time of (3.12), showing that the OpenFOAM implementation of the  $\theta$ -scheme in fact uses the discrete form of the second derivative in time of  $a$  to compute the time evolution of  $a$ .

The  $S$  right-hand sides, for an arbitrary time level, are defined as

$$\mathbf{S}_u = -\mathcal{D}(\phi_f \mathbf{u}_f - \mu_f G_f(\mathbf{u}) - [\mu \boldsymbol{\Gamma}]_f) - \mathbf{G}(p) \quad (3.20a)$$

$$S_\rho = -\mathcal{D}(\phi_f) \quad (3.20b)$$

$$S_T = -\mathcal{D}(\phi_f T_f - \kappa_f G_f(T)) + D_t p + \mu[\mathbf{G}(\mathbf{u}) + \boldsymbol{\Gamma}] : \mathbf{G}(\mathbf{u}) \quad (3.20c)$$

$$S_X = -\mathcal{D}(\phi_f \mathbf{X}_f), \quad (3.20d)$$

We compute the explicit right-hand sides  $S_X^m$  directly from (3.20d). The explicit right-hand sides  $\mathbf{S}_u^m$ ,  $S_\rho^m$  and  $S_T^m$  are computed using (3.15), i.e., OpenFOAM's implementation of the  $\theta$ -scheme, rather than by evaluating (3.20) directly.

Equations (3.20) contain the flux term  $\phi_f$ , required at each face  $f$ . This flux stands at the heart of the finite volume method. It is defined as

$$\phi_f = (\rho \mathbf{u})_f \cdot \mathbf{A}_f, \quad (3.21)$$

and is the flux with which other quantities are transported across the face  $f$ .

The 'coefficients'  $\mu$ ,  $\kappa$  and  $c_p$  are kept constant throughout the time step at their value corresponding to time level  $m$ , such that, conveniently, they only need to be computed once at the beginning of each time step. This is reasonable if these coefficients vary only weakly in time.

---

<sup>†</sup>We use brackets in this notation to avoid confusion with taking a power.

### 3.3 THE MODIFIED PISO ALGORITHM

We consider a time level  $m$  at which we have an accepted solution, starting from which we want to compute the solution at time level  $m + 1$ . The solution at time level  $m$  could also be an initial condition. The time-evolution of the unknowns is described by the set of equations (3.8)–(3.11). These equations are coupled to each other; e.g., the pressure which appears in the right-hand side of the Navier-Stokes equations (3.8) can be related to density using an equation of state. The PISO algorithm finds a solution for the unknowns at time level  $m + 1$  in a segregated way. This means that each solution variable is solved separately while keeping others explicit. As a consequence, multiple steps must be performed in order to find a solution at  $m + 1$  which satisfies the governing equations adequately. In the original PISO algorithm only two corrector steps are performed. In our formulation we generalize the PISO algorithm to act as an iterative scheme. This allows to reduce the error introduced through segregation to a desired tolerance value based on the solution at time level  $m + 1$ , independent of the explicit or implicit evaluation of terms. We denote<sup>‡</sup> the first iterative level by superscript  $(1)$ , the second one by  $(2)$  and the  $k$ th one by  $(k)$  with  $k = 1, 2, \dots, \mathcal{C}$  and  $\mathcal{C}$  the maximum number of iteration levels. For the discretization of the time derivatives for  $\mathbf{u}$ ,  $\rho$  and  $T$  we use OpenFOAM’s implementation of the  $\theta$ -scheme, which reduces to the first order implicit Euler scheme for the first time step. For consistency, in our implementation of the  $\theta$ -scheme for  $\mathbf{X}$  we also use the implicit Euler scheme for the first time step, simply by setting  $\theta = 1$  during the first time step. At the beginning of each new time step the coefficients  $\mu$ ,  $\kappa$  and  $c_p$  are updated, and kept constant throughout all iteration levels. They carry superscript  $m$ , but this is omitted for compactness.

#### 3.3.1 First iteration: semi-implicit predictor step

To initiate the iteration we find a first prediction of our solution. In contrast to the ‘original’ PISO we first perform an explicit extrapolation for density:

$$\frac{\rho^{(1)} - \rho^m}{\Delta t} = -\mathcal{D}(\phi_f^m) \quad (3.22)$$

---

<sup>‡</sup>We use parenthesis here to separate the notations for the iteration level from the notation of the discrete time level.

In many cases this was found to be beneficial for the convergence of the scheme. The new density is used in

$$\frac{\rho^{(1)} \mathbf{u}^{(1)} - \rho^m \mathbf{u}^m}{\Delta t} = -\theta \mathcal{D} \left( \phi_f^m \mathbf{u}_f^{(1)} - \mu_f G_f(\mathbf{u}^{(1)}) - [\mu \boldsymbol{\Gamma}^m]_f \right) - \theta \mathbf{G}(p^m) + (1 - \theta) \mathbf{S}_{\mathbf{u}}^m \quad (3.23)$$

$$c_p \frac{\rho^{(1)} T^{(1)} - \rho^m T^m}{\Delta t} = -\theta \mathcal{D} \left( \phi_f^m T_f^{(1)} - \kappa_f G_f(T^{(1)}) \right) + \theta D_t p^m + \theta \mu \left[ \mathbf{G}(\mathbf{u}^{(1)}) + \boldsymbol{\Gamma}^{(1)} \right] : \mathbf{G}(\mathbf{u}^{(1)}) + (1 - \theta) S_T^m \quad (3.24)$$

to compute  $T^{(1)}$  and  $\mathbf{u}^{(1)}$ , where pressure is kept explicit at level  $m$ . In the first prediction of temperature we use the updated velocity, i.e.,  $\mathbf{u}^{(1)}$ . For the set  $\mathbf{X}$  we employ the fractional step method:

$$\frac{\rho^{(1)} \tilde{\mathbf{X}}^{(1)} - \rho^m \mathbf{X}^m}{\Delta t} = -\theta \mathcal{D} \left( \phi_f^m \tilde{\mathbf{X}}_f^{(1)} \right) + (1 - \theta) S_{\mathbf{X}}^m \quad (3.25)$$

as the first fractional step with intermediate solution  $\tilde{\mathbf{X}}^{(1)}$  and

$$\rho^{(1)} \frac{\mathbf{X}^{(1)} - \tilde{\mathbf{X}}^{(1)}}{\Delta t} = \mathcal{J}_{\mathbf{X}}^m \quad (3.26)$$

as the second fractional step, in which density remains constant. We will provide more details on this approach in Sec. 5.2.

This completes the first iteration (or predictor step), in which we found a prediction for  $\rho^{(1)}$ ,  $\mathbf{u}^{(1)}$ ,  $T^{(1)}$  and  $\mathbf{X}^{(1)}$ .

### 3.3.2 Second iteration: first explicit corrector step

We now formulate a new momentum equation, referred to by Issa et al. [13] as the *explicit corrector* form. First, the right-hand side convective and viscous terms are written as

$$-\mathcal{D} \left( \phi_f^m \mathbf{u}_f^{(2)} - \mu G_f[\mathbf{u}^{(2)}] - [\mu \boldsymbol{\Gamma}^{(1)}]_f \right) \equiv L^{(2)} \mathbf{u}^{(2)} + \mathbf{K}^{(2)}. \quad (3.27)$$

where the  $\boldsymbol{\Gamma}$  term is based on the first iteration of velocity and is therefore explicit.  $L$  is the discretization matrix resulting from the spatial discretization schemes used for the divergence term, interpolation schemes and surface-normal gradient. Although it has a mixed dependence on iteration levels, it carries superscript <sup>(2)</sup> as it is formulated in the second iteration level.  $\mathbf{K}$ , carrying superscript <sup>(2)</sup> for the same reason, contains all explicit parts of the discretization schemes as well as the  $\boldsymbol{\Gamma}^{(1)}$ -term. Next, following

[13], we approximate this as

$$L^{(2)}\mathbf{u}^{(2)} + \mathbf{K}^{(2)} \approx A^{(2)}\mathbf{u}^{(2)} + H^{(2)}(\mathbf{u}^{(1)}) \quad (3.28)$$

with  $A^{(2)} = \text{diag}(L^{(2)})$  the diagonal part of  $L^{(2)}$  and the explicit term

$$H^{(2)}(\mathbf{u}^{(1)}) = (L^{(2)} - A^{(2)})\mathbf{u}^{(1)} + \mathbf{K}^{(2)}. \quad (3.29)$$

Introducing this approximation in the right-hand side of the momentum equation we find the explicit corrector form as in [13]:

$$\begin{aligned} \frac{\rho^{(1)}\mathbf{u}^{(2)} - \rho^m\mathbf{u}^m}{\Delta t} &= \theta H^{(2)}(\mathbf{u}^{(1)}) + \theta A^{(2)}\mathbf{u}^{(2)} \\ &\quad - \theta \mathbf{G}(p^{(2)}) + (1 - \theta) \mathbf{S}_{\mathbf{u}}^m, \end{aligned} \quad (3.30)$$

in which both  $\mathbf{u}^{(2)}$  and  $p^{(2)}$  are unknown. We let  $p$  carry superscript  $(2)$  as it is the pressure that corresponds to the second iteration of the algorithm. Eq. (3.30) can be rewritten as

$$\underbrace{\left[ \frac{\rho^{(1)}}{\theta\Delta t} - A^{(2)} \right]}_{\mathbb{A}^{(2)}} \mathbf{u}^{(2)} = \underbrace{\frac{\rho^m}{\theta\Delta t}\mathbf{u}^m + H^{(2)}(\mathbf{u}^{(1)})}_{\mathbb{H}^{(2)}} + \frac{(1 - \theta)}{\theta} \mathbf{S}_{\mathbf{u}}^m - \mathbf{G}(p^{(2)}), \quad (3.31)$$

in which we defined<sup>§</sup> the parts  $\mathbb{A}^{(2)}$  and  $\mathbb{H}^{(2)}$ . When dividing this by  $\mathbb{A}^{(2)}$ , multiplying by  $\rho^{(1)}$ , interpolating to  $f$  and taking the inner product with  $\mathbf{A}_f$ , we find

$$\begin{aligned} \phi_f^{(2)} = (\rho^{(1)}\mathbf{u}^{(2)})_f \cdot \mathbf{A}_f &= \left[ \rho^{(1)}(\mathbb{A}^{(2)})^{-1} \mathbb{H}^{(2)} \right]_f \cdot \mathbf{A}_f \\ &\quad - \left[ \rho^{(1)}(\mathbb{A}^{(2)})^{-1} \right]_f G_f(p^{(2)}), \end{aligned} \quad (3.32)$$

in which we replaced the interpolation of the pressure gradient dotted with  $\mathbf{A}_f$  by the surface-normal gradient, in agreement with definition (3.7). We can now write the continuity equation in the form

$$\frac{\rho^{(2)} - \rho^m}{\Delta t} = -\theta \mathcal{D}(\phi_f^{(2)}) + (1 - \theta) S_{\rho}^m. \quad (3.33)$$

---

<sup>§</sup>These parts correspond to the `.A()` and `.H()` operations on an `fvMatrix` object in OpenFOAM.

Inserting (3.32) into this form by substituting  $\phi_f^{(2)}$ , we find the *pressure equation*:

$$\begin{aligned} \frac{\psi^{(1)} p^{(2)} - \rho^m p^m}{\Delta t} = & - \theta \mathcal{D} \left( \left[ \rho^{(1)} (\mathbf{A}^{(2)})^{-1} \mathbb{H}^{(2)} \right]_f \cdot \mathbf{A}_f \right) \\ & + \theta \mathcal{D} \left( \left[ \rho^{(1)} (\mathbf{A}^{(2)})^{-1} \right]_f G_f(p^{(2)}) \right) \\ & + (1 - \theta) S_\rho^m, \end{aligned} \quad (3.34)$$

in which we used the EOS (2.8) to substitute  $\rho$  in the left-hand side with

$$\psi^{(2)} = \psi^{(1)} p^{(2)} \quad \text{and} \quad \rho^m = \psi^m p^m \quad (3.35)$$

where  $\psi^{(1)}$  is based on the first predictions for the temperature and mass fractions, see Section 2.2. The pressure equation, containing a Laplacian for pressure, can be solved for the second iteration level pressure  $p^{(2)}$ . This pressure is subsequently used to compute  $\phi_f^{(2)}$  through (3.32) and  $\mathbf{u}^{(2)}$  through (3.31). The new density follows from (3.35). After this we solve the updated temperature equation, i.e.,

$$\begin{aligned} c_p \frac{\rho^{(2)} T^{(2)} - \rho^m T^m}{\Delta t} = & - \theta \mathcal{D} \left[ \phi_f^{(2)} T_f^{(2)} - \kappa_f G_f(T^{(2)}) \right] \\ & + \theta D_t p^{(2)} + \theta \mu \left[ \mathbf{G}(\mathbf{u}^{(2)}) + \mathbf{I}^{(2)} \right] : \mathbf{G}(\mathbf{u}^{(2)}) \\ & + (1 - \theta) S_T^m \end{aligned} \quad (3.36)$$

to find temperature  $T^{(2)}$ . Finally, using two fractional steps we explicitly find for  $\mathbf{X}^{(2)}$ :

$$\frac{\rho^{(2)} \tilde{\mathbf{X}}^{(2)} - \rho^m \mathbf{X}^m}{\Delta t} = -\theta \mathcal{D} \left( \phi_f^{(2)} \mathbf{X}_f^{(1)} \right) + (1 - \theta) S_{\mathbf{X}}^m \quad (3.37)$$

as the first fractional step and

$$\rho^{(2)} \frac{\mathbf{X}^{(2)} - \tilde{\mathbf{X}}^{(2)}}{\Delta t} = \mathcal{J}_{\mathbf{X}}^m \quad (3.38)$$

as the second fractional step. This completes the second iteration (or first explicit corrector step).

### 3.3.3 $k$ th iteration: $(k - 1)$ th explicit corrector step

The next iteration we generalize as the  $k$ th iteration, with  $k > 2$  the iteration level corresponding to the  $(k - 1)$ th explicit corrector step. To begin, we write the

momentum equation in the split operator form

$$\begin{aligned} \frac{\rho^{(k-1)}\mathbf{u}^{(k)} - \rho^m\mathbf{u}^m}{\Delta t} &= \theta H^{(k)}(\mathbf{u}^{(k-1)}) + \theta A^{(k)}\mathbf{u}^{(k)} \\ &\quad - \theta \mathbf{G}(p^{(k)}) + (1-\theta) S_{\mathbf{u}}^m. \end{aligned} \quad (3.39)$$

This can also be written as:

$$\underbrace{\left[ \frac{\rho^{(k-1)}}{\theta\Delta t} - A^{(k)} \right]}_{\mathbb{A}^{(k)}} \mathbf{u}^{(k)} = \underbrace{\frac{\rho^m}{\theta\Delta t}\mathbf{u}^m + H^{(k)}(\mathbf{u}^{(k-1)})}_{\mathbb{H}^{(k)}} + \underbrace{\frac{(1-\theta)}{\theta} S_{\mathbf{u}}^m - \mathbf{G}(p^{(k)})}_{\mathbf{G}(p^{(k)})}. \quad (3.40)$$

This gives the  $k$ -level flux equation

$$\begin{aligned} \phi_f^{(k)} &= \left[ \rho^{(k-1)} (\mathbb{A}^{(k)})^{-1} \mathbb{H}^{(k)} \right]_f \cdot \mathbf{A}_f \\ &\quad - \left[ \rho^{(k-1)} (\mathbb{A}^{(k)})^{-1} \right]_f G_f(p^{(k)}), \end{aligned} \quad (3.41)$$

and the  $k$ -level pressure equation

$$\begin{aligned} \frac{\psi^{(k-1)} p^{(k)} - \psi^m p^m}{\Delta t} &= -\theta \mathcal{D} \left( \left[ \rho^{(k-1)} (\mathbb{A}^{(k)})^{-1} \mathbb{H}^{(k)} \right]_f \cdot \mathbf{A}_f \right) \\ &\quad + \theta \mathcal{D} \left( \left[ \rho^{(k-1)} (\mathbb{A}^{(k)})^{-1} \right]_f G_f(p^{(k)}) \right) \\ &\quad + (1-\theta) S_{\rho}^m, \end{aligned} \quad (3.42)$$

where  $\psi^{(k-1)}$  is computed from the EOS and is based on  $\mathbf{X}^{(k-1)}$ ,  $p^{(k-1)}$  and  $T^{(k-1)}$ . Solving the  $k$ -level pressure equation gives  $p^{(k)}$ , from which the updated flux  $\phi_f^{(k)}$ , velocity  $\mathbf{u}^{(k)}$  and density  $\rho^{(k)} = \psi^{(k-1)} p^{(k)}$  follow. Next, we solve the updated implicit temperature equation

$$\begin{aligned} c_p \frac{\rho^{(k)} T^{(k)} - \rho^m T^m}{\Delta t} &= -\theta \mathcal{D} \left( \phi_f^{(k)} T_f^{(k)} - \kappa_f G_f(T^{(k)}) \right) \\ &\quad + \theta D_t p^{(k)} + \theta \mu \left[ \mathbf{G}(\mathbf{u}^{(k)}) + \Gamma^{(k)} \right] : \mathbf{G}(\mathbf{u}^{(k)}) \\ &\quad + (1-\theta) S_T^m \end{aligned} \quad (3.43)$$

to obtain  $T^{(k)}$ . Using two fractional steps we explicitly find  $\mathbf{X}^{(k)}$ :

$$\frac{\rho^{(k)} \tilde{\mathbf{X}}^{(k)} - \rho^m \mathbf{X}^m}{\Delta t} = -\theta \mathcal{D} \left( \phi_f^{(k)} \mathbf{X}_f^{(k-1)} \right) + (1-\theta) S_{\mathbf{X}}^m \quad (3.44)$$

as the first fractional step and

$$\rho^{(k)} \frac{\mathbf{X}^{(k)} - \tilde{\mathbf{X}}^{(k)}}{\Delta t} = \mathcal{J}_{\mathbf{X}}^m \quad (3.45)$$

as the second fractional step. This completes the  $k$ th corrector step.

### 3.3.4 Going to the next time level

The  $k$ th iteration level can be repeated a number of times until a convergence criterion is met. For example, one could compute the initial residual of the  $k$ -level pressure equation, i.e., by replacing  $p^{(k)}$  by  $p^{(k-1)}$  and taking an adequate norm of the residual. Once this residual drops below a certain pre-specified value, the latest available solution is accepted as the ‘new’ solution at time level  $m + 1$ . For the new time level we can then repeat the algorithm.

This completes the discussion about the PISO algorithm for aerosol dynamics.

## CHAPTER 4

# HOMOGENEOUS AEROSOL NUCLEATION AND CONDENSATION\*

### ABSTRACT

A new numerical method for the solution of an internally mixed spatially homogeneous sectional model for aerosol nucleation and condensation is proposed. The characteristics method is used to predict droplet sizes within a discrete time step. The method is designed such that 1) a pre-specified number of moments of the droplet size distribution may be preserved, 2) there exists no time step stability restriction related to the condensation rate and section size, 3) highly skewed *fixed* sectional distributions may be used and 4) it is straight forward to extend to spatially inhomogeneous settings and to incorporate droplet coagulation and break-up. We derive, starting from mass conservation, a consistent internally mixed multi-species aerosol model. For certain condensational growth laws analytical solutions exist, against which the method is validated. Using two-moment and four-moment-preserving schemes, we find first order convergence of the numerical solution to the analytical result, as a function of the number of sections. As the four-moment-preserving scheme does not guarantee positivity of the solution, a hybrid scheme is proposed, which, when needed, locally reverts back to two-moment preservation, to prevent negativity. As an illustration, the method is applied to a complete multi-species homogeneous nucleation and condensation problem.

### 4.1 INTRODUCTION

An aerosol is defined as a mixture of a particulate phase suspended in a carrier gas. Aerosols are around us everywhere, as clouds, smoke, sprays or dust, and we are exposed to them daily. When the particulate phase consists of liquid droplets, the aerosol is often formed by means of nucleation and condensation, with subsequent coagulation and break-up. These processes must be captured accurately to predict the properties of such an aerosol. We propose a new numerical method for the sectional aerosol formulation proposed in Chp. 2, which is capable of solving the General Dynamic Equation (GDE) for the droplet size distribution of an aerosol

---

\*This chapter is based on Frederix et al. [26]: Characteristics-based sectional modeling of aerosol nucleation and condensation. *Journal of Computational Physics*, submitted.

undergoing nucleation and condensational growth. In contrast to other methods, the new approach does not have a condensational time step restriction, making it an efficient and robust algorithm for predicting aerosol formation and evolution.

In this chapter, we adopt the Eulerian aerosol description discussed in Chp. 2, and set out to develop a robust and stable numerical method for finding a solution to the governing aerosol equations including the effects of nucleation and condensation. In the Eulerian formulation there are three main branches of methods which can be used to determine the size distribution. The first, and generally most precise, is the *continuous method*, in which the size distribution is discretized using conventional methods like the finite element method or the finite difference method (e.g., see [27, 28, 29, 30, 31]). These methods are usually expensive, and almost exclusively applied to spatially homogeneous settings. Also, schemes may become unstable if the condensation rate is high [32]. This problem may be addressed by adding artificial diffusion, or by increasing the number of distribution discretization points, making the method inaccurate or very expensive, respectively. Complementary to continuous methods are *moment methods*, in which no longer the complete distribution is solved, but only a specific number of moments of the distribution. This greatly reduces the degrees of freedom of the system, making moment methods desirable in terms of computational efficiency. The main problem of moment methods is that they require closure, as the moments of interest may depend on higher order moments. To achieve closure, one can make an assumption on the shape of the distribution (e.g., see [33, 34, 35, 36]). However, such an assumption may be too restrictive. A popular alternative to mitigate this problem is the Quadrature Method Of Moments (QMOM) (e.g., see [37, 38, 39, 40, 41, 42, 43, 44]), in which higher order moments are related to lower order ones using quadrature integration. The QMOM method may become numerically challenging and suffers from a non-uniqueness problem [45]. Moreover, it may not be sufficiently general in terms of the shape of the distribution.

In between these two methods there is a third one: the *discrete population balance method*, often referred to as *sectional method* (e.g., see [9, 11, 45, 46, 47, 48, 49]). In this class of methods, the size domain is split up in a number of sections or bins, in which the size distribution function is assumed to be constant. This allows to solve for a total number concentration in each section, rather than the continuous distribution itself. The effects of for example coagulation on the size distribution can now be treated in a discrete way, where a finite number of collision events between two sections is considered, as in [10]. This sets aside the sectional method from the continuous method. A similar ‘discrete’ approach can be taken for condensational growth or droplet break-up, e.g., see [50]. On one hand, although less accurate, the sectional method offers a significant reduction in computational effort, in comparison with continuous methods [32]. On the other hand, in comparison with moment methods, the method is not subject to any sort of constraint in terms of an assumed particle distribution shape. Another key method is the Sectional Quadrature Method of Moments (SQMOM) [51], in which one also divides the size domain into sections,

each having one ‘primary particle’ responsible for the size distribution reconstruction and ‘secondary particles’ used for low-order moment preservation in case of particle interactions. It is shown in [51] that all before-mentioned sectional and quadrature methods are special cases of SQMOM, illustrating the generality of the method and uniting the moment approach with the sectional approach.

In Chp. 2 we introduced a sectional formulation which assigns the particles within a section to a unique ‘representative size’. This allows to exactly preserve a pre-specified number of moments of the distribution, and offers great flexibility on arbitrary grids [10]. In [52] a moving section method was proposed, to solve for condensational growth. Given the hyperbolic character of condensational growth, it is straight forward to incorporate the method of characteristics to convect sections in the size domain along trajectories. This method eliminates numerical diffusion and preserves moments exactly. However, in a spatially inhomogeneous setting, such a method introduces complications when computing spatial gradients [45]. One must either interpolate back to a fixed grid, or one must abandon the idea of using the characteristics, and compute the condensational growth on a fixed grid directly. The former was done by, for example, Mitrakos et al. [45], using a third order polynomial for the interpolation, which is argued to lead to significant reduction of numerical diffusion compared to lower order interpolations. However, only the zeroth moment of the distribution is preserved. Fixed grid methods (e.g., see [53, 54, 55]) show an analogy with the Finite Volume (FV) treatment of a convective term: fluxes of droplets growing from one section to its neighbor are determined by interpolation to section interfaces of the approximate size distribution. As shown in [52], these methods suffer from instabilities. Moreover, they reduce the global numerical time step size significantly, when condensation is rapid.

In this chapter, we introduce a new numerical method to solve for nucleation and subsequent condensational growth. In the ‘spirit’ of Kumar and Ramkrishna [10], the method is designed to exactly preserve a pre-specified number of moments, while using the method of characteristics to compute condensational growth, on a fixed sectional grid. Given a condensational growth law describing the rate at which droplets of certain sizes grow, we find a transformed size space (assuming that this is possible) in which the characteristics associated with condensation become straight lines. The solution is updated analytically along these characteristics, avoiding a numerical time step stability restriction. After the update along the characteristics, the solution is re-distributed over the surrounding representative size-classes with weights such that a pre-specified number of moments is preserved exactly. Although this chapter limits itself to spatially homogeneous settings, the method is designed to be readily extended to spatially inhomogeneous settings, by virtue of the fixed sectional size discretization. Moreover, the new approach seamlessly integrates with the sectional treatment for coagulation and break-up, as proposed by Kumar and Ramkrishna [10]. Our proposed method has many similarities with the SQMOM framework, e.g., the ability to preserve lower-order moments of the distribution

exactly by employing so-called ‘sectional moments’ [51]. In SQMOM the positions of the primary and secondary particles are variable and form part of the solution to preserve a pre-selected number of moments. While SQMOM is elegant it is also quite complex to extend to spatially heterogeneous situations in all its generality. Therefore, in this chapter we focus on the simpler approach based on a strictly fixed sectional distribution and we show that with proper discretization in size space one may also retain a desired number of low order moments. The corresponding method that we arrive at has the significant benefit of being easily extended to general heterogeneous problems as presented in Chp. 5.

We illustrate the method by comparing the numerical solutions of a two-moment- and four-moment preserving implementation with analytical solutions of two basic growth laws. In general, even when the numerical time step is large, a good agreement is shown. For any time step a stable solution is obtained, whereas previous fixed sectional methods show oscillations or significantly diffusive solutions [52]. A four-moment-preserving scheme is shown to capture sharp gradients in the solution more accurately. However, positivity of the solution is no longer guaranteed. To address this problem, a ‘hybrid’ scheme is proposed, which adopts the four-moment scheme and reduces locally to the two-moment solution if necessary, to preserve positivity of the size-distribution function.

In homogeneous aerosol formation freshly nucleated droplets are often several orders of magnitude smaller than their matured counterparts. To effectively capture the nucleation and condensational growth across multiple decades in size, logarithmically distributed sectional grids are implemented. Our method is shown to be resilient, in the sense that a stable solution is produced on such highly skewed grids. Numerical nucleation ‘pulses’ are captured accurately at the relevant size, and propagate in the size domain through condensation. The numerical stability of such propagating pulses is independent of the time step, rendering a scheme in which the time step is only restricted by the typical time of aerosol formation. We apply the method to a multi-species nucleation and condensation simulation.

## 4.2 HOMOGENEOUS AEROSOL NUCLEATION AND CONDENSATION

In Chp. 2 we introduced an Eulerian aerosol model applicable to  $\mathbb{R}^M$ . Here, we reduce the model to a spatially homogeneous setting, such that the size distribution becomes a function of size  $s$  and time  $t$  only i.e.,  $n(s, t)$ . Moreover, because no spatial gradients exist, the compressible continuity equation (2.9) reduces to

$$\partial_t \rho = 0, \quad (4.1)$$

i.e., the mixture density remains constant. The transport equations for  $Y_j$  and  $Z_j$  (Eq. (2.13a) and (2.13a)) can now be written as

$$\rho \partial_t Y_j = -S_j \quad (4.2a)$$

$$\rho \partial_t Z_j = S_j. \quad (4.2b)$$

As in this chapter we are concerned with nucleation and condensation, we decompose the source term  $S_j$  into two contributions, i.e.,

$$S_j = S_j^{\text{cond}} + S_j^{\text{nuc}}. \quad (4.3)$$

these contributions give the total rate of  $j$  species mass concentration being formed through condensation and nucleation, respectively.

On the level of individual droplets in the mixture, we can define  $I_j(s, t)$  as the rate of change of mass of an  $s$ -sized droplet through condensation (or evaporation) of species  $j$  at time  $t$ . Consequently, the total rate of change of the mass concentration of species  $j$  is given by

$$S_j^{\text{cond}} = \int_0^\infty I_j(s, t) n(s, t) ds, \quad (4.4)$$

implying a total rate of change of mass equal to  $S^{\text{cond}} = \sum_j S_j^{\text{cond}}$ . For nucleation, we assume that at a unique critical cluster size  $s^{\text{nuc}}(t)$  droplets are nucleated at a rate  $J^{\text{nuc}}(t)$ , per unit of volume. This gives, for species  $j$ , a mass change rate due to nucleation given by

$$S_j^{\text{nuc}} = s_j^{\text{nuc}}(t) J^{\text{nuc}}(t), \quad (4.5)$$

with  $s_j^{\text{nuc}}(t)$  the mass contribution of species  $j$  to the total mass in a nucleated cluster of mass  $s^{\text{nuc}}(t) = \sum_j s_j^{\text{nuc}}(t)$ .

The GDE, i.e., Eq. (2.24), for the spatially homogeneous continuous distribution function undergoing condensation and nucleation, becomes (see [2])

$$\partial_t n(s, t) = -\partial_s [I(s, t)n(s, t)] + J^{\text{nuc}}(t)\delta(s - s^{\text{nuc}}(t)), \quad (4.6)$$

with  $I(s, t) = \sum_j I_j(s, t)$  the total rate of change of the mass (i.e.,  $d_t s$ ) of a droplet due to condensation or evaporation and  $\partial_s$  the partial derivative to  $s$ .

The main focus of this chapter is concerned with the numerical treatment of nucleation and subsequent condensational growth. Therefore, droplet coagulation and break-up are not accounted for in (4.6). However, the formulation and implementation of coagulation as developed by Kumar and Ramkrishna [10] complies with the sectional methodology that will be presented further on, and can, without much difficulty, be readily implemented.

### 4.3 CHARACTERISTICS-BASED METHOD FOR AEROSOL DYNAMICS

In this section we will develop a method for solving (4.6). First, we briefly discuss the adopted sectional formulation of the droplet transport equation. Next, we isolate the contribution of condensation to (4.6). We formulate a moment-preserving scheme to account for the redistribution of  $n(s, t)$  due to droplet growth. Subsequently, nucleation is incorporated.

#### 4.3.1 Condensational growth

Let us reduce the problem of (4.6) to one without nucleation:

$$\partial_t n(s, t) + \partial_s [I(s, t)n(s, t)] = 0. \quad (4.7)$$

This is a hyperbolic equation in  $s$ -space. When integrating (4.7) over the  $i$ th section (as defined in Sec. 2.5), we find an expression for the rate of change of  $N_i$ :

$$\partial_t N_i + I(y_{i+1}, t)n(y_{i+1}, t) - I(y_i, t)n(y_i, t) = 0. \quad (4.8)$$

which resembles an FV treatment of (4.7) in  $s$ -space. To determine the second and third term in this relation, i.e., the droplet number density fluxes at the upper and lower sectional interfaces,  $n(s, t)$  must be known at each  $y_i$ . We approximate the fluxes by an appropriate interpolation of  $N_i$  to the sectional interface. There are several ways of doing so. Kumar and Ramkrishna [52] give an overview of several methods proposed in literature to estimate the fluxes, for example, by central differencing, upwind, or more elaborate schemes designed to preserve a multitude of distribution moments. However, there are, as mentioned in the introduction, several difficulties with these methods. Here, we take a different approach in solving (4.7). First, we transform (4.7) to a space variable in which the characteristics become straight lines. We then propagate the solutions defined at each representative size  $s_i$  along those characteristics for a given time step. As the new size of the grown droplets originating from  $s_i$  may not necessarily coincide with any of the *fixed* representative sizes in the  $s$ -domain, we must redistribute those droplets over surrounding sections. This is done such that a pre-specified number of moments of the distribution is preserved. There are three benefits to this approach. First, the fixed sectional grid allows for a straight forward extension of the method to a spatially inhomogeneous setting. Second, the method is designed to work with an arbitrary distribution of sections across the size domain, allowing for highly skewed grids. Third, the method does not exhibit a severe time step stability restriction, in contrast to the classical FV treatments, imposed by the condensational growth term.

### 4.3.2 Solution to the condensational growth equation

Let  $\zeta$  be a coordinate which relates to  $s$  as

$$\zeta = \psi(s), \quad (4.9)$$

with  $\psi(s)$  a transformation function which will be defined later. The distribution of droplets  $n(s, t)$  relates to the transformed distribution  $f(\zeta, t)$  in  $\zeta$ -space. As both distributions describe the same collection of droplets, it must be true that

$$\int_a^b n(s, t) ds = \int_{\psi(a)}^{\psi(b)} f(\zeta, t) d\zeta, \quad (4.10)$$

since the range  $[a, b]$  in  $n(s, t)$  must contain the same number of droplets as the transformed range  $[\psi(a), \psi(b)]$  in  $f(\zeta, t)$ . In differential form, this constraint may be written as

$$n(s, t) = f(\zeta, t)\psi'(s), \quad (4.11)$$

with  $\psi'(s) = ds/d\zeta$ , see [56]. Using this relation, we can transform (4.7) to  $\zeta$ -space:

$$\partial_t f(\zeta, t) + \partial_\zeta [I(s, t)\psi'(s)f(\zeta, t)] = 0. \quad (4.12)$$

We now choose the transformation function  $\psi(s)$  such that the product of  $\psi'(s)$  and  $I(s, t)$  becomes independent of  $s$ . Under the assumption that such a  $\psi(s)$  exists (4.12) can be written as

$$\partial_t f(\zeta, t) + \Gamma(t)\partial_\zeta f(\zeta, t) = 0, \quad (4.13)$$

with  $\Gamma(t) = I(s, t)\psi'(s) = d_t\zeta$ . The characteristics are, at time  $t$ , straight lines in the  $(\zeta, t)$  plane if  $\Gamma$  is independent of time. In that case relation (4.13) has the analytical solution  $f(\zeta, t) = f^0(\zeta - \Gamma t)$  with  $f^0$  an initial profile and  $\Gamma$  constant. This expresses that the solution is constant along the characteristics  $d_t\zeta = \Gamma$ . When integrating over the  $i$ th section and using definitions (2.27) and (4.10):

$$D_t \int_{\eta_i}^{\eta_{i+1}} f(\zeta, t) d\zeta = D_t N_i = 0, \quad (4.14)$$

with  $\eta_i = \psi(y_i)$  and  $D_t$  the material derivative  $\partial_t + \Gamma\partial_\zeta$ . We adopt a uniform discretization in time, i.e.,  $t^m = m\Delta t$  with  $m$  the discrete time level. After a time step  $\Delta t$ , droplets residing at a representative size  $\zeta_i = \psi(s_i)$  corresponding to the droplet number density  $N_i^m$  at time level  $m$ , are convected to  $\zeta_i^*$  according to

$$\zeta_i^* = \zeta_i + \Delta t \Gamma^m, \quad (4.15)$$

with  $\Gamma^m = \Gamma(t^m)$ , and  $\zeta_i^*$  the new position in the size domain for  $N_i^m$ , at time level  $t^{m+1}$ .

On the discrete level,  $\zeta_i^*$  does not necessarily coincide with a fixed representative

size. We must distribute  $N_i^m$  over the representative sizes surrounding  $\zeta_i^*$ , to obtain the solution at time  $t^{m+1}$ . Let  $q_i$  be the representative size index *immediately left* of  $\zeta_i^*$  such that  $\zeta_{q_i} \leq \zeta_i^*$  and  $r_i$  the representative size index *closest* to  $\zeta_i^*$ , both under the assumption that  $\zeta_0 < \zeta_i^* < \zeta_{P-1}$  (boundary cases will be discussed later). If we wish, when distributing  $N_i^m$  around  $\zeta_i^*$ , to preserve a number of  $Q$  moments of the distribution, we must also have a number of  $Q$  degrees of freedom to construct this interpolation. If  $Q$  is an even number, then

$$\sum_{k=q_i-Q/2+1}^{q_i+Q/2} a_k h_l(s_k) = h_l(s_i^*) \quad (4.16)$$

and if  $Q$  is an odd number, then

$$\sum_{k=r_i-\lfloor Q/2 \rfloor}^{r_i+\lfloor Q/2 \rfloor} a_k h_l(s_k) = h_l(s_i^*), \quad (4.17)$$

with  $s_i^* = \psi^{-1}(\zeta_i^*)$ ,  $\lfloor x \rfloor = \text{floor}(x)$  and where  $h_l(s)$  is a function expressing a moment of  $s$ , with  $1 \leq l \leq Q$ . Relations (4.16) or (4.17) give a number of  $Q$  equations (i.e., one for each  $l$ ), each containing a number of  $Q$  weights  $a_k$  with which the solution at time level  $m+1$  at the  $k$ th representative size is assigned. We can solve system (4.16) or (4.17) to find all  $a_k$ .

As an illustration we consider a two-moment- and a four-moment-preserving scheme. For the two-moment scheme we would like to preserve droplet numbers and droplet mass. This sets  $h_1(s) = s^0$  (zeroth moment of  $s$ , i.e., droplet number concentration) and  $h_2(s) = s$  (first moment of  $s$ , i.e., the mass concentration). For the four-moment-conserving scheme we select two additional moments:  $h_3(s) = s^2$  and  $h_4 = s^3$ , preserving the variance and the skewness of the distribution, respectively. Using these expressions for  $h_l(s)$ , and setting, as a simple illustration,  $q_i = 1$ , we find for the two-moment scheme the following expressions for the weights:

$$a_1^{2M} = -\frac{s_2 - s_i^*}{s_1 - s_2}, \quad a_2^{2M} = \frac{s_1 - s_i^*}{s_1 - s_2} \quad (4.18)$$

and for the four-moment scheme:

$$\begin{aligned} a_0^{4M} &= \frac{(s_1 - s_i^*)(s_2 - s_i^*)(s_3 - s_i^*)}{(s_1 - s_0)(s_2 - s_0)(s_3 - s_0)}, & a_1^{4M} &= \frac{(s_0 - s_i^*)(s_2 - s_i^*)(s_3 - s_i^*)}{(s_0 - s_1)(s_2 - s_1)(s_3 - s_1)}, \\ a_2^{4M} &= \frac{(s_0 - s_i^*)(s_1 - s_i^*)(s_3 - s_i^*)}{(s_0 - s_2)(s_1 - s_2)(s_3 - s_2)}, & a_3^{4M} &= \frac{(s_0 - s_i^*)(s_1 - s_i^*)(s_2 - s_i^*)}{(s_0 - s_3)(s_1 - s_3)(s_2 - s_3)}, \end{aligned} \quad (4.19)$$

in which the superscripts 2M and 4M denote two- and four-moment weights. Given the fact that, by definition,  $s_i < s_{i+1}$ , and  $s_{q_i} \leq s_i^* < s_{q_i+1}$ , it can be shown that  $a_1^{2M} \geq 0$  and  $a_2^{2M} \geq 0$ : the two-moment scheme always preserves positivity of the

solution since the weights are always positive. For the four-moment scheme, however, it can be shown that  $a_0^{4M} \leq 0$ ,  $a_1^{4M} \geq 0$ ,  $a_2^{4M} \geq 0$  and  $a_3^{4M} \leq 0$ , and therefore positivity is no longer guaranteed. On the other hand, the negative values at  $s_0$  and  $s_3$  must be compensated with larger values at  $s_1$  and  $s_2$ . Therefore we expect the four-moment scheme to approximate a sharp gradient more precisely. Finally, it can be shown that if  $s_i^*$  coincides exactly with  $s_1$ , the solution is carried along the sectional grid without any redistribution.

We also keep track of the mass of each species which is added to or removed from the droplets. The total gain or loss of mass of a droplet originally in section  $i$  is given by

$$\Delta m_i = s_i^* - s_i, \quad (4.20)$$

where  $s_i^* = \psi^{-1}(\zeta_i^*)$ . We define a mass fraction  $W_j$  with which species  $j$  contributes to the total mass change as

$$W_j^m = \frac{I_j(s, t)}{I(s, t)}. \quad (4.21)$$

Note that, with  $I_j(s, t)$  and  $I(s, t)$  having the same proportionality to  $s$ , this fraction is independent of size, and may also be written as

$$W_j^m = \frac{\Gamma_j^m}{\Gamma^m}, \quad (4.22)$$

where  $\Gamma_j^m$  is the species-specific condensation rate, defined as  $I_j(s, t)\psi'(s)$ . With this, we may update the mass fractions as follows:

$$Z_j^{m+1} = Z_j^m + \frac{W_j^m}{\rho} \sum_{i=0}^{\mathcal{P}-1} \Delta m_i N_i^m, \quad Y_j^{m+1} = Y_j^m - \frac{W_j^m}{\rho} \sum_{i=0}^{\mathcal{P}-1} \Delta m_i N_i^m. \quad (4.23)$$

Given these ingredients, our solution algorithm now takes the following form:

1. Create a new empty field  $N_i^{m+1}$ ,  $Z_j^{m+1}$  and  $Y_j^{m+1}$
2. Copy the fields  $Z_j^m$  and  $Y_j^m$  to  $Z_j^{m+1}$  and  $Y_j^{m+1}$ , respectively
3. For all sections  $i$ :
  - (a) Compute the new size of the droplets using (4.15),  $\zeta_i^*$
  - (b) If  $Q$  is an even number, use (4.16) to determine the weights. If  $Q$  is an odd number, use (4.17) to determine the weights.
  - (c) For all weights, add  $a_k N_i^m$  to  $N_k^{m+1}$
  - (d) For all species, use (4.23) to compute  $Z_j^{m+1}$  and  $Y_j^{m+1}$ .

### 4.3.3 Condensational growth boundary treatment

There are three cases in which the boundaries of the computational domain in  $s$  become of influence. It is assumed here that the computational domain is always sufficiently large, such that droplets can never grow beyond the upper boundary of the domain.

1.  $s_i^* < s_0$ . In this case the droplets originally having mass  $s_i$  completely evaporate. They are removed from  $n(s, t)$ , by not assigning them to any  $N_i^{m+1}$ . In terms of the droplet and vapor mass fractions, their mass of species  $j$  is added to  $Y_j$  and removed from  $Z_j$ , for each  $j$ .
2.  $q_i - Q/2 + 1 < 0$  for  $Q$  an even number or  $r_i - \lfloor Q/2 \rfloor < 0$  for  $Q$  and odd number. In this case the scheme partially requires access to non-existing representative sizes, smaller than  $s_0$ . Such a situation may occur for schemes preserving more than two moments, e.g., when nucleation occurs within the first section or when droplets are evaporating into the first section. We resolve this by falling back onto a two-moment scheme.
3.  $q_i + Q/2 > P - 1$  for  $Q$  an even number or  $r_i + \lfloor Q/2 \rfloor > P - 1$  for  $Q$  and odd number. Also here, the scheme accesses non-existing representative sizes, now larger than  $s_{P-1}$ . Again, this is resolved by falling back onto a two-moment scheme.

### 4.3.4 Nucleation

Starting from (4.6), we now focus on the equation with only the contribution of nucleation, i.e.,

$$\partial_t n(s, t) = J^{\text{nuc}}(t) \delta(s - s^{\text{nuc}}(t)). \quad (4.24)$$

This equation is integrated over the  $i$ th section to find the rate of change of  $N_i$ :

$$d_t N_i = \int_{y_i}^{y_{i+1}} J^{\text{nuc}}(t) \delta(s - s^{\text{nuc}}(t)) dz = \begin{cases} (J^{\text{nuc}})^m, & \text{if } y_i \leq (s^{\text{nuc}})^m < y_{i+1} \\ 0, & \text{otherwise.} \end{cases} \quad (4.25)$$

This equation is solved by adopting the previously proposed two-moment scheme: a number concentration of  $\Delta t (J^{\text{nuc}})^m$  is added to the representative sizes left and right to  $(s^{\text{nuc}})^m$  (assuming that  $s_0 \leq (s^{\text{nuc}})^m < s_{P-1}$ ), using the weights as defined by (4.18). This preserves both number and mass of the nucleation burst. Evidently, the size domain must cover  $(s^{\text{nuc}})^m$  in order to capture nucleation. The mass fractions  $Z_j$  and  $Y_j$  are updated according to

$$Y_j^{m+1} = Y_j^m - \frac{\Delta t s_j^{\text{nuc}m} J^{\text{nuc}}}{\rho} \quad (4.26a)$$

$$Z_j^{m+1} = Z_j^m + \frac{\Delta t s_j^{\text{nuc}m} J^{\text{nuc}}}{\rho}, \quad (4.26b)$$

for each  $j$ , to account for the change in mass due to nucleation.

### 4.3.5 Time integration

The homogeneous system is governed by equations (4.2) and (4.6). The system is solved using a fractional step method, in which the right-hand side contributions in (4.2) and (4.6) are solved separately in two steps: one for condensation and one for nucleation. This allows us to implement the proposed solution algorithms for the subproblems (4.7) and (4.24) separately. First, we perform an explicit condensation step over a time step  $\Delta t$ , by employing the algorithm as described in Sec. 4.3.2. The new solutions may be considered as intermediate ones, are labeled as  $Y_j^{m+*}$ ,  $Z_j^{m+*}$  and  $N_i^{m+*}$ , and only reflect the contribution of condensation. Next, starting from these intermediate solutions, we perform an explicit nucleation step using the algorithm as given in Sec. 4.3.4, to find the final solutions at time level  $m + 1$ , i.e.,  $Y_j^{m+1}$ ,  $Z_j^{m+1}$  and  $N_i^{m+1}$ .

## 4.4 ANALYTICAL TEST CASES

In this section we asses the properties of the method by studying homogeneous condensation and nucleation of a single-species system. We introduce three simple growth laws for which an analytical solution can be found. This can be used for validating the numerical method. First, we study the condensational growth of a discontinuous and a log-normal initial distribution, under the absence of nucleation. Second, we study nucleation and subsequent condensational growth of droplets starting from a system without droplets. The selected condensational growth laws and nucleation rate allow for the derivation of an analytical solution, with which the numerical result for both the two-moment- and four-moment-preserving schemes are compared

### 4.4.1 Simple growth models

In the remainder of this section two simple growth laws will be introduced and tested. The first law assumes a constant rate of change of mass of a droplet. The second law relates the rate of change of the droplet mass to the cube root of the mass; for constant liquid density this implies a linear dependence on the droplet diameter. Such linear dependence of the diameter often appears in ‘real’ growth laws, e.g., see [35]. The growth laws are given by

$$I_C(s, t) = \sigma_C \quad \text{and} \quad I_D(s, t) = \sigma_D s^{\frac{1}{3}}, \quad (4.27)$$

respectively. The corresponding Jacobian of the transformation functions  $\psi'(s)$  must be chosen such that its product with the condensation rate becomes constant. This

gives, after integration:

$$\psi_C(s) = as + b \quad \text{and} \quad \psi_D(s) = \frac{3}{2}as^{\frac{2}{3}} + b, \quad (4.28)$$

with constants  $a$  and  $b$  to be chosen. We would like  $\zeta$  to be in between zero and unity. As each expression in (4.28) is monotonic, this leads to  $\psi(s_0) = 0$  and  $\psi(s_{P-1}) = 1$ . With this requirement, the transformation functions are defined:

$$\psi_C(s) = \frac{s - s_0}{s_{P-1} - s_0} \quad \text{and} \quad \psi_D(s) = \frac{s^{\frac{2}{3}} - s_0^{\frac{2}{3}}}{s_{P-1}^{\frac{2}{3}} - s_0^{\frac{2}{3}}}. \quad (4.29)$$

In terms of the characteristic velocity  $\Gamma$ , we find

$$\Gamma_C = \frac{\sigma_C}{s_{P-1} - s_0} \quad \text{and} \quad \Gamma_D = \frac{2\sigma_D}{3[s_{P-1}^{2/3} - s_0^{2/3}]} . \quad (4.30)$$

#### 4.4.2 Condensational growth

First, the effect of condensational growth is studied, in the absence of nucleation. For this, we consider two initial distributions. First, a simple step function:

$$n_{jump}^0(s) = H(s_{jump} - s) - H(-s) \quad (4.31)$$

with  $s_{jump}$  the position of the discontinuity and  $H(s)$  the Heaviside function, and second a log-normal initial distribution:

$$n_{LN}^0(s) = \frac{1}{\sqrt{2\pi} z \log \sigma_g} \exp \left[ \frac{(\log s - \log \text{CMM})^2}{2 \log^2 \sigma_g} \right] \quad (4.32)$$

with CMM the count median mass and  $\sigma_g$  the geometric standard deviation. We set  $\sigma_g = 4/3$ , which is a popular value for a fixed width droplet size distribution, see [12] and [3]. Based on definition (2.27) we can set the initial distribution in terms of the sectional formulation,  $N_i^0$ . Given Eq. (4.13), the analytical solution becomes

$$f(\zeta, t) = f^0(\zeta - \Gamma t). \quad (4.33)$$

Using (4.11) the distribution  $f(\zeta, t)$  is related to  $n(s, t)$  as

$$f(\zeta, t) = \frac{n(s, t)}{\psi'(s)}, \quad (4.34)$$

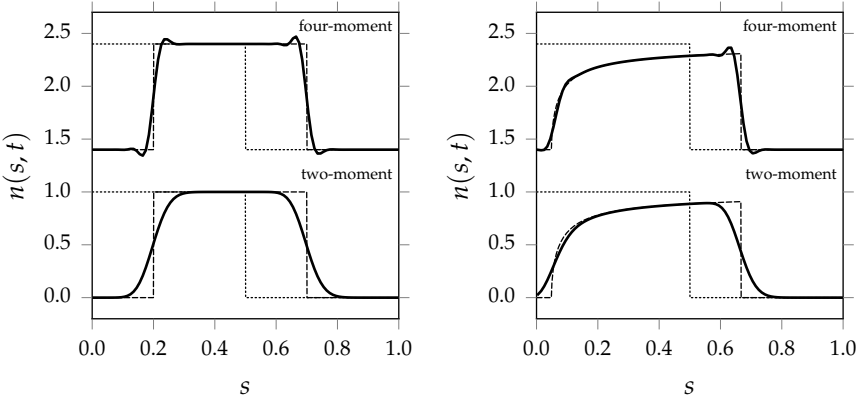


Figure 4.1: Solutions at  $t = 0.2$  for a step function droplet size distribution undergoing constant growth (left) and cube root growth (right), with  $\sigma_C = \sigma_D = 1$ . Shown are the solutions using the two-moment and four-moment scheme, as indicated, vertically offset by 1.2 for visual clarity. The initial condition (...) and analytical solution (--) are also shown. The time step size was  $\Delta t = 10^{-3}$ .

and in a similar way  $f^0$  is related to  $n^0$  as

$$f^0(\zeta - \Gamma t) = \frac{n^0(s_c(t))}{\psi'(s_c(t))}, \quad (4.35)$$

with  $s_c(t) = \psi^{-1}(\zeta - \Gamma t)$  the position on a characteristic as a function of time in  $s$ -space. This gives the analytical solution for the distribution in  $s$ -space at time  $t$

$$n(s, t) = n^0(s_c(t)) \frac{\psi'(s)}{\psi'(s_c(t))}, \quad (4.36)$$

Using for each growth law the corresponding transformation functions, their inverse and the characteristic velocities, (4.29) and (4.30), the analytical solutions for both growth laws become

$$n_C(s, t) = n^0(s - \sigma_C t) \quad \text{and} \quad n_D(s, t) = n^0 \left[ s^{\frac{2}{3}} - \frac{2}{3} \sigma_D t \right]^{\frac{3}{2}} \frac{\sqrt{s^{\frac{2}{3}} - \frac{2}{3} \sigma_D t}}{s^{\frac{1}{3}}}. \quad (4.37)$$

Fig. 4.1 shows the solution for constant and cubic root growth of a jump initial condition at  $t = 0.2$ , with  $\Delta t = 10^{-3}$ ,  $\mathcal{P} = 100$ ,  $y_0 = 0$ ,  $y_{\mathcal{P}} = 1$ ,  $\sigma_C = 1$ ,  $\sigma_D = 1$  and  $s_i$  uniformly distributed across the domain. These parameters are used in the remainder of this text, unless differently specified. Both the two-moment and four-moment schemes show a good agreement with the analytical solution, for both growth laws. The two-moment scheme allows the solution to become diffusive. It was verified that this ‘diffusiveness’ of the solution converges to a maximum when the time

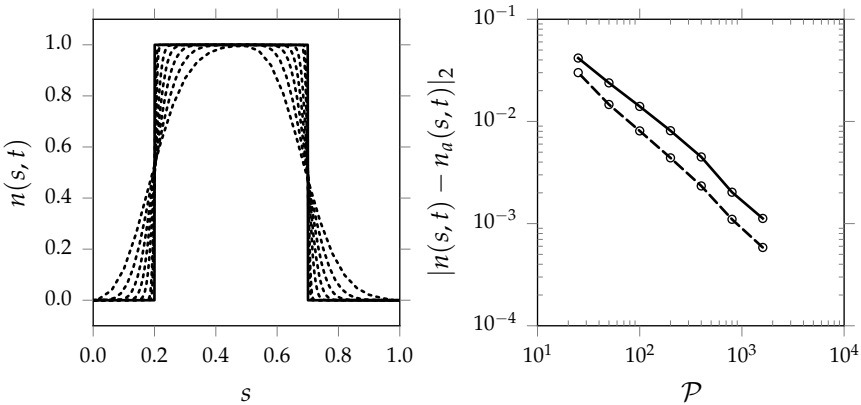


Figure 4.2: Left: the two-moment solutions at  $t = 0.2$  for a step function droplet size distribution undergoing constant growth with  $\sigma_C = 1$ , for  $P = 2^k \times 25$  and  $k = 0, 1, \dots, 6$  ( $\cdots$ ) and the analytical solution ( $-$ ). Right: the convergence of the two-moment ( $-$ ) and four-moment ( $--$ ) solutions corresponding to the left figure, to the analytical solution  $n_a(s, t)$ , as a function of the number of uniformly distributed sections. The time step size was  $\Delta t = 10^{-3}$ .

step size *decreases*, as for a smaller time step size the solution must be redistributed more often, driving the diffusion. The four-moment solution is less diffusive and therefore preserves the discontinuity of the distribution better. However, the four-moment solution allows for negativity, and exhibits over- and undershoot near the discontinuous distribution front. It was verified that the over- and undershoot may be reduced by adopting higher moment schemes, however, positivity can no longer be strictly preserved.

In contrast to the behavior of the solution as a function of  $\Delta t$  with respect to the analytic solution (it becomes more diffusive), we find convergence of the solution to the analytical solution as a function of  $P$ , i.e., the number of sections. Fig. 4.2 shows the two-moment solutions for different numbers of sections, each consecutive solution doubling  $P$ . The two-moment scheme produces, for any  $P$ , a smooth and positive line, whereas the four-moment scheme produces a less-diffusive sharper result but allowing for negativity and oscillations. As Fig. 4.2 (right) shows, both schemes show first order convergence of the  $L^2$ -norm of the difference between the numerical and the analytical solution, as a function of  $P$ . However, the error as quantified by the  $L^2$ -norm is smaller for the four-moment scheme in comparison with the two-moment scheme.

Alternatively to our method, Eq. (4.8) may be integrated in time. For this, as was already mentioned,  $n(s, t)$  must be approximated at each  $y_i$ . Two well-known methods for doing so are the central and upwind interpolation schemes.

First, given (2.27) and assuming that  $n(s, t)$  is constant in the interval  $[y_i, y_{i+1}]$ , we can approximate  $n_i^m$ , i.e., the approximate of  $n(s, t)$  at time level  $m$  and in section

$i$ , as

$$n_i^m = \frac{M_i}{y_{i+1} - y_i}. \quad (4.38)$$

With each  $n_i^m$  known, the central scheme approximates  $n^m(y_i)$  as

$$n^m(y_i) = \frac{n_i^m + n_{i-1}^m}{2} = \frac{1}{2} \left[ \frac{N_i^m}{y_{i+1} - y_i} + \frac{N_{i-1}^m}{y_i - y_{i-1}} \right], \quad (4.39)$$

and the upwind scheme as

$$n^m(y_i) = n_k = \frac{N_k^m}{y_{k+1} - y_k}, \quad (4.40)$$

with

$$k = \begin{cases} i-1, & \text{if } I(y_i, t) \geq 0 \\ i, & \text{otherwise.} \end{cases} \quad (4.41)$$

Expressions (4.39) or (4.40) are introduced in (4.8), which gives a central and upwind discretization for the condensational growth term, respectively. For convenience in implementation, we would like to solve (4.8) explicitly in time. The central scheme, even if it satisfies the Courant-Friedrichs-Lowy (CFL) condition, is known to be unstable. The upwind scheme is stable, known to be diffusive, and restricted by the CFL condition [25]. Our method is not restricted by a CFL condition, and is therefore expected to be more robust. Fig. 4.3 shows the two-moment, four-moment, upwind and central scheme solutions for the droplet growth of a log-normal distribution undergoing constant condensational growth with  $\sigma_C = 1$ ,  $\mathcal{P} = 100$  and  $\Delta t = 10^{-3}$ . Under these conditions, the CFL number, defined as  $CFL = \sigma_C \Delta t / \Delta s$  for constant growth, is equal to  $10^{-1}$ . The solution using the central interpolation scheme shows oscillations in the ‘wake’ of the growing distribution, as was expected due to its unconditional instability. Nevertheless, the droplet distribution is predicted reasonably accurately. The two-moment solution and the upwind interpolation scheme produce the same diffusive solution. The four-moment scheme shows a very good agreement with the analytical solution, apart from a small region left of the distribution in which the four-moment solution becomes negative. We verified that for a fixed time step and an increasing number of sections  $\mathcal{P}$ , the two-moment and four-moment solutions improve in accuracy, as shown by the convergence in Fig. 4.2 (right). This also applies to the solution of both the central and upwind schemes, however, once the CFL number becomes larger than unity a physically reasonable solution is no longer obtained.

In Fig. 4.3 we observe that the solution of the four-moment scheme has a very good agreement with the analytical solution. The scheme has limited artificial diffusion, whereas the two-moment scheme displays considerable diffusive smoothing. The only disadvantage which may keep one from using the four-moment scheme is

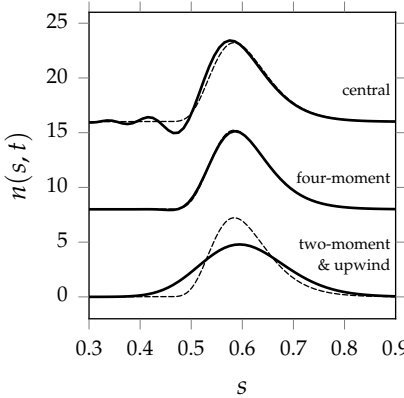


Figure 4.3: Solutions at  $t = 0.4$  for a log-normal droplet size distribution undergoing constant condensational growth, with  $\sigma_C = 1$ ,  $\mathcal{P} = 100$  and  $\Delta t = 10^{-3}$ . Shown are the two-moment and upwind solutions, four-moment and central solutions, as indicated, vertically offset by 8 for visual clarity. The analytical solution is also shown (---).

its inability to strictly preserve positivity. A typical ‘cure’ to this would be to use a limiter scheme; locally revert back to lower-order schemes based on some criterion, to preserve a certain property of the solution. Here, we propose a simple ‘hybrid’ scheme, which does just that: it reverts the four-moment scheme to a two-moment one when the solution becomes negative, as follows.

Given the notation used in (4.16), the contribution to the solution at time level  $m + 1$  of the droplets originally located at  $s_l$  may, for the four-moment scheme, be written as

$$N_k^{m+1} = a_k^{4M} N_l^m, \quad (4.42)$$

with  $a_k^{4M}$  the weights belonging to  $s_l^*$ , the size to which droplets originally at  $s_l$  grew to. The index  $k$  adheres to  $q_l - 1 \leq k \leq q_l + 2$ , for the four-moment scheme. In our hybrid approach, we introduce  $\phi_l$  which allows to balance between four- and two-moment preservation:

$$N_k^{m+1} = \phi_l a_k^{4M} N_l^m + (1 - \phi_l) a_k^{2M} N_l^m. \quad (4.43)$$

For  $\phi_l = 1$  the scheme is four-moment- and for  $\phi_l = 0$  two-moment-preserving. Note that  $a_{q_l-1}^{2M}$  and  $a_{q_l+2}^{2M}$  are zero. Each  $N_i^{m+1}$  retrieves a number of contributions, i.e., droplets which were originally at size  $s_l$  but which grew to, or grew close to,  $s_i$ . We first compute the four-moment conserving solution for any  $l$ . For all  $N_i^{m+1}$  which are negative, we set  $\phi_l$  to zero for all representative sizes which originally held droplets at time level  $m$  which grew into that negative  $N_i^{m+1}$ . Note that for this we must keep track of the ‘connectivity’ between each  $s_l$  at time level  $m$  contributing to  $s_i$  at time level  $m + 1$ . With  $\phi_l$  set, the new ‘hybrid’ solution is computed. The criterion which

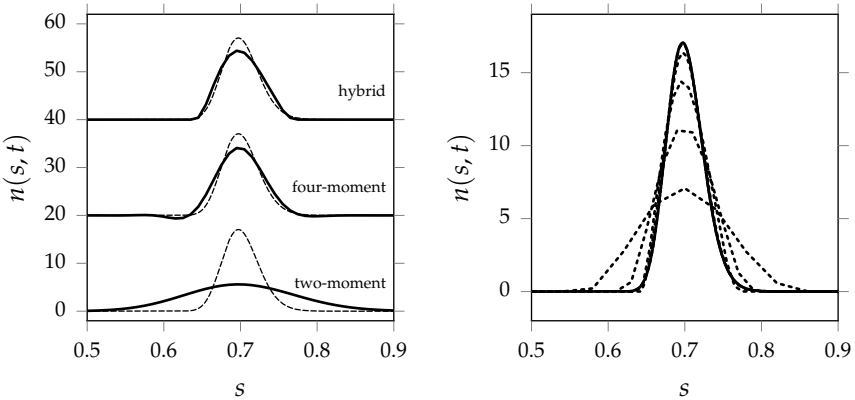


Figure 4.4: Left: solutions at  $t = 0.5$  of a log-normal droplet size distribution with  $\sigma_g = 9/8$ , undergoing constant condensational growth with  $\sigma_C = 1$ ,  $P = 100$  and  $\Delta t = 10^{-3}$ . Shown are the two-moment, the four-moment and the hybrid solutions, as indicated, vertically offset by 20 for visual clarity. The analytical solution is also shown (---). Right: hybrid solutions (···) corresponding to the simulations of the left figure for  $P = 2^k \times 25$  and  $k = 0, 1, \dots, 5$ .

determines the value for  $\phi_l$  depends on the solution at time level  $m + 1$ , which makes (4.43) implicit. Therefore, it is not strictly guaranteed that the new hybrid solution is positive. An extra iteration, i.e., setting all  $\phi_l$  to zero for sections which contributed to remaining negative solutions and recomputing the hybrid solution, remedies this. It is our experience that one extra iteration is sufficient.

Fig. 4.4 shows, along with the two-moment and four-moment-preserving solutions, the hybrid solution for a constant condensational growth law ( $\sigma_C = 1$ ) of a log-normal droplet size distribution with  $\sigma_g = 9/8$ . This geometric standard deviation makes the distribution narrower compared to the previously selected  $\sigma_g$ , which is more challenging for the method. The hybrid solution shows a good agreement with the four-moment solution, while always preserving positivity. The hybrid solution benefits from two worlds: it relies on the two-moment solution when negativity can otherwise not be avoided, and uses the four-moment solution to better preserve sharp gradients in the solution, if possible. Note that when the number of sections is increased, the method automatically produces a more accurate result.

#### 4.4.3 Nucleation and condensational growth

We next consider the numerical solution to the problem of homogeneous simultaneous nucleation and condensation, Eq. (4.6), i.e.,

$$\partial_t f(\zeta, t) + \Gamma \partial_\zeta f(\zeta, t) = J^{\text{nuc}}(t) \delta(\zeta - \zeta^{\text{nuc}}) \quad (4.44)$$

in  $\zeta$ -space, where  $\zeta^{\text{nuc}} = \psi(s^{\text{nuc}})$  is taken as constant. Let us assume that  $f^0(\zeta) = 0$ . A characteristic leaving from  $\zeta^{\text{nuc}}$  at  $t = 0$  has, after some time  $t^*$ , grown to

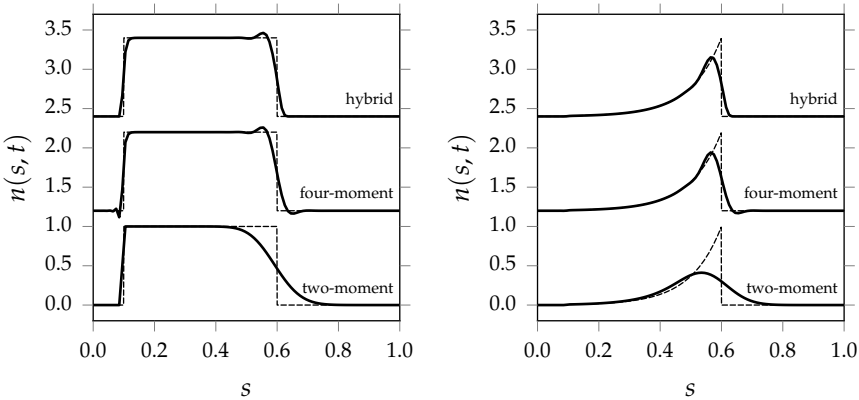


Figure 4.5: Left: solutions of constant condensational growth ( $\sigma_C = 1$ ) of droplets nucleating at  $s^{\text{nuc}} = 0.1$  for constant nucleation ( $J^{\text{nuc}} = 1$ ). Right: the same simulations but for exponentially decaying nucleation, Eq. (4.49). Both figures are for  $\mathcal{P} = 100$ ,  $\Delta t = 10^{-3}$ , at  $t = 0.5$ . The analytical solution (---) is shown and for each scheme the solution is vertically offset by 1.2, for visual clarity.

$\zeta_1 = \zeta^{\text{nuc}} + \Gamma t^*$ . A characteristic leaving a fraction  $dt$  later, will have grown to  $\zeta_2 = \zeta^{\text{nuc}} + \Gamma(t^* - dt)$ . In the time interval  $dt$ , a number of  $J^{\text{nuc}}(t^*) dt$  droplets per unit of volume were nucleated (with  $J^{\text{nuc}}(t)$  a prescribed nucleation rate as a function of  $t$ ). These droplets have grown into  $[\zeta_2, \zeta_1]$ . When integrating  $f(\zeta, t)$  over  $[\zeta_2, \zeta_1]$ , we must recover this droplet number concentration:

$$\int_{\zeta_2}^{\zeta_1} f(\zeta, t) d\zeta = J^{\text{nuc}}(t^*) dt. \quad (4.45)$$

For  $dt \rightarrow 0$ ,  $\zeta_1 - \zeta_2$  goes to zero. Taking the derivative of (4.45) to  $\zeta$  then gives

$$f(\zeta, t) = \frac{J^{\text{nuc}}(t^*)}{\Gamma}, \quad (4.46)$$

where we recall that  $\Gamma = d_t \zeta$  which is constant in time. If at  $t = 0$  nucleation starts and we assume  $f^0(\zeta) = 0$ , then the solution  $f^{\text{nuc}}$  to (4.44) becomes

$$f^{\text{nuc}}(\zeta, t) = \begin{cases} \frac{J^{\text{nuc}}(t^*)}{\Gamma}, & \text{if } \zeta^{\text{nuc}} \leq \zeta \leq \zeta^{\text{nuc}} + \Gamma t \\ 0, & \text{otherwise,} \end{cases} \quad (4.47)$$

where it is assumed that  $\Gamma > 0$  and where  $t^* = (\zeta - \zeta^{\text{nuc}})/\Gamma$ . The solution in terms of the untransformed space  $s$  becomes

$$n(s, t) = f^{\text{nuc}}(\psi^{-1}(s), t)\psi'(s). \quad (4.48)$$

Fig. 4.5 (left) shows the analytical and numerical solutions for constant nucleation rate and constant condensational growth, with  $J^{\text{nuc}} = 1$ ,  $\mathcal{P} = 100$ ,  $\Delta t = 10^{-3}$ ,  $\sigma_C = 1$  and  $s^{\text{nuc}} = 0.1$ , at  $t = 0.5$ . The analytical solution, when starting with a zero initial distribution, is an expanding plateau. The moving discontinuity in  $s$ -space becomes, as was seen before, very diffusive in the two-moment method for the selected time step. The four-moment method approximates the plateau better, but, again, shows oscillations near its sharp moving front. The hybrid method does not exhibit any negativity, but still includes the overshoot in the wake of the moving droplet front. Fig. 4.5 (right) shows, for the same setting as used in Fig. 4.5 (left), the condensational growth of droplets nucleating at  $s^{\text{nuc}} = 0.1$  according to a time-dependent nucleation rate described by

$$J^{\text{nuc}}(t) = \exp(-10 \times t), \quad (4.49)$$

representing exponential decay with a typical time of 0.1. The analytical solution has a discontinuity traveling with velocity  $\Gamma$  through  $\zeta$ -space. The discontinuity is poorly captured by the two-moment preserving scheme, as the solution is very diffusive. The four-moment and hybrid scheme perform better in terms of approximating the discontinuity. Again, we verified that an increase in number of sections leads to an asymptotic convergence towards the analytical solution.

## 4.5 HOMOGENEOUS NUCLEATION AND CONDENSATION

In applications, the condensation and nucleation rates strongly depend on the saturation ratio, which, in turn, depends on quantities such as pressure, temperature and the available amount of vapor. Naturally, the processes of nucleation and subsequent condensation reduce the level of supersaturation, which limits and finally stops those processes. It becomes clear that the mass transport sources  $S_j^{\text{cond}}$  and  $S_j^{\text{nuc}}$ , and their underlying mechanisms, are functions of time. Moreover, nucleation often takes place at droplet sizes much smaller than the matured droplets; condensational transport often spans several decades in the size domain. To test our numerical method, we apply it to this challenging setting.

### 4.5.1 Multi-species nucleation and condensation models

To model the multi-species nucleation rate, we adopt the Classical Nucleation Theory-based (CNT) form as given in [57]. The multi-species condensation rate  $I_j(s, t)$  is given by (see [35] and [57] for details):

$$I_j(s, t) = 2\pi d \mathbb{D}_j^v Y_j^{\text{sat}} \rho \left[ S_j^{\text{sat}} - 1 \right], \quad (4.50)$$

in which the Fuchs and Kelvin correction factors are, for simplicity, set to unity.  $Y_j^{\text{sat}}$  gives the mass fraction associated with saturation over a flat liquid surface under otherwise the same conditions,  $S_j^{\text{sat}}$  is the saturation ratio given by  $Y_j/Y_j^{\text{sat}}$  and  $\mathbb{D}_j^v$  is

the vapor binary diffusivity constant of species  $j$  with respect to the carrier gas. The droplet diameter  $d$  relates to  $s$  as (2.20).

Given (4.50) and (2.20), the condensation rate is proportional to  $s^{\frac{1}{3}}$ . Therefore, we select the Jacobian of the transformation function,  $\psi'(s)$ , to be proportional to  $s^{-\frac{1}{3}}$ . This gives, as was seen before,

$$\psi(s) = \frac{s^{\frac{2}{3}} - s_0^{\frac{2}{3}}}{s_{P-1}^{\frac{2}{3}} - s_0^{\frac{2}{3}}}. \quad (4.51)$$

The total transformed condensation rate is given by  $\Gamma(t) = \psi'(s) \sum_j I_j(s, t)$ , and is, by construction, constant with respect to  $s$ .

We consider a model system of air with perfectly saturated ethanol and propanol vapors, at  $T_0 = 275$  K. We adopt the thermo-physical properties of both alcohols as given in [57]. The mixture is described with Amagat's law, i.e., the total volume of the mixture is equal to the sum of partial volumes. For a system only containing air and the two saturated alcoholic vapors, the mixture density is set using

$$\rho = \left[ \sum_j \frac{Y_j}{\varrho_j^v} \right]^{-1}, \quad (4.52)$$

with  $\varrho_j^v$  the mass density of *pure* species  $j$  in vapor state, at the given temperature. Using in this relation the fact that  $\sum_j Y_j + Z_j = 1$  and the mass fractions  $Y_2$  (ethanol) and  $Y_3$  (propanol) are at saturation, the mixture density becomes

$$\rho = \varrho_j^v - \frac{1}{kT_0} \sum_{j=2}^3 \left[ \frac{\varrho_1^\ell}{\varrho_j^v} - 1 \right] p_j^{\text{sat}} m_j, \quad (4.53)$$

with  $k$  the Boltzmann constant,  $p_j^{\text{sat}}$  the saturation pressure and  $m_j$  the molecular mass. With  $\rho$  known, the mass fractions for the two alcohols may be computed using Antoine's relation [58]:

$$Y_j = \frac{p_j^{\text{sat}} m_j}{\rho k T_0}, \quad (4.54)$$

and the remaining unknown mass fraction of air using  $Y_1 = 1 - Y_2 - Y_3$ . Air is modeled as an ideal gas with a molar weight of 29 g/mole.

#### 4.5.2 Droplet size distribution solutions and sensitivity

We consider the following situation. At  $t = 0$  a saturated mixture is instantly cooled from  $T_0 = 275$  K to  $T_1 = 265$  K. It is assumed that both mixture density and pressure remain constant, however, the saturation pressures of the two species decrease. Both alcohols attain a supersaturated state which allows for nucleation and

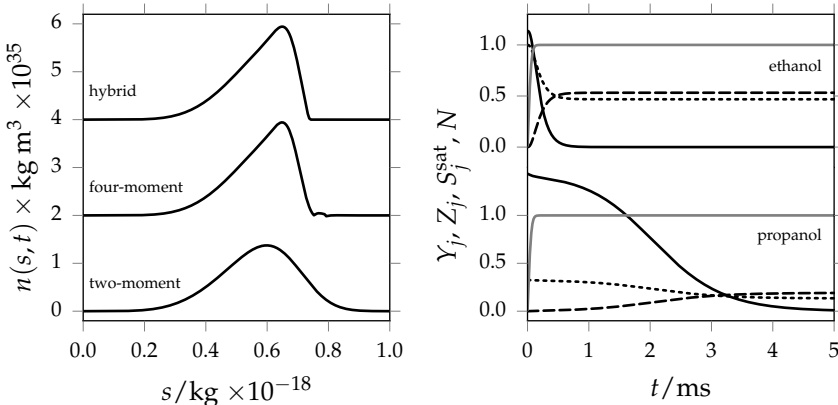


Figure 4.6: A two-species alcohol nucleation and condensation simulation, using  $\mathcal{P} = 200$  (uniform distribution),  $\Delta t = 10^{-6}$  s  $y_0 = 0$  kg and  $y_{\mathcal{P}} = 10^{-18}$  kg. Left: the droplet size distribution at  $t = 10^{-3}$  s for the indicated schemes, each vertically offset by  $2 \times 10^{35}$  for visual clarity. Right: the time-dependent solutions for ethanol and propanol (as indicated ) in terms of their mass fractions  $Y_j$  (···) and  $Z_j$  (---) and saturation ratio  $S_j^{\text{sat}}$  (—). The mass fractions are scaled by  $Y_1(t = 0)$ , and we subtract 1 from the saturation ratios. The gray lines show the total number of droplets in the system scaled by its maximum.

subsequent condensational growth. We discretize the size domain setting  $\mathcal{P} = 200$  with uniformly distributed sections. Using CNT, nucleation occurs for this particular setting at approximately  $8 \times 10^{-24}$  kg, at which clusters contain on the order of 100 molecules. The nucleated clusters are assigned to the first section. They grow to a mass in the order of  $10^{-19}$  kg under the selected conditions. Although containing millions of molecules, these droplets are still at sub micron-scale, in terms of their diameter. Fig. 4.6 (left) shows the droplet size distribution after nucleation and condensation have finished, at  $t = 10^{-3}$  s, for the three proposed schemes. The hybrid scheme preserves the sharp gradient of the droplet front, while not allowing for oscillations near the sharp front in  $n(s, t)$ . In contrast, we observe a considerably more diffusive prediction based on the two-moment scheme and some slight oscillations and change of sign in  $n(s, t)$  when using the four-moment preserving approach. Fig. 4.6 (right) shows, for the hybrid scheme, the transient behavior of the saturation rate and vapor and liquid mass fractions, for both ethanol and propanol, as well as the total number of droplets per unit of volume in the system. Ethanol, having a smaller molecular mass, condenses more rapidly. The condensation of propanol is relatively slow. The composition of droplets, uniform across  $s$ , is initially dominated by ethanol but shifts as time advances to include propanol, too.

The typical size of nucleated droplets is several orders of magnitude smaller than that of the matured droplets. If we would like to accurately resolve all size scales, we must cover several orders of magnitude with the sectional model. A typical approach of doing so is to use a strongly non-uniform sectional division. Here, we

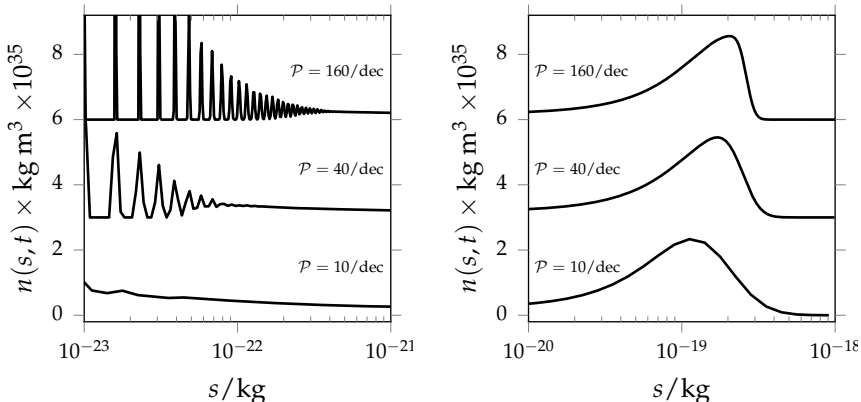


Figure 4.7: Droplet size distribution solutions for a two-species nucleation and condensation simulation using the two-moment scheme and a logarithmic grid. Shown are results at  $t = 1.6 \times 10^{-4}$  s with the time step size set to  $\Delta t = 10^{-7}$  s, for three indicated values of  $\mathcal{P}$  (in number of sections per decade).

select a logarithmically distributed sectional division of discrete droplet sizes. Rather than using a fixed section size, such a grid yields a fixed number of representative size-classes per decade and a uniform distribution in log  $s$ -space. Fig. 4.7 shows, for the two-moment scheme, the results for three logarithmic grids, using 10, 40 and 160 sections per decade, with  $y_0 = 10^{-24}$  kg and  $y_{\mathcal{P}} = 10^{-18}$  kg. The small and large size ranges are shown separately in Fig. 4.7 (left and right, respectively). Results are shown at  $t = 1.6 \times 10^{-4}$  s, which, after inspection of Fig. 4.6 (right), is a point in time at which nucleation is actively taking place. The time step size was set to  $\Delta t = 10^{-7}$  s. With such a rather large time step size, and the fine resolution which the logarithmically distributed sectional grid offers, droplets are nucleated, captured in a section very close to the real size of nucleation  $s^{\text{nuc}}$ , and subsequently convected across several sections within one time step. This can be seen in Fig. 4.7 (left), where the distribution is represented by a number of spikes for the solutions on the finer 40 and 160 sections/decade grids. At each discrete time step a nucleation event takes place, adding new droplets to the section containing size  $s^{\text{nuc}}$ , according to Eq. (4.25). In the next time step, these droplets grow to a new size as given by Eq. (4.15), being displaced a distance in  $s$ -space equal to the time step size  $\Delta t$  times the condensational growth rate. This implies that the spikes in Figure 7a represent discrete nucleation ‘bursts’, while the distance between each spike in size space is governed by the condensation rate. These spikes may have a width larger than one section, as droplets are always distributed after the ‘convection in size space’ step to two or more sections in the two-moment scheme. For the coarse grid, the solution appears as a somewhat smoother line. The larger scales of the distribution into which droplets grow, see Fig. 4.7 (right), is shown to be reasonably accurately resolved with 40 or more sections/decade. For 10 sections/decade, the matured distribution is

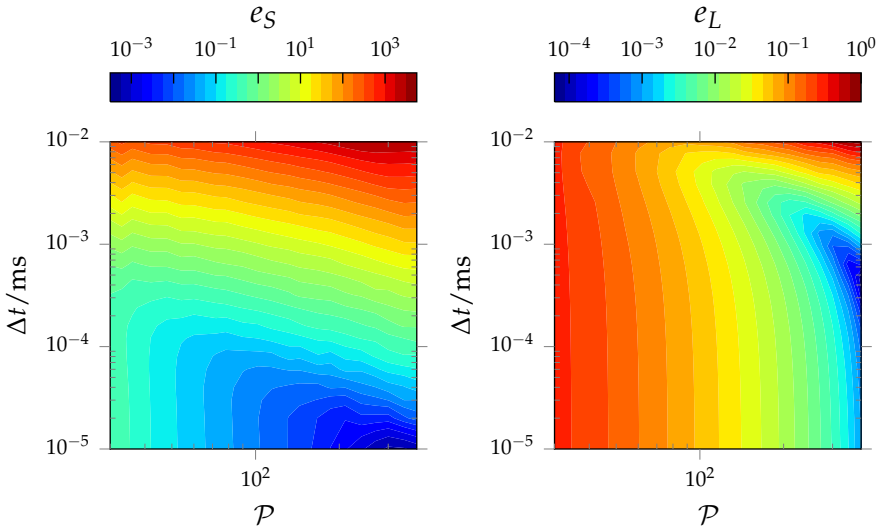


Figure 4.8: The error (4.55) at  $t = 1.6 \times 10^{-4}$  s, using the two-moment scheme. Left: small droplet sizes ( $e_S$ ). Right: large droplet sizes ( $e_L$ ).

predicted with quite some error as the two-moment method is very diffusive.

Fig. 4.7 illustrates an important advantage of our method. Independent of the non-uniformity of the selected sectional grid, a robust solution is produced. Even though for the chosen large time step at small scales the computed distribution is strongly influenced by temporal discretization error, this does not appear to influence the large scale distribution into which most droplets grow. Conversely, if one is interested in the distribution at the smaller scales, an adequately small time step must be chosen. We look into this convergence next.

To investigate the accuracy with which  $n(s, t)$  can be obtained, and the dependence of the accuracy on  $\Delta t$  and  $\mathcal{P}$ , we introduce the scaled error  $e$  with respect to a reference solution:

$$e^2 = \frac{\int_{s_l}^{s_u} [n(s, t) - n_{ref}(s, t)]^2 ds}{\int_{s_l}^{s_u} [n_{ref}(s, t)]^2 ds} = \frac{\sum_i^* [n_i(t) - n_{ref}(s_i, t)]^2 \Delta s_i}{\sum_i^* [n_{ref}(s_i, t)]^2 \Delta s_i}, \quad (4.55)$$

with  $s_l$  and  $s_u$  the lower and upper bound of the domain of interest,  $\sum_i^*$  a summation over all  $i$  adhering to  $s_l \leq s_i \leq s_u$  and  $\Delta s_i = y_{i+1} - y_i$ , the width of section  $i$ . The reference solution  $n_{ref}(s, t)$  is computed with  $\Delta t = 5 \times 10^{-9}$  s and  $\mathcal{P} = 500$  sections, for which the solution was found to be smooth and quite independent of further temporal and sectional refinements. We compute  $e$  for both the small scales ( $s_l = 0$  and  $s_u = 4 \times 10^{-21}$  kg) and the large scales ( $s_l = 4 \times 10^{-21}$  and  $s_u = \infty$  kg), and refer to them as  $e_S$  and  $e_L$ , respectively. Fig. 4.8 shows isolines for  $e_S$  and  $e_L$ , in the

$(\mathcal{P}, \Delta t)$  plane. It is clearly shown that the error in the small scale region is primarily dominated by the time step, in particular if  $\Delta t > 10^{-3}$  ms. We observe that the error becomes quite independent of the chosen grid for sufficiently large  $\Delta t$ ; it only pays off to increase  $\mathcal{P}$  at correspondingly low time step sizes. For the large scales, the dependency of the error is reversed; for approximately  $\Delta t < 10^{-3}$  ms, the error only depends on the number of sections, not on the chosen time step.

Comparing Fig. 4.8 left and right, it can be seen that in the larger scales the error, as expressed by (4.55), is generally smaller than in the smaller scales. The robustness of the characteristics-based solution method makes it possible, when one is only interested in the final distribution at larger scales, to use relatively large time steps. Conversely, to resolve the small scales accurately, a correspondingly small time step must be chosen. Such dependence on  $(\Delta t, \mathcal{P})$ , albeit at lower error levels, also applies to the four-moment and the hybrid method.

#### 4.6 CONCLUSIONS

A new computational method was proposed for the computation of nucleation and subsequent condensational growth. We adopted a fixed sectional approach, which allows for a straight forward extension to a spatially inhomogeneous setting. The droplets are assumed to be ‘internally mixed’, i.e., their composition is independent of droplet size. Condensational growth is solved using the method of characteristics, in which we transform the transport equation for the distribution to a size space in which the characteristics become straight lines. This method, taking advantage of the analytical solution of the hyperbolic convection equation, does not suffer from a time step restriction for condensational growth. During a time step of arbitrary size, droplets are convected along the characteristics, and assigned to sections adjacent to the new size of the droplets. This redistribution of droplets to representative sizes is designed to preserve a pre-specified number of moments of the droplet size distribution, meaning that droplet number concentrations are assigned to sections with weights, such that the total diameter, surface, volume, or other moments of the size distribution are preserved. The time-integration of both the droplet size distribution equation and the vapor and liquid mass fraction equations occurs consistently by construction; any change in mass as described by the size distribution is reflected in the corresponding mass fractions.

We tested the method using a two-moment- and four-moment-preserving scheme, by comparing the numerical results with analytical solutions, using assumed steady condensation and nucleation rates. The two-moment scheme was shown to be quite diffusive on coarse section divisions. The four-moment scheme preserves sharp gradients in the distribution with higher accuracy. However, this method allows for negativity of the size distribution function, which is unphysical. We proposed a hybrid scheme, which locally reverts to the positivity-preserving two-moment scheme, if necessary. The hybrid scheme showed a very good agreement with the

four-moment solution, without suffering from negative solutions, in both a pure condensational growth problem as well as in a nucleation problem.

Finally, the method was applied to a multi-species nucleation and condensation problem. In such a setting the size domain spans several orders of magnitude. We adopted a logarithmic distribution of sections. Given the absence of a time step stability criterion, which is often related to the section sizes, our method was shown to perform well on such logarithmic grids. At small sizes, numerical nucleation pulses are captured accurately, while being propagated to larger sizes, often crossing several sections within one time step. Given the relatively small temporal truncation error in the larger size scales, it is computationally attractive to use large time step sizes. Our method is shown to be capable of doing that.

In this chapter we have presented a numerical method for the computation of nucleation and condensational growth in a sectional formulation. Although only applied to spatially homogeneous settings, the method is designed to be readily extended to spatially inhomogeneous settings. Moreover, the method is compatible with the fixed sectional treatment of coagulation as presented by [10]. In the next chapter, we will modify and apply the method to spatially inhomogeneous, time-dependent settings, incorporating diffusion, convection and coagulation.



# CHAPTER 5

## AEROSOL FORMATION AND TRANSPORT\*

### ABSTRACT

The characteristics-based sectional method (CBSM) offers an Eulerian description of an internally mixed aerosol. In Chp. 4 it was shown to be robust and capable of exact preservation of lower order moments, allowing for highly skewed sectional droplet size distributions. In this chapter we apply CBSM to a spatially varying flow, by incorporating the fractional step method. In this way an accurate time integration of the spatial terms in the transport equations for the velocity, mass fractions and sectional droplet concentrations is achieved. Integrating CBSM into the compressible PISO (Pressure-Implicit with Splitting of Operators) algorithm allows for phase change and corresponding changes in pressure. We apply CBSM to a lid-driven cavity flow. First, the steady state isothermal flow solution is validated against published data. Next, by releasing a saturated vapor into the cavity while cooling the walls, we simulate formation of aerosol. The accuracy of the solution is studied, as well as the performance of the CBSM scheme in the spatially varying context. The solution of the velocity is shown to be accurate, even at CFL (Courant-Friedrichs-Lowy) numbers of unity. The feasibility of the developed method is demonstrated in a 3D complex geometry studying the aerosol generation via nucleation of hot vapors cooled by a dilution stream of cold air in a double-mixing tee system. The sectional approach delivers detailed information about the aerosol formation and size distribution of the droplets in the domain.

### 5.1 INTRODUCTION

In Chp. 4 CBSM was proposed and illustrated in spatially homogeneous conditions of aerosol formation. The current chapter extends this development and presents the corresponding method with which aerosol dynamics can be simulated in heterogeneous situations. This completes the necessary step toward a method that can be applied to realistic conditions of multiphase flow and phase changes. Such application is shown for aerosol formation in a 2D cavity and in a 3D double-mixing tee configuration.

---

\*This chapter is based on Frederix et al. [59]: Application of the characteristics-based sectional method to spatially varying aerosol formation and transport. *Journal of Aerosol Science*, submitted.

The CBSM uses the condensational characteristics in the size domain to solve for nucleation and subsequent condensational growth of droplets. CBSM is based on the sectional formulation of Kumar and Ramkrishna [10], in which each section contains a pre-specified representative size around which droplets are ‘sampled’. By distributing nucleated, grown or coagulated droplets over adjacent sections, one can analytically preserve a pre-selected number of moments of the size distribution. This is essential to conserve number and mass density, or other moments of the distribution. A second advantage which was introduced by CBSM is that, by using an analytic solution for condensational growth through tracking the characteristics of condensation, a robust algorithm is formulated not suffering from a severe time step restriction. Third, CBSM was shown to work on a highly skewed distribution of sections, e.g., a logarithmic distribution, which allows to span many orders of magnitude in the size domain at acceptable costs. To capture nucleation accurately, this was shown to be essential. Finally, through exact moment preservation CBSM may be constructed such that non-negativity of the size distribution solution is guaranteed.

Hitherto, CBSM was only applied to a spatially homogeneous setting, in which the General Dynamic Equation (GDE), Eq. (2.24), for the size distribution reduces to one dimension, i.e., the size coordinate. This simplifies the presentation significantly, as one is only concerned with the size space, not physical space. Also, we did not consider any coupling of the aerosol processes to the fluid flow. In practice, however, condensation and evaporation will have an effect on pressure, velocity and temperature, indicating that CBSM must be embedded in an algorithm to solve for the dynamics of the flow. In this chapter we apply CBSM to a spatially inhomogeneous setting, in which the aerosol mixture is subject to species convection and diffusion. This poses two challenges. First, we would like to retain CBSM’s previously mentioned main strengths in the inhomogeneous setting. Second, we would like to couple the aerosol dynamics to the dynamics of the flow.

The first challenge is addressed by implementing the fractional step method, allowing to time-integrate the transport equations in multiple steps. This allows to isolate ‘internal’ terms from ‘external’ ones, where ‘internal’ refers to an exclusive dependence on the droplet size. Roughly speaking, we first convect and diffuse, and then nucleate, condense and coagulate. The sum of the internal and external contributions yields, within one time step, an approximate solution at the end of the time step. An additional benefit of this approach is that the time integration of the convective part is not constrained by the explicit integration of the condensational growth as is done in CBSM. In fact, any suitable time integration scheme may be selected to approximate the change of mass concentrations due to convection or diffusion. The second challenge is addressed by a proper integration of CBSM in the compressible PISO algorithm [15, 13, 12] (see Chp. 3). At both the PISO predictor level and subsequent corrector levels CBSM is taken into consideration, as the condensation and nucleation confront us with transport between different phases, which may lead, on account of the mixture equation of state, to a change in pressure. This possibly

drives the flow, and causes a coupling between aerosol processes and fluid transport.

We apply CBSM to spatially varying flow using the fractional step method. All ‘external’ contributions are time-integrated using the  $\theta$ -scheme [25], formally giving second order accuracy. We apply the method to lid-driven cavity flow. First, the method is validated against incompressible steady state numerical cavity flow solutions of Erturk et al. [60] and Ghia et al. [61]. At constant temperature and relatively small Reynolds numbers, we find a very good agreement. Next, we advance to a more specific setting in which an amount of saturated vapor is released in the cavity, while the cavity walls are cooled. This leads to nucleation of droplets near the walls, and subsequent condensational growth. We use a logarithmic distribution of sections, such that nucleation may be captured accurately while also the much larger condensational scales are retained accurately. We first study qualitatively the production of aerosol by considering the droplet size distribution along the horizontal and vertical centerlines. We demonstrate that, by using the sectional formulation and the logarithmic distribution of sections, 1) aerosol is captured accurately at small droplet sizes and 2) the droplet size distribution can be completely recovered from the sectional data at any discrete spatial position and in time.

To illustrate the applicability of the method, we also apply the method to aerosol nucleation in a double-mixing tee, in which a hot saturated vapor is diluted by two perpendicular and opposite cold dilution flows. We show that detailed information about the droplet size distribution can be recovered.

The layout of this chapter is as follows: in Sec. 5.2 a detailed description of the numerical method is given. A numerical study of the accuracy and robustness of the method is given in Sec. 5.3 and Sec. 5.4, in which 2D and 3D examples of complex flows with nucleating aerosols are presented. Concluding remarks are collected in Sec. 5.5.

## 5.2 EXTENSION OF THE CBSM TO A SPATIALLY VARYING SETTING

In Chp. 2 we introduced an Eulerian aerosol model applicable to  $\mathbb{R}^M$ . In Chp. 4 the model was reduced to a spatially homogeneous setting such that, among other variables, the size distribution function  $n(s, \mathbf{x}, t)$  became  $n(s, t)$ . In that homogeneous setting CBSM was formulated. In the current chapter the spatial dimensionality of the model as introduced in Chp. 2 is retained. This means that the continuity equation (2.9) holds, as well as the transport equations for  $Y_j$  and  $Z_j$ , Eq. (2.13a) and Eq. (2.13b), respectively. For the droplet size distribution  $n(s, \mathbf{x}, t)$  the full spatially inhomogeneous GDE is adopted. This means that Eq. (4.6) can be written in the full form Eq. (2.24) where we specify the source term  $J(s, \mathbf{x}, t)$  as

$$\begin{aligned}\partial_t n(s, \mathbf{x}, t) = & -\nabla \cdot [\mathbf{u}n(s, \mathbf{x}, t)] - \partial_s[I(s, \mathbf{x}, t)n(s, \mathbf{x}, t)] \\ & + J^{\text{nuc}}(\mathbf{x}, t)\delta(s - s^{\text{nuc}}(t)) + J^{\text{coa}}(s, \mathbf{x}, t),\end{aligned}\quad (5.1)$$

with  $I(s, \mathbf{x}, t)$  the condensation rate and  $J^{\text{nuc}}(\mathbf{x}, t)$  the nucleation rate, both already introduced in Sec. 4.2, and  $J^{\text{coa}}(s, \mathbf{x}, t)$  the coagulation rate.

The  $j$ th species vapor-to-liquid mass transfer rate  $S_j$  present in (2.13) contains the contributions of condensation and nucleation, i.e.,

$$S_j = S_j^{\text{cond}} + S_j^{\text{nuc}}. \quad (5.2)$$

As shown in Chp. 4, these are related to the  $j$ th species  $s$ -sized droplet condensation rate  $I_j(s, \mathbf{x}, t)$  and nucleation rate  $J^{\text{nuc}}(\mathbf{x}, t)$  as

$$S_j^{\text{cond}} = \int_0^\infty I_j(s, \mathbf{x}, t) n(s, \mathbf{x}, t) ds \quad (5.3a)$$

$$S_j^{\text{nuc}} = s_j^{\text{nuc}}(t) J^{\text{nuc}}(\mathbf{x}, t), \quad (5.3b)$$

with  $s_j^{\text{nuc}}$  the mass of species  $j$  in a so-called critical cluster of nucleation.

The coagulation source term in (5.1) is, in the limit of a continuous distribution, given by [2]:

$$\begin{aligned} J^{\text{coa}}(s, \mathbf{x}, t) = & \frac{1}{2} \int_0^s \beta(\tilde{s}, s - \tilde{s}) n(s, \mathbf{x}, t) n(s - \tilde{s}, \mathbf{x}, t) d\tilde{s} \\ & - \int_0^\infty \beta(s, \tilde{s}) n(s, \mathbf{x}, t) n(\tilde{s}, \mathbf{x}, t) d\tilde{s}, \end{aligned} \quad (5.4)$$

in which the first integral accounts for freshly created  $s$ -sized droplets by coagulation of two smaller droplets, the second integral for the removal of  $s$ -sized droplets by coagulation with any other droplet and  $\beta(s, s')$  the coagulation kernel for the coagulation of a  $s$ -sized and  $s'$ -sized droplet. For the coagulation kernel we adopt the description given by Lee and Chen [62]. Following [35], the condensation rate is given by Eq. (4.50) and the multi-species nucleation rate is given in [57].

The well-known compressible PISO method is extended to incorporate CBSM. To use the techniques presented in Chp. 4 without further modification, we must isolate the spatially independent (i.e., independent with respect to physical space) contributions in (2.13a), (2.13b) and (5.1) from the spatial ones. We use the fractional step method for this, incrementally ‘adding’ each right-hand side contribution to the solution.

### 5.2.1 Fractional steps in the $\theta$ -method

Let us consider the following abstract PDE:

$$\partial_t u(\mathbf{x}, t) = f_1(u(\mathbf{x}, t)) + f_2(u(\mathbf{x}, t)), \quad (5.5)$$

in which the rate of change of an unknown  $u(\mathbf{x}, t)$  depends on two source terms  $f_1$  and  $f_2$ , representing spatially dependent (e.g., convection and diffusion) and spatially independent (e.g., condensation, nucleation and coagulation) sources, respectively.

We would like to time-integrate the contribution of  $f_1$  with the  $\theta$ -scheme [25], in which the contribution of  $f_1$  is evaluated by a fraction of  $\theta$  at the new time level and a fraction of  $(1 - \theta)$  at the old time level. This allows for second order convergence if  $\theta = \frac{1}{2}$  [25]. The contribution of  $f_2$  is taken explicitly. This choice is motivated by the fact that CBSM treats condensational growth and nucleation explicitly. We find

$$\frac{u^{m+1} - u^m}{\Delta t} = \theta f_1(u^{m+1}) + (1 - \theta) f_1(u^m) + f_2(u^m), \quad (5.6)$$

where  $u$  is discretized in time on  $t^m$  and  $t^{m+1} = t^m + \Delta t$ . Equivalent to (5.6) we can find  $u^{m+1}$  in two fractional steps:

$$\frac{\tilde{u}^{m+1} - u^m}{\Delta t} = \theta f_1(u^{m+1}) + (1 - \theta) f_1(u^m) \quad (5.7a)$$

$$\frac{u^{m+1} - \tilde{u}^m}{\Delta t} = f_2(u^m), \quad (5.7b)$$

where  $\tilde{u}^{m+1}$  is an intermediate solution. It is easy to verify that when  $\tilde{u}^{m+1}$  is eliminated from (5.7), equation (5.6) is obtained. The fractional step-form allows for the implementation of two separate solution algorithms, e.g., CBSM can be used to solve (5.7b). Note, however, that (5.7a) represents a three-point scheme in time if  $\theta > 0$  yielding unknowns at time level  $t^{m+1}$  and an intermediate time  $\tilde{t}^{m+1}$ . If one wants to successively solve (5.7a) and (5.7b)—which is desirable here, to implement CBSM—the  $f_1(u^{m+1})$  contribution must be iteratively updated by a previous iterative solution of (5.7b) for  $u^{m+1}$ . Let  $k = 1, 2, \dots, \mathcal{C}$  denote the iteration level, which is the same definition of  $k$  as used in Sec. 3.3. We then propose the following iterative scheme:

$$\frac{\tilde{u}^{(k)} - u^m}{\Delta t} = \theta f_1(u^{(k-1)}) + (1 - \theta) f_1(u^m) \quad (5.8a)$$

$$\frac{u^{(k)} - \tilde{u}^{(k)}}{\Delta t} = f_2(u^m), \quad (5.8b)$$

where superscript  $(k)$  denotes<sup>†</sup> the  $(k)$ th iteration level. For  $k = 1$  the  $\theta$ -term in (5.8a) contains  $u^{(k-1)}$  which is unavailable. We set this term to  $\tilde{u}^{(k)}$ , meaning that for the first iteration (5.8a) becomes implicit with respect to  $\tilde{u}^{(k)}$ . This choice will be motivated later. For  $k > 1$  the first term in the right-hand side of (5.8a) is explicitly computed using the solution for  $u$  at the previous iteration, i.e.,  $u^{(k-1)}$ . At the final iteration the solution is accepted as the ‘final answer’, i.e.,  $u^{m+1} = u^{(\mathcal{C})}$ . For sufficiently large  $\mathcal{C}$ ,  $u^{(\mathcal{C}-1)} \approx u^{(\mathcal{C})} = u^{m+1}$ , and (5.8) becomes of the desired form (5.7).

---

<sup>†</sup>We use parenthesis here to separate the notations for the iteration level from the notation of the discrete time level.

### 5.2.2 Implementation of the fractional step method in PISO

In the compressible PISO algorithm for aerosol dynamics a solution is found to the set of equations (2.9), (2.10) and (2.12) in a segregated way, by means of an implicit predictor step and a number of corrector steps, see Chp. 3. The fact that iterations are required to find an acceptable solution allows to integrate the  $\theta$ -method-based fractional step scheme in a straightforward way. Let us consider the  $j$ th species mass fraction transport equations, written in short-hand notation as:

$$\partial_t(\rho Y_j) = f_1(Y_j) + f_2(Y_j) \quad (5.9a)$$

$$\partial_t(\rho Z_j) = g_1(Z_j) + g_2(Z_j), \quad (5.9b)$$

where  $f_1(Y_j)$  and  $g_1(Z_j)$  contain the effects of spatial convection-diffusion and  $f_2(Y_j)$  and  $g_2(Z_j)$  the effects of condensation-nucleation, and the GDE written as

$$\partial_t(\rho M_i) = h_1(M_i) + h_2(M_i) + h_3(M_i), \quad (5.10)$$

with  $h_1(M_i)$ ,  $h_2(M_i)$  and  $h_3(M_i)$  the effects of spatial convection, condensation-nucleation and coagulation, respectively. Here, we formulated the GDE in terms of sectional droplet number concentration  $M_i$  as is detailed in Sec. 2.5. The solution of the mass fractions is coupled to pressure through the equation of state (2.8). This means that (5.9) must be integrated into PISO. Following closely the scheme proposed in the previous section, we again use iterative level  $k$  where  $k = 1$  now is the so-called *implicit predictor step* and  $k > 1$  are the *explicit corrector steps*, analogously to Chp. 3. Using

$$\frac{\rho^{(k)} \tilde{Y}_j^{(k)} - \rho^m Y_j^m}{\Delta t} = \theta f_1(Y_j^{(k-1)}) + (1 - \theta) f_1(Y_j^m) \quad (5.11a)$$

$$\rho^{(k)} \frac{Y_j^{(k)} - \tilde{Y}_j^{(k)}}{\Delta t} = f_2(Y_j^m). \quad (5.11b)$$

We propose the following algorithm:

- *First iteration: semi-implicit predictor step,  $k = 1$ .* At this level the  $(k-1)$ th iteration level required in the right-hand side of (5.11a) is unavailable. Instead, we solve

$$\frac{\rho^{(1)} \tilde{Y}_j^{(1)} - \rho^m Y_j^m}{\Delta t} = \theta f_1(\tilde{Y}_j^{(1)}) + (1 - \theta) f_1(Y_j^m) \quad (5.12a)$$

$$\rho^{(1)} \frac{Y_j^{(1)} - \tilde{Y}_j^{(1)}}{\Delta t} = f_2(Y_j^m). \quad (5.12b)$$

In the right-hand side the  $\theta$ -term depends implicitly on  $\tilde{Y}_j^{(1)}$ . This choice extends

from the idea that in PISO first an implicit predictor is performed. Also, due to this choice (5.12) reduces to the exact PISO form when  $f_2 = 0$ . Density  $\rho^{(k)}$  in (5.11) is set to  $\rho^{(1)}$  (i.e., the first prediction for density) in agreement with the PISO algorithm from Chp. 3. To solve (5.12b) we use CBSM as discussed in Chp. 4.

- *Second iteration: first explicit corrector step,  $k = 2$ .* Before solving equation (5.11) the mixture compressibility is updated and the pressure equation is solved to find a corrected pressure  $p^{(2)}$  and corresponding density  $\rho^{(2)}$ , see Sec. 3.3. This density is used to find  $Y_j^{(2)}$ , solving

$$\frac{\rho^{(2)} \tilde{Y}_j^{(2)} - \rho^m Y_j^m}{\Delta t} = \theta f_1(Y_j^{(1)}) + (1 - \theta) f_1(Y_j^m) \quad (5.13a)$$

$$\rho^{(2)} \frac{Y_j^{(2)} - \tilde{Y}_j^{(2)}}{\Delta t} = f_2(Y_j^m), \quad (5.13b)$$

where the right-hand side of (5.13a) is now completely explicit. We use CBSM to solve (5.13b).

- *$k$ th iteration:  $(k - 1)$ th explicit corrector step.* The form (5.11) is used with the  $\theta$ -term in the right-hand side of (5.11a) depending explicitly on the previous iteration of the solution. We use CBSM to solve (5.11b).

In an obvious and similar way this approach is applied to integrate equations (5.9b) and (5.10) into PISO, with the only difference that the coagulation source term  $h_3$  in Eq. (5.10) is incorporated in a third fractional step which is performed only once after the PISO correctors. As coagulation has no effect on the mixture properties (mass fractions remain the same), coagulation creates no coupling with other equations, and can therefore be solved separately. For this, we use the method as proposed by Kumar and Ramkrishna [10], which integrates seamlessly with the proposed sectional formulation.

For the discretization of all transport equations we embrace the finite volume framework as implemented in OpenFOAM and as introduced in Chp. 3. Using Gauss's theorem, the divergence terms and Laplacians are rewritten to cell-surface integrals. As OpenFOAM offers a collocated cell-centered framework, we must interpolate to the cell faces. For the Laplacian terms, as well as the divergence terms for velocity and temperature and the gradient of pressure, we use the linear interpolation scheme. For the treatment of the divergence terms for the  $Y_j$ ,  $Z_j$  and  $M_i$  transport equations, we prefer, out of physical considerations, a positivity-preserving scheme. The central scheme is known to allow negativity. Apart from the upwind scheme, there are numerous limiter schemes available in OpenFOAM which preserve positivity. These schemes locally reduce to an upwind interpolation, depending on the local ratio of successive gradients of the solution such that the solution remains total

variation diminishing. However, the limiter function may yield a different value for each  $Y_j$ ,  $Z_j$  and  $M_i$ , adding different amounts of diffusion per solution field. This means that different interpolations are used, possibly breaking consistency in terms of (2.2) and (2.31). A ‘global’ limiter should be designed, yielding the same limiter value for each field. However, this is beyond the scope of this chapter. Therefore, we adopt the upwind scheme for the interpolation in the divergence terms for  $Y_j$ ,  $Z_j$  and  $M_i$ , giving a diffusive but consistent and non-negative solution.

The PISO convergence criterion is based on the pressure equation residual as defined in [12]. In the remainder of this chapter we set the PISO convergence criterion to  $10^{-7}$  Pa, which was shown to be sufficient in [12]. Since the total pressure is in the order of  $10^5$  Pa, this convergence criterion gives, roughly speaking, a precision of approximately 12 decimals in  $p$ . For practical purposes this is an unnecessarily large reduction of the splitting error. However, for the resolution studies presented later on this high accuracy avoids that the splitting error ‘overshadows’ the temporal and spatial discretization errors.

For the time discretization we set  $\theta = \frac{1}{2}$ , effectively yielding the Crank-Nicolson scheme [25].

### 5.3 AEROSOL FORMATION AND TRANSPORT IN A LID-DRIVEN CAVITY FLOW

In this section the aerosol model and the PISO-integrated CBSM are applied to the canonical problem of two-dimensional lid-driven cavity flow. This problem is well known, and extensively studied in literature concerning steady flow in an incompressible context. Although we assume a compressible description of the flow, in the limit of isothermal low Mach flow our steady state solutions are expected to be close to the incompressible ones. Ghia et al. [61] provide accurate steady state numerical solutions for incompressible cavity flow at various Reynolds numbers. Many other authors have done similar studies, see for example Erturk et al. [60] for an overview. These benchmark data allow for a validation of our numerical solution of the lid-driven cavity flow.

Having established a foundation for the steady-state solution, we study the transient flow, starting from a quiescent state, and include the formation, evolution and transport of aerosol. Using a typical case, the aerosol processes are illustrated and the resulting droplet size distributions are studied. We investigate dependence of the solution, in terms of the formed aerosol, on the CBSM scheme, number of sections  $\mathcal{P}$ , time step size  $\Delta t$  and grid cell size  $\Delta x$ . The study of this problem assists in 1) establishing confidence in the method and 2) to show control of the numerical error.

#### 5.3.1 Validation of two-dimensional cavity flow solution

In the remainder of this section we consider the benchmark data as presented by Erturk et al. [60]. Their data was, in turn, validated against those of Ghia et al. [61]. We consider Reynolds number  $Re = 1000$  and  $Re = 5000$ .

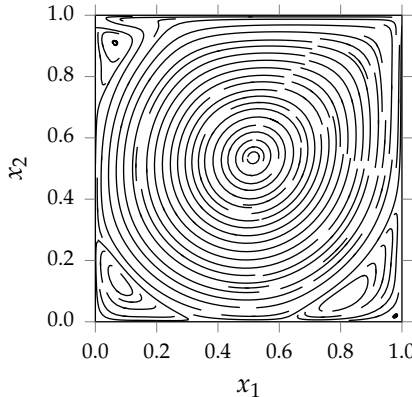


Figure 5.1: Streamlines of the steady state solution for  $Re = 5000$ . The simulations was run using a uniform  $256^2$  grid, and  $\max(\text{CFL}) = 0.5$ .

<b>grid</b>	$e_{hor}$	<b>order</b>	$e_{ver}$	<b>order</b>
$32^2$	0.1665		0.1448	
$64^2$	0.0496	1.832	0.0440	1.814
$128^2$	0.0133	1.931	0.0119	1.926
$256^2$	0.0027	2.213	0.0024	2.213

Table 5.1: Convergence of  $e_{hor}$  and  $e_{ver}$  for a grid cell size sequence, using a  $512^2$  mesh as reference solution at  $Re = 1000$ .

Fig. 5.1 shows the typical geometry of the lid-driven cavity. The size of the cavity is here set to  $L = 1$  m. Moreover, the velocity of the lid is set to  $\mathbf{u} = (1, 0)$  m/s. If we set the density of the fluid inside the cavity to unity too, the definition of the Reynolds number reduces to  $Re = 1/\mu$ . By setting the viscosity of the fluid we have control over the flow Reynolds number.

We specify no-slip boundary conditions for velocity and zero-gradient boundary conditions for pressure. At  $t = 0$  s we have  $\mathbf{u} = 0$  m/s and set the lid in motion instantly. Temperature is kept uniform at the walls.

Fig. 5.1 shows the steady state streamlines of the flow for  $Re = 5000$ , at constant temperature, computed using a uniform  $256^2$  grid and a variable time step size  $\Delta t$  restricted by  $\max(\text{CFL}) = 0.5$ . Qualitatively, the three corner vortices resemble those shown in [60] well. Fig. 5.2 shows the perpendicular velocity at the horizontal and vertical centerlines of the cavity flow, at steady state for  $Re = 1000$  and  $Re = 5000$ , along with data points from [60]. Even though we adopt a compressible formulation, a good visual agreement is found between our simulated flow and the incompressible steady state solutions of [60].

These results were obtained using a uniform  $256^2$  grid. To assess the quality of

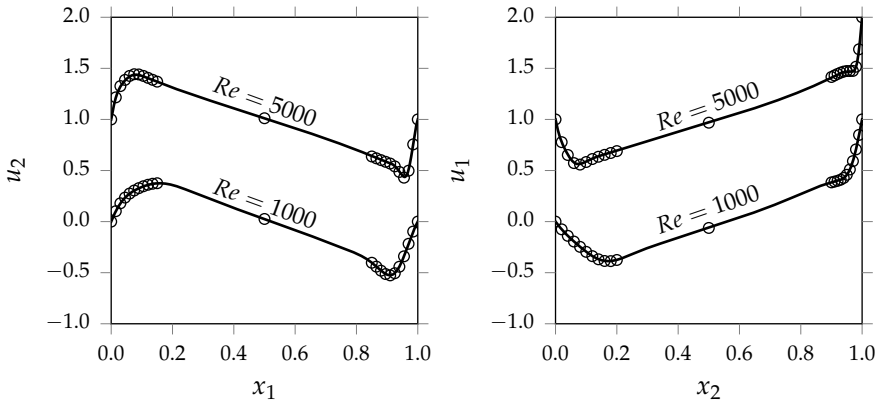


Figure 5.2: Left: the  $x_2$ -component of the velocity along the horizontal centerline. Right: the  $x_1$ -component of the velocity along the vertical centerline, for two Reynolds numbers. The data points ( $\circ$ ) are taken from [60]. The simulations were run using a  $256^2$  grid, and  $\max(\text{CFL}) = 0.5$ . The curves for  $Re = 5000$  are elevated by 1 for visual clarity.

the grid, we introduce convergence measures  $e_{hor}$  and  $e_{ver}$ , defined as

$$e_{hor}^2 = \frac{\int_0^L [u_2 - u_2^{\text{ref}}]^2 dx}{\int_0^L [u_2^{\text{ref}}]^2 dx} \quad (5.14a)$$

$$e_{ver}^2 = \frac{\int_0^L [u_1 - u_1^{\text{ref}}]^2 dy}{\int_0^L [u_1^{\text{ref}}]^2 dy}, \quad (5.14b)$$

where  $\mathbf{u} \equiv (u_1, u_2)$  and  $\mathbf{u}^{\text{ref}}$  a reference solution. Eq. (5.14a) is evaluated at  $x_2 = L/2$  and Eq. (5.14b) at  $x_1 = L/2$  with  $\mathbf{x} \equiv (x_1, x_2)$ . Tbl. 5.1 shows  $e_{hor}$  and  $e_{ver}$  for four different grids, with respect to a reference solution taken at a fine uniform  $512^2$  grid. Both measures decrease approximately at second order with an increase in the number of grid points. For the  $128^2$  grid both convergence measures are approximately 1%, indicating that the solution for velocity is, with respect to the chosen grid, represented quite accurately.

### 5.3.2 Aerosol dynamics in lid-driven cavity flow

Having studied and validated the solution of our method for the isothermal flow problem, we now introduce aerosol formation through nucleation, aerosol evolution through condensation and aerosol transport. We do this by starting with a quiescent state in which a certain amount of vapor is present. As the lid of the cavity sets the mixture in motion, it is also cooled by an imposed lower boundary temperature. Conditions are such that the vapor becomes supersaturated, allowing for nucleation and subsequent condensational droplet growth. We consider, for

variable	unit	IC	BC
$T$	K	$T_0$	$T_\infty$
$\mathbf{u}$	m/s	(0, 0)	(1, 0) for $x_2 = L$ , (0, 0) for $x_2 \neq L$
$p$	Pa	$10^5$	zero gradient
$Z_{DBP}$	-	0	zero gradient
$M_i$	$\text{kg}^{-1}$	0	zero gradient
$Y_{DBP}$	-	$Y_{DBP}^{\text{sat}}(T_0)f(\mathbf{x})$	zero gradient
$Y_{air}$	-	$1 - Y_{DBP}$	zero gradient

Table 5.2: List of initial conditions (IC) and boundary conditions (BC) for the cavity. The BCs apply for  $\mathbf{x} = (x_1, 0), (x_1, L), (0, x_2), (L, x_2)$ .

convenience, a single-species mixture of DBP (Dibutyl Phthalate) vapor with air. Rather than subscript  $j$ , we use  $_{air}$  and  $_{DBP}$  to denote species-specific variables. We use the physiochemical properties as specified in [12].

Tbl. 5.2 shows a list of initial and boundary conditions. The mixture, initially at  $T_0 = 373.15$  K, is cooled by setting the temperature of the walls to  $T_\infty = 273.15$  K at  $t = 0$ . At  $T = T_0$  the saturation mass fraction of DBP in air is given by  $Y_{DBP}^{\text{sat}}(T_0)$ . To avoid heavy aerosol formation at the wall,  $Y_{DBP}$  is initially set to  $Y_{DBP}^{\text{sat}}(T_0)$  weighted by a scaling field  $f(\mathbf{x})$ , adhering to

$$f(\mathbf{x}) = \max\left[1 - \frac{2|\mathbf{x} - \mathbf{x}_c|}{L}, 0\right], \quad (5.15)$$

with  $\mathbf{x}_c = \frac{1}{2}(L, L)$ . This creates a ‘cone’ of vapor concentration with zero vapor concentration at the walls. Through vapor diffusion, however, nucleation is still expected to occur at the wall.

The mass of DBP is small for the given initial conditions ( $\max(Y_{DBP}) \approx 8.65 \times 10^{-4}$ ). If we approximate the mixture as pure air, then using the physiochemical properties given in [12] the Reynolds number of the flow becomes  $Re = 1.927 \times 10^7 L/T$ . We set  $L = 0.075$  m to achieve a Reynolds number of approximately 5000 at lower temperatures.

In classical nucleation theory the mass of nucleation  $s^{\text{nuc}}$ , also referred to as the critical cluster or nucleus size, is given by [2]:

$$s^{\text{nuc}} = \frac{\pi}{6} \left[ \frac{4\sigma V_m}{\ln(S)k_B T} \right]^3 \varrho_{DBP}^\ell, \quad (5.16)$$

where  $\sigma$  is the surface tension,  $V_m$  the molecular volume,  $S^{\text{sat}}$  the saturation ratio and  $k_B$  the Boltzmann constant. When saturation is large the critical cluster size decreases. Theoretically, the max saturation which may be achieved is  $\max S^{\text{sat}} =$

$Y_{DBP}^{\text{sat}}(T_0)/Y_{DBP}^{\text{sat}}(T_\infty)$ , i.e., in the case of an instant cooling from  $T_0$  to  $T_\infty$  at  $\mathbf{x}_c$ . Using this together with Eq. (5.16) gives an estimate for the smallest droplet sizes which we must resolve in order to capture nucleation. In our setting,  $\min(s^{\text{nuc}})$  is approximately  $10^{-24}$  kg. In practice it suffices to set the lower boundary of the first section, i.e.,  $y_0$ , to  $10^{-23}$  kg. An estimate for the upper boundary of the last section is more difficult to make, since the maximum droplet size depends on a complex interaction of nucleation, condensation and coagulation, which, in turn, depend on a non-trivial development of the temperature and flow in the cavity. In the remainder of this section we set the upper boundary of the last section to  $y_P = 10^{-15}$  kg. We verified that for this setting less than 1% of the droplet mass grows beyond this size. Given the large range in possible droplet scales, i.e.,  $10^{-23} \leq s \leq 10^{-15}$ , we use a logarithmic distribution of section sizes and assign a fixed number of sections per decade. This was shown to give good results for capturing spatially homogeneous nucleation and condensation in Chp. 4.

Fig. 5.12 shows development of the temperature and aerosol mixture at three instants  $t^* = 3, 4, 5$ , where  $t^*$  is the non-dimensional time, defined as

$$t^* = \frac{tU}{\pi L}, \quad (5.17)$$

i.e., the time  $t$  scaled by the approximate time of one revolution in the steady state. In this equation  $U$  is the magnitude of the velocity of the cavity lid. The flow transports the vapor to the right wall, at which nucleation and subsequent condensation starts, enabled by the lower temperature near the wall. At  $t^* \approx 3$ , the initially generated aerosol droplets complete a rotation through the cavity. We verified that for  $t \rightarrow \infty$ , the mean temperature reduces to  $T_\infty$ . Moreover, because of the dependence of density on temperature, the pressure drops too.

Fig. 5.3 shows the spatial average of the scaled temperature  $\bar{T}^*$ , scaled pressure  $\bar{p}^*$ , scaled DBP vapor and liquid mass fractions  $\bar{Y}^*$  and  $\bar{Z}^*$ , respectively, and the standard deviation of the scaled temperature,  $\sigma(T^*)$ , all as a function of scaled time  $t^*$ . These scaled quantities are defined as follows

$$T^* = \frac{T - T_\infty}{T_0 - T_\infty}, \quad p^* = \frac{p - p_\infty}{p_0 - p_\infty}, \quad Y^* = \frac{Y_{DBP}}{Y_0}, \quad Z^* = \frac{Z_{DBP}}{Y_0}, \quad (5.18)$$

with  $p_0$  the initial pressure,  $p_\infty$  the static pressure of the mixture at  $T_\infty$  and  $Y_0$  the saturation mass fraction of DBP at  $T_0$ . Both the spatially averaged pressure and temperature are shown to decrease towards their theoretical steady state solutions  $T_\infty$  and  $p_\infty$ , or,  $T^* = 0$  and  $p^* = 0$ . The standard deviation of temperature also decreases, albeit slowly. The majority of the exchange of DBP vapor to liquid droplets occurs within the first two time units, as is shown by the spatial averages of  $Y^*$  and  $Z^*$ .

In each computational cell and at any discrete time the droplet size distribution, expressed in sections, is known. From the sectional data the four-dimensional

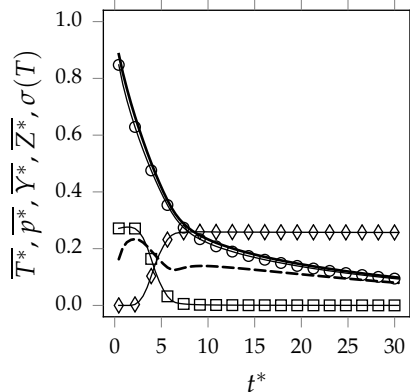


Figure 5.3: Spatial averages of  $T^*$  (solid),  $p^*$  ( $\circ$ ),  $Z^*$  ( $\diamond$ ) and  $Y^*$  ( $\square$ ), and spatial standard deviation of  $T^*$  (---), as a function of non-dimensional time  $t^*$ .

droplet size distribution  $n(s, \mathbf{x}, t)$  may be reconstructed. Fig. 5.4 shows  $n(s, \mathbf{x}, t)$  in the  $(x_1, \log s)$ -plane across the horizontal centerline, and  $n(s, \mathbf{x}, t)$  in the  $(x_2, \log s)$ -plane across the vertical centerline, for  $t^* = 3$  and  $t^* = 5$ . A clear development of the distributions along the two centerlines is apparent. At the right wall the majority of the droplets reside in smaller size classes, and they appear to grow to larger ones while moving into the domain and passing the vertical centerline. Moreover, the matured droplet size distributions at later times show multiple ‘layers’, see the dashed lines in Fig. 5.4. These layers are formed due to multiple cycles of nucleation coming together, enabled by the circulation of the flow and the non-uniformity of the temperature. At the walls, in particular at  $t^* = 3$  in Fig. 5.4, diffusion-driven droplet nucleation is shown.

### 5.3.3 Numerical sensitivity of the solution

In the previous section we have shown a number of results for a typical lid-driven cavity simulation on a  $128^2$  grid, a time step size of  $\Delta t = 16 \times 10^{-5}$  s and an 8 sections/decade sectional distribution. The question remains: how accurate are these results and do we have control over the numerical error? This will be addressed in this section.

First, we investigate the grid dependence of the solution. Fig. 5.5 shows, for a sequence of 5 grids, the horizontal and vertical centerline solutions for the mass fraction of DBP,  $Z_{DBP}$ , for fixed  $\mathcal{P}$  and  $\Delta t$ . The solution changes considerably as the grid is refined, due to the applied first order upwind scheme in the convective terms. However, the solution appears to converge at sufficiently high resolutions. As discussed before, it is possible to trade in the upwind scheme for a flux limiter scheme, which would still preserve positivity of the solution. However, this limiter should be ‘global’ with respect to  $M_i$ ,  $Z_j$  and  $Y_j$ , yielding one value for each field,

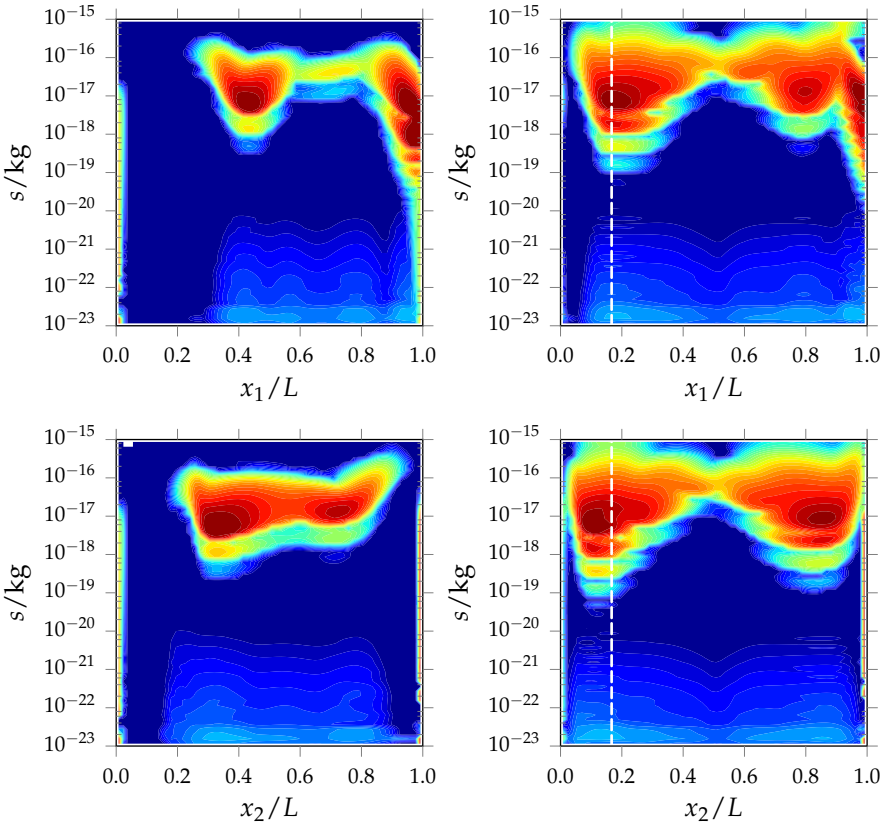


Figure 5.4: The droplet size distribution on the horizontal centerline (top) and vertical centerline (bottom) at times  $t^* = 3$  (left) and  $t^* = 5$  (right). The colormap schematically indicates the value of  $\log n(s, \mathbf{x}, t)$  as a function of  $(x_1, \log s)$  or  $(x_2, \log s)$ . The dashed lines correspond to  $\mathbf{x} = (L/6, L/2)$  and  $\mathbf{x} = (L/2, L/6)$ , the two positions used in Fig. 5.6 and Fig. 5.7.

in order to preserve constraints (2.2) and (2.31). The default schemes available in OpenFOAM do not offer this property. We choose here consistency over accuracy, but acknowledge that for most applications relaxing constraints (2.2) and (2.31) by virtue of improving the overall accuracy of the solution may be acceptable too.

Next, the dependence of the solution on the number of sections and the chosen CBSM scheme is studied. Fig. 5.6 shows for a refinement sequence in  $\mathcal{P}$  the droplet size distribution, at two positions (corresponding to the dashed lines in Fig. 5.4), for the two-moment and hybrid CBSM schemes. The distribution is plotted in  $\log s$ -space, in which the sections have uniform width. Convergence is shown as  $\mathcal{P}$  increases. The results for the two-moment scheme are generally more diffusive and smoother than the hybrid scheme, for the same  $\mathcal{P}$ . However, as  $\mathcal{P}$  increases, small details which are already visible in the hybrid solution also appear in the two-moment result. Both the two-moment and hybrid solution converge towards the same solutions, however, the

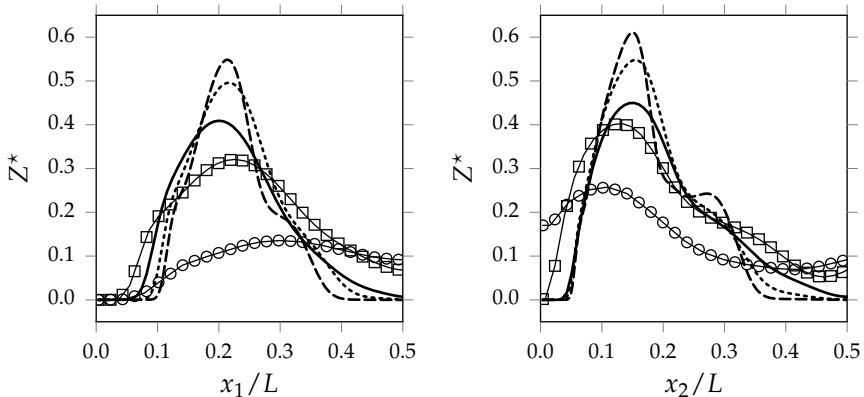


Figure 5.5: DBP mass fraction  $Z_{DBP}$  of the horizontal (left) and vertical (right) centerline at  $t^* = 5$  for a  $32^2$  ( $\circ$ ),  $64^2$  ( $\square$ ),  $128^2$  (—),  $256^2$  (···) and  $512^2$  (---) grid. The simulation was run with  $\mathcal{P} = 8$  sections/decade and  $\Delta t = 16 \times 10^{-5}$  s. Only the first half of the centerlines are shown, for visual clarity.

hybrid one preserves sharp gradients better at lower  $\mathcal{P}$ . This property was already established in the spatially homogeneous case, see Chp. 4.

In the modeling of the aerosol size distribution it is common to not fully resolve the distribution, but to work in terms of moments of an assumed distribution. An assumption that is often made is that  $\log d$  is normally distributed. Since  $\log s$  is proportional to  $\log d$ , Fig. 5.6 should, under the log-normal assumption, give a Gaussian bell curve. However, this is clearly not the case, motivating the effort to implement the sectional approach.

The dependence of the solution on the time step size  $\Delta t$  is illustrated in Fig. 5.7. At two positions the distribution is shown for a sequence of decreasing time step sizes. The dependence of the solution is, for the chosen range of  $\Delta t$ , not as strong as the dependence of the solution on  $\mathcal{P}$ . A clear convergence is shown, though.

In Sec. 5.2 CBSM was integrated within compressible PISO, along with the Crank-Nicolson time discretization scheme, using a fractional step method. This effort was undertaken to retain a second order accurate time integration for the velocity, temperature and pressure solutions. Tbl. 5.3 shows, for a sequence of  $\Delta t$  refinement,  $e_{hor}$  and  $e_{ver}$ . The reference solution is taken at  $\Delta t = 4 \times 10^{-5}$  s. The order of convergence is shown to be smaller than, but close to second order. More importantly, the solution for the perpendicular velocity at the cavity centerlines using  $\Delta t = 64 \times 10^{-5}$  s is shown to be within 2% of the reference solution, in terms of  $e_{hor}$  and  $e_{ver}$ .

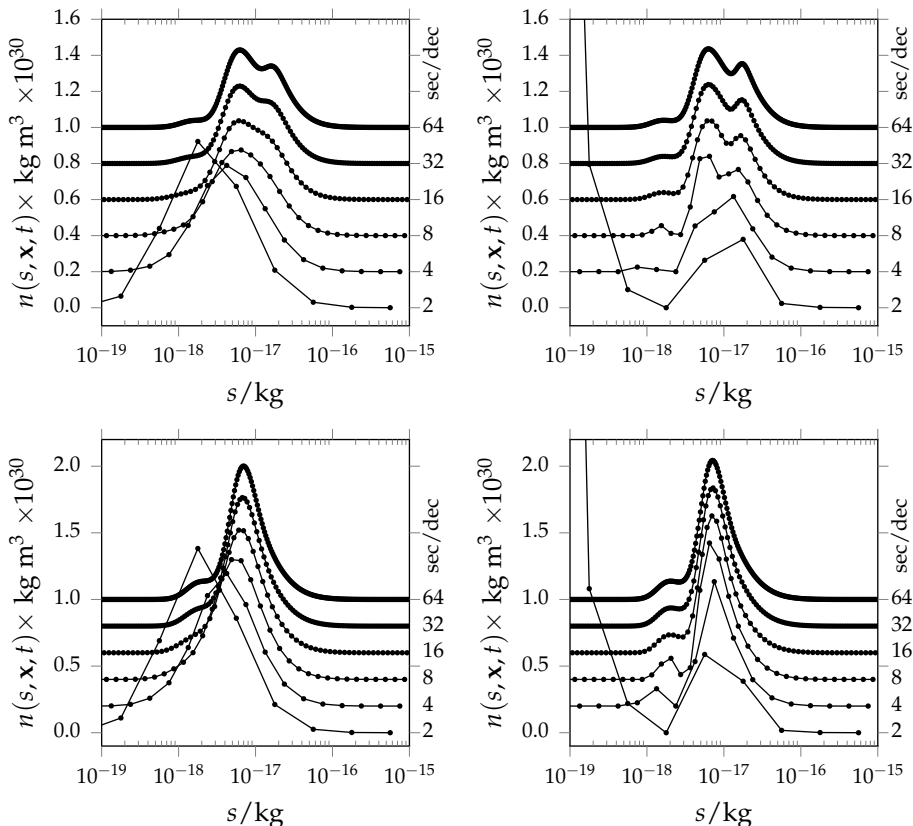


Figure 5.6: Droplet size distribution at  $t^* = 5$  for 2, 4, 8, 16 and 32 sections per decade, as indicated. Each line in this sequence has a vertical offset of  $2 \times 10^{29} \text{ kg}^{-1} \text{ m}^{-3}$  with respect to the previous, for visual clarity. Shown are results for the two-moment CBSM scheme (left), the hybrid CBSM (right), at  $\mathbf{x} = (L/2, L/6)$  (top) and at  $\mathbf{x} = (L/6, L/2)$  (bottom). The used grid was  $128^2$  and  $\Delta t = 16 \times 10^{-2} \text{ ms}$ . The dots indicate the sectional representative sizes.

$\Delta t \times 10^{-2} \text{ ms}$	$e_{hor}$	order	$e_{ver}$	order	max(CFL)
64	0.01641		0.01724		0.96
32	0.00739	1.4897	0.00703	1.5658	0.48
16	0.00294	1.5866	0.00256	1.6559	0.24
8	0.00087	1.8365	0.00067	1.9558	0.12

Table 5.3: Convergence of  $e_{hor}$  and  $e_{ver}$  for a time step size sequence, using  $\Delta t = 4 \times 10^{-2} \text{ ms}$  as reference solution.

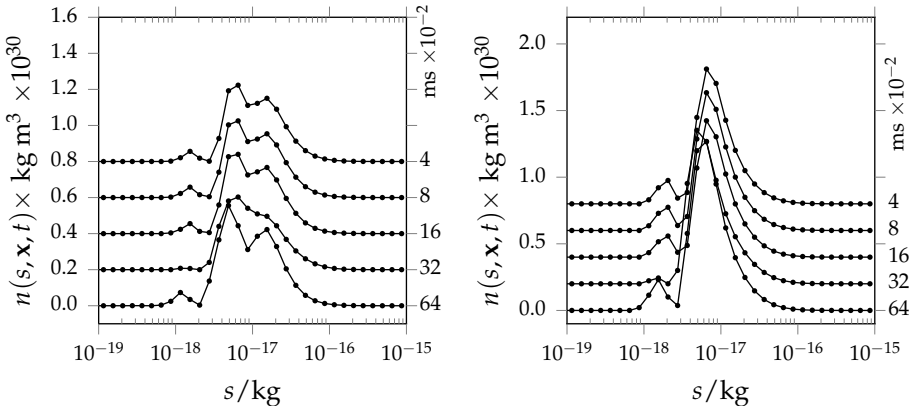


Figure 5.7: Droplet size distribution at  $t^* = 5$  for  $\Delta t = 64, 32, 16, 8, 4 \times 10^{-2} \text{ ms}$ , as indicated. Each line in this sequence has a vertical offset of  $2 \times 10^{29} \text{ kg}^{-1} \text{ m}^{-3}$  with respect to the previous, for visual clarity. Shown are results at  $x = (L/2, L/6)$  (left) and at  $x = (L/6, L/2)$  (right). The used grid was  $128^2$  and  $\mathcal{P} = 8$  sections/decade, while using the hybrid CBSM scheme. The dots indicate the sectional representative sizes.

## 5.4 AEROSOL NUCLEATION IN A DOUBLE-MIXING TEE

To illustrate the applicability of the developed method in a 3D complex geometry, in this section we will present simulations of the flow with nucleating aerosol undergoing dynamic evolution in a double-mixing tee chamber. The double-mixing tee is one of the many compartments present in the in-vitro exposure system developed by Vitrocell®, which is a subject of ongoing scientific investigations (Thorne and Adamson [63], Adamson et al. [64], Majeed et al. [65]) to characterize its functionality for delivering a controlled dose of substances during in-vitro toxicological assessment. In Sec. 5.4.1 we give a brief introduction to the geometry, flow conditions and computational grid used for the simulation. Subsequently, in Sec. 5.4.2, quantitative predictions of the aerosol that is generated will be discussed. The purpose of these simulations is to demonstrate the suitability of the method without pursuing high-resolution grid-independence of the results.

### 5.4.1 Geometry, mesh and flow conditions

We simulate nucleation from saturated vapors of DBP flowing into the double-mixing tee chamber, which are cooled down by a dilution flow. The choice to work with DBP is made to keep a close connection with the previous section. It is an interesting test situation for the modeling and simulation method, although the relevance of DBP nucleation is largely academic. The geometry used for the simulations, together with the dimensions of the system are presented in Fig. 5.8. The main pipe has a diameter  $D = 6 \text{ mm}$ . Two dilution pipes of diameter  $D/2$  are attached to the main pipe. In our simulations, the main pipe extends to  $8.3D$  upstream of the

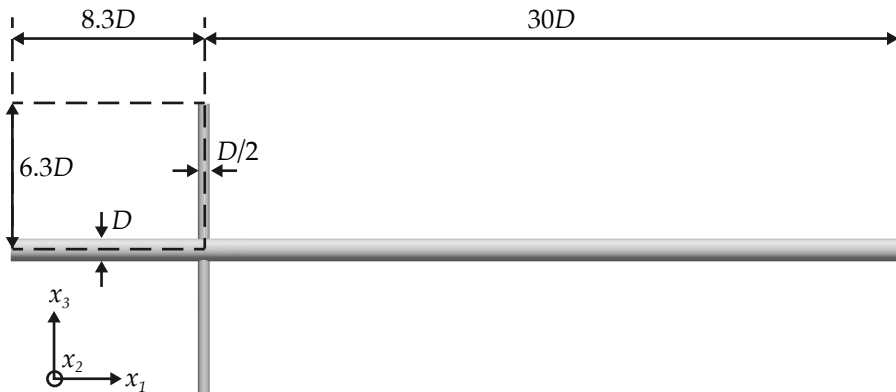


Figure 5.8: Computational domain geometry based on the diameter of the main pipe  $D = 6$  mm with two dilution legs with the diameter  $D/2$ .

junction and  $30D$  downstream and the lengths of the dilution pipes are  $6.3D$  each. These dimensions allow to consider the flow in the central mixing region as quite independent of the inflow and outflow conditions imposed at the various entry and exit points.

Flow simulations with coalescing aerosol droplets were performed previously in this geometry [66]. The mesh is based on the non-dimensional cell sizes for a flow rate of 12 L/min as reported in [66]. Polyhedral cells are used close to the double-mixing tee region. Further downstream, the mesh elements are extruded in the axial direction on both sides. The total mesh size is about 2.6 million cells and we use it for simulations of a relatively low flow rate of 3 L/min. A typical cross section of the main pipe contains approximately  $40^2$  to  $50^2$  cells. This allows to adequately capture the flow structures as emerge in the central mixing region. It was shown in [66] that the resolution is sufficient to capture the expected unsteady flow in the mixing chamber. For more details regarding the mesh the reader is referred to [66]. The time step is restricted by the CFL condition, where the max CFL number is allowed to be 0.75.

The saturated DBP vapor inflow rate (carrying both saturated vapor and air) for typical test conditions is 1.5 L/min and the dilution flow is 0.75 L/min per mixing-tee leg. This gives in total 3 L/min downstream of the mixing chamber, a bulk Reynolds number  $Re = 636$  based on the main pipe diameter and an average flow-through time of approximately 0.1 s. Parabolic velocity profiles and zero-gradient pressure conditions were applied to all inlets and a fixed atmospheric pressure boundary condition is imposed at the outlet. The hot DBP vapors entering the system at temperature  $T_0$  are cooled down by the two dilution flows, both at temperature  $T_\infty$ .  $T_0$  and  $T_\infty$  take the same values as used in Sec. 5.3, i.e.,  $T_0 = 373.15$  K and  $T_\infty = 273.15$  K. Also in agreement with Sec. 5.3, at the main inlet we set a uniform perfect saturation condition for the DBP vapor mass fraction:  $Y = Y_{DBP}^{\text{sat}}(T_0)$  at the

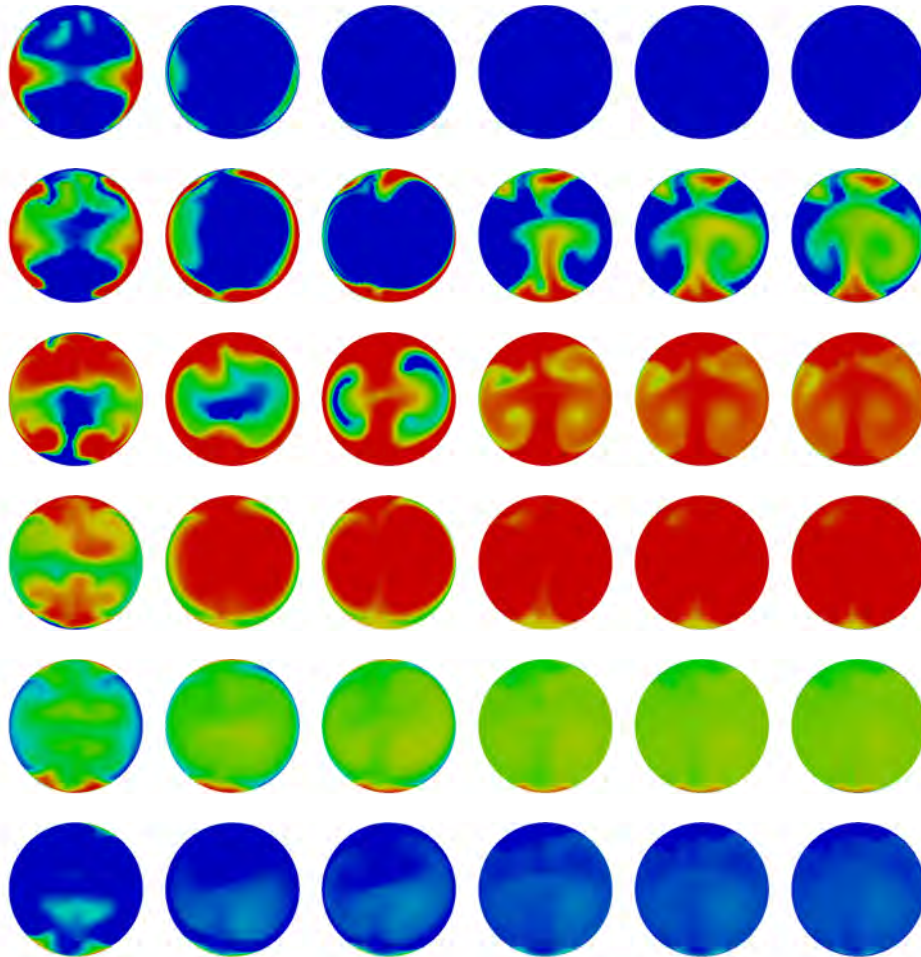


Figure 5.9: Instantaneous cross section plots of the droplet number concentration taken at a well-developed flow snapshot ( $t = 1 \text{ s}$ ). From left to right:  $x_1/D = 0.7, 1.7, 2.7, 5.7, 7.7$  and  $9.7$  downstream of the center of the tee. From top to bottom: particle diameter  $d = 19 \text{ nm}, 31 \text{ nm}, 50 \text{ nm}, 80 \text{ nm}, 0.13 \mu\text{m}$  and  $0.21 \mu\text{m}$ . The color scale is logarithmic. Red indicates  $N = 10^{13} \text{ m}^{-3}$  or higher and blue indicates  $N = 10^{10} \text{ m}^{-3}$  or lower.

inlet (again, physiochemical properties are taken from [12]). Adiabatic conditions are applied on all geometry walls.

The previous section suggests that for these conditions, when using the hybrid CBSM scheme, a reliable sectional solution is obtained at 8 sections/decade, see for example Fig. 5.6. We use this value for the number of sections in the double-mixing tee simulations.

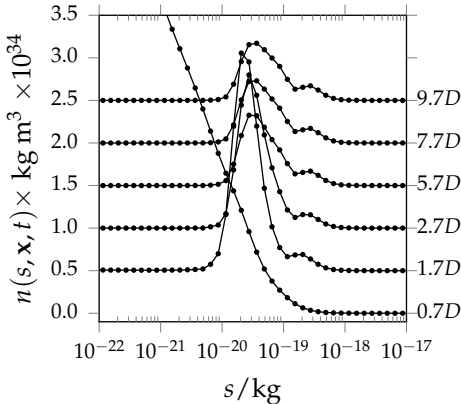


Figure 5.10: Instantaneous cross section-averaged droplet size distributions taken at well-developed flow conditions ( $t = 1$  s), at  $x_1 = 0.7D, 1.7D, 2.7D, 5.7D, 7.7D$  and  $9.7D$  as indicated, downstream of the center of the tee. Each distribution is vertically offset by  $5 \times 10^{33} \text{ kg}^{-1} \text{ m}^{-3}$ . The dots indicate the sectional representative sizes.

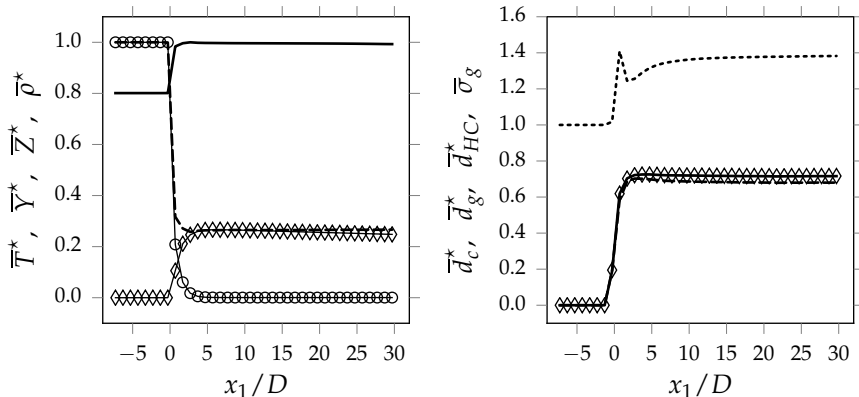


Figure 5.11: Left: the non-dimensional temperature  $\bar{T}^*$  (---), density  $\bar{\rho}^*$  (—), DBP vapor mass fraction  $\bar{Y}^*$  (○), DBP liquid mass fraction  $\bar{Z}^*$  (◇). Right: the count mean diameter  $\bar{d}_c^* = \bar{d}_c/10^{-7}$  (solid), geometric mean diameter  $\bar{d}_g^* = \bar{d}_g/10^{-7}$  (---), theoretical count mean diameter  $\bar{d}_{HC}^* = \bar{d}_{HC}/10^{-7}$  (◇) and geometric standard deviation  $\bar{\sigma}_g$  (···). All curves are as a function of the scaled horizontal coordinate where  $x_1/D = 0$  is the center of the tee.

#### 5.4.2 Aerosol flow results

Localized mixing of the hot saturated DBP vapor flow with the cold air flow triggers nucleation of the aerosol together with its further immediate growth by condensation, which is captured by the sectional method. The dilution flow generates a shear layer while entering the main pipe flow, causing flow instability and shedding of vortical flow structures that laminarize further downstream at the selected flow Reynolds number. This was shown in [66]. The vapor flow is abruptly cooled by

the convective supply of cold air, leading to very sharp temperature gradients in the mixing chamber. Aerosol is generated in close proximity to the shear layer. Fig. 5.9 shows, for six droplet sizes, the instantaneous droplet number concentrations at six consecutively placed cross sections of the pipe downstream of the mixing chamber. In this snapshot, the formation of aerosol is clearly asymmetric in space, due to the unsteady behavior of the flow. It can be seen that several flow structures are formed. These structures are, by visual inspection, not smaller than  $D/5$ . We expect that the formed aerosol is captured reliably on our computational mesh with 4-5 grid cells available for the smallest scales in the solution. Fig. 5.9 shows that close to the mixing chamber there are many small droplets. At larger distances the small droplets have grown to larger sizes due to condensation. Droplets of sizes around  $d = 80$  nm are present most significantly. For larger distances from the mixing chamber the concentration plots appear to become more uniform. Visually comparing cross section five and six (at distances  $7.7D$  and  $9.7D$ ), we conclude that around this distance the evolution of the aerosol has ceased.

In Fig. 5.10, the cross section-averaged size distribution is shown. Clearly, close to the mixing chamber many small droplets exist. The shape of the distribution is significantly different in comparison to later cross sections, due to nucleation. For larger distances it is shown that a relatively narrow distribution is formed which, for even larger distances, grows into a weakly bi-modal wider distribution.

In Fig. 5.11 cross section-averaged quantities that depict the behavior of the flow and aerosol in the main pipe geometry are presented. In the remainder, we denote cross section-averaging by an overline. The scaled (indicated by  $*$ ) and cross section-averaged vapor mass fraction  $\bar{Y}^*$  nucleates and subsequently condenses near  $x = 0$  m turning into the scaled liquid mass fraction  $\bar{Z}^*$ . This process is driven by a significant drop of the temperature,  $\bar{T}^*$ , caused by the cold dilution flow. Because of the cold incoming dilution flow the density  $\bar{\rho}^*$  (scaled by the steady state solution  $\rho_\infty$ ) increases and the partitioning between vapor and air mass fractions is affected. Without dilution, the downstream value of  $\bar{Z}^*$  would become the upstream value of  $\bar{Y}^*$ , i.e., all vapor is turned into liquid, both having the same concentration. This was the case in the cavity, see for example Fig. 5.3. With dilution, the liquid concentration is reduced, as shown in the solution for  $\bar{Z}^*$ .

In Fig. 5.11 a number of statistical mixture quantities are presented (in red). First, the cross section-averaged count mean diameter  $\bar{d}_c$  is shown, directly computed from the sectional simulation data, as [3]:

$$\bar{d}_c = \frac{\sum_i M_i d_i}{\sum_i M_i}, \quad (5.19)$$

with  $d_i$  the diameter of a droplet in section  $i$ . If no droplets are present on the cross section surface,  $\bar{d}_c$  is set to zero. Fig. 5.11 shows, as expected, an increase in  $\bar{d}_c$  as a function of downstream position. The droplet size is one order of magnitude smaller

than reported in case of the laminar flow diffusion chamber [67], as well as in the cavity, because of cooling of saturated vapors by the high dilution flow rather than mainly diffusive cooling. In this case, more rapid cooling leads to a larger number of droplets at smaller sizes.

The cross section-averaged geometric standard deviation  $\bar{\sigma}_g$  is shown, also directly computed from the simulation data, using

$$\ln \sigma_g = \sqrt{\frac{\sum_i M_i (\ln d_i - \ln d_g)^2}{\sum_i M_i}}, \quad (5.20)$$

and where  $d_g$  is the geometric mean diameter, given by

$$\ln d_g = \frac{\sum_i M_i \ln d_i}{\sum_i M_i}, \quad (5.21)$$

of which its cross section-average  $\bar{d}_g$  is also shown in Fig. 5.11. In the case of a log-normal size distribution, a common assumption to reduce the complexity of the aerosol model, the geometric mean diameter  $d_g$  equals the count median diameter CMD. In that case we can use the so-called Hatch-Choate conversion equations [3] to compute  $d_c$  from  $d_g$  and  $\sigma_g$ :

$$d_{HC} = \text{CMD} \exp \left[ \frac{1}{2} \ln^2 \sigma_g \right], \quad (5.22)$$

where  $d_{HC}$  becomes the ‘theoretical’ count mean diameter. The level of agreement between this theoretical prediction and the value obtained from the full simulation is a measure for the log-normality of the distribution. Fig. 5.11 shows that both cross section-averaged quantities are close to each other with a relative deviation less than 1%, suggesting log-normality. After inspection of the actual cross-section averaged distributions in Fig. 5.10 we conclude that for distances away from the nucleation zone the log-normal assumption appears quite effective (distributions are rather symmetrical in log s-space). However, within the nucleation zone in the center of the mixing tee the log-normal distribution is clearly invalid because there is a preference for smaller droplet sizes. This motivates the use of the sectional method, in order to capture nucleation accurately and hence also predict correct sizes of the aerosol further downstream.

The cross section-averaged geometric standard deviation  $\sigma_g$  remains well below 1.5, suggesting that over the plane of averaging droplets are rather mono-disperse. Close to the nucleation zone, around  $x_1/D = 0$ , the geometric standard deviation is largest, due to the presence of both freshly nucleated droplets as well as already condensed droplets. This example illustrates that CBSM is capable of efficiently resolving both sizes.

## 5.5 CONCLUSIONS

In this chapter we adapted the CBSM method to the complete set of fluid equations of motion for a compressible flow formulation with a dispersed aerosol liquid phase. By using the fractional step method, spatial terms could be isolated from the ‘internal’ terms such as those describing coalescence, condensational growth and nucleation. This allowed for the introduction of CBSM to solve the spatially homogeneous size distribution equation, embedded in a spatially heterogenous setting.

First, the method was applied to the modeling of aerosol formation in a lid-driven cavity. The accuracy of the method, the control we have over the truncation error and the influence of two different CBSM schemes (two-moment-preserving and hybrid), were studied by means of a grid refinement sequence, in terms of spatial, temporal and sectional resolution. The dependence of the solution on the chosen grid resolution is, for the cavity, large, given that all convective terms are treated using the first order upwind scheme. However, convergence of the solution is shown. We also measured a convergence of the solution for a sectional refinement sequence, for both CBSM distribution schemes. The hybrid scheme, reducing from four-moment to two-moment-preservation to avoid negativity, as was shown in Chp. 4, gives at coarse (i.e., 8 sections per decade) sectional distributions already sharp results. Finally, we showed that the accuracy of the time integration of the velocity and pressure remains as desired; a simulation with a CFL number of unity is shown to be within 2% of a simulation with a 16 times smaller time step size.

The cavity simulations demonstrated the feasibility of the extension of the CBSM method to spatially heterogeneous settings, yet still in two spatial dimensions. To illustrate the feasibility and applicability of the developed method further, we applied it to the simulation of aerosol formation in a double mixing-tee. The CBSM provided detailed information regarding the unsteady and spatially varying formed aerosol size distributions. It was shown that in the double mixing-tee the size distribution grows to a distribution which could be effectively modeled as a log-normal distribution. However, within the nucleation zone, the droplet size distribution is far from log-normal, motivating the choice for a sectional method.

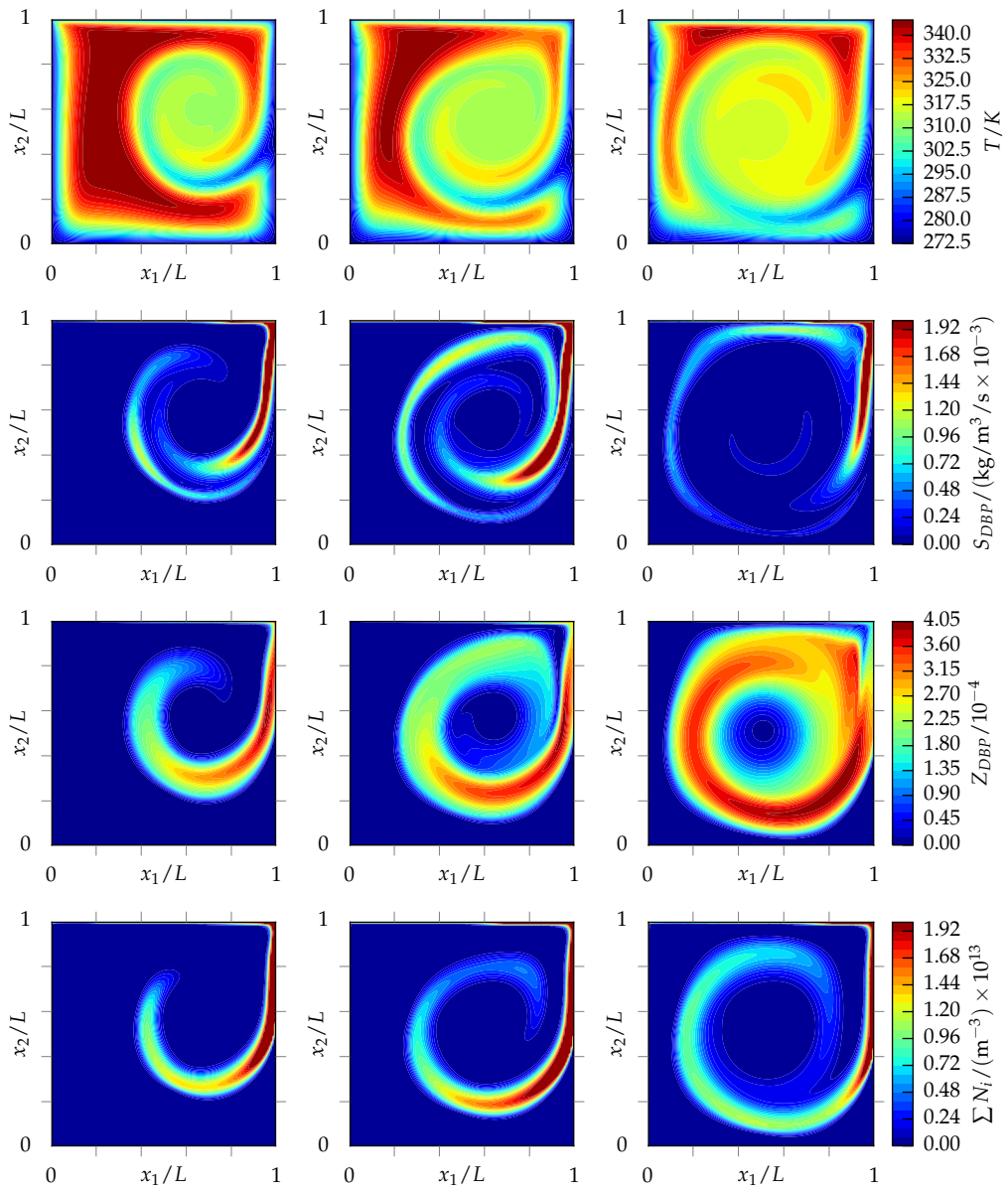


Figure 5.12: A schematic representation of the temperature  $T$ , condensation rate  $S_{DBP}$ , liquid mass fraction  $Z_{DBP}$  and total droplet number concentration  $\rho \sum M_i$  (from top to bottom) at  $t^* = 3$ ,  $t^* = 4$  and  $t^* = 5$  (from left to right). The color indicates the magnitude of the respective quantity. The simulations were performed on a  $128^2$  grid using  $\Delta t = 16 \times 10^{-2}$  ms,  $\mathcal{P} = 8$  sections/decade and the hybrid CBSM scheme.

## CHAPTER 6

# NON-ISOKINETIC AEROSOL SAMPLING\*

### ABSTRACT

An aerosol can be modeled, in an Eulerian context, using the ‘internally mixed’ description, meaning that the composition of the droplet phase is locally independent of droplet size. Effectively, a multi-species aerosol mixture is then described by vapor and liquid concentrations, and the droplet size distribution. We adopt a sectional approach to discretize the size distribution, allowing for arbitrarily shaped size distributions. Due to a higher mass density of the dispersed phase of an aerosol with respect to its carrier gas, inertia and gravity may lead to droplet drift; the dispersed phase no longer follows streamlines of the average mixture mass. We account for this by introducing extra convection terms in the compressible mass concentration and droplet number concentration transport equations, based on a size-dependent drift velocity. The governing set of compressible drift-augmented transport equations is discretized, using a finite volume collocated cell-centered framework. Fluxes, derived from face interpolations, are constructed, implementing two internal consistency relations: the first moment of the droplet size distribution must always represent the total liquid mass concentration in the system, and all mass fractions must always sum to unity. We validate the computational model by predicting the aspiration efficiency of aerosol samplers. We compare aspiration predictions based on the solution of the full droplet velocity equation including the Stokes or Schiller-Naumann drag coefficient with the solution of the simpler local equilibrium approximation. All models agree well with each other for Stokes number  $St < 0.2$ . For larger Stokes numbers it is necessary to solve the full droplet velocity equation. Our results generally agree well with the Belyaev & Levin (B&L) model, but for  $St = \mathcal{O}(10^{-1})$  and for large sampler velocity ratios  $U_0/U > 5$ , with  $U_0$  the ambient velocity and  $U$  the sampler velocity, we find a small deviation between our results and B&L due to large droplet accumulation in the re-circulation zone at the leading edge of the sampler wall, which invalidates the one-way coupling assumption of the model.

---

\*This chapter is based on Frederix et al. [68]: Prediction of non-isokinetic sampling with a sectional drift flux model. *Computers & Fluids*, submitted.

## 6.1 INTRODUCTION

Often the dispersed phase in an aerosol has a much larger mass density than the medium in which it is suspended. When the aerosol mixture is moving, the droplets carry more momentum. Depending on the typical relaxation time  $\tau$  of their motion, they may not follow streamlines of the carrier gas. This is called inertial drift. In this chapter we incorporate this drift into the sectional description of the aerosol and apply this model to non-isokinetic aerosol aspiration, which provides a detailed validation point. Three drift models will be compared using a numerical approach that implements two central consistency relations, i.e., preservation of total vapor and liquid mass fractions and total liquid mass in droplets.

When we adopt a multi-species Eulerian description of the aerosol mixture, we capture the aerosol by liquid and vapor mass concentration fields. To introduce more detail, one may extend this description by including the droplet size distribution, either by solving for a pre-selected number of moments of that distribution, or by resolving the distribution as a whole (e.g., see [34] for an overview of different techniques). A common assumption in Eulerian aerosol modeling is that the dispersed phase has the same velocity as the carrier gas,  $\mathbf{u}$ . In the absence of any source terms, the mixture is then convected with  $\mathbf{u}$  without changing its composition in terms of chemical species or in terms of droplet sizes. When drift is notable, one must abandon the idea of a common velocity for the vapor and liquid. In Chp. 2 we developed a compressible multi-species Eulerian aerosol method, in which the size distribution was discretized in so-called ‘sections’ [9, 10], which we will extend with drift in this chapter.

To introduce a drift term in the transport equations for liquid mass and droplet number concentrations we must first develop an understanding of the motion of a single droplet with diameter  $d$  immersed in a carrier gas, as expressed by a velocity  $\mathbf{v}$ . We can then use  $\mathbf{v}$  to describe the motion of a collection of droplets of size  $d$ , as contained in a single section of the sectional discretization. This, in turn, leads to an understanding of the motion of the total liquid concentration. There are many models describing the motion of a single droplet, for example, the well-known Maxey and Riley [69] equation. As an alternative, it is popular to consider the droplet velocity as a small perturbation of  $\mathbf{u}$  in  $St$ . To first order in  $St$ , the model for the droplet velocity  $\mathbf{v}$  becomes a simple expression, see for example [70], [71] or [72]. Of course, for this alternative approach to work  $\tau$ , the particle relaxation time, must be small with respect to the typical time scale associated with  $\mathbf{u}$ , which is generally the case for small droplets only. As discussed in [72], another reason  $\tau$  must be small is that for large  $\tau$  the velocity field  $\mathbf{v}$  is no longer a unique solution to the equation it adheres to; if relaxation times are large, droplets may cross paths. This, it is argued, refutes the Eulerian approach where only one velocity field at spatial position  $\mathbf{x}$  and time  $t$  for a particular type of droplet can exist. The generally more expensive Lagrangian approach would then be required. To the contrary, in this chapter we retain the

Eulerian approach but do limit ourselves to the small- $\tau$  regime. In other words, the velocity  $\mathbf{v}$  belonging to a particular type of droplet becomes a spatial average of all possible velocities at point  $(\mathbf{x}, t)$  of that type of droplet.

In literature, most authors employing Eulerian techniques have reduced the droplet velocity modeling to the so-called *local equilibrium model*, i.e., the first order expansion of  $\mathbf{u}$  in  $St$ . This is called ‘local equilibrium’, because the acceleration of the droplet is assumed equal to the acceleration of the surrounding carrier gas. For example, in [73, 74, 75, 76, 77, 78] aerosol deposition at walls was considered, with droplet drift as one of the driving mechanism for deposition. In this chapter we apply both the local equilibrium model, as well as the full model of the droplet velocity.

To assess on the one hand the consistent sectional method, and on the other hand the validity of our droplet motion modeling, we choose to apply the model to non-isokinetic aerosol sampling. In aerosol sampling droplet drift plays a major role. When measuring an aerosol from ambient flow, a sample should be drawn. This often causes a perturbation of the ambient flow, leading to droplet drift. Due to this drift, the sampled aerosol size distribution, in turn, may not be equal to the ambient ‘true’ aerosol size distribution. In literature, much effort is spent on understanding non-isokinetic sampling. A well-studied problem is that of the cylindrical sampler, which draws aerosol from the ambient flow into a cylindrical pipe, operated at a velocity often different than the ambient velocity. For the iso-axial case, where the cylindrical sampler is placed inline with the aerosol flow, a well known description is the semi-empirical model of B&L [79, 80]. Many other authors have published experimental studies, e.g., [81, 82, 83, 84], or numerical studies, e.g., [85, 86, 87, 88], of iso-axial aerosol sampling for a large range of velocity ratios and Stokes numbers. Generally, it can be concluded that the B&L model gives a fair prediction of the ‘aspiration’ of aerosol by the sampler. For example, Rader and Marple [82] found good agreement between their experimental data and B&L for the range  $0.005 < St < 10$  and  $0.2 < U_0/U < 5$  with an accuracy within 10% [89]. For us, the relatively simple and well-understood setting of iso-axial sampling as captured by the B&L model offers an opportunity for the validation of the new method. Also, in the limit of  $\tau$  becoming too large for the local equilibrium approximation, we test the validity of our ‘full’ solution of the droplet equation of motion.

The layout of this chapter is as follows. In Sec. 6.2 we will, starting from the equation of motion for the droplet size distribution, construct a set of equations describing a compressible ‘internally mixed’ [2] multi-species aerosol in an Eulerian way, including a new drift flux term. We will demonstrate that these equations are consistent with each other in terms of two consistency relations. Also, we introduce three models for the description of the size-dependent droplet velocity: the local equilibrium model, the full Stokes model and the full Schiller-Naumann drag coefficient model. Next, in Sec. 6.3, we will adopt a finite volume method and discretize the transport equations accordingly. Again, special attention is paid to retaining the consistency among the equations, also in their discrete forms. In Sec. 6.4 we will

describe the iso-axial cylindrical thin-walled sampler simulation setup to which we apply our model for the prediction of non-isokinetic aerosol sampling. First, confidence in the method is established by looking at the convergence of the solution as the computational grid is refined. Next, we assess how the aspiration depends on the droplet Stokes number and velocity ratio, and how our predictions, using all three droplet velocity models, compare to the model of B&L. Finally, we will summarize this chapter in the conclusions, Sec. 6.5.

## 6.2 EULERIAN DROPLET DRIFT MODEL

In Chp. 2 we introduced the internally mixed multi-species Eulerian model that we adopt for the description of the aerosol dynamics. In the current chapter, we extend it to incorporate drift flux terms, based on a size-dependent drift velocity. The considerations taken in arriving at the drift flux model will be discussed here. We also discuss three models that we use to compute the drift velocity.

### 6.2.1 Transport equations

In Sec. 2.2 we introduced the mass fraction vectors  $\mathbf{Y}$  and  $\mathbf{Z}$  for a number  $N$  vapors and liquids, respectively. These vectors were shown to adhere to the *unity constraint* (2.2), simply stating that all components of  $\mathbf{Y}$  and  $\mathbf{Z}$  should add up to unity, by definition. In Sec. 2.3 we introduced the continuity equation (2.9) for a mixture with density  $\rho$  and velocity  $\mathbf{u}$ . This equation is then expanded in ‘species space’ to arrive at the transport equations for the individual components of  $\mathbf{Y}$  and  $\mathbf{Z}$ . In this chapter, we write these equations as

$$\partial_t(\rho Y_j) + \nabla \cdot (\rho \mathbf{u} Y_j) = \mathcal{R}_j \quad (6.1a)$$

$$\partial_t(\rho Z_j) + \nabla \cdot (\rho \mathbf{u} Z_j) = \mathcal{S}_j, \quad (6.1b)$$

where the right-hand side source terms  $\mathcal{R}_j$  and  $\mathcal{S}_j$  may account for diffusion or phase change effects such as nucleation and condensation. We assume that inter-species mass transfer, usually in the form of chemical reactions, is absent. We will leave  $\mathcal{R}_j$  and  $\mathcal{S}_j$  unspecified here, but require that  $\sum_j (\mathcal{R}_j + \mathcal{S}_j) = 0$ , to be consistent with (2.9).

Eq. (6.1b) provides information about the evolution of the liquid mass concentration for each species, under the assumption that the overall liquid motion is equal to the mixture motion, requiring the liquid droplets to be sufficiently small. We may readily relax this assumption by incorporating the droplet size distribution instead. In fact, the liquid mass is present in the form of many dispersed droplets, suggesting that the liquid phase may also be described by the droplet size distribution  $n(s, \mathbf{x}, t)$ , where  $s$  is the mass of a droplet. This formulation, already introduced in Sec. 2.4, is useful for the description of processes that depend on the size of a droplet, such as droplet drift. For the evolution of the droplet size distribution, we introduce the GDE, Eq. (2.24). Extending the model as given by (6.1) to include droplet motion that

differs from the mixture motion, we replace the mixture velocity  $\mathbf{u}$  in the GDE with the size-dependent droplet velocity  $\mathbf{v}(s)$ <sup>†</sup>, which is written as

$$\mathbf{v}(s) = \mathbf{u} + \mathbf{u}^\ell(s), \quad (6.2)$$

where  $\mathbf{u}^\ell(s)$  is the liquid drift velocity of an  $s$ -sized droplet with respect to the motion of the carrier gas,  $\mathbf{u}$ . The corresponding new ‘perturbed’ GDE for  $n(s, \mathbf{x}, t)$  can be expressed as

$$\partial_t n(s, \mathbf{x}, t) + \nabla \cdot [\mathbf{u}n(s, \mathbf{x}, t)] + \nabla \cdot [\mathbf{u}^\ell(s)n(s, \mathbf{x}, t)] = J(s, \mathbf{x}, t), \quad (6.3)$$

where the right-hand side source term  $J(s, \mathbf{x}, t)$  may account for phase change, internal droplet redistribution due to coagulation and break-up and droplet diffusion, equal to its definition earlier in Sec. 2.4. Eq. (6.3) contains two convective fluxes: one with respect to  $\mathbf{u}$  and a second one with respect to  $\mathbf{u}^\ell(s)$ . The latter flux term expresses that droplets can move independently of the mixture. This extension requires to also modify (6.1) to adequately reflect this additional velocity. Moreover, the continuity equation reflecting mass conservation must be augmented with an extra conservative divergence term incorporating the local appearance or removal of droplets by drift. We turn to this task next.

Let us first consider the droplet size distribution for an internally mixed aerosol, as was discussed in [59]. The first moment of this size distribution is required to be equal to the total mass concentration of droplets as expressed by the *consistency relation* (2.23) in Sec. 2.4. This equation implies that  $\rho Z$  (with  $Z = \sum_j Z_j$ ) and  $n(s, \mathbf{x}, t)$  are mutually consistent and it allows us to relate the droplet drift to the rate of change of the total droplet mass concentration. By multiplying (6.3) by  $s$ , and then taking the integral from 0 to  $\infty$  in  $s$ , we find

$$\partial_t (\rho Z) + \nabla \cdot (\rho \mathbf{u} Z) + \nabla \cdot \left( Z^{-1} \mathbf{f} Z \right) = \mathcal{J}, \quad (6.4)$$

where we have introduced the product  $Z^{-1}Z$  (which is unity) into the drift divergence terms, for later use, and where

$$\mathbf{f} = \int_0^\infty s \mathbf{u}^\ell(s) n(s, \mathbf{x}, t) ds \quad \text{and} \quad \mathcal{J} = \int_0^\infty s J(s, \mathbf{x}, t) ds. \quad (6.5)$$

The flux  $\mathbf{f}$  can be considered as the total flux of liquid concentration drifting away from the mixture motion. The source term  $\mathcal{J}$ , affecting the first moment of the distribution, i.e., the total droplet mass concentration, generally only contains phase change and diffusion, as processes such as coagulation and break-up only redistribute mass in size space, but create or remove none. Recalling that  $Z = \sum_j Z_j$  and introducing this

---

<sup>†</sup>The velocity  $\mathbf{v}(s)$  is in fact, just like  $\mathbf{u}$ , a function of  $(\mathbf{x}, t)$  too, but this dependence is omitted for compactness.

in (6.4), we can expand (6.4) in  $j$ -space as

$$\partial_t(\rho Z_j) + \nabla \cdot (\rho \mathbf{u} Z_j) + \nabla \cdot (Z^{-1} \mathbf{f} Z_j) = \mathcal{J}_j, \quad (6.6)$$

where  $\mathcal{J}_j$  is the species-specific source term. For (6.6) to be consistent with (6.4), we must only require that  $\sum_j \mathcal{J}_j = \mathcal{J}$ . In the case of no drift, the third term of the left-hand side is zero and we should recover the original transport equation for  $Z_j$  in which liquid is convected by  $\mathbf{u}$  only, Eq. (6.1b). This is only true if  $\mathcal{J}_j = \mathcal{S}_j$ :

$$\partial_t(\rho Z_j) + \nabla \cdot (\rho \mathbf{u} Z_j) + \nabla \cdot (Z^{-1} \mathbf{f} Z_j) = \mathcal{S}_j, \quad (6.7)$$

The expansion in  $j$ -space is further elaborated in Appx. 6.A, establishing its benefits. Satisfying separately (6.7) for each  $j$  automatically satisfies (6.4) as well. The product  $Z^{-1} Z_j$  as found in (6.7) can be considered as the mass fraction of liquid species  $j$  with respect to the total *liquid* mass concentration. Therefore, the flux  $Z^{-1} \mathbf{f} Z_j$  in (6.7) can be interpreted as the total flux of  $j$ -species liquid concentration drifting away from the mixture.

The transport equation of  $j$ -species liquid mass concentration, Eq. (6.7), is fully consistent with that of the size distribution, Eq. (6.3), imposed by the consistency relation (2.23). We set out to formulate a new drift continuity equation, but for this we must still consider the transport of vapor concentration,  $\rho Y_j$ . From a physical point of view we assume that when droplets drift, the volume they ‘vacate’ is replenished by a counterflow of vapor mixture of equal volume. In this way, given our compressible mixture equation of state (2.8) which is based on the idea that volume is an extensive quantity, pressure remains uniform. We now introduce a compensating vapor drift term, to account for this counterflow. Without the explicit compensation of volume, the pressure would locally change due to droplet drift, which leads to a pressure gradient-induced flow in  $\mathbf{u}$ . This would affect the complete mixture. Let  $\rho^v$  denote the local mean vapor density and  $\rho^\ell$  the local mean liquid density, as defined in Sec. 2.4. Then the total vapor mass concentration drift flux, compensating for the droplet mass drift flux, is given by

$$\mathbf{h} = \gamma \mathbf{f}, \quad (6.8)$$

with  $\gamma = \rho^v / \rho^\ell$ , and the  $j$ -species-specific contribution is taken as  $Y^{-1} \mathbf{h} Y_j$ , i.e., weighed with the relative contribution of species  $j$  to the total local vapor mass, where  $Y = \sum_j Y_j$ . Subtracting this compensating flux (it is in opposite direction relative to the liquid flux) from the left-hand side of Eq. (6.1a), we find

$$\partial_t(\rho Y_j) + \nabla \cdot (\rho \mathbf{u} Y_j) - \nabla \cdot (Y^{-1} \mathbf{h} Y_j) = \mathcal{R}_j \quad (6.9)$$

Since we have chosen to compensate the supply or removal of volume as a result of droplet drift by an equal vapor mixture volume, inevitably the local density will de-

crease when droplets are moving away, because generally  $\gamma \ll 1$ . This perturbation of density should be accounted for in the continuity equation, and in the corresponding pressure equation. By adding (6.7) to (6.9), and summing over  $j$  we find (recall we required that  $\sum_j (\mathcal{R}_j + \mathcal{S}_j) = 0$ ):

$$\partial_t \rho + \nabla \cdot (\rho \mathbf{u}) + \nabla \cdot [\mathbf{f}(1 - \gamma)] = 0. \quad (6.10)$$

When  $\gamma = 1$ , the compensating vapor volume has the same mass as the drifting droplets, leading to zero net mass change by drift. Indeed, in that case the third term in Eq. (6.10) becomes zero, reducing it to the drift-free continuity equation (2.9)

To summarize, we now established a set of transport equations for mass concentration, Eq. (6.10), liquid and vapor species-specific mass concentrations, Eq. (6.7) and (6.9), and for the droplet size distribution, Eq. (6.3), for the compressible Eulerian description of a multi-species internally mixed aerosol. Consistency among these equations is enforced by the mass fraction unity constraint, Eq. (2.2), and the first moment mass concentration constraint, Eq. (2.23).

### 6.2.2 Drift velocity model

In the previous subsection we introduced the droplet velocity  $\mathbf{v}(s)$ , Eq. (6.2), differing from the mixture velocity  $\mathbf{u}$  by a drift velocity. We will now introduce three models describing the droplet velocity. Following [71] the motion of a single  $s$ -sized droplet can, in a Lagrangian way, be described by Newton's second law of motion, i.e.,

$$s d_t \mathbf{v}(s) = \mathbf{f}_D + \mathbf{f}_G, \quad (6.11)$$

where we only include the drag force  $\mathbf{f}_D$  and the gravitational force  $\mathbf{f}_G$  as the dominant contributions for droplets with  $\gamma \ll 1$  [90]. The drag force can be written as [91]

$$\mathbf{f}_D = -\frac{1}{2} A_d \rho^\ell C_D |\mathbf{u}^\ell| \mathbf{u}^\ell, \quad (6.12)$$

with cross-sectional droplet area  $A_d$  and drag coefficient  $C_D$ . The gravity force acting on the droplet is given by

$$\mathbf{f}_G = (\rho^\ell - \rho^v) V_d \mathbf{g}, \quad (6.13)$$

with droplet volume  $V_d$  and gravitational acceleration vector  $\mathbf{g}$ .  $C_D$  is a function of the droplet Reynolds number, given by

$$Re_d = \frac{d \rho^v |\mathbf{u}^\ell|}{\mu}, \quad (6.14)$$

with droplet diameter  $d$  and vapor mixture viscosity  $\mu$ . For sufficiently low  $Re_d$  (see [91] for more detail),  $C_D$  takes the form of Stokes drag,

$$C_{D,St} = \frac{24}{Re_d}. \quad (6.15)$$

This can be extended to higher droplet Reynolds number using the empirical ‘Schiller-Naumann’ drag coefficient [91]. For sufficiently low  $Re_d$ ,

$$C_{D,SN} = \frac{24}{Re_d} \left[ 1 + 0.15 Re_d^{0.687} \right]. \quad (6.16)$$

After these preparations, we introduce three different drift velocity models that will be investigated further in this chapter:

1. *Stokes model.* Eq. (6.11) constitutes a partial differential equation (PDE) in the Eulerian context. We may express the material time derivative as:

$$d_t \mathbf{v}(s) = \partial_t \mathbf{v}(s) + (\mathbf{v} \cdot \nabla) \mathbf{v}(s). \quad (6.17)$$

Under the assumption that Stokes drag applies, the PDE for  $\mathbf{v}(s)$ , given a mass  $z$  and corresponding diameter  $d$ , becomes

$$\partial_t \mathbf{v}(s) + [\mathbf{v}(s) \cdot \nabla] \mathbf{v}(s) = -\frac{1}{\tau} [\mathbf{v}(s) - \mathbf{u}] + (1 - \gamma) \mathbf{g}, \quad (6.18)$$

with the droplet relaxation time

$$\tau = \frac{\rho^\ell d^2}{18\mu}. \quad (6.19)$$

Eq. (6.18) can be solved numerically for  $\mathbf{v}(s)$ , as we will discuss in Sec. 6.3. Note that  $\mathbf{v}(s) \equiv \mathbf{v}(s, \mathbf{x}, t)$ , i.e., a Eulerian velocity field expressing the time-, space- and size-dependent droplet velocity.

2. *Manninen’s reduced Stokes model.* Solving Eq. (6.18) increases the computational effort notably. Manninen et al. [71] proposed reduced the complexity of (6.18) by introducing a local equilibrium approximation, in which the acceleration of a droplet is equal to the acceleration of the fluid, i.e.,

$$d_t \mathbf{v}(s) \approx d_t \mathbf{u}. \quad (6.20)$$

This assumption is valid when droplets adapt rapidly to any change in their surrounding flow. If the Stokes number, expressing the ratio of the droplet relaxation time with the typical time scale of the fluid, is small, then the local equilibrium approximation should be accurate [71]. The Stokes number is given

by

$$St = \frac{\tau U_0}{L}, \quad (6.21)$$

with typical flow velocity scale  $U_0$  and length scale  $L$ . Since droplets are, in the regime where (6.20) is valid, closely following the flow, it is also appropriate to select  $C_{D,St}$  as the drag coefficient, since  $Re_d$  is small for these droplets. This gives, after reshuffling (6.18), an expression for the approximate droplet velocity:

$$\mathbf{v}(s) = \mathbf{u} + \tau[(1 - \gamma)\mathbf{g} - d_t \mathbf{u}]. \quad (6.22)$$

This velocity can be seen as the velocity necessary to enable a droplet acceleration equal to that of the surrounding fluid. Mora and Rosner [70] showed that, in effect, the form of (6.22) is a first order expansion of (6.18) in  $St$ , more formally indicating the necessity of  $\tau$  being small with respect to the time scale of the fluid,  $L/U$ . The acceleration  $d_t \mathbf{u}$  can be directly obtained from the flow solution. This will be discussed in Sec. 6.3.

3. *Schiller-Naumann model.* If we select  $C_{D,SN}$  as the drag coefficient, then we find

$$\partial_t \mathbf{v}(s) + [\mathbf{v}(s) \cdot \nabla] \mathbf{v}(s) = -\frac{1 + 0.15 Re_d^{0.687}}{\tau} [\mathbf{v}(s) - \mathbf{u}] + (1 - \gamma) \mathbf{g}. \quad (6.23)$$

Note that  $Re_d$  is a function of  $\mathbf{v}(s)$ , making also the right-hand side of (6.23) non-linear with respect to  $\mathbf{v}(s)$ . The method used for solving this equation is, among other topics, discussed in the next section.

To summarize, in this Section we formulated the Eulerian drift flux model. The drift velocity is based the particle velocity, for which we developed three candidate models. The model, on the analytical level, satisfies two consistency relations, by construction. Next, we will incorporate the sectional method for the discretization of the GDE while also explicitly preserving the consistency that was established in the analytical model.

### 6.3 A SECTIONAL METHOD RETAINING MASS FRACTIONS AND LIQUID MASS

In the previous section, we motivated a set of equations for the compressible Eulerian description of an internally mixed multi-species aerosol with droplet drift. At the analytical level we showed that two consistency relations, one for the mass fractions (2.2) and one for the first moment of the droplet size distribution (2.23), were satisfied. In this section, we will adopt the sectional formulation (see Sec. 2.5) to approximate a solution for the set of equations. Furthermore, at the discrete level we develop our method such that the two consistency relations are satisfied by construction. Also in this section we discuss the adopted solution algorithm for the non-linear droplet velocity equations, which were introduced in the previous section.

Before we begin, we introduce the sectional formulation of the droplet size distribution for the drift-amended GDE (6.3). By taking the integral of this equation over a sectional interval  $[y_i, y_{i+1}]$  and by introducing definition (2.27) we find

$$\partial_t(\rho M_i) + \nabla \cdot (\rho \mathbf{u} M_i) + \nabla \cdot (\rho \mathbf{u}_i^\ell M_i) = \mathcal{J}_{M_i}, \quad (6.24)$$

where  $M_i$  and  $\mathcal{J}_{M_i}$  carry the same definition as in Sec. 2.5. The drift velocity  $\mathbf{u}_i^\ell = \mathbf{u}^\ell(s_i)$  is only evaluated at  $s_i$  due to the Dirac delta function representation of  $n(s, \mathbf{x}, t)$  in (2.25). In terms of the sectional discretization the consistency relation (2.23) remains equivalent to Eq. (2.31) at the level of the sectional discretization of  $n(s, \mathbf{x}, t)$ .

### 6.3.1 Finite volume discretization

OpenFOAM offers a cell-centered collocated finite volume (FV) framework, in which we solve our system of equations. A detailed analysis of the integration of the Pressure-Implicit with Splitting of Operators PISO method in OpenFOAM was presented in Chp. 3. In this framework, next, we include aerosol droplet drift. In the finite volume method we consider a computational volume  $V$  with  $F$  faces, labeled by  $f = 1, 2, \dots, F$  and  $\mathbf{A}_f$  the outward normal face vector with  $|\mathbf{A}_f| = A_f$ , i.e., the surface area of face  $f$ . Integrating (6.24) over the volume  $V$ , we find, approximating  $\rho M_i$  and  $\mathcal{J}_{M_i}$  as constant in  $V$ ,

$$\partial_t(\rho M_i) + \mathcal{D}(\phi_f M_{i,f}) + \mathcal{D}(\phi_{i,f}^\ell M_{i,f}) = \mathcal{J}_{M_i}, \quad (6.25)$$

with fluxes

$$\phi_f = (\rho \mathbf{u})_f \cdot \mathbf{A}_f \quad \text{and} \quad \phi_{i,f}^\ell = (\rho \mathbf{u}_i^\ell)_f \cdot \mathbf{A}_f, \quad (6.26)$$

where  $\phi_f$  is the convective flux and  $\phi_{i,f}^\ell$  the additional section  $i$  drift flux. Also,  $M_{i,f} = (M_i)_f$  where  $(\cdot)_f$  denotes interpolation to the face  $f$ , which we address momentarily. In (6.25) the  $\mathcal{D}$ -function represents the discrete counterpart of the divergence term as a function of the specified flux, see definition Eq. (3.5). What remains is the discretization of the time derivative. We illustrate the remaining part of the development of our method by adopting the notationally compact implicit Euler scheme. We stress, however, that our approach remains applicable to any other time discretization scheme. Using the implicit Euler scheme, (6.25) may be time integrated from discrete time  $t^m$  at time level  $m$  to  $t^{m+1} = t^m + \Delta t$  at time level  $m + 1$ , as

$$\frac{(\rho M_i)^{m+1} - (\rho M_i)^m}{\Delta t} = -\mathcal{D}(\phi_f M_{i,f})^{m+1} - \mathcal{D}(\phi_{i,f}^\ell M_{i,f})^{m+1} + \mathcal{J}_{M_i}^{m+1}. \quad (6.27)$$

This equation can be solved using the compressible PISO algorithm, as shown in Chp. 3. The choice of interpolation scheme for the computation of  $M_{i,f}$  is essential for the preservation of positivity of  $M_i$ . For example, the linear interpolation scheme is known to produce oscillations near sharp gradients; it is not monotonicity preserving.

The upwind scheme, on the other hand, takes  $M_{i,f}$  equal to  $M_i$  coming from the upwind direction, where the upwind direction is determined by the sign of the flux. The upwind scheme is TVD (Total Variation Diminishing). TVD schemes were shown to have the monotonicity property, i.e., the number of local extrema in the solution does not increase and local minima are nondecreasing and local maxima are nonincreasing [92]. This also means that when starting with a positive solution, a TVD scheme preserves positivity.

Generally, a TVD scheme determines its interpolation weights based on a limiter function. This limiter, in turn, is a function of the transported solution variable itself, as well as the face flux. In the case of (6.27), both divergence terms may be easily combined into one flux,  $\phi_f + \phi_{i,f}^\ell$ , on which the limiter can be based. For now, we leave the choice of interpolation scheme for  $M_{i,f}$  undetermined (this choice will be addressed in Sec. 6.4), but assume that an appropriate interpolation is used that guarantees positivity of  $M_i^{m+1}$ .

The set of  $\mathcal{P}$  equations (6.27) forms the discrete counterpart of the droplet size distribution transport equation (6.3). While for (6.3) we then enforced the analytical constraint (2.23) to find the consistent transport equation for  $Z$ , we will now follow a similar route for the numerical model starting from (6.27), and applying the discrete counterpart of (2.23), i.e., condition (2.31), to the transport equation for  $M_i$ . Multiplying (6.27) by  $s_i$  and summing over  $i$ , we find

$$\frac{(\rho Z)^{m+1} - (\rho Z)^m}{\Delta t} = -\mathcal{D}(\phi_f Z_f)^{m+1} - \mathcal{D}(Z_f^{-1} \phi_f^\ell Z_f)^{m+1} + \mathcal{J}^{m+1}, \quad (6.28)$$

where

$$\phi_f^\ell = \sum_i s_i \phi_{i,f}^\ell M_{i,f} \quad (6.29)$$

and  $\mathcal{J}$  given by (6.5). By following the same steps as in Sec. 6.2, but now at the discrete level, we may guarantee that the first moment consistency relation as expressed by (2.23) also holds discretely. Following this strategy, we expand (6.28) in  $j$ -space, which gives

$$\frac{(\rho Z_j)^{m+1} - (\rho Z_j)^m}{\Delta t} = -\mathcal{D}(\phi_f Z_{j,f})^{m+1} - \mathcal{D}(Z_f^{-1} \phi_f^\ell Z_{j,f})^{m+1} + \mathcal{S}_j^{m+1}. \quad (6.30)$$

To ensure that this equation is consistent with (6.28) in the sense that summing (6.30) over  $j$  yields (6.28), we require that

$$Z_f = \sum_j Z_{j,f}. \quad (6.31)$$

This relation has an important numerical consequence, i.e., it implies that  $Z_f$  must be computed from the individual  $Z_{j,f}$  interpolants, and not by first computing  $Z$  at cell

centers and then interpolating this to the faces. While at high spatial resolutions the differences between  $\sum_j Z_{j,f}$  and  $\left(\sum_j Z_j\right)_f$  may be small, we adhere to the alternative definition of  $Z$  at the faces, following (6.31).

For convenience of implementation, we combine both convective terms in (6.30) into a single one, containing one flux on which the interpolation scheme can be based. This gives

$$\frac{(\rho Z_j)^{m+1} - (\rho Z_j)^m}{\Delta t} = -\mathcal{D} \left( \left[ \phi_f + Z_f^{-1} \phi_f^\ell \right] Z_{j,f} \right)^{m+1} + \mathcal{S}_j^{m+1}. \quad (6.32)$$

The term between square brackets on the right-hand side forms the flux with which  $Z_j$  is transported at face  $f$ . At the level of implementation, a difficulty with this form is that the flux contains  $Z_f^{-1}$ , which is undefined for  $Z_f \rightarrow 0$ . For numerical stability, the following form, where we multiply the flux by  $Z_f$  and divide  $Z_{j,f}$  by  $Z_f$ , improves this:

$$\frac{(\rho Z_j)^{m+1} - (\rho Z_j)^m}{\Delta t} = -\mathcal{D} \left( \left[ \phi_f \tilde{Z}_f + \phi_f^\ell \right] \frac{Z_{j,f}}{Z_f + \epsilon} \right)^{m+1} + \mathcal{S}_j^{m+1}, \quad (6.33)$$

where the term between the square brackets is the total flux on which the interpolation scheme used for  $Z_{j,f}$  and  $Z_f$  is based. This form has three consequences:

1. The number  $\epsilon$  is a very small number. In case of  $Z_f = 0$  as computed according to (6.31), the introduction of  $\epsilon$  prevents division by zero. For  $Z_f \rightarrow 0$ , which, due to positivity, also implies that  $Z_{j,f} \rightarrow 0$  for all  $j$ , the term  $Z_{j,f}/(Z_f + \epsilon)$  also goes to zero; no liquid is present and no liquid is convected.
2. The convected scalar becomes  $Z_f^{-1} Z_{j,f}$ , which is non-linear in  $Z_j$ . We compute it explicitly, based on the latest iterative solution in the PISO algorithm, see Chp. 3.
3. Inside the flux there appears a  $Z_f$  which received an additional tilde in its notation. The reason for this is that  $\tilde{Z}_f$  inside the flux cannot be computed from a limiter interpolation scheme which is based on the flux, as this  $\tilde{Z}_f$  is part of the flux itself. We should therefore choose a different form for this  $\tilde{Z}_f$ , and therefore label it with a tilde, indicating this. Due to the first moment consistency relation (2.31) we can compute  $\tilde{Z}_f$  as

$$\tilde{Z}_f = \sum_i s_i M_{i,f}, \quad (6.34)$$

where each  $M_{i,f}$  is computed by a TVD interpolation scheme.

Equation (6.33) is the discrete equivalent of (6.7). By the same token, we can

discretize the  $Y_j$ -equation (6.9) in an analogous way:

$$\frac{(\rho Y_j)^{m+1} - (\rho Y_j)^m}{\Delta t} = -\mathcal{D} \left( \left[ \phi_f \tilde{Y}_f - \gamma \phi_f^\ell \right] \frac{Y_{j,f}}{Y_f + \epsilon} \right)^{m+1} + \mathcal{R}_j^{m+1}, \quad (6.35)$$

where, as before, we have introduced  $\epsilon$  for robustness. The term in the square brackets in the right-hand side is identified as the flux with which  $Y_{j,f}/Y_f$  is convected. Also, we introduced  $\tilde{Y}_f$  for which we derive an expression next.

Adding (6.33) and (6.35) to each other and summing the result over  $j$  (recall that  $\sum_j (\mathcal{R}_j + \mathcal{S}_j) = 0$ ) gives the discrete form of the continuity equation (6.10), i.e.,

$$\frac{\rho^{m+1}(Y + Z)^{m+1} - \rho^m(Y + Z)^m}{\Delta t} = -\mathcal{D} \left( \phi_f \left[ \tilde{Y}_f + \tilde{Z}_f \right] + \phi_f^\ell [1 - \gamma] \right)^{m+1}, \quad (6.36)$$

provided that when summing (6.35) over  $j$  we have

$$\frac{\sum_j Y_{j,f}}{Y_f} = 1, \quad (6.37)$$

which is analogous to (6.31). After comparison of this discrete form of the continuity equation with its exact counterpart, (6.10), it becomes clear that we must require  $\tilde{Y}_f + \tilde{Z}_f = 1$ . To guarantee this, we compute  $\tilde{Y}_f$  as

$$\tilde{Y}_f = 1 - \tilde{Z}_f = 1 - \sum_i s_i M_{i,f}. \quad (6.38)$$

The final form of the discrete density equation becomes

$$\frac{\rho^{m+1} - \rho^m}{\Delta t} = -\mathcal{D} \left( \phi_f + \phi_f^\ell [1 - \gamma] \right)^{m+1}. \quad (6.39)$$

It is shown in Appx. 6.B that this form, along with (6.33) and (6.35) satisfies the unity constraint (2.2).

### 6.3.2 Iterative solution algorithm for the drift velocity

In the previous section we proposed three models for the description of the droplet velocity  $\mathbf{v}$ : the Stokes model (6.18), Manninen's reduced Stokes model (6.22) and the Schiller-Naumann model (6.23). The local equilibrium assumption used in Manninen's model allows to find an algebraic expression for  $\mathbf{v}$  which is a prime reason for the popularity of this model. For the Stokes and Schiller-Naumann models a separate PDE must be solved with the mixture velocity  $\mathbf{u}$  as an input. Both these models contain a non-linearity with respect to the solution variable  $\mathbf{v}$ , in the convective transport term and in case of the Schiller-Naumann model, also in the drag force term. We solve both models iteratively. We illustrate the solution scheme by adopting

the implicit Euler method for the discretization of the time derivative, for notational compactness. However, in actual simulations we use the  $\theta$ -scheme [25].

Let  $k = 1, 2, \dots, \mathcal{K}$  be an iteration level and  $\mathbf{v}^{(k)}$  an intermediate approximate solution of  $\mathbf{v}^{m+1}$  at iteration level  $k$ . By using the notation introduced in the previous subsection, we may discretize (6.18) and (6.23) as

$$\begin{aligned} \frac{\mathbf{v}^{(k)} - \mathbf{v}^m}{\Delta t} + \mathcal{D}\left(\phi_{\mathbf{v}, f}^{(k-1)} \mathbf{v}_f^{(k)}\right) - \mathbf{v}^{(k)} \mathcal{D}\left(\phi_{\mathbf{v}, f}^{(k-1)}\right) \\ = -\frac{a(\mathbf{v}^{(k-1)})}{\tau} \left(\mathbf{v}^{(k)} - \mathbf{u}^{m+1}\right) + (1 - \gamma) \mathbf{g}, \end{aligned} \quad (6.40)$$

where, for convenience of implementation in OpenFOAM, we used the identity  $(\mathbf{v} \cdot \nabla) \mathbf{v} = \nabla \cdot (\mathbf{v} \mathbf{v}) - \mathbf{v}(\nabla \cdot \mathbf{v})$ . The divergence of the droplet velocity field is not necessarily zero, due to a ‘compressible’ behavior of droplets. Particles may gather or scatter, depending on the flow conditions. In (6.40) we defined  $a$ , where  $a(\mathbf{v}) = 1$  for the Stokes model and  $a(\mathbf{v}) = 1 + 0.15 Re_d^{0.687}$  for the Schiller-Naumann model. The flux  $\phi_{\mathbf{v}, f}^{(k-1)}$  is defined as

$$\phi_{\mathbf{v}, f}^{(k-1)} = \mathbf{v}_f^{(k-1)} \cdot \mathbf{A}_f \quad (6.41)$$

and is computed before solving (6.40) for the next iterative solution  $\mathbf{v}^{(k)}$ . We accept the solution for  $\mathbf{v}^{(k)}$  as  $\mathbf{v}^{m+1}$  once  $|\mathbf{v}^{(k)} - \mathbf{v}^{(k-1)}| < \epsilon_v$ , where  $\epsilon_v$  is some pre-defined tolerance, for all computational cells. For  $k = 1$  the velocity  $\mathbf{v}^{(k-1)}$  present in (6.40) is not available, and we set it to  $\mathbf{v}^m$ .

At this point we have formulated the analytical drift flux model and introduced their discretized counterparts, which were shown to also be consistent in terms of the two consistency relations. Next, we will use the model in the description of non-isokinetic aerosol sampling.

#### 6.4 ASPIRATION EFFICIENCY OF A THIN-WALLED SAMPLER

As a means of validation of our model, we apply it to the prediction of axial aspiration efficiency, in which a cylindrical aerosol sampler is placed inline with an ambient aerosol flow. The aerosol sampler draws in aerosol from ambient flow into an orifice and leads it to a size or count measurement device. It is usually operated on a velocity different than the ambient velocity, leading to curvature in the flow around or into the sampler. In turn, this curvature generates size-dependent droplet drift; the sampler may sample a different aerosol size distribution than present in the ambient flow. The ratio between the measured droplet concentration and the ambient droplet concentration, for a fixed droplet size, is called the ‘aspiration efficiency’.

In this section we will first discuss the adopted simulation geometry and mesh, as well as the boundary conditions and initial conditions of the simulation. Next, we present results of the aspiration efficiency for different Stokes numbers and different

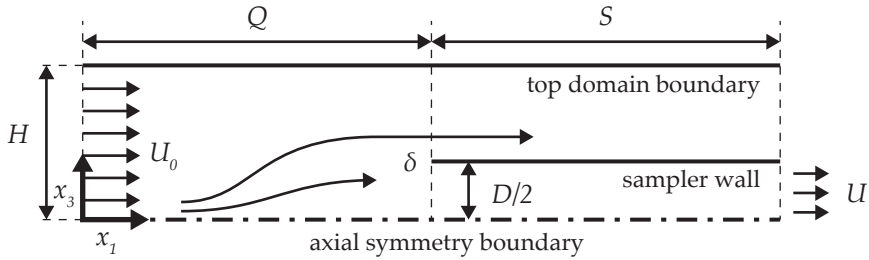


Figure 6.1: Schematic overview of the cylindrical sampler device with cross section-averaged sampling velocity  $U$  and ambient velocity  $U_0$ , carrying the aerosol to be sampled.

velocity ratios between ambient velocity and sampling velocity. We compare our results against the semi-empirical model of Belyaev and Levin [79, 80], using the three droplet velocity models.

#### 6.4.1 Geometry, mesh, boundary- & initial conditions

Fig. 6.1 shows a schematic overview of the simulation setup. We use a two-dimensional axisymmetric wedge setting, with the axis of symmetry located at  $x_3 = 0$ , along the  $x_1$  direction with  $\mathbf{x} = (x_1, x_2, x_3)$ . At  $x_1 = 0$  we have an inlet, imposing a uniform velocity  $U_0$  in the  $x_1$  direction and releasing aerosol into the domain. The entrance of the sampling pipe is located a distance  $Q$  from the inlet, modeled by a wall at  $x_3 = D/2$  and  $x_1 > Q$ . The sampling pipe extends from  $x_1 = Q$  to  $x_1 = Q + S$ , i.e., over a distance  $S$ . The upper domain boundary is located at  $x_3 = H$ . The outlet boundary, at  $x_1 = Q + S$ , is split up in the *sampler outlet* for  $0 < x_3 < D/2$  and the *ambient outlet* for  $D/2 + \delta \leq x_3 < H$ . The sampler wall has thickness  $\delta$ . With respect to the sampler diameter  $D$  we choose the other dimensions as follows:  $Q = 2.5D$ ,  $S = 8D$ ,  $H = 4.5D + D/16$  and  $\delta = D/16$ . For these spatial dimensions we verified that when increasing their values they did not notably influence the results, indicating that the boundary conditions are imposed far enough from the sampler inlet region not to affect the flow solution much. The diameter is set to  $D = 0.002$  m. This gives, with  $U_0 = 1$  m/s, a flow-through time of 0.021 s. We use this  $U_0$  in all simulations.

We use an orthogonal structured mesh with hexahedral cells. We use four variants of the same mesh, each a refined version of its coarser sibling. We also apply cell grading of factor 2 (i.e., the smallest cell is a factor 2 smaller than the largest cell), always towards the leading edge of the sampler, as we expect that most resolution is required in resolving the flow around the sampler's leading edge. Around the leading edge the cells are close to square in the  $(x_1, x_3)$ -plane. Tbl. 6.1 shows the number of grid points for each line segment and for each mesh.

Each simulation is started from a quiescent state. In the interval  $t \in [0, 0.1]$  s we ramp up the Dirichlet boundary condition for the velocity  $\mathbf{u}$  linearly from 0 to  $U_0$  with  $U_0 = 1$  m/s (in  $x_1$ -direction). At both the sampler and ambient outlet we set a zero gradient boundary condition for the velocity, i.e., we assume that the

line segment	mesh			
	A	B	C	D
$x_1 \in [0, Q]$	20	30	60	90
$x_1 \in [Q, Q + S]$	64	96	192	288
$x_3 \in [0, D/2]$	4	6	12	18
$x_3 \in [D/2, D/2 + \delta]$	1	1	2	3
$x_3 \in [D/2 + \delta, H]$	32	48	96	144

Table 6.1: Number of grid cells per line segment. Cell grading of  $f = 2$  is applied to each segment except the fourth one, and grading is always such that the smallest cell is closest to the leading edge of the sampler wall. The chosen grid resolution and grading is such that cells near the sampler leading edge are close to square in shape in the  $(x_1, x_3)$ -plane.

flow is well-developed once it reaches either outlet. At the sampler wall a no-slip boundary condition is applied for the velocity. For the  $\mathbf{v}$  field we set exactly the same boundary conditions as for the  $\mathbf{u}$  field. For the pressure we set a zero gradient boundary condition at the inlet and a Dirichlet boundary condition at the ambient outlet, i.e.,  $p = 10^5$  Pa. We control the sampling velocity  $U$  by setting a fixed pressure gradient at the sampler outlet. If the flow would be perfectly parabolic inside the sampler, the Poiseuille flow pressure drop equation could be applied, which is of the form

$$\nabla p \sim -\frac{\mu U}{D^2}, \quad (6.42)$$

with  $\mu$  the fluid viscosity. We found that for the current setting the following formula for the pressure gradient boundary condition results in a reasonably accurate simulated velocity  $U$ :

$$\nabla p = -23 \frac{\mu U}{D^2}. \quad (6.43)$$

By setting a pressure gradient according to this formula using the desired sampler outlet velocity  $U$ , the resulting simulated sampler outlet velocity will be close to this  $U$ . The coefficient 23 in this relation is an empirically determined number, and accounts for the flow pattern upstream of the outlet. Finally, we define the sampling velocity ratio as

$$R = \frac{U_0}{U}. \quad (6.44)$$

We only release aerosol droplets into the domain once the flow has achieved a steady state. The flow is sufficiently converged to steady state at around 10 flow-through times. Therefore, for  $t < 0.2$  we only have carrier gas in the domain. To achieve this, in a two-species system, we set  $Y_1 = 1$ ,  $Y_2 = 0$ ,  $Z_1 = 0$  and  $Z_2 = 0$ , for  $t < 0.2$ , where label 1 identifies the carrier gas and label 2 the released aerosol-forming species. For  $t \geq 0.2$  we release aerosol into the domain by setting  $Z_2(x_1 = 0) = Z_2 =$

$10^{-6}$  and  $Y_1(x_1 = 0) = \mathcal{Y}_1 = 1 - \mathcal{Z}_2$  at the inlet, while  $Y_2(x_1 = 0)$  and  $Z_1(x_1 = 0)$  remain zero. The total liquid mass of the second species consists of a collection of droplets. Also at the inlet the discrete first moment constraint (2.31) should hold. We assume that each section contains the same number of droplets, so that  $M_i = \text{const}$ . This implies that, using (2.31), the boundary condition for  $M_i$  at  $x_1 = 0$  becomes

$$M_i(x_1 = 0) = \mathcal{M} = \frac{Z_2}{\sum_i s_i} \quad \text{for} \quad t \geq 0.2, \quad (6.45)$$

and zero for  $t < 0.2$ . We define the droplet inlet number concentration  $N_0 = \rho(x_1 = 0)\mathcal{M}$  for later use.

The temperature  $T$  is initially set to  $T_0 = 293.15\text{ K}$ , and is kept uniform by setting a Dirichlet boundary condition at the inlet and the sampler wall, both equal to  $T_0$ . All other boundaries are insulating, i.e., zero normal gradient of temperature. A negligible heat production inside the domain occurs due to viscous heating and mechanical work.

At the top domain boundary we apply a zero normal gradient boundary conditions for all fields, implying that the boundary is located sufficiently far from any flow perturbations.

For the carrier gas we use the physiochemical properties of air, i.e., its compressibility ratio is given by  $\chi_1 = 3.5 \times 10^{-3} / \text{K s}^2\text{m}^{-2}$  [12], which gives at atmospheric pressure and at temperature  $T_0$  a density of approximately  $1.2\text{ kg/m}^3$ . For the second species we set its liquid density of pure constituent to  $\rho_2^\ell = 3.96 \times 10^3\text{ kg/m}^{-3}$ , corresponding to that of Aloxite test powders [93]. Because the mixture consists almost exclusively of air, the viscosity of the mixture is taken equal to that of air:  $\mu = 1.81 \times 10^{-5}\text{ kg/(m s)}$ . This gives, with sampler tube diameter  $D$  the typical length scale of the problem, a flow Reynolds number of  $Re = \rho D U_0 \mu^{-1} \approx 132$ , with  $\rho$  the mixture density. Under these conditions a steady flow will develop.

For the interpolations required for the convective terms in the  $\mathbf{u}$  and  $\mathbf{v}$  equations we use the Minmod limiter scheme<sup>‡</sup> [94]. This gives, in this particular setting, reliable non-oscillatory solutions for the two velocity fields, even for the coarse mesh A. For the interpolation scheme for  $M_i$ ,  $Z_j$  and  $Y_j$  used in the convective terms (e.g., the scheme used to compute  $Z_{j,f}$  in (6.33)), we use Van Leer's limiter<sup>§</sup> [95]. This scheme gives monotonicity preservation of the solution, as well as satisfaction of the constraint relations (2.2) and (2.31) always up to machine precision. For all other interpolations, for example, in the Laplacian terms, we use the central scheme. The time derivates are discretized with the  $\theta$ -scheme [25] with  $\theta = 0.6$ , formally making the time integration first order, but introducing some implicit damping of the higher frequencies in the solution. In our experience, with  $\theta = 0.6$ , the time-varying behavior of the solution is still accurate and the temporal truncation error is in magnitude close to the one

<sup>‡</sup>Called Minmod in OpenFOAM.

<sup>§</sup>Called vanLeer01 in OpenFOAM, which is a "strictly bounded" version of the Van Leer limiter.

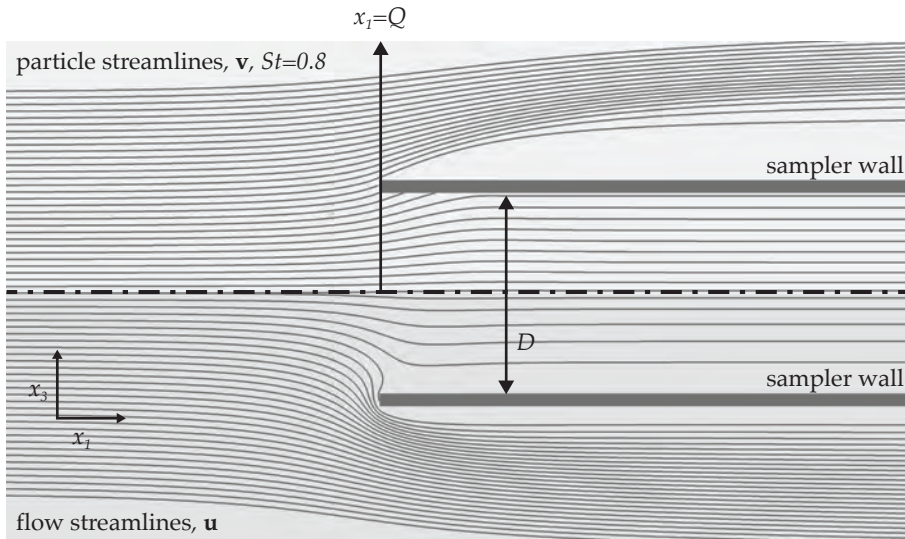


Figure 6.2: Streamlines of the steady state velocity field  $\mathbf{u}$  (lower half) and steady state droplet velocity field  $\mathbf{v}$  with  $St = 0.8$  (upper half). The simulations were performed on mesh D for  $R = 10$ .

achieved with  $\theta = 0.5$ . We expect that, given that the solution should approach a steady state, the time integration scheme plays a small role in the numerical error of the simulation. The time step is limited by a Courant-Friedrich-Lowy (CFL) condition, requiring that  $CFL \leq 0.5$  for all computational cells. This CFL condition produced a stable solution for all simulations, while not being too demanding.

#### 6.4.2 General solution & grid dependence

Fig. 6.2 shows the streamlines (created by integrating tracer paths in the instantaneous velocity field) for the steady state solution of  $\mathbf{v}$  (upper half) and  $\mathbf{u}$  (lower half, mirrored in the symmetry axis), the former taken at  $St = 0.8$ , for sampling velocity ratio  $R = 10$ . The velocity  $\mathbf{v}$ , describing the trajectory of droplets, is ‘smoother’, due to the larger momentum carried by the dispersed phase. Droplets ‘overshoot’ the motion of the fluid. For this  $R$  the flow is such that there are streamlines, close to the leading edge of the sampler wall, for which the fluid velocity becomes negative in  $x_1$ -direction; there exists a circulation zone. Fig. 6.3 shows a close-up of the leading edge for four different values of  $R$ . Both the streamlines for  $\mathbf{u}$  and  $\mathbf{v}$  are shown, now for  $St = 0.17$ . As  $R$  increases, the circulation zone becomes more pronounced. It is shown that for the two largest  $R$  values droplets start to cluster near the tip of the sampler wall, due to the streamlines of  $\mathbf{v}$ . In particular, for  $R = 10$ , the  $\mathbf{v}$ -streamlines are almost perpendicular to the inside of the sampler wall.

Fig. 6.4 (left) shows the first component of the scaled fluid velocity and scaled droplet velocity, for all four meshes, plotted over the line  $x_1 = Q$  (the line shown

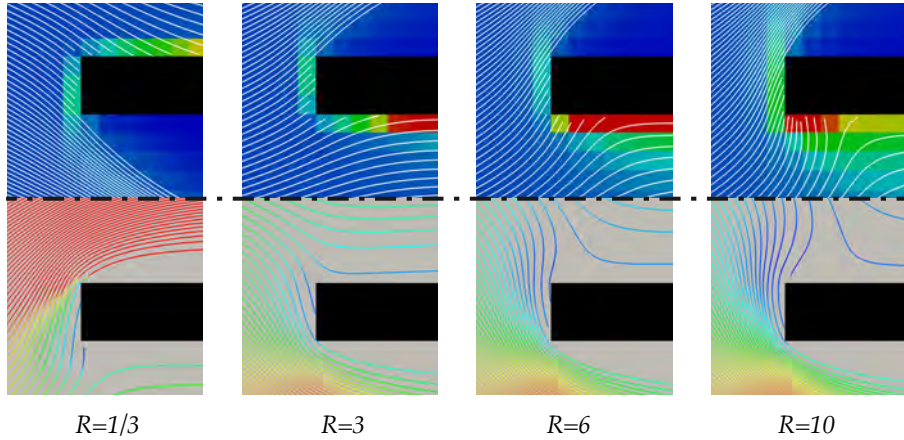


Figure 6.3: Closeups of the leading edge of the sampler wall (black) for four values of  $R$  with  $v$ -streamlines for  $St = 0.17$  (upper half) and  $u$ -streamlines (lower half). Color in the upper half indicates the droplet number concentration of particles, linearly from low to high: blue – green – yellow – red, with red representing  $10 \times N_0$ . Color in the lower half indicates the magnitude of  $u_1/U_0$ , with  $0.1 < u_1/U_0 < 1$ . The dash-dotted line indicates the line about which the upper half is mirrored into the lower half. Clustering of particles near the leading edge of the pipe increases as  $R$  increases.

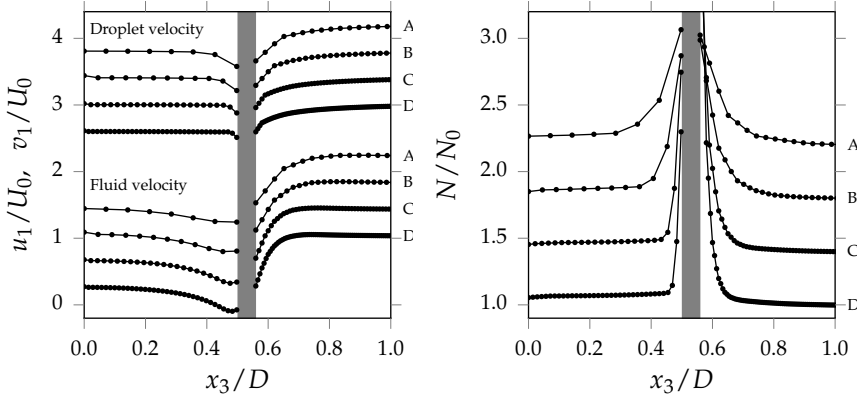


Figure 6.4: Left: the scaled  $x_1$ -component fluid and droplet velocity profiles. Right: the scaled droplet number concentration. Both plots are along a line in  $x_3$ -direction for  $x_1 = Q$ , i.e., the entrance of the sampler, shown for the four meshes as indicated. The Stokes number of the droplets for which  $v_x$  and  $N$  are plotted was  $St = 0.8$ . The marked area shows the position in  $x_3$  of the sampler wall. The simulations were performed for  $R = 10$  and using the Stokes model for  $\mathbf{v}$ . The lines are vertically offset for visual clarity.

in Fig. 6.2). The sampler wall is marked by gray. Convergence of the solution as a function of grid resolution is clearly appreciated by visual inspection. Also, the circulation zone is more pronounced for the two finest meshes, with larger negative

velocities. By inspection of Fig. 6.4 (left) we conclude that mesh C already gives adequate results. Fig. 6.4 (right) shows an equivalent image for the scaled droplet number concentration for droplets with  $St = 0.8$ . As the mesh resolution increases the gradient of  $N/N_0$  becomes sharper at both sides of the sampler wall. Mesh C gives a comparable solution to the one of mesh D.

To illustrate the ‘response’ of droplets for different Stokes numbers, Fig. 6.5 (left) shows for four typical Stokes numbers the scaled droplet concentration near the sampler wall. Quite remarkably, there is some intermediate Stokes number,  $St = \mathcal{O}(10^{-1})$  (in the current setting corresponding to a droplet diameter of  $d = \mathcal{O}(1) \mu\text{m}$ ), for which we find a peak in droplet number concentration at the wall. Qualitatively, this behavior is also visible in the results of [87]. For larger and smaller Stokes numbers the droplet accumulation at the wall is shown to be less pronounced. Fig. 6.5 (right) shows the  $x_1$ -component of the droplet velocity for a series of increasing Stokes numbers, also at the sampler inlet. For small Stokes numbers, i.e., small droplet relaxation times, the droplet velocity is seen to reduce to the fluid velocity, as expected. For very large Stokes numbers the droplet velocity appears to be only marginally affected by the flow conditions at the sampler inlet; they ‘penetrate’ the sampler due to their large carried momentum. We argue that in between these two regimes, there exists a regime for which the negative velocity of the fluid in the circulation zone, inducing a negative force on the droplets, is balanced by the momentum-induced inward motion of the droplets: they aggregate. This is also illustrated well by Fig. 6.3, where for  $R = 10$  the droplet streamlines are almost perpendicular to the inside of the sampler wall. In this particular setting, for  $R = 10$ , this intermediate regime is found near  $St = \mathcal{O}(10^{-1})$ .

#### 6.4.3 Aspiration efficiency predictions & validation

As can be clearly seen in Fig. 6.2, the streamlines of the droplets tend to ‘overshoot’ the fluid flow. Droplet trajectories deviate from fluid trajectories with a bias into the sampler, whereas the fluid flows around the sampler wall. The sampled aerosol concentration becomes larger than the ambient one. This bias can be expressed in terms of an ‘aspiration efficiency’  $A$ . We compute  $A$  from the mass flux of droplets at the sampler inlet, i.e., at  $x_1 = Q$  and  $s \leq D/2$ .

The droplet mass flux at the sampler inlet for section  $i$  is, at the discrete level, given by

$$\Phi_i = \sum_{f \in \mathcal{F}^s} A_f \left[ \phi_f + \phi_{i,f}^\ell \right] M_{i,f} s_i, \quad (6.46)$$

where the summation is over  $f \in \mathcal{F}^s$  with  $\mathcal{F}^s$  the set of faces exactly at  $x_1 = Q$  inside the sampler, i.e.,  $x_3 < D/2$ . If droplets would not drift, their trajectories would coincide with those of the fluid motion, and the sampler should ‘receive’ a representative droplet concentration. The hypothetical ‘drift-free sampler inlet droplet

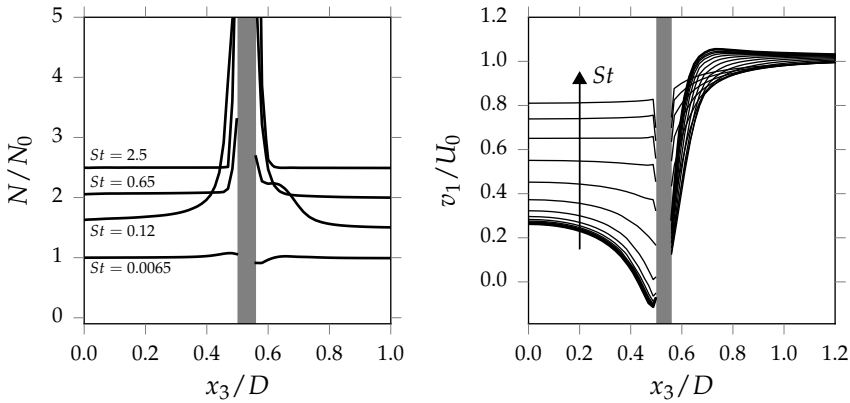


Figure 6.5: Left: the scaled number concentration of droplets along the vertical line at  $x_1 = Q$ , i.e., at the sampler inlet, four typical Stokes numbers each vertically offset by 0.5 for visual clarity. Right: the scaled droplet velocity  $x_1$ -component along the line  $x_1 = Q$ , for increasing  $St$ . In opposite direction of the arrow, the top 7 lines are for  $St = 2.1, St = 1.4, St = 0.96, St = 0.65, St = 0.44, St = 0.30$  and  $St = 0.21$ . The simulations were performed for  $R = 10$  on mesh D using the Stokes model for  $\mathbf{v}$ .

mass flux' for section  $i$  can be defined as

$$\Phi_{0,i} = \sum_{f \in \mathcal{F}^s} A_f \phi_f \mathcal{M} s_i. \quad (6.47)$$

The ratio between (6.46) and (6.47) is an indication for the change in sampled droplets of section  $i$  and is defined as the aspiration ratio, i.e.,

$$A_i = \frac{\Phi_i}{\Phi_{0,i}}. \quad (6.48)$$

For  $St \rightarrow 0$  the aspiration  $A_i$  becomes unity; the small-droplet sample is representative for the concentration of those droplets in the ambient flow, as expected. The velocity of very large droplets remains roughly constant at the velocity with which they are released into the domain,  $U_0$ , due to their large carrier momentum. In that case  $A_i$  becomes proportional to  $R$ .

Fig. 6.6 (left) shows the aspiration  $A$  as a function of  $\log St$ , for three velocity ratios  $R$ , computed on mesh D. For the coarser meshes the aspiration curves are very similar to those of mesh D, suggesting that the aspiration process is not very sensitive to the spatial resolution of the mesh. As expected, for each  $R$ , the aspiration reduces to unity for  $St \rightarrow 0$ .

Fig. 6.6 (left) also shows the semi-empirical model of B&L [79, 80]. Generally, we find a very good agreement of our model with the results of the B&L model. This is particularly true for all Stokes numbers, provided  $R < 5$ . Conversely, for droplets

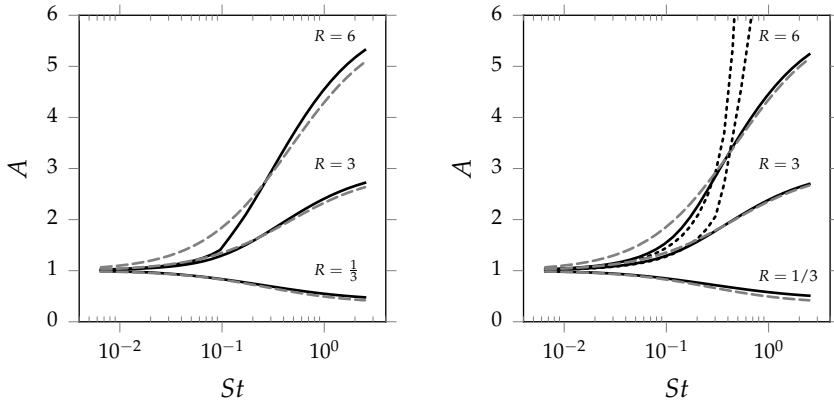


Figure 6.6: Simulated aspiration curves as a function of  $St$  for  $R = 1/3$ ,  $R = 3$  and  $R = 6$ . Left: full Stokes model (—). Right: Schiller-Naumann model (—) and Manninen's model (···). On both figures the Belyaev-Levin model (---) is shown. All results were computed using Mesh D.

for which  $St = \mathcal{O}(10^{-1})$  and  $R > 5$  an underprediction of  $A$  appears with respect to B&L. We argue that this is due to the sharp increase in concentration of the droplets near the leading edge of the sampler, as was shown in Fig. 6.5 and explained in the previous subsection. In the case of large concentrations two-way coupling between the droplet and fluid phase, four-way coupling between droplets or collisions with the sampler wall will become important and are expected to lead to corresponding corrections in the aspiration predictions. This aspect is beyond the current chapter and will not be considered further.

The results shown in Fig. 6.6 (left) were computed using the full Stokes (FS) model for the description of the droplet velocity  $\mathbf{v}$ . In Fig. 6.6 (right) we introduced two other models: Manninen's reduced Stokes (MRS) model and the Schiller-Naumann (SN) model. The FS model and SN model display very similar aspiration curves for all  $St$  and  $R$  studied. Also, the MRS model agrees quite well with the other two for sufficiently small particles with  $\log St < -0.7$ , i.e.,  $St < 0.2$ , although the differences become more visible with increasing  $R$ . For larger  $St$  the MRS model sharply over-predicts the aspiration, both in comparison with the FS and SN models as well as the semi-empirical model of B&L. As argued before, it was expected that the MRS model is only valid for small Stokes numbers, which is convincingly illustrated by the results shown in Fig. 6.6. Even though  $\tau$  becomes of the same order as the typical time associated with the flow, i.e.,  $St = 1$ , our Eulerian model is capable of predicting a reasonably correct aspiration. This demonstrates that the Eulerian approach may still be applicable in Stokes regimes for which the Lagrangian approach is argued to be more suitable [72].

Whereas Fig. 6.6 shows the aspiration as a function of  $St$ , which, in turn, is proportional to  $d^2$  (see (6.19) and (6.21)), it is also interesting to see the dependence

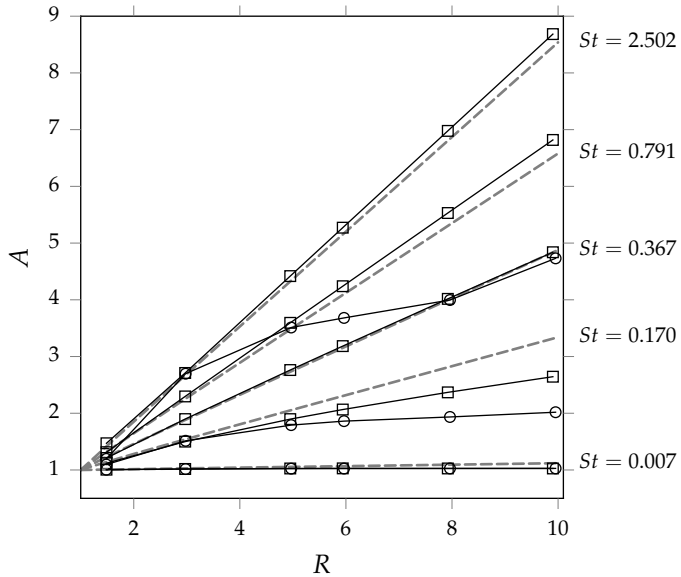


Figure 6.7: Simulated aspiration curves as a function of  $R$  for various Stokes numbers, using the Stokes model ( $\square$ ) and Manninen's model ( $\circ$ , only shown for the three lowest  $St$  numbers). Also shown is the Belyaev-Levin model (---). The results are computed on mesh B.

of the aspiration on the sampling velocity ratio  $R$ . Fig. 6.7 shows, for a selection of Stokes numbers,  $A$  as a function of  $R$ , comparing the Stokes and Manninen's model. For the two largest Stokes numbers in Fig. 6.7 we did not attempt to predict the aspiration using the MRS model, as Fig. 6.6 already indicated that this model is no longer accurate in that regime. For the intermediate Stokes numbers,  $\mathcal{O}(10^{-1})$ , again, we see an underprediction of  $A$ , in the range  $R > 5$ , roughly speaking. For these  $R$  the re-circulation zone inside the sampler becomes more pronounced and affects the accumulation of aerosol droplets at the leading edge of the sampler. For very large Stokes numbers the curves turn to  $A = R$ , meaning that aspiration becomes proportional to  $R$  in that limit, as is also predicted by the B&L model.

## 6.5 CONCLUSIONS

In this chapter we developed a multi-species internally mixed Eulerian compressible aerosol model, in which the particulate phase is described both by a mass fraction for each species and a droplet size distribution. Starting from the GDE we introduced a drift term, accounting for the fact that droplets may follow different trajectories with respect to the carrier gas, due to inertia, drag and gravity. We adopted three models for the description of the droplet motion: the full Stokes drag model (FS), Manninen's reduced Stokes model (MRS) and the Schiller-Naumann drag model (SN).

In the derivation of the governing set of equations of the droplet size distribution and species-specific vapor and liquid mass concentrations, we retained consistency among the transport equations in terms of two relations that should identically hold. The first consistency relation ensures that the mass fractions sum up to unity and the second consistency relation ensures that the first moment of the droplet size distribution corresponds to the total liquid mass in the system, as expressed by the liquid mass fractions.

To solve the set of equations we adopted a finite-volume cell-centered collocated numerical method, and discretized the continuous size distribution using the sectional method. Special attention was paid to satisfying the two consistency relations also at the discrete level. This led to two requirements on the interpolations of mass fractions to the cell faces: when computing the total liquid or vapor mass concentration at the cell face, we must first interpolate each species-specific mass concentration to the face and then sum. Also, we adopted a formulation of the numerical convective flux which gives a robust method, by preventing division by zero if no liquid is present.

To demonstrate the capability and validity of the method and to assess the three droplet velocity models we studied the problem of aerosol aspiration in a cylindrical sampler. We modeled the sampler geometry by exploiting the axial symmetry of the setup. First, we established confidence in the method by considering the solution of the velocity profile and droplet concentration profile at the sampler inlet, for four different meshes, each a refined version to its coarser sibling. Convergence of the solution was clearly visible. Next, we studied the behavior of the droplet phase as a function of Stokes number. It was shown that there exists an intermediate Stokes number range around  $St = \mathcal{O}(10^{-1})$  for which droplets aggregate near the leading edge of the sampler. It was argued that at such Stokes numbers droplets are ‘trapped’ in the recirculation zone that forms. We showed that the aspiration, expressing the ratio of droplet flux with the hypothetical droplet flux of a non-drifting aerosol can be accurately predicted even at very modest spatial resolutions.

It was shown that for  $St < 0.2$  all three droplet velocity models agree well with each other for the range of considered velocity ratios  $R$ . As expected for larger Stokes numbers, the local equilibrium assumption loses its validity and the MRS model deviates significantly from both the SN and FS models, as well as the semi-emperical model of B&L. The SN and FS droplet velocity model agree well with each other and with B&L for the studied range of  $St$  and sampler velocity ratio  $R$ , provided  $R < 5$ . Beyond  $R > 5$  differences appear at all  $St$  values. We argue that this is due to the increase in droplet accumulation near the leading edge of the sampler for such Stokes numbers. For small and large Stokes numbers outside the  $St = \mathcal{O}(10^{-1})$  regime our predictions for the aspiration efficiency agree well with B&L for any  $R$ .

## 6.A IMPLICATION OF THE CHOSEN Z-EQUATION EXPANSION

Starting from Eq. (6.4) we can write

$$\partial_t(\rho Z_j^{-1} Z_j Z) + \nabla \cdot (\rho \mathbf{u} Z_j^{-1} Z_j Z) + \nabla \cdot (Z^{-1} \mathbf{f} Z_j^{-1} Z_j Z) = 0, \quad (6.49)$$

where we set, to study only the influence of droplet drift, the right-hand side to zero. After applying the product rule this relation can be written as

$$\begin{aligned} \partial_t(\rho Z_j) + \nabla \cdot (\rho \mathbf{u} Z_j) + \nabla \cdot (Z^{-1} \mathbf{f} Z_j) \\ - \rho Z_j \Gamma^{-1} [\partial_t \Gamma + (\mathbf{u} \cdot \nabla) \Gamma + (\{\rho Z\}^{-1} \mathbf{f}) \cdot \nabla \Gamma] = 0, \end{aligned} \quad (6.50)$$

where

$$\Gamma = \frac{Z_j}{Z}. \quad (6.51)$$

If we adopt (6.7) (with the right-hand side also set to zero), this implies that

$$(\partial_t + [\mathbf{u} + \boldsymbol{\omega}] \cdot \nabla) \Gamma = D_t^\ell \Gamma = 0, \quad (6.52)$$

where  $D_t^\ell$  is the material derivative with respect to velocity  $\mathbf{u} + \boldsymbol{\omega}$  and with

$$\boldsymbol{\omega} = \frac{\int_0^\infty z \mathbf{u}^\ell(s) n(s, \mathbf{x}, t) ds}{\int_0^\infty z n(s, \mathbf{x}, t) ds}, \quad (6.53)$$

where we replaced  $\rho Z$  and  $\mathbf{f}$  by (2.23) and (6.5), respectively. The velocity  $\boldsymbol{\omega}$  is the mass-weighted drift velocity, or, the drift velocity of average mass. Given this, the physical implication of (6.52) is that  $\Gamma$ , the partitioning between  $Z_j$  and  $Z$ , i.e., the composition of the liquid mixture, remains constant on the characteristic

$$d_t \mathbf{x} = \mathbf{u} + \boldsymbol{\omega}. \quad (6.54)$$

From a physical point of view this seems reasonable. For example, when  $\mathbf{u}^\ell(s)$  is constant the characteristic velocity reduces to  $\mathbf{u} + \mathbf{u}^\ell = \mathbf{v}$ , which is the ‘true’ droplet velocity  $\mathbf{v}$ , see (6.2). Indeed, along  $\mathbf{v}$  the composition of the droplets remains constant, which is a reasonable property of the model.

## 6.B UNITY PRESERVATION OF THE DISCRETE MASS FRACTION EQUATIONS

In Sec. 6.3 we derived the discrete forms of the  $Y_j$ ,  $Z_j$  and  $\rho$  equations, (6.35), (6.33) and (6.39), respectively. It was claimed that these forms preserve unity of the sum of mass fractions. Here we will demonstrate this.

At time  $t^m$  we have the solution  $\rho^m$ ,  $Y_j^m$  and  $Z_j^m$ . We assume that

$$(Y + Z)^m = 1, \quad (6.55)$$

where  $Y = \sum_j Y_j$  and  $Z = \sum_j Z_j$ . Equation (6.36) is the result of adding (6.33) and (6.35) to each other and summing that over  $j$ . Subtracting this from the final discrete continuity equation (6.39), we find

$$\begin{aligned} \frac{\rho^{m+1}(1 - [Y + Z]^{m+1}) - \rho^m(1 - [Y + Z]^m)}{\Delta t} = \\ -\mathcal{D}\left(\phi_f + \phi_f^\ell[1 - \gamma]\right)^{m+1} + \mathcal{D}\left(\phi_f[\tilde{Y}_f + \tilde{Z}_f] + \phi_f^\ell[1 - \gamma]\right)^{m+1}. \end{aligned} \quad (6.56)$$

Using (6.38), i.e.,  $\tilde{Y}_f + \tilde{Z}_f = 1$ , the two terms in the right-hand side cancel each other. If we then introduce (6.55) in the left-hand side the  $\rho^m$ -term drops out and we find that

$$(Y + Z)^{m+1} = 1, \quad (6.57)$$

i.e., if the mass fraction solutions at  $t^m$  sum up to unity, then so will those at  $t^{m+1}$ : 'unity' is preserved.

## CHAPTER 7

# INERTIAL AND DIFFUSIONAL AEROSOL DEPOSITION\*

### ABSTRACT

This chapter presents a sectional Eulerian aerosol model for size-dependent droplet deposition at walls of the domain, driven by both diffusion and inertia. The model is based on the internally mixed assumption and employs the formulation for compressible aerosols. It is validated in a bent pipe geometry against models and experimental and numerical data from literature. Good agreement is found in both the diffusion and inertial deposition regimes. To improve the overprediction of inertial deposition by a boundary treatment that adopts zero-gradient droplet wall velocity, we use a Lagrangian sub-grid model, based on an analytical solution of the droplet motion near the wall. In the bent pipe setting this sub-grid model is found to reduce the overprediction of deposition and is less sensitive to grid refinement. We also show that refining the computational mesh near the pipe wall improves the predicted deposition efficiency, significantly. Finally, we present a parameter study varying the Reynolds number and the bend curvature. The deposition efficiency curve is recorded for droplet diameters ranging from the nanometer scale to beyond the micrometer scale. The complete size range is simulated in only one simulation, due to the sectional approach. In the diffusion-dominated regime an increase in Reynolds number leads to a gradual enhancement of deposition. In the inertial regime, where droplet drift dominates deposition, a much stronger dependence on the Reynolds number is found. The dependence of the deposition on the bend curvature is less pronounced. The results shown in this chapter may establish the role of Eulerian simulation in predicting deposition of aerosol droplets and may be useful for understanding size-dependent aerosol deposition in other more complex confined geometries.

### 7.1 INTRODUCTION

Two of the main mechanisms of aerosol deposition are inertial impaction and diffusion [3]. Both processes are strongly size dependent; small aerosol droplets deposit due to high diffusivity, large droplets due to large momentum and intermediately

---

\*This chapter is based on Frederix et al. [96]: Eulerian modeling of inertial and diffusional aerosol deposition in bent pipes. *International Journal of Multiphase Flow*, submitted.

sized droplets deposit more scarcely. In a setting where the Reynolds number is sufficiently high so that gravitational settling becomes negligible, this leads to the well-known deposition efficiency curve which has a characteristic 'V' shape. This was observed in many kinds of geometry that involve aerosol deposition, e.g., in respiratory flow [97, 98, 99] or flow around an object [70, 100]. The exact shape of this deposition curve characterizes the filtration efficiency of an object or geometry, and is very useful for understanding aerosol deposition. In this chapter we will employ the Eulerian sectional modeling approach presented earlier, to predict the filtration characteristics of a bend pipe geometry for all aerosol droplet sizes ranging from the nanometer scale to beyond the micrometer scale. We show that accurate predictions may be achieved provided the near-wall dynamics are accurately represented.

In the previous chapters we developed the Eulerian, sectional, internally mixed aerosol model capable of predicting the evolution of the droplet size distribution undergoing nucleation, condensation, evaporation, coagulation and droplet drift. We formulated a compressible model in which the mixture density is constituted by a number of chemical species, either present as vapor or in the form of liquid droplets. The droplet drift aspect of the model, incorporating the inertia-driven mechanism of droplet streamlines deviating from those of the carrier gas, was validated in the setting of aerosol sampling, see Chp. 6. Building on that foundation, in this chapter we extend this model to include droplet diffusion and wall deposition. The main objective of this chapter is to present the model and to validate our Eulerian approach against data from literature, in both the diffusion and the inertial regime. Moreover, we study how predictions depend on the chosen grid and boundary treatment for the droplet velocity.

The sectional Eulerian model retains a compressible formulation in which the mixture density is composed of both vapors and liquids, mitigating a passive scalar approach as is done in many other works, e.g., [74, 78]. This couples the aerosol processes, such as droplet drift and diffusion but also nucleation and condensation (see Chp. 5) to the transport equations for mass, momentum and energy. This may be relevant in cases where mixture compressibility is important, or where temperature changes are large. However, also in systems with small temperature variations the compressible fluid framework is beneficial for obtaining general and accurate models as reliable constitutive relations can be formulated explicitly. In combination with a pressure-based approach this combines consistency in the physical model with computational efficiency. In Chp. 6 we developed a scheme which, by construction, implements two constraint equations ensuring 1) that species mass fractions always add up to unity and 2) that the first moment of the size distribution is also reflected in the liquid mass concentration solution.

We apply our model to the simulation of aerosol flow through a bent pipe. The bent pipe geometry offers a simple setting in which the mechanisms behind aerosol deposition can be systematically studied. In fact, the bent pipe can be used as a highly idealized mouth-throat model to emulate aerosol droplet deposition in the human

airways, see [101]. By studying the bent pipe a qualitative impression can be formed of both the flow and aerosol deposition patterns.

The bent pipe problem has been studied by many authors and therefore offers a reliable and well-understood point of reference. Earlier theoretical works studied particle trajectories in the bent pipe given an approximate flow field [102, 103, 104]. More recently, many authors have published CFD simulations of particle deposition in bends using Lagrangian (e.g., [105, 106, 107, 108]) or Eulerian methods (e.g., [74, 109, 110, 111, 112, 113]). Others have studied aerosol deposition in pipe bends experimentally, e.g., [101, 106, 114, 115]. The seminal work of Pui et al. [114] is key in the literature concerning bent pipe aerosol deposition efficiency and a clear source for validation. For example, Pilou et al. [74] found good agreement for Reynolds numbers  $Re = 100$  and  $Re = 1000$  and Vasquez et al. [113] found good agreement for  $Re = 1000$  while an overprediction of the deposition efficiency for  $Re = 100$  was observed.

Most bent pipe studies focused on the ‘inertial deposition regime’, looking at aerosol droplets or particles with a Stokes number typically larger than 0.01. For these droplets it is their inertia that leads to a collision with a geometry wall. However, as noted before, sufficiently small droplets may also deposit by diffusion. In fact, in many applications the aerosol droplet size is such that droplet diffusion and inertia are two important effects, e.g., see [78, 97, 116]. To validate our sectional Eulerian aerosol model, we consider aerosol deposition in a bent pipe for droplet sizes ranging from the nanometer scale to beyond the micrometer scale. This enormous size-range is the unique feature of our model: within one formulation the corresponding deposition efficiency curve spanning the complete size domain is predicted. Moreover, the sectional formulation spanning many decades in droplet sizes allows for a straightforward extension to include aerosol processes such as nucleation, condensation, evaporation and coagulation or break-up, as was done in previous chapters. The combination of these capabilities forms a unique and quite complete aerosol model.

For large droplets we compare the predictions of our model against aforementioned experimental and numerical bent pipe studies. For small droplets we compare against the analytical straight pipe diffusional deposition model of Ingham [117]. In both regimes we find good agreement, provided sufficient spatial resolution of the solution is adopted.

In this chapter we present a detailed numerical study of our model for droplet diffusion, drift and subsequent deposition. We study the two cases presented by [114], for Reynolds number  $Re = 100$  and  $Re = 1000$ , on five different meshes in which we compare results obtained with or without grid refinement near the wall. We use two boundary treatments for the droplet velocity at the wall, i.e., a ‘zero-gradient’ boundary treatment, keeping the droplet velocity from cell center to the wall constant, and a Lagrangian sub-grid model as proposed by [78], employing the analytical solution of the droplet equation of motion near the wall in a linearized flow field. The Lagrangian sub-grid model is shown to decrease the overestimation of the

deposition efficiency, and generally is less resolution sensitive. We show that the wall grid-refined meshes improve the predictions of the deposition curve significantly. We also present a parameter study for the dependence of the deposition efficiency on the Reynolds number and the bend curvature. An enhancement of both diffusion and inertial deposition is shown for increasing Reynolds number whereas the dependence on the bend curvature is small.

The layout of this chapter is as follows. First, in Sec. 7.2, the Eulerian sectional model is presented. As we extend Chp. 6, we summarize what was presented there and incorporate a droplet diffusion term. Two boundary treatments for the droplet velocity at the wall are discussed. In Sec. 7.3.1 we present the bend pipe geometry and in Sec. 7.3.2 the fluid velocity solution is validated against data from [74]. Next, in Sec. 7.3.3 the grid sensitivity of the solution is shown using both the zero-gradient and Lagrangian sub-grid model wall treatments. We validate the inertial and diffusion regime of the deposition curve in Sec. 7.3.4 and 7.3.5, respectively. Finally, in Sec. 7.3.6 we present a parameter study.

## 7.2 EXTENSION OF THE MODEL WITH DRIFT, DIFFUSION AND DEPOSITION

In this section we introduce the mathematical framework for the description of droplet drift, diffusion and deposition of an internally mixed multi-species aerosol. We follow closely the terminology of Chp. 6 and derive concentration transport equations from the droplet size distribution equation. For completeness, some of the results established in the previous chapter will be repeated here. Consistency is ensured by the constraint equation (2.23), relating the liquid mass concentrations to the first moment of the droplet size distribution. First, we extend the drift model of Chp. 6 with an additional droplet diffusion term. Next, we introduce the Stokes-Einstein model used for the description of the size-dependent droplet diffusivity. We write the new model, now also containing droplet diffusion, in a form similar to that presented in Chp. 6. The boundary treatment allowing simultaneous droplet deposition by diffusion and drift is discussed. Finally, the chosen temporal and spatial discretization methods are presented.

### 7.2.1 An internally mixed aerosol drift and diffusion model

Following Chp. 6 and [2] we introduce the General Dynamic Equation (GDE) for the size distribution, now also including droplet diffusion:

$$\begin{aligned} \partial_t n(s, \mathbf{x}, t) + \nabla \cdot [\mathbf{u} n(s, \mathbf{x}, t)] + \nabla \cdot [\mathbf{u}^\ell(s) n(s, \mathbf{x}, t)] \\ = \nabla \cdot [\mathbf{D}^\ell(s) \nabla n(s, \mathbf{x}, t)] + J(s, \mathbf{x}, t), \end{aligned} \quad (7.1)$$

where  $\mathbf{v}(s) = \mathbf{u} + \mathbf{u}^\ell(s)$  is the size-dependent droplet velocity with  $\mathbf{u}$  the mixture velocity and  $\mathbf{u}^\ell(s)$  the liquid drift velocity of an  $s$ -sized droplet with respect to

the motion of the carrier gas. The coefficient  $\mathbb{D}^\ell(s)$  is the size-dependent droplet diffusivity and  $J(s, \mathbf{x}, t)$  the source term accounting for possible phase change, droplet coagulation or break-up. Eq. (7.1) corresponds to Eq. (6.3) but contains the additional contribution of droplet diffusion.

The chosen internally mixed formulation of the aerosol mixture description was already introduced in Chp. 2. An implication of the internally mixed description is that the total liquid mass can be computed both from the liquid mass fraction fields and the first moment of the droplet size distribution. In fact, it was shown that a consistency relation can be formulated in the form of Eq. (2.23), which will be recalled here for completeness:

$$\rho Z = \int_0^\infty s n(s, \mathbf{x}, t) ds, \quad (7.2)$$

where  $Z = \sum_j Z_j$ . This denotes the mutual consistency between liquid mass concentrations and the droplet size distribution. To maintain this consistency, we impose (7.2) to the GDE, by multiplying the GDE by  $s$  and taking the integral over  $s$  on  $[0, \infty)$ . This gives, after employing (7.2):

$$\partial_t(\rho Z) + \nabla \cdot (\rho \mathbf{u} Z) + \nabla \cdot (Z^{-1} \mathbf{f}^{\text{drift}} Z) - \nabla \cdot (Z^{-1} \mathbf{f}^{\text{diff}} Z) = \mathcal{J}, \quad (7.3)$$

where we introduced the scalar product  $Z^{-1}Z = 1$  for later use, and where

$$\begin{aligned} \mathbf{f}^{\text{drift}} &= \int_0^\infty s \mathbf{u}^\ell(s) n(s, \mathbf{x}, t) ds, & \mathbf{f}^{\text{diff}} &= \int_0^\infty s \mathbb{D}^\ell(s) \nabla n(s, \mathbf{x}, t) ds, \\ \text{and} \quad \mathcal{J} &= \int_0^\infty s J(s, \mathbf{x}, t) ds. \end{aligned} \quad (7.4)$$

The drift flux  $\mathbf{f}^{\text{drift}}$  and source term  $\mathcal{J}$  were also retrieved in Chp. 6, however, in addition we now also have a diffusional flux  $\mathbf{f}^{\text{diff}}$ . If we write the total ‘additional’ flux as

$$\mathbf{f} = \mathbf{f}^{\text{drift}} - \mathbf{f}^{\text{diff}}, \quad (7.5)$$

then Eq. (7.3) becomes mathematically equivalent to the equation for the rate of change of  $\rho Z$  in Chp. 6. All subsequent derivations done in Chp. 6 therefore also apply to (7.3), with the sole difference being that the flux  $\mathbf{f}$  now includes both diffusion and drift. The transport equations for the species-specific liquid and vapor mass concentrations become

$$\partial_t(\rho Z_j) + \nabla \cdot (\rho \mathbf{u} Z_j) + \nabla \cdot (Z^{-1} \mathbf{f} Z_j) = \mathcal{S}_j, \quad (7.6a)$$

$$\partial_t(\rho Y_j) + \nabla \cdot (\rho \mathbf{u} Y_j) - \nabla \cdot (Y^{-1} \mathbf{h} Y_j) = \mathcal{R}_j, \quad (7.6b)$$

with  $\mathcal{S}_j$  and  $\mathcal{R}_j$  the liquid and vapor mass concentration source terms, and  $\mathbf{h} = \gamma \mathbf{f}$  the vapor correction flux with  $\gamma = \rho^v / \rho^\ell$  the ratio between total vapor concentration

and liquid concentration.

The drift and diffusion continuity equation becomes

$$\partial_t \rho + \nabla \cdot (\rho \mathbf{u}) + \nabla \cdot [\mathbf{f}(1 - \gamma)] = 0, \quad (7.7)$$

where the third term in the right-hand side accounts for the change in mixture mass density as a result of droplet appearance or removal due to drift or diffusion.

To summarize, we have included a diffusional flux term  $\mathbf{f}^{\text{diff}}$  in the total ‘additional’ flux  $\mathbf{f}$ . We call this flux ‘additional’, because it drives transport away from streamlines  $\mathbf{u}$ . The remaining part of the derivation to arrive at the transport equations for  $Y_j$  and  $Z_j$  is exactly equal to that in Chp. 6. Also, this formulation allows to follow the same numerical procedures.

### 7.2.2 The Stokes-Einstein model for Brownian diffusion

The diffusive flux  $\mathbf{f}^{\text{diff}}$  depends on the size-dependent diffusivity  $\mathbb{D}^\ell(s)$ . This diffusivity also appears in the diffusion term in the GDE. We adopt the Stokes-Einstein equation, providing a model for the Brownian diffusivity of a spherical body. It implies [3]

$$\mathbb{D}^\ell(s) = \frac{k_B T C_c}{3\pi\mu d}, \quad (7.8)$$

with  $k_B$  the Boltzmann constant, temperature  $T$ , Cunningham correction factor  $C_c$ , mixture viscosity  $\mu$  and droplet diameter  $d$  related to  $s$  with Eq. (2.20). We compute the Cunningham correction factor, accounting for surface slip of small droplets, as [3]

$$C_c = 1 + \frac{\lambda}{d} \left( 2.34 + 1.05 \exp \left[ -0.39 \frac{d}{\lambda} \right] \right), \quad (7.9)$$

with  $\lambda$  the mean free path of the vapor mixture. For  $d \gg \lambda$  this function becomes unity. For  $d \ll \lambda$ ,  $C_c$  becomes proportional to  $d^{-1}$ , making the diffusivity (7.8) increase quadratically as  $d$  becomes smaller.

### 7.2.3 A sectional finite volume method

The set of equations (7.1), (7.6) and (7.7) is equivalent to the equations used in Chp. 6 with exception to the diffusion term in (7.1) and the diffusion flux added to  $\mathbf{f}$ . It is straight-forward to extend the numerical formulation proposed in Chp. 6 to the current model. For completeness, we summarize the main components of the numerical method. For more detail see Chp. 6.

In the sectional formulation we discretize the size distribution using a number of sections, each represented by a unique size  $s_i$  and a corresponding droplet number concentration  $N_i \equiv \rho M_i$  in units  $\text{m}^{-3}$ . We can introduce this discrete formulation into (7.1). For section  $i$  we then find

$$\partial_t (\rho M_i) + \nabla \cdot (\rho \mathbf{u} M_i) + \nabla \cdot \left( \rho \mathbf{u}_i^\ell M_i \right) = \nabla \cdot \left( \mathbb{D}_i^\ell \nabla \rho M_i \right) + \mathcal{J}_{M_i}, \quad (7.10)$$

with  $\mathcal{J}_{M_i}$  the  $i$ th section source term and  $\mathbb{D}_i^\ell = \mathbb{D}^\ell(s_i)$ . The consistency relation (7.2) becomes, in discrete terms

$$Z = \sum_i s_i M_i. \quad (7.11)$$

We consider the computational volume  $V$  as introduced in Sec. 3.2. Integrating (7.10) over this volume, applying Gauss theorem and dividing by  $V$ , we find

$$\partial_t(\rho M_i) + \mathcal{D}\left(\phi_f M_{i,f}\right) + \mathcal{D}\left(\phi_{i,f}^{\text{drift}} M_{i,f}\right) - \mathcal{D}\left(\phi_{i,f}^{\text{diff}}\right) = \mathcal{J}_{M_i}, \quad (7.12)$$

with fluxes

$$\begin{aligned} \phi_f &= (\rho \mathbf{u})_f \cdot \mathbf{A}_f, & \phi_{i,f}^{\text{drift}} &= \left(\rho \mathbf{u}_i^\ell\right)_f \cdot \mathbf{A}_f \\ \text{and} & & \phi_{i,f}^{\text{diff}} &= \mathbb{D}_{i,f}^\ell \nabla_f (\rho M_i) \cdot \mathbf{A}_f. \end{aligned} \quad (7.13)$$

In these relations the subscript  $f$  denotes interpolation to face  $f$ . The operator  $\nabla_f$  denotes the gradient at face  $f$ , which is directly related to cell-centered values of its argument and face-to-cell-center distances using an adequate scheme, e.g., the second order central scheme. The  $\mathcal{D}$ -function represents the discrete counterpart of the divergence term as a function of the specified flux, see definition Eq. (3.5).

As is done in Chp. 6, the discrete consistency relation (7.11) is applied to (7.12). This gives an expression for the rate of change of  $\rho Z$ :

$$\partial_t(\rho Z) + \mathcal{D}\left(\phi_f Z_f\right) + \mathcal{D}\left(Z_f^{-1} \phi_f^\ell Z_f\right) = \mathcal{J}, \quad (7.14)$$

where

$$\phi_f^\ell = \sum_i s_i \left( \phi_{i,f}^{\text{drift}} M_{i,f} - \phi_{i,f}^{\text{diff}} \right), \quad (7.15)$$

which is the discrete counterpart of  $\mathbf{f}$  at face  $f$ . The form (7.14) is identical to the discretized transport equation for  $\rho Z$  in Chp. 6 with the only exception the definition of the liquid flux  $\phi_f^\ell$  which now also includes diffusional transport. To arrive at the discretized transport equations for  $\rho Y_j$  and  $\rho Z_j$ , the same derivation can be followed as in Chp. 6.

The discretized equation for the species-specific liquid mass concentration is treated as

$$\partial_t(\rho Z_j) + \mathcal{D}\left(\left[\phi_f \tilde{Z}_f + \phi_f^\ell\right] \frac{Z_{j,f}}{Z_f}\right) = S_j, \quad (7.16)$$

where we introduce  $\tilde{Z}_f$  computed as

$$\tilde{Z}_f = \sum_i s_i M_{i,f}, \quad (7.17)$$

The discrete transport equation for vapor concentration becomes likewise

$$\partial_t(\rho Y_j) + \mathcal{D} \left( [\phi_f \tilde{Y}_f - \gamma \phi_f^\ell] \frac{Y_{j,f}}{Y_f} \right) = R_j, \quad (7.18)$$

where  $\tilde{Y}_f$  is computed as

$$\tilde{Y}_f = 1 - \tilde{Z}_f. \quad (7.19)$$

Adding (7.16) and (7.18) to each other and summing over  $j$  gives the discrete continuity equation:

$$\partial_t \rho + \mathcal{D} \left( \phi_f + \phi_f^\ell [1 - \gamma] \right), \quad (7.20)$$

which is the discrete counterpart of (7.7).

The time derivatives in (7.16), (7.18) and (7.20) can be discretized with a suitable scheme. In Chp. 6 it was shown that the time discretization preserves unity of the mass fractions at a new time level if 1) the sum of the mass fraction fields is unity at the old time levels and 2) if

$$\frac{\sum_j Z_{j,f}}{Z_f} = 1 \quad \text{and} \quad \frac{\sum_j Y_{j,f}}{Y_f} = 1, \quad (7.21)$$

which is ensured by computing  $Z_f$  and  $Y_f$  in (7.16) and (7.18) as the sum (over  $j$ ) of all individually interpolated fields  $Z_{j,f}$  and  $Y_{j,f}$ , respectively.

#### 7.2.4 Deposition boundary treatment

When we use a no-slip boundary condition for the mixture velocity  $\mathbf{u}$  then  $\mathbf{u}$  is zero at the wall. The only two mechanisms allowing for droplet deposition on such walls are then, see Eq. (7.1), a non-zero drift velocity  $\mathbf{u}^\ell(s)$ , or a non-zero gradient of  $n(s, \mathbf{x}, t)$  perpendicular to the wall, i.e.,  $\nabla n(s, \mathbf{x}, t) \cdot \mathbf{n}$  with  $\mathbf{n}$  the general wall normal. At the discrete level, this translates into saying that  $\phi_{i,f}^{\text{drift}} \neq 0$  to enable inertial deposition or  $\phi_{i,f}^{\text{diff}} \neq 0$  to enable diffusional deposition, with  $f$  a face at the wall, see Eq. (7.12). We discuss these contributions next.

First, we consider inertial deposition. We consider a computational volume  $V$  located next to a wall with cell center position  $\mathbf{x}_c$  and the face center at the wall located at  $\mathbf{x}_f$ , see Fig. 7.1 (left). The cell-outward unit normal of the wall face  $f$  is defined as

$$\mathbf{n}_f = \frac{\mathbf{A}_f}{A_f}, \quad (7.22)$$

and is shown in Fig. 7.1 (left). At the cell center we have a fluid velocity  $\mathbf{u}$  and  $i$ th section droplet velocity  $\mathbf{v}_i = \mathbf{v}(s_i)$ . For very small droplets these two vectors become identical, and the drift velocity, i.e.,  $\mathbf{u}_i^\ell = \mathbf{v}_i - \mathbf{u}$  tends towards zero. Given the no-slip boundary condition for  $\mathbf{u}$  at the wall, the droplet velocity at  $\mathbf{x}_c$ , for very small

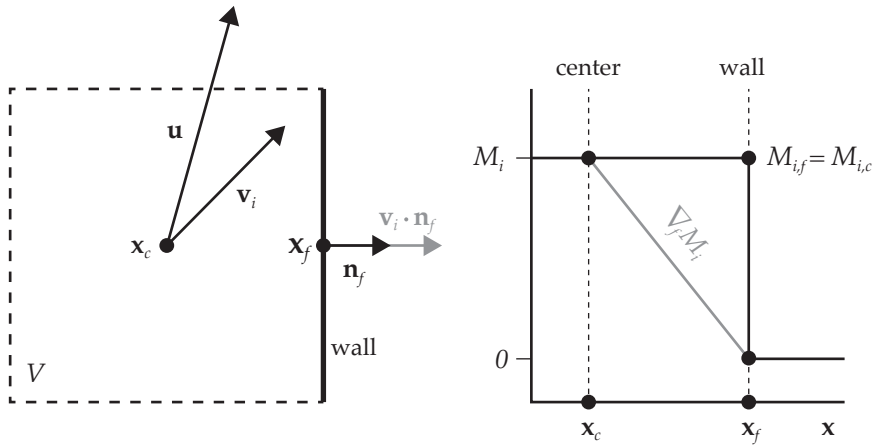


Figure 7.1: Left: A schematic overview of a computational volume with a wall face and the velocity boundary conditions. The cell center is located at  $x_c$  and the wall face at  $x_f$ . At the cell center the fluid has velocity  $\mathbf{u}$  and the droplets of size  $s_i$  velocity  $\mathbf{v}_i$ . The wall has outward unit normal  $\mathbf{n}_f$ . The wall-inward component of the droplet velocity,  $\mathbf{v}_i \cdot \mathbf{n}_f$ , is shown in blue. Right:  $M_i$  as a function of  $x$  near the wall. For drift the concentration  $M_i$  at the wall is approximated as cell-centered value  $M_{i,c}$ . The gradient  $\nabla_f M_i$  at the wall is approximated by the blue line working with  $M_i = 0$  at the wall.

droplets, will also tend to zero as the computational grid is refined. We now assume that droplets maintain their velocity  $\mathbf{v}_i$  close to the wall. This leads to the following *zero-gradient extrapolation model* (ZGM):

$$\text{BC}(\mathbf{v}_i) \text{ at the wall} \rightarrow \begin{cases} \nabla \mathbf{v}_i \cdot \mathbf{n} = 0, & \text{if } \mathbf{v}_i \cdot \mathbf{n} > 0 \\ \mathbf{v}_i = 0, & \text{otherwise} \end{cases} \quad (7.23a)$$

$$\text{BC}(n(s, \mathbf{x}, t)) \text{ at the wall} \rightarrow \nabla n(s, \mathbf{x}, t) \cdot \mathbf{n} = 0, \quad (7.23b)$$

which, for the drift velocity, is a mixed Dirichlet-Neumann boundary condition based on the condition  $\mathbf{v}_i \cdot \mathbf{n} > 0$ . If this condition is satisfied then the droplets close to the wall have a velocity pointing into the wall, and we set the droplet velocity *at the wall* to be equal to this velocity (i.e., the face-normal gradient of  $\mathbf{v}_i$  is zero). If this condition is not satisfied, we set the droplet velocity at the wall to zero. The boundary condition for  $n(s, \mathbf{x}, t)$  is of type Neumann, enforcing a zero gradient solution perpendicular to the wall. At the discrete level we implement the ZGM deposition boundary treatment as follows:

$$\mathbf{v}_{i,f} = \max(\mathbf{v}_{i,c} \cdot \mathbf{n}_f, 0) \mathbf{n}_f \quad (7.24a)$$

$$M_{i,f} = M_{i,c} \quad (7.24b)$$

$$\rho_f = \rho_c \quad (7.24c)$$

where subscript  $(\cdot)_c$  denotes the cell centered value corresponding to the control volume of which  $f$  is a face. Eq. (7.24a) sets  $\mathbf{v}_{i,f}$  equal to the face-normal component of  $\mathbf{v}_{i,c}$  if this component is positive, or otherwise to zero. Note that (7.24a) always sets a vector at face  $f$  inline with  $\mathbf{n}_f$ , discarding the components of  $\mathbf{v}_c$  orthogonal to the face normal. This can be done as the drift droplet flux, expressed by Eq. (7.13), contains the inner product with  $\mathbf{A}_f$ , making only the wall-normal component of  $\mathbf{v}$  relevant.

The ZGM deposition boundary treatment can lead to a significant overprediction of the droplet velocity at the wall [78]. In practice, as droplets travel from  $\mathbf{x}_c$  to  $\mathbf{x}_f$ , they decelerate. Longest and Oldham [78] proposed a *Lagrangian sub-grid model (LSM)*, employing the analytical solution of the droplet trajectory in between cell center and face center, assuming a linear decrease of the wall-normal fluid velocity to zero at the wall. Following their work, the equation of motion for the wall-normal velocity of a droplet in section  $i$ , undergoing only Stokes drag, is given by [91]

$$d_t v_{i,f} = \tau^{-1} (u_f - v_{i,f}), \quad (7.25)$$

where  $v_{i,f} = \mathbf{v}_i \cdot \mathbf{n}_f$ ,  $u_f = \mathbf{u} \cdot \mathbf{n}_f$  and

$$\tau = \frac{\rho^\ell d^2}{18\mu} \quad (7.26)$$

the droplet relaxation time. The mixture velocity, at the interval  $[\mathbf{x}_c, \mathbf{x}_f]$ , can be assumed to linearly decrease to zero, i.e.,

$$u = -\frac{x}{\delta_f} u_c, \quad (7.27)$$

with  $x = (\mathbf{x} - \mathbf{x}_f) \cdot \mathbf{n}_f$  the wall-normal coordinate,  $\delta_f = |\mathbf{x}_f - \mathbf{x}_c|$  the cell-to-face distance and  $u_c = \mathbf{u}_c \cdot \mathbf{n}_f$  the wall-normal fluid velocity at cell center. Inserting (7.27) into (7.25) yields a second order ‘spring-damper’ ordinary differential equation for wall-normal droplet position  $x$ , to which the well-known solution is given by [78]. We can now determine the time  $t_f$  at which  $x = -d/2$ , i.e., the first time at which the droplet intercepts the wall. At this time the ‘interception droplet velocity’  $v_{i,f}(t_f)$  is computed, and used as the value for  $\mathbf{v}_i$  at the wall:

$$\mathbf{v}_i = v_{i,f}(t_f) \mathbf{n}_f. \quad (7.28)$$

We model a perfectly absorbing boundary to approximate diffusional deposition. When droplets hit a wall they are absorbed instantly, and removed from the domain. Diffusional deposition, as concluded before, is driven by  $\nabla n(s, \mathbf{x}, t) \cdot \mathbf{n}$  being non-zero at the wall. However, in the two previously defined deposition boundary conditions

term	scheme	comment
$\partial_t$	Crank-Nicolson [25]	For any partial time derivative
$\mathbf{u}_f, T_f$	Van Leer limiter [95]	vanLeer in OpenFOAM
$Y_{j,f}, Z_{j,f}, M_{i,f}$	Van Leer limiter [95]	vanLeer in OpenFOAM
$\mathbf{v}_{i,f}$	Upwind	Provides good convergence
$\nabla$ (cell-center gradient)	Central	linear in OpenFOAM
$\nabla^2$ (Laplacian)	Central corrected	
$\nabla_f$ (face-normal gradients)	Central corrected	linear with non-orth. corr.

Table 7.1: Chosen numerical schemes for the discretization of the indicated terms.

we set  $\nabla n(s, \mathbf{x}, t) \cdot \mathbf{n}$  to be zero: the numerical treatment of the drift deposition prevents diffusional deposition. Also at the discrete level we encounter this problem. Fig. 7.1 (left) sketches the solution of  $M_i$  near the wall. At the wall,  $M_i$  attains the value of  $M_i$  at the cell center, indeed showing no gradient at the wall. However, due to the perfectly absorbing boundary condition, we compute the gradient of  $M_i$  at the face *in the diffusion flux* as if  $M_i$  is zero at the wall to induce diffusion transport towards the wall. If we retain (7.24c), then this translates into saying

$$\nabla_f(\rho M_i) = \rho \nabla_f M_i = -\frac{\rho_c M_{i,c}}{\mathbf{x}_f - \mathbf{x}_c} \quad \text{at} \quad \mathbf{x}_f, \quad (7.29)$$

which is also schematically shown in Fig. 7.1 (left) by the blue line.

Even though the discrete implementations are conflicting, we use (7.24a) or (7.28) for the computation of the *drift deposition flux* and (7.29) for the computation of the *diffusional deposition flux*. This approach was also adopted in the drift flux models of Xi and Worth Longest [73] and Longest and Oldham [78], and proved to be successful.

### 7.2.5 Schemes & methods

We implement our model in OpenFOAM, using the compressible PISO (Pressure Implicit with Splitting of Operator) algorithm as documented in Chp. 3. Together with the transport equations for  $n(s, \mathbf{x}, t)$  (discretized in terms of  $M_i$ ),  $Y_j$ ,  $Z_j$  and  $\rho$  as presented before, we solve the Navier-Stokes equations for the mixture velocity  $\mathbf{u}$  and the energy equation for temperature  $T$ , see Chp. 3. In the PISO algorithm the continuity equation (7.7) is rewritten into the pressure equation, using an equation of state, see [15, 13]. In OpenFOAM we must select suitable spatial and temporal schemes for the discretization of the equations. Tbl. 7.1 shows an overview of our choices. All discretization schemes listed in Tbl. 7.1 are the standard schemes implemented in OpenFOAM.

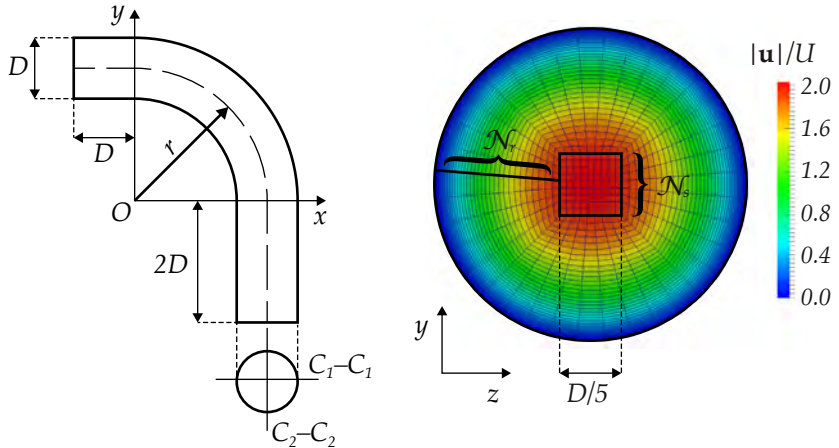


Figure 7.2: Left: schematic overview of the bent pipe geometry. The inlet extension has length  $D$ , the outlet extension length  $2D$ , with  $D$  the pipe diameter. The bent has radius  $r$ . Right: cross section of the O-type mesh, shown for Mesh C, with the internal block of width  $D/5$ , number of internal square cells  $\mathcal{N}_s$  and number of radial cells  $\mathcal{N}_r$ . The color indicates the magnitude of the parabolic inlet velocity profile.

### 7.3 BENT PIPE AEROSOL DEPOSITION VALIDATION

In this section we use our model and method to simulate aerosol droplet deposition in bent pipe geometries. For the description of the bent pipe geometry, Sec. 7.3.1, we closely follow the works by [74], [104], [113] and [114], all of which studied inertial deposition in two geometrically different  $90^\circ$  bent pipes, each operated at a different Reynolds number. In Sec. 7.3.2 we present the solution of the flow field and compare against data from literature. In Sec. 7.3.3 we assess the convergence of the solution, in terms of deposition efficiency, as a function of grid density and time, for the ZGM and LSM deposition velocity boundary treatments. Next, we compare both the inertial and diffusional deposition results against data from literature, in Sec. 7.3.4 and Sec. 7.3.5, respectively. Finally, having established confidence in both the numerical quality of the solution as well as the physical appropriateness, we study how the deposition efficiency in both the inertial and diffusion regime, depends on the flow Reynolds number and the bend curvature ratio (both to be formally defined later).

#### 7.3.1 The bent pipe setup

Fig. 7.2 shows schematically the bent pipe geometry. In agreement with [74], the inlet of the bent section is extended by a distance  $D$ , and the outlet by a distance  $2D$ , with  $D$  the diameter of the pipe, as depicted. We retain this choice in geometry to allow direct comparison with the results of [74]. Following [114] we set

$$R^* = \frac{r}{R} \quad (7.30)$$

as the curvature ratio, i.e., the ratio of bend radius  $r$  and pipe radius  $R$  defined as  $R = D/2$ . The Reynolds number is defined as

$$Re = \frac{\rho U D}{\mu}, \quad (7.31)$$

with bulk velocity  $U$ . The Stokes number, expressing the ratio between droplet inertial time scale and the fluid convective time scale, is given by

$$St = \frac{\rho^\ell d^2 U}{18 \mu R}. \quad (7.32)$$

where  $\rho^\ell$  is the liquid droplet density and  $d$  the droplet diameter. Note that the Stokes number is based on  $R$  whereas the Reynolds number is based on  $D$ , in accordance to [114]. The Peclet number, introduced here for later use, expresses the ratio of convective and diffusive droplet transport. It is defined as

$$Pe = \frac{UD}{\mathbb{D}^\ell}, \quad (7.33)$$

with  $\mathbb{D}^\ell$  the size-dependent diffusivity, as given by (7.8). In the bent pipe geometry an important quantity is the Dean number, defined as

$$De = \frac{Re}{\sqrt{R^*}}. \quad (7.34)$$

The flow field in bends of circular cross section only depends on this number, expressing the ratio of the centrifugal and inertial forces to the viscous forces.

Tbl. 7.2 lists all values for the simulation parameters, based on water droplets immersed in air at room temperature  $T_0$  and atmospheric pressure  $p_0$ . In all simulations we set the Reynolds number by specifying  $U$ , while keeping  $D$ ,  $\rho$  and  $\mu$  constant. This renders both  $Pe$  and  $St$  linearly proportional to  $Re$ , as both quantities are linearly proportional to  $U$ . Simulations are essentially governed only by  $Re$  and  $R^*$  [89]. We set gravity to zero, such that gravitational settling of droplets is neglected. In [74] and [113] it was concluded that the effects of gravity were found to be relatively small for the two studied cases in their work. These cases we will also consider, motivating our choice to neglect gravitational droplet settling.

For the mesh we apply an ‘O-type multiblock structure’ as was done in [74]. The pipe cross section contains an internal square of size  $D/5$ , to avoid very small computational volumes at the pipe centerline, as would appear in a purely cylindrical mesh. The internal square is extended to the pipe wall by an enclosing cylindrical mesh, see Fig. 7.2 (right). Towards the pipe wall we apply a boundary layer grid refinement, such that in radial direction cells at the wall are a factor 5 smaller than cells at the internal square. We introduce five different grids, A, B, C, D and E, each

parameter	value	unit
$\mu$	$1.81 \times 10^{-5}$	$\text{m}^2/\text{s}$
$\rho$	1.1898	$\text{kg}/\text{m}^3$
$\rho^\ell$	$10^3$	$\text{kg}/\text{m}^3$
$T_0$	293.15	K
$D$	$4 \times 10^{-3}$	m
$r$	$R^* D / 2$	m
$U$	$Re \mu / (\rho D)$	m/s
$p_0$	$10^5$	Pa
$\mathbf{g}$	0	$\text{m}/\text{s}^2$

Table 7.2: Simulation parameters for water droplets carried by air at room temperature and atmospheric conditions. The fluid velocity through the pipe is based on the Reynolds number.

being a refined version of its parent with A being the coarsest. Also, we define five non-graded grids, identical to the five graded grids but without a boundary layer grid refinement. In the pipe cross section, the mesh is defined by  $\mathcal{N}_s$  and  $\mathcal{N}_r$ , being the number of cells spanning one side of the internal square and the number of cells in radial direction from the internal square to the pipe wall, respectively. These two numbers are also indicated in Fig. 7.2 (right). Along the pipe axis cells have a uniform spacing, chosen such that their width in axial direction is equal to the width in cross-sectional direction of a cell within the internal square. The number of cells in axial direction is a function of  $R^*$ . Tbl. 7.3 gives the values for  $\mathcal{N}_s$ ,  $\mathcal{N}_r$  and  $\mathcal{N}_t$  for each grid. The total number of cells,  $\mathcal{N}_t$ , is indicated in Tbl. 7.3 for  $R^* = 7$ . The meshes are chosen such that  $\mathcal{N}_t$  roughly doubles from one mesh to the next. This means that the typical cell dimension  $\Delta x$  decreases roughly by a factor  $2^{1/3}$ . In that sense, Mesh E contains cells only a factor  $2^{4/3}$  smaller in typical size with respect to Mesh A.

For the boundary conditions we apply the ones selected in Chp. 6 for inlet, outlet and wall, in addition to the ZGM or LSM boundary treatment for inertial deposition and the perfectly absorbing boundary condition in the computation of the diffusion terms. The fluxes for the liquid concentrations follow directly from (7.13), and are computed explicitly. At time  $t = 0$  we start from a quiescent state in which no aerosol is present in the system. For each section we set as inlet condition  $M_i = M_0$ , as is done in Chp. 6. We use a distribution of sectional representative sizes  $s_i$  which is evenly spaced in log  $d$ -space, and ranges from approximately  $d = 2 \text{ nm}$  as the smallest size to  $d = 50 \mu\text{m}$  as the largest size. We set a parabolic inlet velocity profile with its maximum at  $2U$ , for both  $\mathbf{u}$  and  $\mathbf{v}_i$ . This profile is ramped starting from a quiescent state  $\mathbf{u} = 0$  over the time interval  $t \in [0, \tilde{\tau}]$ , with

$$\tilde{\tau} = \frac{L}{U} \quad (7.35)$$

mesh	$\mathcal{N}_s$	$\mathcal{N}_r$	$G$	$\mathcal{N}_t$	$\Delta x_c/D$	$\Delta x_w/D$
A-no-bl	5	9	1	41.820	0.04000	0.035858
B-no-bl	7	12	1	104.720	0.02857	0.02988
C-no-bl	9	16	1	234.549	0.02222	0.02241
D-no-bl	11	20	1	459.459	0.01818	0.01792
E-no-bl	14	25	1	922.488	0.01429	0.01434
A	5	20	5	86.700	0.03568	0.007136
B	7	26	5	211.344	0.02752	0.005503
C	9	34	5	465.885	0.02108	0.004217
D	11	44	5	944.163	0.01632	0.003263
E	14	55	5	1.893.528	0.01307	0.002613

Table 7.3: Definition of the used meshes with  $\mathcal{N}_s$  the number of cells for a side of the internal square,  $\mathcal{N}_r$  the number of cells in radial direction,  $G$  the linear grading factor in radial direction (indicating the ratio between the smallest and largest cell, with the smallest cell at the wall) and  $\mathcal{N}_t$  the total number of computational cells for  $R^* = 7$ . The ‘no-bl’ suffix implies that no grid refinement to the wall is applied, i.e.,  $G = 1$ .

where  $L$  is the centerline length of the pipe. The time  $\tilde{\tau}$  is the bulk flow-through time of the system, a quantity which we can use to define the non-dimensional flow-through time  $t^*$  as

$$t^* = \frac{t}{\tilde{\tau}}. \quad (7.36)$$

For  $t > \tilde{\tau}$  the parabolic inlet fluid and droplet velocity profile remains constant with its maximum at  $2U$ .

### 7.3.2 Flow solution

In the work of Pui et al. [114] inertial deposition of aerosol is experimentally studied using two cases:  $Re = 100$ ,  $R^* = 7$  and  $Re = 1000$ ,  $R^* = 5.7$ . These two cases were also numerically investigated by [74], [104] and [113]. We compare our flow solutions against the well-established results of Pilou et al. [74].

Fig. 7.2 (left) shows pipe cross section lines  $C_1-C_1$  and  $C_2-C_2$ . Along these two lines we compute the scaled axial velocity magnitude, i.e.,  $|\mathbf{u}|/U$ . Fig. 7.3 shows this quantity along  $C_1-C_1$  and  $C_2-C_2$  for the bend inlet (I), halfway the pipe bend (H) and at the bend outlet (O) for the  $Re = 100$  and  $Re = 1000$  cases, computed on the five refined meshes, A to E. Also, the data of Pilou et al. [74] is shown. For most cross section lines the results are very close to each other. Generally, we find good agreement with [74], for all meshes. We see a notable change in the solution towards the literature data for both cases as the mesh is refined. This is in agreement with the observations of [113], where the  $Re = 100$  solution becomes effectively grid-independent beyond  $10^6$  cells while the  $Re = 1000$  solution becomes nearly grid-independent for  $3.3 \times 10^6$  cells.

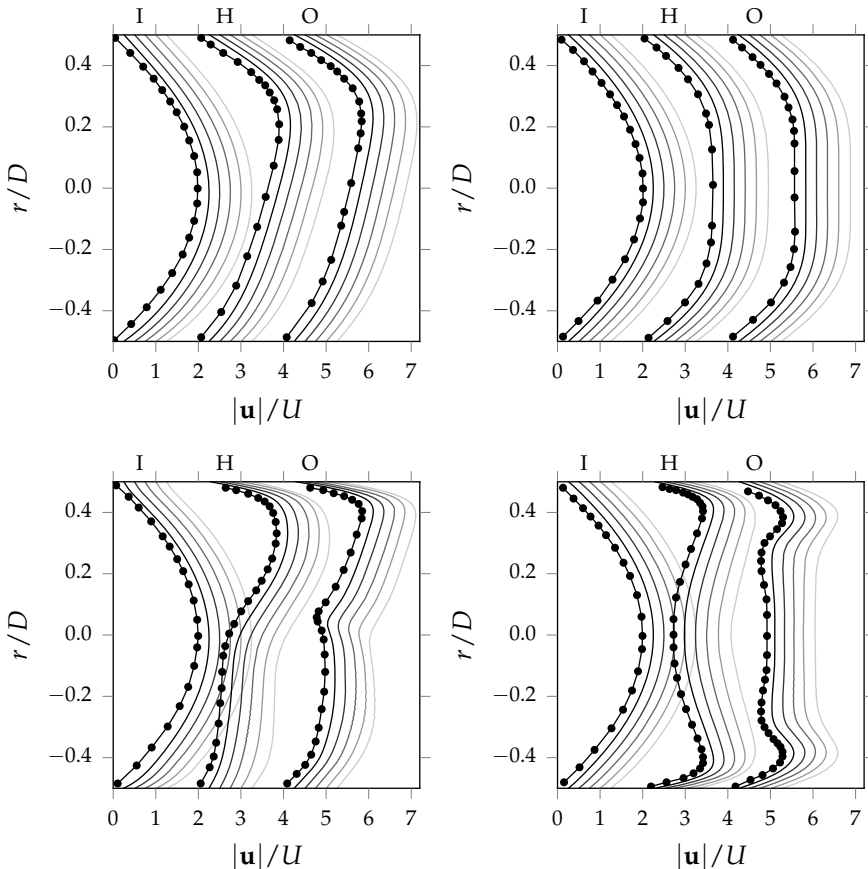


Figure 7.3: Bent pipe steady state axial velocity profiles for  $Re = 100$  (top row) and  $Re = 1000$  (bottom row), along pipe cross sections  $C_1-C_1$  (left column) and  $C_2-C_2$  (right column), at the bend inlet (I), halfway the bend (H) and at the bend outlet (O), each horizontally offset for better visibility of the profiles. From gray to black (—) meshes A–E are shown. The cross sections  $C_1-C_1$  and  $C_2-C_2$  are defined in Fig. 7.2 (left). The data of Pilou et al. [74] (●) is also shown.

In this chapter we are in particular focusing on the accuracy of the solution in terms of the diffusion and inertial deposition. We will present the assessment of the grid dependence of those quantities in the next section. We conclude that our flow predictions agree well with data from literature.

### 7.3.3 Convergence of the deposition efficiency

A relevant quantity in the study of aerosol deposition is the *deposition efficiency*  $\eta$ , defined as the ratio of ‘that what deposits in the system’ over ‘that what enters the system’. At the numerical level, we define the deposition efficiency for droplet

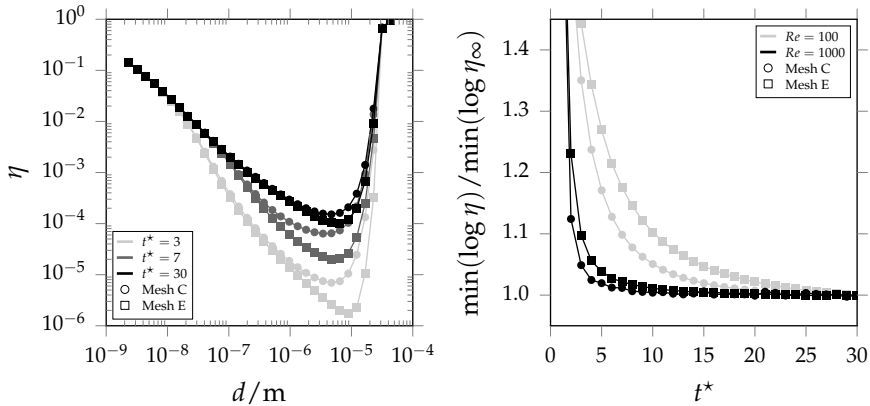


Figure 7.4: Left: The  $Re = 100$  deposition efficiency  $\eta$  for a range of droplet diameters  $d$ , shown at three non-dimensional flow-through times  $t^*$  for Mesh C ( $\circ$ ) and Mesh E ( $\square$ ). Right: the convergence of the scaled minimum of the logarithm of  $\eta$  in time, for  $Re = 100$  (gray) and  $Re = 1000$  (black), for Mesh C ( $\circ$ ) and E ( $\square$ ). The value for  $\eta_\infty$  is taken at  $t^* = 30$ . Both figures contain results using the ZGM boundary treatment.

section  $i$  as

$$\eta_i = \frac{\sum_{f \in \mathcal{W}} \Phi_{i,f}}{\sum_{f \in \mathcal{I}} \Phi_{i,f}}, \quad (7.37)$$

with  $\mathcal{W}$  and  $\mathcal{I}$  the set of faces belonging to the wall and inlet, respectively, and

$$\Phi_{i,f} = (\phi_f + \phi_{i,f}^{\text{drift}}) M_{i,f} + \phi_{i,f}^{\text{diff}} \quad (7.38)$$

the total flux of  $s_i$ -sized droplets crossing face  $f$ . Note that the fluxes contain the face  $f$  surface area through their corresponding definitions (7.13), such that summing them over the sets  $\mathcal{W}$  and  $\mathcal{I}$  represents the numerical equivalent of a surface integral. In the sectional formulation we can now, given a sectional distribution spanning some space in  $s$ , compute how  $\eta$  depends on the size  $s$ .

Fig. 7.4 (left) shows the logarithm of the deposition efficiency as a function of the logarithm of droplet diameter  $d$ . In this log-log space we recover a V-shaped deposition efficiency curve, where the left side of the V is governed by diffusional deposition and the right side by inertial deposition. For small  $d$  the droplet diffusivity increases, increasing diffusional deposition in turn. For large  $d$  the droplet inertial time scale becomes larger and droplets drift away from the carrier gas trajectory, increasing inertial deposition.

Our time-resolving algorithm allows to obtain  $\eta$  as a transient quantity. It will take some time before  $\eta$  has, given the initial condition of quiescence, converged to its steady state solution. Fig. 7.4 (left) shows  $\eta$  as a function of  $d$  for four non-dimensional flow-through times  $t^*$ , for Mesh C and Mesh E. As  $t^*$  increases, the  $\eta$ -curves are seen to approach a steady state, for both meshes. Fig. 7.4 (right) shows how the minimum

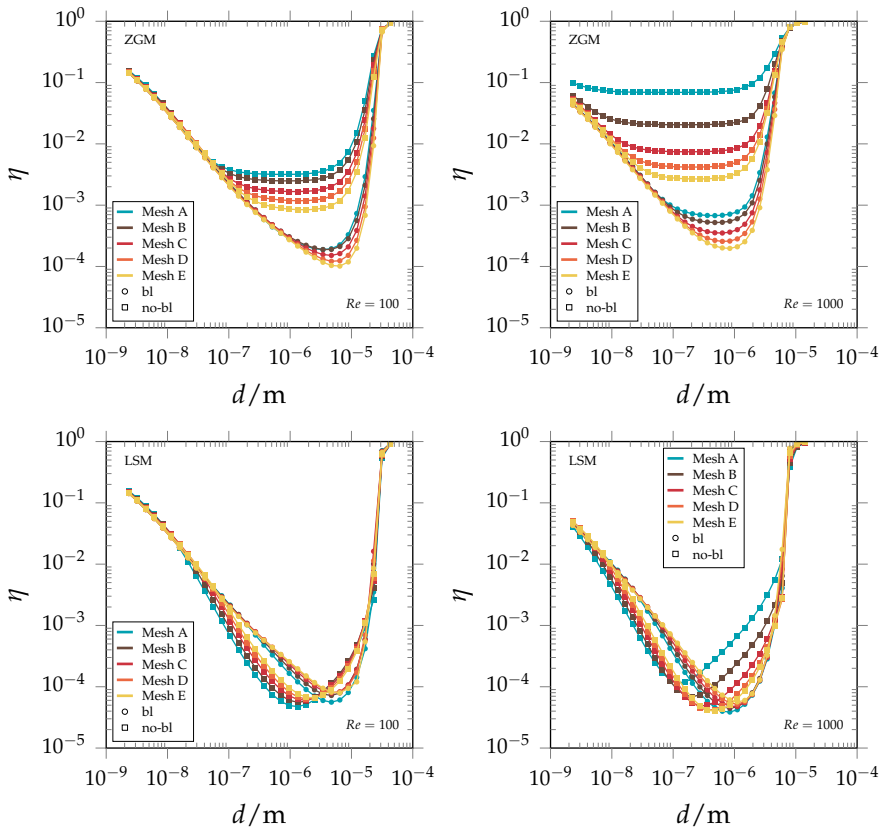


Figure 7.5: The grid dependence of the  $\eta$ -curve for  $Re = 100$  (left column) and  $Re = 1000$  (right column), for all meshes as defined by Tbl. 7.3, using the ZGM boundary condition (top row) and LSM boundary treatment (bottom row).

of the  $\eta$ -curve settles as a function of non-dimensional flow-through time  $t^*$ . For the  $Re = 100$  case, having a smaller Reynolds and Dean number, steady state is only attained around  $t^* = 30$ , whereas the  $Re = 1000$  case converges more rapidly. Also, an increase in grid density is shown to increase the transient time. For the 'no-bl' meshes (see Tbl. 7.3) the transient time amounts to less than 5 flow-through times (not shown in Fig. 7.4). In the remainder of this chapter all presented results are taken at  $t^* = 30$ , i.e., the bulk flow was allowed to pass the complete length of the pipe 30 times, before recording the steady-state deposition efficiency  $\eta$ . This was found adequate, as at this time all curves in Fig. 7.4 (right) have become reasonably 'flat', indicating steady state.

Fig. 7.5 show, for  $Re = 100$  and  $Re = 1000$ , the deposition efficiency computed on all five meshes, with or without boundary layer, using the LSM and ZGM wall velocity boundary treatment. The 'no-bl' meshes produce a deposition efficiency

curve very dissimilar to that of the refined meshes with a large grid dependence, clearly indicating the relevance of a boundary layer mesh. Considering the solutions for Mesh A to E, we see that the deposition efficiency is only sensitive to the mesh density in the bottom of the V-shape, where  $\eta$  has dropped to about  $10^{-4}$ . In the diffusion-driven left arm and inertia-driven right arm of the deposition efficiency curve the results are close to grid-independent. The ZGM boundary treatment gives, as expected, a significant overprediction of the deposition efficiency, in particular for the ‘no-bl’ meshes and for the coarser wall-refined meshes. For the LSM boundary treatment the solution is much less grid sensitive, although for the ‘no-bl’ meshes the deposition efficiency for  $Re = 1000$  around the bottom of the V varies notably. Both the ZGM and LSM boundary treatments appear to produce the same efficiency curve on the finest mesh E, both for  $Re = 100$  and  $Re = 1000$ .

To study the grid dependence of the solution quantitatively we introduce the deposition curve integral

$$e = \int_{\Omega} \log \eta \, d \log d, \quad (7.39)$$

in which  $\Omega$  is the domain in  $d$  shown in Fig. 7.5. This relation is approximated numerically by a simple Riemann sum over all sections. Tbl. 7.4 gives  $e$  for the five meshes. Also shown in this table is convergence measure  $\Delta e$ , defined as:

$$\Delta e^2 = \int_{\Omega} (\log \eta - \log \eta_{\text{parent}})^2 \, d \log d \quad (7.40)$$

where  $\eta_{\text{parent}}$  belongs to the coarser parent mesh.  $\Delta e$  indicates how, with each refinement step, the solution changes in log-space. Generally, for finer meshes it is shown that  $\Delta e$  becomes smaller in both the  $Re = 100$  and  $Re = 1000$  case, for both boundary conditions, indicating that the solution converges. This information can also be visually distilled from Fig. 7.5 where the lines for Mesh D and E are closer to each other than those of Mesh A and B. Only for the LSM boundary treatment  $\Delta e$  appears to increase from mesh D to E. However, the solutions for  $\eta$  are already quite close to each other here, as shown by the relatively small size of  $\Delta e$ .

Fig. 7.6 shows deposition curve integral  $e$  as function of  $\Delta x_w$  as given by Tbl. 7.3. From Mesh A to E  $\Delta x_w$  decreases roughly one decade. In particular for  $Re = 1000$ ,  $e$  appears to converge to approximately  $-10$  as  $\Delta x_w$  becomes smaller. For  $Re = 100$  this is less visible, however, the range of change of  $e$  for different grids is smaller.

Fig. 7.5 and 7.6 and Tbl. 7.4 indicate that in most practical cases a computation performed on the refined Mesh A using the LSM boundary treatment gives a numerically adequate estimate of the deposition efficiency in the diffusion, intermediate (i.e., the bottom of the deposition curve) and inertial regime. Having established an impression of the numerical robustness of the solution in terms of the velocity field and deposition efficiency both as a function of grid density, the question remains how physically accurate the deposition predictions are. We will address this question next by investigating the inertial and diffusional deposition contributions.

mesh	ZGM				LSM			
	$Re = 100$		$Re = 1000$		$Re = 100$		$Re = 1000$	
	$e$	$\Delta e$	$e$	$\Delta e$	$e$	$\Delta e$	$e$	$\Delta e$
A	-10.6504		-8.5292		-11.1078		-11.1078	
B	-10.6997	0.0912	-8.7147	0.1347	-11.0100	0.2043	-11.0100	0.2043
C	-10.8659	0.1355	-8.9851	0.1925	-11.0513	0.0873	-11.0513	0.0873
D	-11.0330	0.1346	-9.2011	0.1581	-11.1357	0.0597	-11.1357	0.0597
E	-11.1617	0.1050	-9.3787	0.1338	-11.2297	0.0809	-11.2297	0.0809
A-no-bl	-8.1494		-3.7008		-10.1781		-10.1781	
B-no-bl	-8.4141	0.1736	-5.2680	0.8712	-10.1647	0.1731	-10.1647	0.1731
C-no-bl	-8.8241	0.2551	-6.4054	0.6614	-10.2836	0.1432	-10.2836	0.1432
D-no-bl	-9.1576	0.2101	-6.9599	0.3429	-10.3990	0.1065	-10.3990	0.1065
E-no-bl	-9.4727	0.2030	-7.3554	0.2536	-10.5079	0.1016	-10.5079	0.1016

Table 7.4: Deposition curve integral  $e$ , Eq. (7.39), and convergence measure  $\Delta e$ , Eq. (7.40), for  $Re = 100$  and  $Re = 1000$ , ZGM and LSM and for all five meshes.

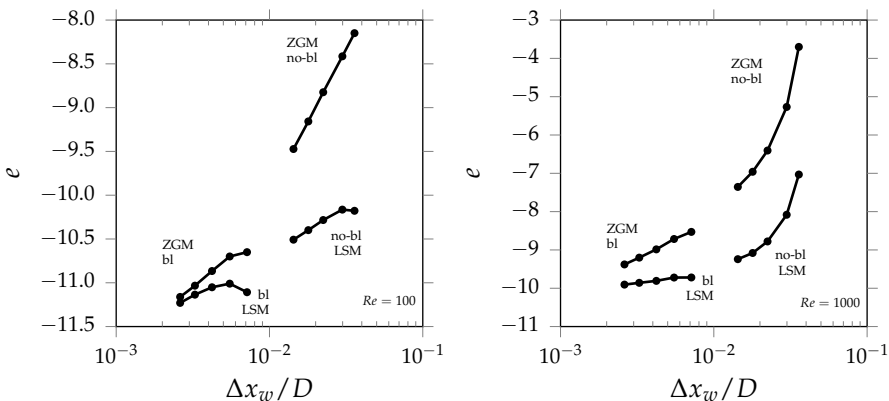


Figure 7.6: Deposition curve integral  $e$ , Eq. (7.39), as function of the typical scaled wall grid cell size  $\Delta x_w/D$ , for  $Re = 100$  (left) and  $Re = 1000$  (right), with (bl) and without (no-bl) boundary layer and with the LSM or ZGM boundary treatment for the droplet wall velocity, as indicated.

### 7.3.4 Inertial deposition

On the ‘inertial side’ of the deposition efficiency curve much research is already available in literature. Cheng and Wang [102] investigated numerically the inertial deposition of aerosol based on an analytical approximation of the fluid velocity in a bent pipe. Pui et al. [114] presented experimental results, whereas Pilou et al. [74] and Vasquez et al. [113] published numerical deposition data. Fig. 7.7 shows our predictions in comparison with data of aforementioned authors, computed on mesh A and C using the ZGM boundary treatment. It is shown that the grid-dependence of the solution is small. For both  $Re = 100$  and  $Re = 1000$  we see good agreement with [102] and [113]. Vasquez et al. [113] also adopted an Eulerian aerosol model and solved the

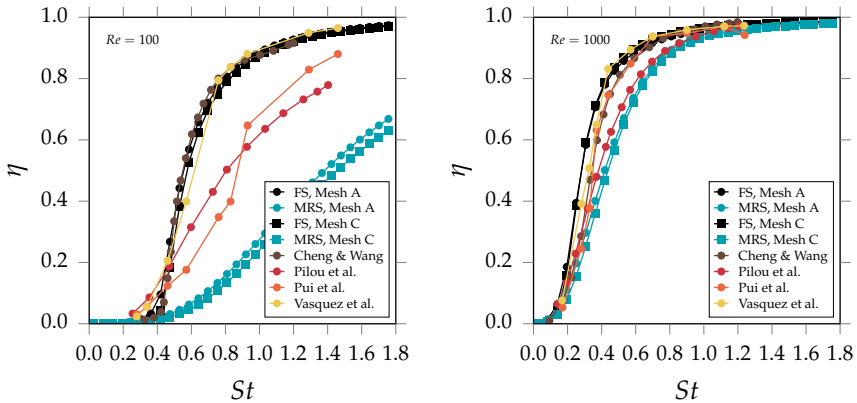


Figure 7.7: Inertial deposition efficiency as a function of  $St$  for  $Re = 100$  (left) and  $Re = 1000$  (right), computed on Mesh A ( $\square$ ) and C ( $\circ$ ) using the ZGM droplet velocity boundary treatment and the ‘Full Stokes’ model and ‘Manninen’s reduced Stokes’ model [71]. Also shown are the predictions of Cheng and Wang [102], Pilou et al. [74], Pui et al. [114] and Vasquez et al. [113], as indicated.

Eulerian equations for the droplet velocity  $\mathbf{v}$  (here referred to as ‘Full Stokes’ (FS)) without introducing the *local equilibrium approximation*, see Chp. 6. Good agreement of our predictions is therefore expected. Pilou et al. [74] also model the aerosol drift in an Eulerian setting, but implement the local equilibrium approximation for  $\mathbf{v}$  (here referred to as ‘Manninen’s Reduced Stokes’ (MRS) model [71]). Our MRS predictions lay close to those of [74] for  $Re = 1000$ . However, for  $Re = 100$  we see an unexplained and significant difference corresponding to a factor 2 in  $St$ . It is advised to reconsider this particular aspect as it may result from a simple difference in definitions of scales. In Chp. 6 it was concluded that for  $St > 0.2$  the MRS model produces a prediction of the droplet velocity which deviates significantly from the FS model solution. This conclusion is affirmed by our results for the prediction of inertial droplet deposition. For  $Re = 100$  our data, while in agreement with [102] and [113], shows a notable difference with the experimental data of Pui et al. [114]. For  $Re = 1000$  the agreement is much better. In general we conclude from Fig. 7.7 that our predictions correspond well to the range of literature data.

### 7.3.5 Diffusional deposition

For small Reynolds numbers or large curvature ratios (i.e.,  $De$  is small), the flow through a smoothly bent pipe is very similar to the flow through a straight pipe. Fig. 7.3 illustrate this well; the  $Re = 100$  velocity solutions resemble more closely the symmetric parabolic Poiseuille flow profile than those for  $Re = 1000$ . In the limit of  $Re \rightarrow 0$  or  $R^* \rightarrow \infty$  (provided that the flow remains laminar) the aerosol diffusional deposition reduces to its straight pipe solution of equivalent pipe length. Ingham [117] studied this problem and found a convenient analytical expression

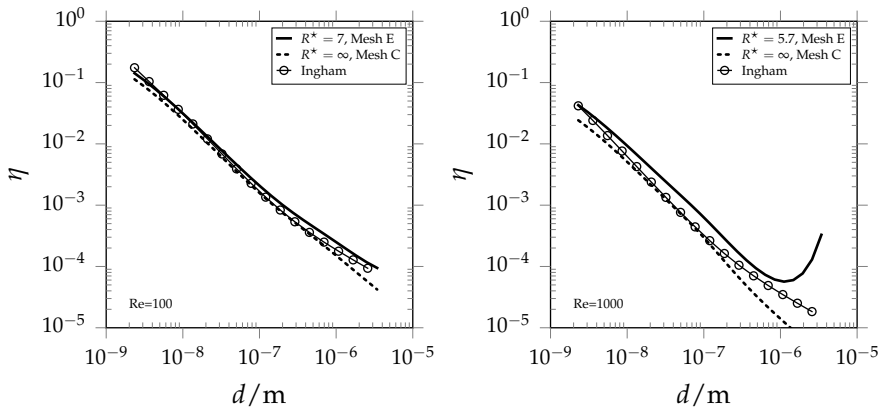


Figure 7.8: As a function of  $d$  the diffusional deposition for  $Re = 100$  (left) and  $Re = 1000$  (right), computed on Mesh E. Also shown is the model of Ingham and simulated deposition efficiency results for  $R^* = \infty$ , i.e., a straight pipe, with a mesh equivalent to that of C.

approximating the cross section averaged aerosol concentration as a function of  $Pe$  and pipe length, given a uniform inlet aerosol concentration and developed parabolic velocity profile. Ingham's expression, in terms of  $\eta$ ,  $Pe$  and pipe length  $L$ , is given by the series

$$\eta_I = 1 - \sum_k \alpha_k \exp \left( -\beta_k \left[ \frac{\delta}{Pe} \right]^{\gamma_k} \right), \quad (7.41)$$

with  $\delta = L/D$  the ratio between axial pipe length  $L$  and the pipe diameter, and coefficients  $\alpha_k$ ,  $\beta_k$  and  $\gamma_k$  given by [117]. This  $\eta$  gives a prediction of the diffusional deposition efficiency of a straight pipe. Ingham gives an approximate expression retaining only 4 terms and shows that this is of good accuracy. In arriving at this result it is assumed that droplet diffusion in axial direction can be neglected. This assumption is valid for  $Pe \gg 1$  [117], i.e., when convective transport dominates diffusive transport. Therefore, we expect that for small  $Pe$ , i.e., for small droplets, the Ingham equation becomes less reliable.

Fig. 7.8 shows the deposition efficiency, for  $Re = 100$  and  $Re = 1000$ , and for a straight pipe with axial length equal to that of the  $Re = 100$  or  $Re = 1000$  bent pipe geometry operated at equal conditions. A good agreement is shown between Ingham's model and the straight pipe solution. For  $d < 10$  nm our predictions slowly deviate from Ingham as  $Pe$  starts to approach unity. We see that for all displayed  $d$  there is a deposition efficiency *enhancement* for the bent pipe case with respect to the straight pipe solution which appears to be quite uniform in  $d$ . This enhancement becomes more pronounced as  $Re$  (or  $De$ ) increase. We identify two possible mechanisms driving this enhancement:

1. Fig. 7.3 show that the fluid is ‘pushed’ towards the outer edge of the bend where, in comparison with a straight pipe, more surface is available to deposit,

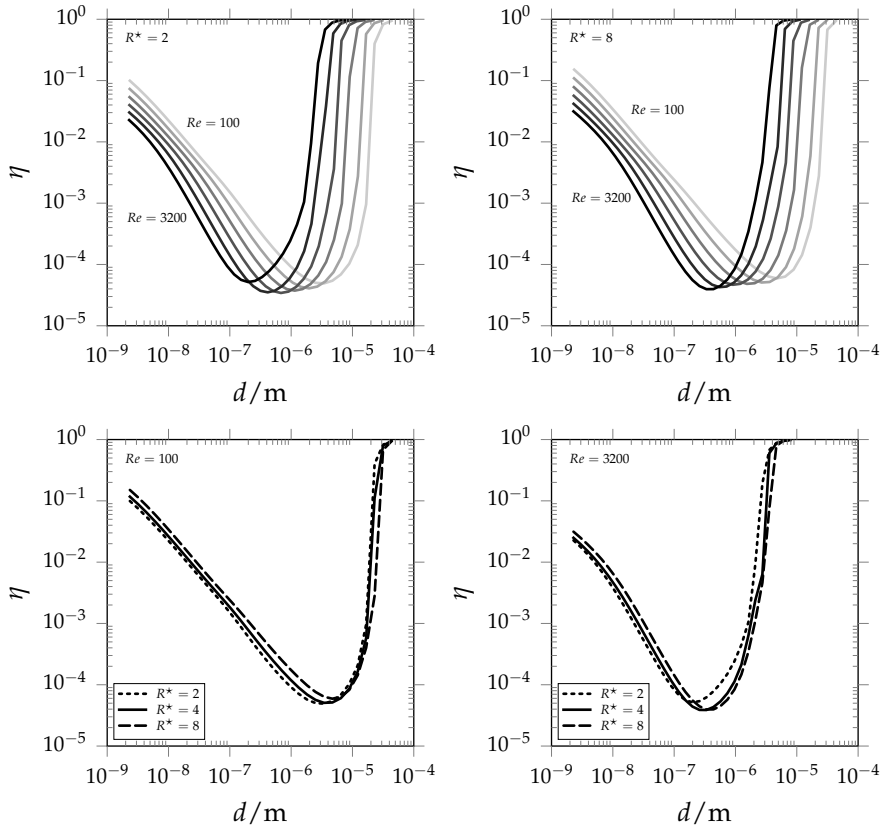


Figure 7.9: Deposition curves computed on Mesh A using the LSM inertial droplet velocity boundary treatment for a range of  $Re$  with constant  $R^*$  as indicated (top row) and for a range  $R^*$  with constant  $Re$  as indicated (bottom row).

increasing the diffusional deposition flux.

2. Due to the bulk of the flow being pushed towards the outer edge, the perfectly absorbing boundary condition may induce a sharper gradient in comparison with the straight pipe solution, also increasing the diffusional deposition flux.

We conclude that in the range of validity of Ingham's model, we find good agreement with our numerical predictions of the straight pipe flow. For the bent pipe there is an increase in diffusion-driven deposition. An interesting question that arises is how this deposition enhancement depends on the characteristics of the bent pipe flow, as expressed by  $De$ , or  $Re$  and  $R^*$ . We turn to this next.

### 7.3.6 $Re$ and $R^*$ -dependence

Even though we see a strong grid dependence of the solution of  $\log \eta$ , the solution is sufficiently robust to investigate qualitative changes in the solution as the

parameters of the bent pipe change. We identify  $Re$  and  $R^*$  as two such parameters, which we vary by setting  $U$  and  $r$ , respectively. Our model is unique as it allows predictions of both the diffusive and the inertial range within one approach. Intuitively speaking, increasing  $Re$  makes the flow more small-scale but also reduces the flow-through time. On the other hand, increasing  $R^*$  makes the bend more gradual but also increases the flow-through time. These are opposing trends that we quantify next. Fig. 7.9 shows the deposition efficiency for a range of  $Re$  and  $R^*$ , as indicated, computed on the wall-refined Mesh A using the LSM droplet velocity boundary condition.

In Fig. 7.9 (top row)  $R^*$  is kept constant at 2 or 8, while  $Re$  is varied. On the inertial side of the curve we see a clear increase of  $\eta$ . For example, at  $d = 4 \mu\text{m}$  we see an increase of four decades in  $\eta$  from  $Re = 100$  to  $Re = 3200$ . In the diffusion regime for constant  $d$  the deposition efficiency decreases with increasing  $Re$ . From  $Re = 100$  to  $Re = 3200$  the deposition efficiency, for the smallest shown droplet diameter, decreases roughly by a factor 5, for both values of  $R^*$ . However, the residence time decreases by a factor 32. This indicates that as  $Re$  increases, the diffusional deposition is enhanced. This was also shown in Fig. 7.8.

For the results shown in Fig. 7.9 (bottom row) the Reynolds number is kept constant at 100 or 3200, and  $R^*$  is varied. In general, the deposition curve is not very sensitive to the shown changes in  $R^*$ . An enhancement in the inertial regime is shown as  $R^*$  decreases while in the diffusion regime an enhancement is shown as  $R^*$  increases, due to a larger droplet residence time.

## 7.4 CONCLUSIONS

In this chapter we presented a compressible Eulerian internally mixed sectional aerosol model. We incorporated droplet drift and droplet diffusion, in turn driving droplet deposition. We proposed two boundary treatments for the sectional droplet number concentrations and drift velocity, to enable both diffusion and inertial deposition. We introduced the ZGM zero-gradient boundary treatment for the droplet velocity, and the LSM Lagrangian sub-grid model boundary treatment, based on the work of [78]. We validated the model by means of simulation of bent pipe deposition. We found a numerically reliable solution on meshes with wall refinement while using the LSM droplet velocity boundary treatment. In both the diffusion and inertial regime we identified clear trends which agreed well with literature.

The sectional formulation was shown to have the ability to model a polydisperse aerosol without requiring any assumption on the shape or moments of the size distribution. We specified a uniform distribution (uniform with respect to the sectional concentrations  $M_i$ ) spanning a droplet diameter domain of  $2 \times 10^{-3} \leq d \leq 5 \times 10^1 \mu\text{m}$  where the representative sectional sizes were uniformly distributed in  $\log d$ -space. In a single simulation the deposition patterns and efficiencies were computed for this complete droplet size domain, resulting in deposition efficiency curves as a

function of  $R^*$  and  $Re$ . This feature makes the method extremely useful in modeling of polydisperse aerosols.

To validate the method, we compared against experimental and numerical data from literature for inertial deposition in a bent pipe geometry for two Reynolds numbers and bent radii. Generally, we found good agreement with the numerical predictions of [102] and [113], where, for the latter case, the ‘Full Stokes’ (FS) Eulerian equation of motion for droplet velocity was solved, as was done in this chapter. When employing the ‘Manninen Reduced Stokes’ (MRS) model in the prediction of particle velocities we saw, for the low Reynolds case  $Re = 100$  and  $St > 0.1$ , a significant deviation from both experimental and numerical data from literature. Also for the  $Re = 1000$  case we saw a smaller but notable difference. This encourages, in agreement with Chp. 6, the choice for solving the full droplet equation of motion, instead of a simplified model as was done in for example [74].

Our approach showed very good agreement to the analytical aerosol diffusion model of [117] when applied to a straight pipe. Only for very small droplets, where the Peclet number becomes smaller, a deviation from theory was shown. This is to be expected, since the analytical solution for pipe diffusional deposition is no longer valid there.

Having validated both deposition regimes, finally, we tested the dependence of the deposition curve on the Reynolds number  $Re$  and curvature ratio number  $R^*$ . We used relatively coarse meshes and discussed only qualitative trends. When increasing  $Re$  we saw deposition enhancement. Also, a larger  $Re$  was shown to lead to a significant increase in inertial deposition. a ten-fold increase in  $Re$  leads, for  $d = 4 \mu\text{m}$ , to a deposition enhancement of roughly four order of magnitude. The increase in  $R^*$  was such that the pipe length increases as well. This means that, at constant flow rate, the droplets have more time to diffuse, indeed increasing deposition in the diffusion regime slightly. In the inertial regime we saw a small increase as  $R^*$  becomes larger.



# CHAPTER 8

## AEROSOL DEPOSITION IN HUMAN LUNGS\*

### ABSTRACT

An Eulerian internally mixed aerosol model is used for predictions of deposition inside a realistic cast of the human upper airways. The model, formulated in the multi-species and compressible framework, relies on the sectional discretization of the droplet size distribution function to accurately capture size-dependent aerosol dynamics such as droplet drift, gravitational settling and diffusion accurately. These three mechanisms are implemented in a consistent way in the model, guaranteeing that the total droplet mass as given by the droplet size distribution is always equal to the total droplet mass due to the mass concentration fields. To validate the model, we simulate monodisperse glycerol aerosol deposition inside the lung cast, for which experimental data is available. We examine two boundary treatments to compute the inertial droplet deposition velocity: a zero-gradient extrapolation model and a more elaborate Lagrangian sub-grid model. We show that even on coarse meshes we have good agreement with the experimental data in case the sub-grid model is used. In case the mesh contains a well-resolved boundary layer near the wall of the cast we also find good agreement with the experimental data using the simpler zero-gradient boundary treatment. Finally, we study the size-dependent deposition inside the lung cast for a polydisperse aerosol with droplet sizes ranging from the nanometer scale to beyond the micrometer scale. The typical ‘V-shape’ deposition curve is recovered, in which the inertial and diffusional deposition regimes may be recognized. The sectional method provides detailed information of local deposition patterns inside the cast while agreeing well with experimental data on regional deposition.

### 8.1 INTRODUCTION

Aerosol research plays a major role in various branches of science and engineering. These branches concern environmental and atmospheric problems (weather, pollution, indoor air quality), engineering applications linked with sprays (combustion or cooling) or inhalation-related challenges (medical devices and dosimetry). Synergy of both experimental and computational approaches is required in order to

---

\*This chapter is based on Frederix et al. [118]: Size-dependent aerosol deposition in a model of the upper human airways. *Journal of Aerosol Science*, to appear.

foster deeper understanding of transport, evolution and dynamics of aerosols during inhalation. Clearly, experiments give detailed insight into the physical processes and can build confidence in computational models that often need simplifications to become computationally feasible. In support, once a computational model is validated, it may serve in research areas and applications for which experiments are difficult or even impossible to conduct. A straightforward example concerns the modeling of aerosols flowing in the airways for which simulations support complex experiments and challenge experimental methods by giving insight into geometrical complexities of the flow in the respiratory tract. In this chapter we present our unique thermophysically coupled and consistent computational approach to model, simulate and validate complex flow deposition in the human airways. In addition, we directly confront computational predictions with experimental findings obtained from exactly the same lung cast geometry. In total, we establish a close agreement between experimental deposition data and results obtained with our Eulerian sectional aerosol model.

Simulations of aerosol deposition and respiratory tract flow analysis as a subject of computational investigations for medical and toxicological applications were studied since many years (see the review in [119]). Various physical models were validated taking into account distinct levels of complexity and detail, starting from the basic formulation of droplet physics, through the development of the General Dynamics Equation (GDE) for the aerosol, and finally the application of this equation to more complex flows linked with numerical developments of Computational Fluid Dynamics (CFD) methods.

The overall goal of applying CFD to simulate the flow inside the respiratory tract is to compute the total, regional and local deposition dosimetry, which develops over successive breathing cycles. In [120] a study was presented estimating dosimetry values based on the developed models for aerosol droplets in the size range  $0.01\text{--}10\ \mu\text{m}$ , for a long exposure time. In [121] realistic tracheobronchial airways at transient air-flow conditions were simulated at 15 and 60 L/min flow conditions. It was concluded that the local flow patterns, which influence particle deposition, are largely affected by secondary flows. Airway geometry as well as the flow rate play important roles. One of the important challenges in simulation of respiration is related to the development of appropriate and realistic physiology-based boundary conditions [122].

Simultaneously, researchers indicate the importance of lung geometry motion on the deposition (see [123]). As simulations of many branches of the airways geometry are still computationally challenging, many researchers studied flows in representative simplified geometries like for example the triple bifurcation geometry used in [124]. For similar reasons, turbulence, which was identified in the trachea region even for low respiration conditions, is often not resolved but simulated with the use of some turbulence model [125]. Similar to our approach, various physical processes were taken into account in the framework presented in [98]. The framework was built in the Eulerian context and was compared against existing computational and experimental data. The quality of the computed deposition data for sub-micron particles

strongly depends on the resolution of the boundary layer in time-dependent flow simulations. Since for complex geometries this requires considerable computational power, Lagrangian-based velocity corrections were proposed to improve the computational accuracy of deposition [78]. In order to incorporate aerosol physics for evolving liquid-based aerosols, Lagrangian and Eulerian models were built that incorporate vapor–liquid mass transport (see [126], [127]). The effectiveness of both Eulerian and Lagrangian models is studied from the perspective of accuracy and computational cost [128]. Moreover, researchers payed attention to asymmetries present in particular human respiratory tracts [129]. These need to be taken into account in simplified deposition models in order to make relevant conclusions.

Validation of the developed computational models is crucial. Numerous works were devoted to this topic either in simplified or complex geometries (see [130, 131, 132, 133, 134, 135, 136, 137, 138]). Validation of CFD models is not limited to the human respiratory tract alone, e.g., also for rat lungs simulations are performed [139]. As the CFD efforts are mainly dedicated and applied to the upper-respiratory tract, attempts are made to develop computational models that account for the deposition in the alveolar region [140] and also link deposition with tissue transfer [141]. The developed methods can be validated on the basis of existing experimental data, but should also be computationally verified with respect to the numerical discretization methods used to obtain the simulation data. Growing computational capabilities allow to simulate larger problems with more complete and richer physics [141], that can also be fully resolved spatially and temporally if adequate computational resources, careful meshing of the domain and accurate methods are combined. Computational aerosol models require not only a fundamental and robust mathematical description of aerosol dynamics to be accurate. Their accuracy is equally dependent on the geometry and meshing in order to capture transient and interlinked processes (e.g., turbulence or diffusion and impaction of sub-micron particles).

In Chp. 7 we presented an internally mixed sectional Eulerian aerosol model, designed to incorporate droplet inertial drift, sedimentation and Brownian motion. These three aerosol dynamics mechanisms drive droplet deposition in the airways. The size-dependence of these mechanisms is naturally accounted for due to the sectional representation of the droplet size distribution. In Chp. 7 the model was designed to respect the ‘consistency relation’; at both the analytical and numerical level the total droplet mass is equally reflected in the mass concentration fields as well as by the droplet size distribution. The model was applied to the simulation of deposition in bent pipes, and both the diffusional and inertial deposition regimes were identified and studied in one comprehensive model. The bent pipe geometry offers a reliable and well-understood point of reference for validation against other experimental, theoretical and numerical deposition data. However, the bent pipe case differs primarily in terms of the complexity of its geometry. The scope of this chapter is to apply the internally mixed Eulerian aerosol model to a complex geometry that is a close representation of the actual geometry of the upper airways and to study the

local and regional deposition patterns of aerosol droplets of different sizes. Furthermore, a special focus is set on comparing simulated regional aerosol deposition in the cast segments to experimentally obtained data measured by [142] during steady-state conditions using a physical cast of the same geometry. The experimental data was obtained using a cast model consisting of several segments from the mouth cavity down to the seventh generation of branches of the lung, each representing distinct features of the respiratory tract, which can be measured for deposited mass. For the glycerol aerosol to which the cast is exposed, it was shown in Chp. 7 that for the relevant Reynolds and Stokes numbers both diffusional and inertial deposition is relevant. It was also shown that in this intermediate deposition regime—the regime where diffusion and inertia are two effects of similar magnitude—it becomes numerically quite challenging to model deposition accurately. This makes the experimental data presented in [142] extremely useful in validating our Eulerian aerosol model in realistic geometries, particularly in relation to capturing the near-wall behavior.

As was done in Chp. 7 for the bent pipe, we simulate the aerosol transport and deposition using a number of different meshes with and without boundary layer mesh refinement. We include the ‘primary’ zero-gradient extrapolation model (ZGM) boundary treatment as well as the more elaborate Lagrangian sub-grid model (LSM) boundary treatment (see [78]) to approximate the inertial deposition velocity at the wall. It is shown that on meshes without boundary layer refinement a significant overprediction of the deposition rate occurs. When applying the LSM boundary treatment, all meshes, both with and without near-wall refinement, are capable of producing a reliable prediction of the per-segment deposition rate in comparison with the regional experimental data. When looking more closely at the local deposition patterns within each cast segment, it is shown that for meshes without boundary layer refinement, the deposition appears very pixelated. If accurate predictions are required of deposition patterns with local length scales smaller than the typical features of the lung cast, refined mesh quality near the wall is required.

Using the finest mesh with near-wall refinement and the LSM boundary treatment for the inertial velocity of droplets near the wall, we simulate a scenario where a uniform droplet size distribution spanning over a size range from 10 nm to 20  $\mu\text{m}$  is released inside the lung cast. The deposition efficiency as a function of size is studied for several generations of the lung cast. For the largest particles enhanced deposition efficiency is shown in the throat segment of the cast, hindering these particles from penetrating the lung further. The typical ‘V-shape’ Chp. 7 deposition curve is recovered, where in the left leg of this curve deposition is driven by diffusion and the right leg by inertia. Of the total deposited mass, we also show how the deposition is partitioned across the several generations of the lung cast.

The outline of this chapter is as follows. In Sec. 8.2 we present simulations which mimic the experimental setup presented in [142], and compare against these experimental data of regional deposition. We study various computational settings, addressing the influence on deposition of both the mesh refinement at the wall and

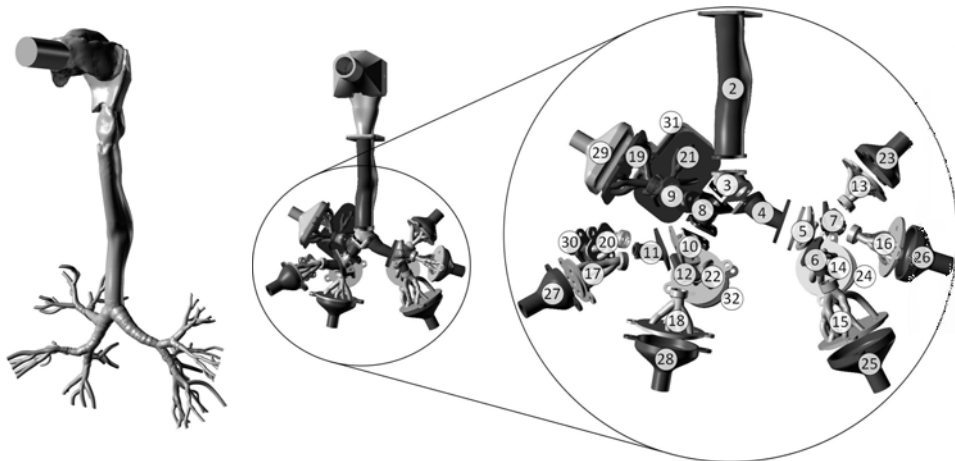


Figure 8.1: Left: visualization of the lung cast geometry. Right: visualization of the segmented cast as used in the experiment with segment numbers as indicated. See [142].

the boundary treatment for the inertial deposition velocity. In Sec. 8.3 we simulate a large size range of droplets and study the regional deposition as a function of droplet size. In Sec. 8.4 we conclude the findings.

## 8.2 VALIDATION AGAINST LUNG CAST DEPOSITION EXPERIMENTS

In Chp. 7 the Eulerian aerosol model for droplet deposition by diffusion and drift was presented. In this section, the model will be applied to prediction of aerosol lung deposition. The main goal of this is to validate the model, as experimental data for regional deposition in a realistic cast of the upper human airways is available. First the experimental setup is discussed, as well as the experimental conditions at which the lung cast was operated. These conditions must be mimicked accurately, to allow for proper comparison between the numerical and experimental results. Next, the numerical setup is discussed in and finally we study the deposition rate of aerosol inside the lung cast. Due to the construction of the cast, detailed deposition rates can only be measured per segment experimentally. The per-segment data can also be recovered from the numerical setup. Several simulations will be compared against the experimental data, for different computational grids and comparing the two boundary treatments as sketched in the previous section.

### 8.2.1 Experimental setup

In Nordlund et al. [142] experiments in a realistic cast of the human upper respiratory tract are presented. In this chapter we accurately represent the geometry of this cast numerically, as well as the conditions at which the cast is operated. For completeness, we give a brief overview of the main features of the lung cast.

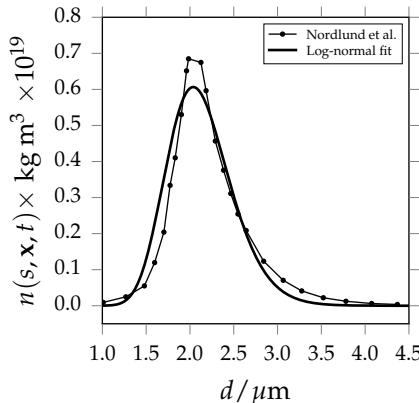


Figure 8.2: The glycerol droplet size distribution at the inlet of the cast for the physical experiment ( $\bullet$ ) [142] and the numerical simulation (—).

The lung cast is based on the original model of [143]. It is a segmented airway model consisting of an oral cavity and subsequent segments down to the seventh generation of lung branching. Fig. 8.1 (left) shows a visualization of the in silico representation of the human tracheobronchial tree. In the right figure a close-up is shown of the branching geometry as used in the experiment, where it can be clearly seen that the cast is built up of 32 segments, constructed to explicitly distinguish the geometrical features of the airways. The internal geometry of the cast is based on a combination of a digital reference model of the human tracheobronchial tree [144] and the oral cavity [145]. The numbering of segments is from top to bottom starting with the oral cavity, as shown in Fig. 8.1. Segments 23–32 are outlet segments to connect the relatively small highest generation branches in one larger outlet (see Fig. 8.1). The flow rate at each of these 10 outlets was set such that the total inlet flow rate is 15 L/min, corresponding to flow conditions in the sedentary regime [146]. The outlet flow rates are specified in Nordlund et al. [142], and correspond to flowrates related to the pneumatic resistance of the model, as reported by [143].

Once a steady-state flow is achieved inside the lung cast, an aerosol can be released at the inlet of the mouth. The chosen aerosol was a glycerol-air mixture with a count median aerodynamic diameter of  $2.1 \mu\text{m}$  and a geometric standard deviation of 1.19. This particle size distribution corresponds to the largest sizes which could be reliably created with the aerosol generation method, i.e., a Condensation Monodisperse Aerosol Generator (CMAG), see Nordlund et al. [142]. Fig. 8.2 shows the experimental droplet size distribution as taken from Nordlund et al. [142]. It can be seen that the highest droplet number concentration is located at  $2 \mu\text{m}$ , while the distribution spans from approximately  $1 \mu\text{m}$  to  $4 \mu\text{m}$ . Also shown in this figure is a log-normal fit to the experimental distribution, with the count median diameter (CMD) set to  $2.1 \mu\text{m}$  and the geometric standard deviation to  $\sigma = 1.19$  (see [3]). Both

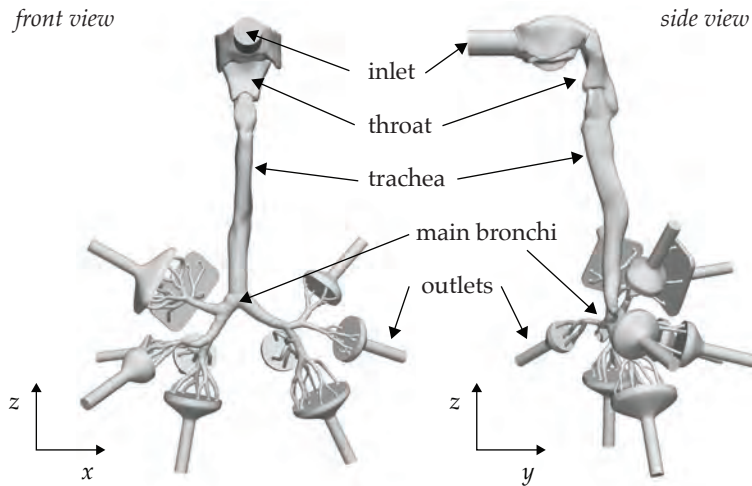


Figure 8.3: Front and side view of the lung cast geometry as used in simulations.

lines are close to each other and we conclude that a log-normal distribution based on the given CMD and  $\sigma$  represent the experimental droplet size distribution well. In the next subsection we use the mathematically convenient log-normal distribution in our numerical model.

After the lung cast is exposed to the aerosol flow for one hour, the cast can be disassembled into separate segments. The deposited glycerol mass is extracted from each segment by rinsing it with a known amount of 2-propanol solution. Using Gas Chromatography-Mass Spectrometry (GC-MS) the concentration levels of glycerol in the extraction solutions can be measured. The concentration levels are then translated into deposition rates, given the total volume of rinsing solution used and the cast exposure time (1 hour). The segments 23–32 which are connected to filters which absorb all aerosol droplets which have not deposited inside the cast. These segments, including their filters, are rinsed and measured for glycerol concentration in the same way. Each outlet is connected to a flow controller to be able to set the flow rate through each outlet individually. The sum of all deposited masses of glycerol of all segments is equal to the total mass of glycerol which entered the system.

### 8.2.2 Numerical setup

Fig. 8.3 shows the front and side view of the lung cast geometry as used in our simulations. It is a direct copy of the model used for the physical experiments. The inlet, throat, trachea, main bronchi and outlets are shown. As in the physical experiment, the highest generation is connected to a conically-shaped outlet segments. The inlet and outlets have cylindrical extrusions, such that the flow into and out of the cast may naturally develop without the inlet and outlet condition being of major influence. In order to simulate inside the geometry using a finite volume method, we must create a computational mesh of the geometry. Three computational grids are

parameter	value	unit
$\mu$	$1.81 \times 10^{-5}$	$\text{m}^2/\text{s}$
$\rho_{\text{air}}^v$	1.1898	$\text{kg}/\text{m}^3$
$\rho_{\text{gly}}^\ell$	1258	$\text{kg}/\text{m}^3$
$T_0$	298.15	K
$p_0$	$10^5$	Pa
$\Phi$	15	L/min
$\mathbf{g}$	(0, 0, -9.81)	$\text{m}/\text{s}^2$

Table 8.1: Simulation parameters for glycerol droplets carried by air at room temperature and atmospheric conditions. The  $v$  superscript denotes a vapor and  $\ell$  a liquid.

used to test the mesh dependency of the numerical results. Two meshes (coarse A and fine B) are constructed without boundary layer refinement (-no-bl suffix), and a finer mesh B was constructed also with boundary layer refinement (-bl suffix). On those three distinct meshes simulations are performed using the LSM (-LSM suffix) and ZGM (-ZGM suffix) boundary treatments for the velocity of particles at the wall. Identification of the presented results given a mesh and boundary conditions follows from the syntax which is constructed from the abbreviations (e.g., A-no-bl-LSM to denote results obtained on the coarse grid A, without refinement in the boundary layer close to the wall and with the LSM for the inertial deposition velocity).

In order to determine the necessary cell sizes, Reynolds Averaged Navier-Stokes (RANS) simulations are performed. The commercial StarCCM+ code, version 10.2, is used and the SST  $k - \omega$  turbulence model is applied. For the determination of the characteristic scales, the resting condition of 15 L/min steady-state flow rate is applied. The bulk computational cell size for the fine mesh B is based on the Taylor scale computed from the RANS simulations (for details see [147]). For the boundary layer the non-dimensional wall distance for wall-bounded flows is also computed based on the RANS simulations and the first layer of cells is located at  $y^+ = 0.5$ , while the last layer has a similar size as the bulk cell size.

The Taylor scale is estimated between  $4.5 \times 10^{-4}$  and  $7.5 \times 10^{-4}$  m, depending on the particular lung regions, while the thickness of the first cell of the triangular prism layer for the selected flow and  $y^+ = 0.5$  is found to be  $6 \times 10^{-5}$  m. Depending on the lung region the boundary layer mesh consists of 7 to 10 cell layers, with thicknesses consecutively growing towards the bulk with a stretching ratio equal to 1.2. For all meshes generated in StarCCM+, the quality of the polyhedral elements is set as high as possible in the software setup to obtain a smaller number of cells, and in particular a smaller number of non-orthogonal cells. The mesh A (coarse) was constructed by coarsening the resolution of mesh B with a factor of two. In total, mesh A-no-bl has 583,088 cells, mesh B-no-bl 1,750,042 cells and mesh B-bl 4,021,078 cells.

Tbl. 8.1 lists the physical parameters used in the simulations. For the viscosity we

variable	inlet	outlets	walls
$Z_{\text{gly}}$	$10^{-5}$	ZG	ZG (drift) and 0 (diffusion)
$Y_{\text{air}}$	$1 - Z_{\text{gly}}$	ZG	–
$M_i$	$M_0$	ZG	ZG (drift) and 0 (diffusion)
$T$	$T_0$	ZG	$T_0$
$\mathbf{u}$	ZG	From [142]	(0, 0, 0) m/s
$\mathbf{v}_i$	$\mathbf{u}$	ZG	LSM or ZGM
$p$	$p_0$	ZG	ZG

Table 8.2: Boundary conditions for the given variables and boundary regions. ZG stands for zero-gradient.

use that of air. The liquid density of glycerol is taken from [142]. The physical experiment was performed at atmospheric conditions and room temperature. Temperature and pressure changes inside the lung can be assumed to be small such that the system is effectively isothermal. This allows to neglect effects such as condensational growth, evaporation and nucleation, and allows to take the physical parameters listed in Tbl. 8.1 as constant. In agreement with the experiment the flow rate at the inlet  $\Phi$  is set to 15 L/min.

Tbl. 8.2 lists the boundary conditions for the solution variables for the inlet, ten outlets and wall boundary regions. We set the mass fraction of glycerol to a low but arbitrary value of  $10^{-5}$ . Since for such a dilute aerosol there is only one-way coupling (see [148], the corresponding volume fraction of glycerol is much smaller than  $10^{-5}$  due to its density) between flow and particulate phase, the concentration of droplets has no effect on the flow or deposition patterns. Also, when discretizing the size space in several sections, these sections do not communicate with each other due to the omitted effects of condensation, evaporation, coagulation, etc, although each representative size  $s_i$  associated with a section responds in its own way to the flow. This response depends on the sectional diffusivity  $\mathbb{D}_i \equiv \mathbb{D}(s_i)$  and sectional droplet velocity  $\mathbf{v}_i \equiv \mathbf{v}(s_i)$  consisting of the velocity of the gas mixture  $\mathbf{u}$  and the size dependent drift velocities of the droplets. For convenience, we choose to set an arbitrary uniform distribution in sectional space, i.e.,  $M_i = M_0$  at the inlet. Using the consistency relation (2.23) it can be derived that  $M_0 = Z_{\text{gly}} / \sum_i s_i$  at the inlet, with  $Z_{\text{gly}}$  the local mass fraction of glycerol. To represent the relevant size space of the glycerol inlet distribution shown in Fig. 8.2 accurately, we choose  $\mathcal{P} = 8$  and a distribution of equally sized sections in  $d$  over the domain  $d = [1, 4] \mu\text{m}$ . The representative sizes  $s_i$  are chosen at the center of each section in  $d$ -space. By using the fact that mass fractions sum up to unity, we set the carrier gas mass fraction to  $Y_{\text{air}} = 1 - Z_{\text{gly}}$  at the inlet such that droplets are following mixture streamlines. We force the droplet phase at the inlet to have no drift velocity, i.e.,  $\mathbf{v}_i = \mathbf{u}$  at the inlet. The aerosol enters the cast under atmospheric pressure  $p_0$ . We assume that due to the

term	scheme	comment
$\partial_t$	$\theta$ -scheme [25]	All time derivative, $\theta = 0.6$
$\mathbf{u}_f, T_f$	Linear upwind	linearUpwind in OpenFOAM
$Y_{j,f}, Z_{j,f}, M_{i,f}$	Van Leer limiter [95]	vanLeer in OpenFOAM
$\mathbf{v}_{i,f}$	Upwind	Provides good convergence
$\nabla$ (cell-center gradient)	Central	linear in OpenFOAM
$\nabla^2$ (Laplacian)	Central corrected	linear with non-orth. corr.
$\nabla_f$ (face-normal gradients)		

Table 8.3: Chosen numerical schemes for the discretization of the indicated terms.

cylindrical outlet extensions as shown in Fig. 8.3 the flow is sufficiently developed such that a zero-gradient boundary condition can be set for all variables at all outlets. Only the fluid velocity  $\mathbf{u}$  is set using a Dirichlet boundary condition. We impose an outward Poiseuille profile with a total flow rate as specified in [142]. The sum of all the outlet flow rates equals  $\Phi$ . For both  $M_i$  and  $Z_{\text{gly}}$  we use the zero-gradient boundary condition when computing the drift flux at the geometry walls and a Dirichlet boundary condition of zero when computing the diffusive flux to mimic a perfectly absorbing surface. No boundary condition is necessary for vapor at the walls because we set the wall vapor flux to zero. For the mixture velocity  $\mathbf{u}$  a no-slip condition is applied while we use either the LSM or ZGM boundary treatments for  $\mathbf{v}_i$  as will be indicated, at the walls. We start each simulation at  $t = 0$  with a quiescent system containing only air at pressure  $p_0$  and temperature  $T_0$ . In the time interval  $t = [0, 0.1]$  s the outlet velocities are linearly ramped to their values corresponding to a total inlet flow rate of  $\Phi$ . For the given conditions and meshes all simulations attain a steady state. The results presented in the remainder of this text are taken at  $t = 4$  s, a point in time for which all simulations are converged sufficiently to this steady state. We conclude this from the fact that the total flux of droplets leaving the system (via deposition or the outlets) is approximately equal to the total flux of droplets entering the system, to within 5%.

Tbl. 8.3 shows the numerical schemes used for the various terms in the set of governing equations. For the partial time derivatives we use the  $\theta$ -scheme [25] with  $\theta = 0.6$ . This gives extra implicit damping and improves convergence to the steady state. We use the ‘linear upwind’ scheme in the computation of both temperature and velocity at cell faces. This interpolation scheme is a second order upwind-biased scheme and uses the gradient of the velocity to explicitly ‘improve’ the interpolation from an upwind direction. The Van Leer limiter [95] is used to interpolate  $Y_j$ ,  $Z_j$  and  $M_i$  to cell faces. This combination of schemes for the particular terms performed well in Chp. 6 and 7 and is therefore selected here too.

### 8.2.3 Deposition efficiency results and comparison

When integrating the third term in the left-hand side and the first term in the right-hand side in Eq. (7.1) over a section and using definition (2.29) it can be seen

that the total sectional number concentration flux at a wall is given by

$$\phi_i = -\rho \mathbf{u}^\ell M_i + \rho D_i^\ell \nabla M_i, \quad (8.1)$$

which has unit  $\text{m}^{-2}\text{s}^{-1}$ , i.e., it gives the section  $i$  number of droplets passing per unit area per unit time. Multiplying this by  $s_i$  gives the total mass of droplets in section  $i$  passing per unit area per unit time, i.e.,

$$\text{flux}_i = \phi_i s_i. \quad (8.2)$$

The value of  $\text{flux}_i$  can be computed at the walls of the lung cast, thereby allowing to assess the deposition in different parts of the lung cast.

Fig. 8.4 shows the deposition patterns in terms of the flux of droplets in section  $i = 3$  with size  $d = 1.93 \mu\text{m}$  close to the value of CMD of the log-normal size distribution as shown in Fig. 8.2. The lung cast is shown only for segments 1–12 for better visibility of the first bifurcation. The deposition flux is presented for mesh A without boundary layer mesh refinement and mesh B with and without boundary layer mesh refinement. The left column shows results using the ZGM deposition velocity boundary treatment and the right column using the LSM. The color represents the flux scaled by the surface-averaged inlet flux. It can be seen that locally the deposition flux exceeds 0.025% of the inlet flux. For the ‘no-bl’ meshes with the ZGM boundary treatment it is quite difficult to distinguish deposition patterns with a sensible length scale; the deposition appears very pixelated. Moreover, with respect to the other simulations the deposition pattern shows a large overprediction of deposition. This corresponds to the observations made in Chp. 7, where deposition in a bent pipe was studied. When the computational mesh was not refined near the wall of the domain, the ZGM boundary treatment showed large overpredictions of deposition, in particular for droplets in the  $\mu\text{m}$  range with flow Reynolds numbers equivalent to the ones in the lung cast ( $\mathcal{O}(10^3)$ , see [142] for a detailed overview of the per-segment Reynolds numbers). For the ‘no-bl’ meshes with the LSM treatment, some trends in the deposition pattern become visible—although the deposition is still quite pixelated. For example, a symmetric gradient in deposition flux is shown at the inlet extension. Moreover, at the saddle point of the first bifurcation (this point is enlarged in the insets in Fig. 8.4 for each simulation), an increase of deposition is shown compared to the primary bronchi.

For mesh B with boundary layer mesh refinement the deposition patterns become much smoother and less pixelated, for either boundary treatment scheme. Features of the geometry are now clearly reflected in the deposition patterns. Quite interestingly, the primary bronchi show a ‘zebra-like’ deposition pattern with rings of local maxima and minima. This deposition pattern appears related to actual anatomical structures in the bronchi walls. After visual inspection we note that the distances between these rings correspond to the length scale of the oscillatory structure of the lung surface,

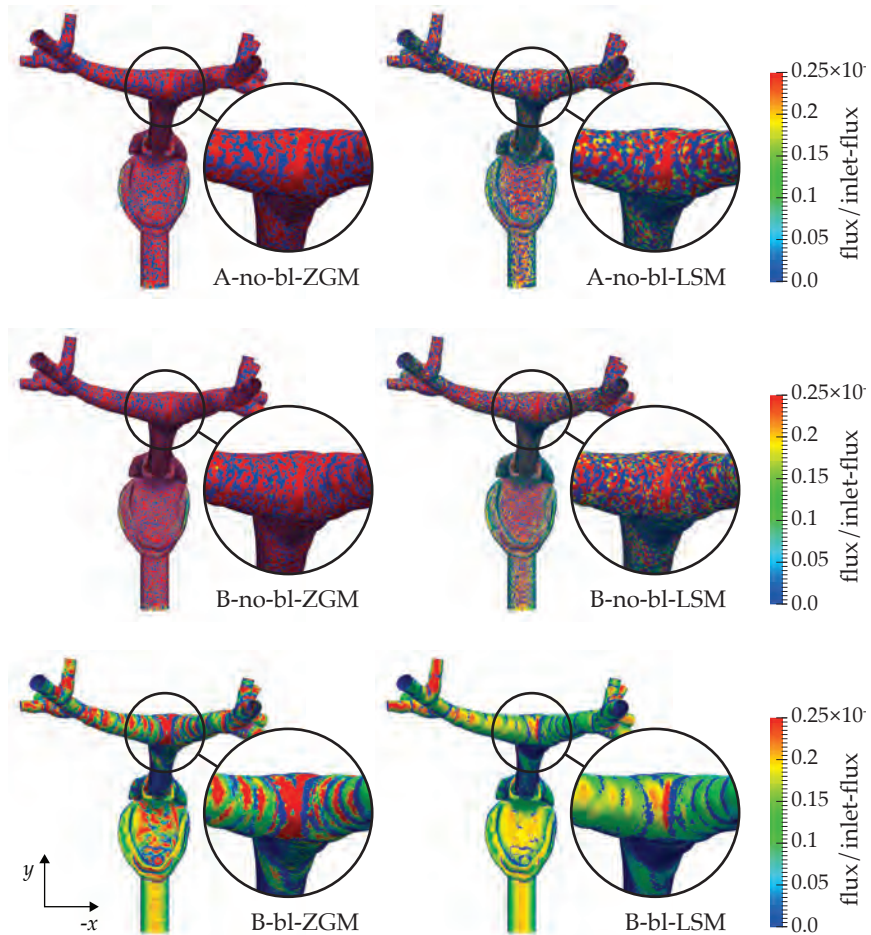


Figure 8.4: Deposition fluxes for  $d = 1.93 \mu\text{m}$  glycerol droplets for the meshes A-no-bl, B-no-bl and B-bl, comparing the LSM and ZGM droplet velocity wall treatments. The color indicates the flux scaled by the surface-averaged inlet flux. The inset shows an enlarged image of the first bifurcation. Only segments 1–12 are shown.

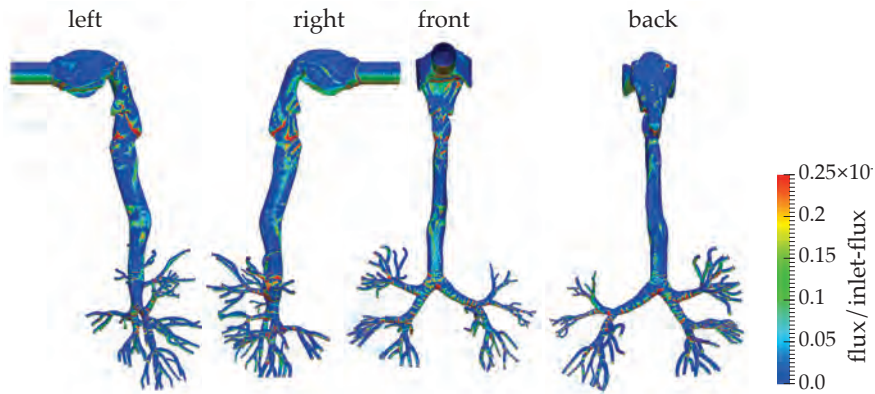


Figure 8.5: Left, right, front and back view of the deposition flux for  $d = 1.93 \mu\text{m}$  glycerol droplets using mesh B with boundary layer mesh refinement at the wall and the ZGM inertial droplet velocity boundary treatment. Segments 1–12 are shown.

as a result of the tracheal and bronchi rings. Also features in the mouth cavity can be clearly distinguished. Fig. 8.5 shows the left, right, front and back view of the ‘B-bl-ZGM’ deposition results for the same droplet size. Here too, features of the geometry can be seen in the pattern of deposition. For example, cavities inside the Larynx are clearly visible due to large deposition there.

After these qualitative considerations, we turn to quantitative comparison against experimental data next. In the physical experiment the total deposition rate  $R_k$  in units of  $\mu\text{g}/\text{hr}$  were measured for each cast segment  $k$ . To allow direct comparison of our simulations against this experimental data, we post-process our results in the following way:

1. In the simulations an arbitrary level of inlet concentration was set, i.e., at the inlet the mass fraction for glycerol is  $Z_{\text{gly}} = 10^{-5}$ . This must be accounted for to reflect the experimental inlet concentration. In the experiment all aerosol droplets are either captured by the segments due to deposition, or by the filters at the ten separate outlets. This means that summing all the rates corresponding to all the segments and outlets gives the total influx, from which the experimental  $Z_{\text{gly}} = 10^{-5}$  at the inlet can be derived. We scale our deposition rates by the ratio of experimental and numerical  $Z_{\text{gly}} = 10^{-5}$ .
2. At the inlet we have specified  $\mathcal{P} = 8$  sections covering the size domain  $d = [1, 4] \mu\text{m}$  in diameter, each with a droplet number concentration of  $M_0$ . To accurately mimic the total experimental deposition rate, the sectional deposition fluxes must be scaled by the log-normal size distribution as shown in Fig. 8.2. We use a weighted average of the sectional fluxes to compute the total per-segment

deposition rate

$$R_k = \sum_i w_i \int_{A_k} \text{flux}_i \, dA, \quad (8.3)$$

with  $A_k$  the surface area of the  $k$ th segment and  $w_i$  the weight belonging to the  $i$ th section. We let  $w_i$  correspond to the surface area underneath a unit log-normal distribution with given CMD and  $\sigma$  corresponding to the part of the size domain for which section  $i$  is representative. The  $i$ th section covers  $[y_i, y_{i+1}]$  in the size domain in terms of mass, and  $[d_i, d_{i+1}]$  in terms of diameter. The unit log-normal distribution can be written as [3]:

$$f(d) = \frac{1}{\sqrt{2\pi} d \log \sigma} \exp \left( -\frac{(\log d - \log \text{CMD})^2}{2 \log^2 \sigma} \right). \quad (8.4)$$

Using  $\sigma$  and CMD as given above, we define the sectional weights as

$$w_i = \int_{d_i}^{d_{i+1}} f(d) \, dd. \quad (8.5)$$

This well-known integral can be expressed using the erf-function. Integrating  $f(d)$  from zero to  $\infty$  gives unity. The sum  $\sum_i w_i$  represents the integral of  $f(d)$  from  $d_1 = 1 \mu\text{m}$  to  $d_{P+1} = 4 \mu\text{m}$  and has a value of  $0.99988\dots$ , indicating that the relevant size domain of the distribution is captured quite completely with the chosen sections.

With these two post-processing steps completed we can compare the numerical results against the experimental data. Fig. 8.6 shows both the experimental and numerical data for each cast segment. The numerical data were obtained for six different setups using two meshes, with and without boundary layer grid refinement and the two boundary treatments. For the ZGM boundary treatment (left figure) it is shown that for the adopted spatial resolution and without grid refinement near the wall (i.e., '-no-bl-ZGM' suffix in the legend) a large overprediction of deposition occurs. In fact, the ratio between  $R_k$  for experimental data and 'no-bl-ZGM' numerical data is more than one order of magnitude. The deposition is so large that a significant amount of droplets has already deposited before reaching the outlets, therewith reducing  $R_k$  significantly for  $k > 22$ .

When using the LSM boundary treatment on mesh B with boundary layer grid refinement, the numerical deposition rate agrees well with the experimental data. Given the sensitivity of the experimental data (indicated by the gray area in Fig. 8.6) it is remarkable how close the numerical predictions are with the measurements. For  $13 \leq k \leq 22$  it appears that the 'B-bl-ZGM' results show a small systematic overprediction of the experimental data, although the ratio between  $R_k$  for experiment and simulation remains within one decade.

The numerical results using the LSM scheme, see Fig. 8.6 (right), show for any

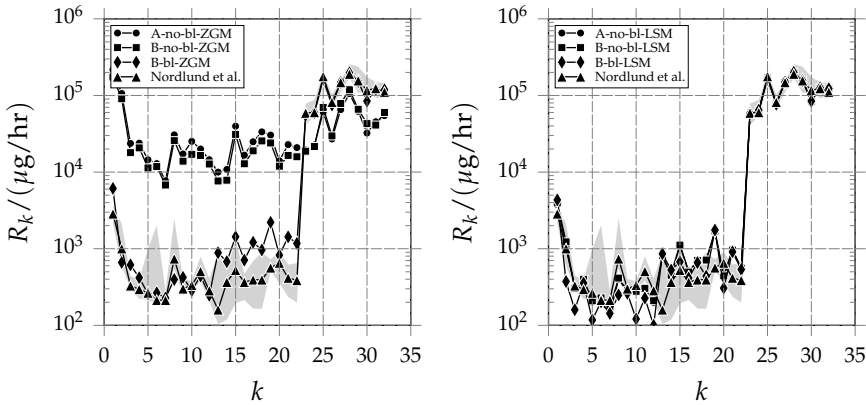


Figure 8.6: Per-segment (indexed by  $k$ ) deposition rates for the simulations and physical experiment as indicated. Left shows the ZGM boundary treatment results and right those for the LSM boundary treatment. Segments 23–32 contain the outlet filters and therefore a large part of the total deposition rate. The gray area marks the range between highest and lowest experimentally measured values, for each  $k$ . The points marked as Nordlund et al. are the average of the experimental repetitions.

of the adopted meshes a good agreement with experimental data. These results correspond to the right column of pictures in Fig. 8.4. It was noted before that the deposition fluxes for the ‘no-bl’ meshes are quite pixellated. Still, the integral quantities  $R_k$  for each segment  $k$  (they are integral quantities due to the surface integral in Eq. (8.3)) correspond reasonably well to both the experimental data as well as the predictions for  $R_k$  using the wall-refined ‘bl’ meshes. In practice, the added value of numerical simulation over physical experiment is that local deposition patterns may be accurately resolved instead of only getting regional deposition information as in the experiments. If this is required, then meshes with sufficient resolution near the wall are necessary. Conversely, under-resolved simulations yield correct per-segment deposition rates but this may be more of a coincidence than a numerically reliable simulation feature. In fact, if the most detailed impression of the solution is clearly under-resolved, then any agreement of integral quantities with experiments is rather fortuitous. The results clearly establish that reliable results are achieved at proper spatial resolution and that particularly the resolution of the boundary layer is crucial for high-quality predictions.

### 8.3 SIZE-DEPENDENT DEPOSITION IN THE HUMAN UPPER AIRWAYS

In the previous section we have validated our numerical approach against experimental data. We see good agreement for meshes with sufficient resolution near the wall. Also, using the LSM boundary treatment the lack of resolution near the wall can

be partially compensated by adopting a Lagrangian sub-grid model. In this section we extend the previous simulations by increasing the size domain and number of sections such that both the diffusional and inertial deposition regimes (see Chp. 7) may be captured. We do this using the ‘B-bl-LSM’ setup, i.e., mesh B with boundary layer refinement and the LSM boundary treatment for the deposition velocity. This setup was shown to give accurate results in comparison with the experimental lung cast data, while producing visually smooth deposition flux fields.

We set the number of sections to  $\mathcal{P} = 16$  using an equidistant sectional distribution in log  $d$ -space spanning  $d \in [10^{-2}, 20] \mu\text{m}$ , with the representative sizes halfway each section in log  $d$ -space. For these sizes, based on the work discussed in Chp. 7, we expect that both the diffusional and inertial deposition regimes are included. All initial and boundary conditions remain equal to those used in the previous section. Using the sectional consistency relation (2.31) we set a sectional droplet number concentration equal to  $M_i = Z_{\text{gly}} / \sum_i s_i$  for all sections at the inlet.

We study quantitatively the deposition behavior inside the lung cast, as a function of droplet size. To that end, we introduce the following quantity:

$$\eta_g(s_i) = -\frac{\int_{A_g} \text{flux}_i \, dA}{\int_{A_{\text{inlet}}} \text{flux}_{\text{inlet}} \, dA}, \quad (8.6)$$

representing the per-generation deposition efficiency of droplets of size  $s_i$ , for lung structures of generation  $g$ , with  $A_g$  the wall surface of all segments belonging to generation  $g$ . The ‘connectivity’ between cast segment  $k$  and lung generation  $g$  is explained by [142], where a detailed table indicates to which generation  $g$  segment  $k$  belongs. The numerator of (8.6) denotes the total number of droplets in section  $i$  depositing on the wall of the  $g$ th generation of the lung cast, per unit of time. The denominator denotes the total flux of droplets in section  $i$  that enters through the inlet. As this has a negative sign, the definition of  $\eta_g$  contains a minus sign. In short,  $\eta_g$  gives the mass deposition rate of droplets of size  $s_i$  into lung cast wall belonging to generation  $g$  with respect to the inflow rate.

Fig. 8.7 (left) shows  $\eta_g$  in a bar diagram for the different groups of lung generations. The experimental lung cast is constructed such that segments  $k > 12$  contain multiple lung generations belonging to  $g > 3$ . These segments are grouped together. Clearly, a ‘V-shaped’ deposition efficiency is shown, with approximately  $d \approx 0.8 \mu\text{m}$  separating the predominantly diffusional regime from the predominantly inertial regime. This also shows that the glycerol distribution as used in the previous Section with  $\text{CMD} = 2.1$  is close to the minimum of the V-curve, indicating that diffusional and inertial deposition are both relevant deposition mechanisms. For the section representing the largest droplets, the total efficiency of the lung cast is close to unity; almost all droplets have deposited, leaving no chance for droplets to escape through the outlets. In Fig. 8.7 (right) the partitioning of deposition in the various size classes and generation of lung structures is shown. Of the total mass which deposits per unit

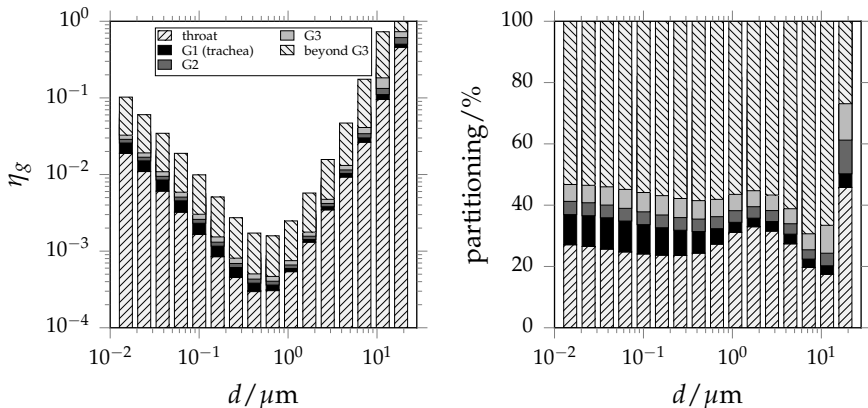


Figure 8.7: Per-generation deposition efficiency  $\eta_g$  (left) and the per-generation partitioning of the deposition efficiency (right). For  $k > 12$  the segments include multiple generations, and are grouped together with segments which contain the same generations (see [142]). Each segment is counted only once.

of time, the shades indicate what percentage of those droplets deposit in which generation of the lung. It can be seen that approximately half of the depositing droplets deposit in the throat and first three generations. Only for the section containing the largest droplets, almost all droplets deposit early on in the lung cast. In fact, approximately half of those large droplets entering the mouth deposit inside the throat. The partitioning of deposition with respect to the lung generation is reasonably uniform in the size domain for  $d < 0.4 \mu\text{m}$ , i.e., the diffusional deposition regime. In the inertial regime the partitioning of deposition depends on size. For example, the throat has an enhanced deposition with respect to the total deposition for approximately  $0.4 < d < 2 \mu\text{m}$ . For  $2 < d < 10 \mu\text{m}$  the percentage of deposition in the throat decreases as deposition inside higher generations becomes more dominant and for  $d > 10 \mu\text{m}$  a rapid increase of deposition inside the throat and trachea occurs. This is the result of a complex geometry-dependent interplay of droplet inertia, drag and gravity. Droplet diffusivity is negligible for droplets with relatively large diameters.

The per-generation deposition efficiency  $\eta_g$  is proportional to the number of droplets depositing inside the parts of the cast belonging to generation  $g$ . In some respect, this could be misleading, since some generations may be very efficient in capturing droplets but have only a small amount of surface area to capture these droplets. To assess the efficiency with which each lung generation captures droplets independent of its amount of lung tissue surface area, we may alternatively have a look at a per-generation average of  $\text{flux}_i$ , indicating more objectively the deposition efficiency of a lung generation as a function of droplet size. Note, however, that inevitably higher generations receive fewer droplets due to the fact that they have already deposited in earlier generations, reducing the flux. We define the per-generation

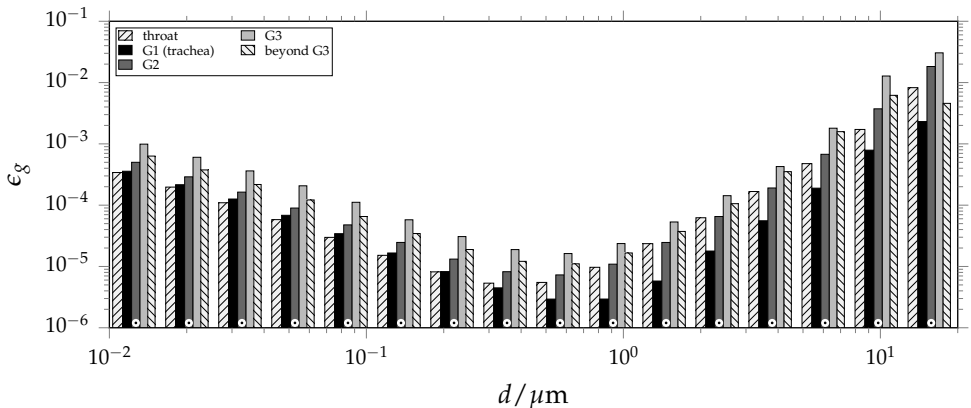


Figure 8.8: The per-generation surface-averaged deposition flux efficiency, per section. The shades are associated with different generations of the lung (as indicated), where all lung cast segments belonging to generation 4 or higher are grouped together. The dot at the foot of each set of bars indicates the droplet diameter to which those bars apply.

surface-averaged deposition efficiency as

$$\epsilon_g(s_i) = - \frac{A_g^{-1} \int_{A_g} \text{flux}_i \, dA}{A_{\text{inlet}}^{-1} \int_{A_{\text{inlet}}} \text{flux}_{\text{inlet}} \, dA} = \frac{A_{\text{inlet}}}{A_g} \eta(s_i). \quad (8.7)$$

This quantity is shown in Fig. 8.8 for the different groups of lung generations as introduced before. It can be seen in Fig. 8.8 that the largest surface-averaged deposition efficiency is G3, for all droplet sizes shown. This generation consists of segments 5 and 8 of the lung cast, i.e., the second bifurcation, after the main bronchi. In the inertial regime for approximately  $d > 0.3 \mu\text{m}$  the surface-averaged efficiency of G1 (i.e., segment 2, trachea) is always much smaller than the other deposition efficiencies. This is because segment 2 resembles closely a vertically placed pipe. Due to gravity larger droplets fall through this pipe without having a large probability of colliding with a wall, while diffusion is not significant. Only for the last section shown in Fig. 8.8 the group of generations beyond G3 has one of the smallest surface-averaged efficiency with respect to the other groups. This is because deposition in earlier generations is so significant that only a drastically reduced number of droplets reaches these later generations, reducing deposition there. This is in agreement with the data shown in Fig. 8.7.

## 8.4 CONCLUSIONS

Size-dependent aerosol deposition in a realistic cast of the human upper airways was studied using an Eulerian internally mixed multi-species aerosol model Chp. 6, in

which the size distribution was discretized using a sectional method. This allowed to capture size-dependent aerosol dynamics such as inertial aerosol drift, gravitational settling and droplet diffusion, accurately and without prior assumptions on the shape or moments of the droplet size distribution. The model was derived in Chp. 2, 6 and 7. An important component of the model is the consistency relation; by construction, the total droplet mass concentration is always equally reflected by both the droplet size distribution and the mass concentration fields. The consistency relation was used to derive transport equations for the species vapor and liquid mass fractions from the drift and diffusion-augmented GDE.

In [142] an experimental study of aerosol deposition in a realistic cast of the human upper airways was presented. A monodisperse glycerol aerosol was released inside the cast and per segment of the cast the total deposited mass could be measured. We compared predictions of our model against the experimental data for regional droplet deposition. We introduced two treatments for the numerical computation of the inertial droplet velocity at the wall: a simple zero-gradient extrapolation model and a Lagrangian sub-grid model [78]. On coarse computational grids without mesh refinement near the wall, both ZGM and LSM yield pixellated deposition patterns. When improving the mesh quality by refining the mesh near the wall, deposition patterns become much smoother and features of these patterns induced by the geometry of the cast can be identified. When looking at the deposition rate integrated over the surface area of a segment of the cast (e.g., the throat, trachea and first bifurcation form one segment), the use of the ZGM boundary treatment results in an overprediction of more than one order of magnitude while with LSM the overprediction significantly reduces and agrees well with the experimental data on any of the adopted meshes. Nevertheless, if the detailed deposition patterns are under-resolved for either boundary treatment a rather pixellated prediction of deposition patterns is found. Agreement of integral quantities with experimental data, as observed with LSM even on coarse meshes, could be somewhat fortuitous. Reliable results are achieved only at proper spatial resolution, where in particular the resolution of the boundary layer is crucial.

Finally, we studied size-dependent aerosol deposition inside the lung cast by exposing it to a polydisperse aerosol spanning a large size range from 10 nm to 20  $\mu\text{m}$ . The typical ‘V-shape’ Chp. 7 deposition curve was recovered, where the left leg of the curve is predominantly governed by diffusional deposition and the right side predominantly by inertial deposition. These results were obtained in a single simulation by virtue of the sectional approach, in which a massively polydisperse aerosol may be modeled at once. The deposition rates for each segment of the cast could be grouped into deposition rates for each generation of anatomical structures in the cast. We presented the partitioning of the total deposition for each generation, and quantified the size-dependent deposition also for droplets that penetrate deeper into the lung. For large droplets we saw that most deposition took place inside the throat. The deposition of small droplets in the diffusional side of the size domain was

much more uniform across the various generations of lung structures.

We also studied the surface-averaged deposition efficiency for each generation of the lung. This quantity captures the deposition rate, and reports how well a particular airway generation captures droplets independent of the surface area of the lung generation. We showed that the second generation of the lung tree, i.e., the bifurcation of the main bronchi, has the largest surface-averaged efficiency. For small droplet sizes the throat is much less effective in capturing droplets than other generations of the lung tree, whereas for large sizes the throat's efficiency increases due to inertial droplet motion.

This chapter demonstrated the successful application of the sectional compressible Eulerian aerosol model inside complex geometries. This model, unique in its consistent formulation and allowing to embed well-known constitutive thermophysical laws for the description of the mixture, remained computationally feasible for the adopted meshes and sectional discretization. Rich aerosol physics were introduced in the model, allowing for a non-trivial development of an initial size distribution due to size-dependent inertial droplet drift, gravitational settling, diffusion and eventual deposition.

#### ACKNOWLEDGEMENTS

Many thanks go to Arne Siccama (NRG) for development and generation of the computational meshes and to the team from Brno University of Technology (M. Belka, F. Lízal, J. Jedelský, J. Elcner and M. Jicha) for making available the experimental results.

## CHAPTER 9

# CONCLUSION

The aim of this thesis was to develop models for aerosol dynamics and numerical tools that assist in finding a solution to those models. In Chp. 2 we presented a general formulation of the aerosol model. This model was derived in a Eulerian context, meaning that we are not tracking individual particles but are rather concerned with continuous properties of the aerosol as a field in space and time. To that end, at the heart of the model we introduced the droplet size distribution, expressing the number of droplets at  $(s, \mathbf{x}, t)$  with droplet size  $s$ , position  $\mathbf{x}$  and time  $t$ . We took the sectional approach to discretize the size domain in several sections, or intervals. For each section a governing partial differential equation could be derived, with a right-hand side depending on the considered aerosol dynamics. For such a PDE, in essence forming a scalar transport equation with the scalar representing the droplet number concentration in a section, we developed the compressible PISO algorithm to find a time-evolving solution to the problem. Our form of the PISO algorithm, presented in Chp. 3, was based on the compressible formulation of the continuity equation. The PISO algorithm, originally designed as a non-iterative method, was generalized to an iterative scheme such that a convergence criterion of choice could be specified to reduce the error due to equation splitting, to an arbitrarily low value. For the spatial discretization we adopted the finite volume method alongside a cell-centered collocated computational grid. Essential in the finite volume method is the integration of the governing set of transport equations over a cell volume. This allows to write divergence terms as surface integrals, requiring the computation of fluxes across the cell volume surface.

The PISO algorithm was discussed for a set of governing equations in which the aerosol dynamics contributing to the problem was captured in a right-hand side source term without being detailed. In Chp. 4–8 the aerosol dynamics was discussed and appropriate methods were developed, which all follow the framework laid down by the PISO algorithm together with the finite volume method. The studied aerosol dynamics include droplet nucleation, condensational growth and droplet evaporation, droplet drift and diffusion and aerosol deposition. These mechanisms were generally discussed in the introduction of this thesis, Chp. 1. The main results and conclusions from Chp. 4–8 will now be summarized.

In Chp. 4 the characteristics-based sectional method (CBSM) was developed for the solution of the hyperbolic spatially homogeneous condensational growth and

nucleation equation. The use of the method of characteristics, employing the analytical solution of the droplet growth model, was shown to have no time step stability restriction related to the condensation rate, and worked on highly skewed sectional distributions. The method was designed to work with fixed sectional distributions in order for a swift extension of the method to the spatially inhomogeneous setting, allowing in addition to preserve a pre-specified number of moments of the droplet size distribution exactly. The method was illustrated using a two-moment, four-moment and ‘hybrid’ formulation. It was shown that the two-moment scheme preserves positivity of the solution, whereas the four-moment scheme captured sharp nucleation fronts more accurately but could lead to negative solutions. The hybrid formulation employed the four-moment scheme, but reduced to a two-moment formulation in case of an unphysical negative solution. When compared with analytical solutions of simple nucleation and condensational growth laws, the hybrid scheme showed to be more accurate than the two-moment scheme without allowing for negativity. Finally, the method was applied to a homogeneous multi-species nucleation and condensation problem using two alcohols. The alcohols nucleate very rapidly and the method was shown to produce a robust solution even for large time steps. The convergence of the solution was studied as a function of the time step size and number of sections.

In Chp. 5 CBSM was extended to the spatially inhomogeneous setting, embedding CBSM inside the PISO algorithm using the fractional step method. This allowed to separate spatial contributions to the rate of change of the droplet size distribution from the non-spatial ones. For the non-spatial ones the hyperbolic condensational growth equation was recovered, which could be solved using the method of characteristics. As a test case, we applied the extended CBSM to the simulation of aerosol formation in lid-driven cavity flow. The spatial interaction of flow and temperature was shown to lead to the formation of aerosol droplets. At each discrete point in space the droplet size distribution was computed without a-priori assumptions on the shape or moments of the distribution. Non-trivial size distributions were uncovered, which showed a ‘layered’ shape due to separate nucleation events induced by the rotation of the flow. These aerosol processes are more general than for example a log-normal size distribution assumption can capture. Finally, to show the feasibility of the sectional method, we simulated aerosol formation in a three-dimensional double mixing-T, in which a saturated vapor flow in a pipe was cooled by two lateral flows leading to supersaturation of the vapor and subsequent nucleation and condensational growth. Detailed information of the development of the droplet size distribution could be computed.

Having studied aerosol formation due to nucleation and condensational growth, we next turned to the modeling of aerosol drift. In Chp. 6 we developed a drift flux model in which aerosol droplets are no longer assumed to follow carrier gas streamlines exactly. To the contrary, we let aerosol droplets, as a function of size, adhere to their own equations of motion including inertia, drag and gravity. Once the droplet velocity becomes unequal to the one of the carrier phase, a drift velocity

with which droplets move with respect to the carrier phase can be defined. This drift locally alters the mixture density, which gives rise to an additional source term in the continuity equation. In the development of the drift model, special attention was paid to the proper implementation of the ‘consistency relation’ on both the analytical and numerical level. This consistency relation can be viewed as a constraint between the droplet size distribution and mass concentrations. It states that the total liquid mass as given by the droplet size distribution must be equal to the total liquid mass as given by the mass concentration fields. We employed the consistency relation to deduce consistent liquid concentration transport equations starting from the General Dynamic Equation (GDE). The GDE described the rate of change of the droplet size distribution. Next, we employed the drift model to the simulation of an aerosol sampler. The flow around an aerosol sampler may contain quite some curvature if the sampler is operated at a sampling velocity different than the ambient flow velocity. This curvature leads to aerosol aspiration; depending on their size droplets may enter the sampler in an amount that may be larger or smaller than is present in the oncoming flow that is being sampled. This would clearly obscure the measured aerosol size distribution. We compared our predictions against experimental data from literature and found good agreement. We tested both the ‘full Stokes model’ in which the droplet velocity is solved from the full PDE including Stokes drag, and the ‘local equilibrium model’ in which the droplet velocity can be approximated using an algebraic equation when assuming that the acceleration of a droplet is approximately equal to the local acceleration of the carrier gas. An important conclusion of Chp. 6 was that the local equilibrium model produced good estimates of the droplet velocity only for sufficiently small droplets ( $St < 0.2$ ).

Droplet drift is one of the driving forces behind droplet deposition on solid walls. In Chp. 7 we extended the drift flux aerosol model with droplet Brownian motion and with the capability to capture aerosol deposition. We embedded the diffusional droplet flux inside a total additional flux. This allowed to adopt the same methodology as used in Chp. 6 in order to respect the consistency relation. To compute the deposition flux it was required to compute the droplet velocity at the wall. We introduced a ‘primary’ boundary treatment, relying on a zero-gradient extrapolation of the cell-centered droplet velocity to the wall, and a Lagrangian sub-grid model boundary treatment, in which the analytical solution of the wall-normal equation of motion of a droplet was used as a sub-grid model to improve the prediction of the droplet velocity at the wall. We applied the model to simulate deposition in a bent pipe. The deposition efficiency curve, showing how well the bent pipe captures droplets due to deposition as a function of droplet size, was shown to exhibit the well-known ‘V-shape’, where the left leg of the V is dominated by diffusional deposition and the right leg by inertial deposition. The well-understood and often-studied bent pipe geometry allowed for validation of our model against an array of data published in literature. At the inertial side of the deposition efficiency curve we found good agreement with other experimental and numerical data. At the

diffusional side we compared against an analytical model for deposition in straight pipes. For small Reynolds numbers the flow inside the bent pipe was very similar to that of a straight pipe and we found good agreement between our results for small droplets and the analytical diffusional deposition model. In general, in agreement with literature we found that the zero-gradient boundary treatment for the droplet velocity led to a significant overprediction of the deposition efficiency. When refining the computational grid towards the wall the overprediction was shown to reduce. In combination with the Lagrangian sub-grid model boundary treatment the deposition efficiency was shown to be much lower—even on coarse unresolved grids. Finally, we studied the dependency of the size-dependent deposition efficiency curve on the Reynolds number and bent curvature. It was shown that an increase in Reynolds number led to an enhancement of both diffusional and inertial deposition inside the bent. The dependence on the bent curvature was less pronounced.

The bent pipe offered a well-known academic setting to validate our Eulerian aerosol deposition model. In Chp. 8 the model was further validated in a realistic cast of the human upper airways. In this cast physical experiments were performed in which the cast was exposed to a reasonably monodisperse glycerol aerosol. The cast, constructed of several segments representing distinct features of the respiratory tract, could be taken apart and measured for the per-segment deposited mass. With our model we simulated the same setting and compared against the experimentally determined deposition rates. We performed simulations on several grids using the zero-gradient and Lagrangian sub-grid model droplet velocity boundary treatments. For the coarse mesh without boundary layer mesh refinement a large overprediction of the per-segment deposition rate was observed when using the zero-gradient boundary treatment. To the contrary, even on coarse meshes the Lagrangian sub-grid model boundary treatment delivered results for the deposited fraction quite close to the experimental data. When looking at local deposition patterns, the results appeared quite pixellated on coarse meshes, suffering from significant under-resolution. Only on the finest mesh with boundary layer mesh refinement the deposition patterns appeared to be smooth and physical. Additional to the comparison against experimental data we also simulated polydisperse aerosol flow through the lung cast. The introduced aerosol covered a size range of approximately 10 nm to 10  $\mu\text{m}$ . As was the case in the bent pipe geometry, a ‘V-shape’ deposition efficiency curve was recovered. These simulations demonstrated both the feasibility and utility of the sectional Eulerian aerosol model applied to realistic and complex settings.

## BIBLIOGRAPHY

- [1] H. Yu, M. Chin, T. Yuan, H. Bian, L.A. Remer, J.M. Prospero, A. Omar, D. Winker, Y. Yang, Y. Zhang, et al. The fertilizing role of African dust in the Amazon rainforest: A first multiyear assessment based on data from cloud-aerosol Lidar and infrared pathfinder satellite observations. *Geophysical Research Letters*, 42(6):1984–1991, 2015.
- [2] S.K. Friedlander. *Smoke, Dust, and Haze: Fundamentals of Aerosol Dynamics*. Oxford University Press, 2<sup>nd</sup> edition, 2000.
- [3] W.C. Hinds. *Aerosol Technology*. John Wiley & Sons, Inc., 2<sup>nd</sup> edition, 1999.
- [4] S.M. Walas. *Phase equilibria in chemical engineering*. Butterworth, 1985.
- [5] B.R. Bird, W.E. Stewart, and E.N. Lightfoot. *Transport Phenomena*. John Wiley & Sons, Inc., 2<sup>nd</sup> edition, 2007.
- [6] VDI Gesellschaft Verfahrenstechnik und Chemieingenieurwesen. *VDI Heat Atlas*. Springer, 2010.
- [7] V. Giovangigli. Convergent iterative methods for multicomponent diffusion. *IMPACT of Computing in Science and Engineering*, 3(3):244–276, 1991.
- [8] D. Ramkrishna. *Population balances theory and applications to particulate systems in engineering*. Academic Press, 2000.
- [9] F. Gelbard, Y. Tambour, and J.H. Seinfeld. Sectional representations for simulating aerosol dynamics. *Journal of Colloid and Interface Science*, 76(2):541–556, 1980.
- [10] S. Kumar and D. Ramkrishna. On the solution of population balance equations by discretization—I. A fixed pivot technique. *Chemical Engineering Science*, 51(8):1311–1332, 1996.
- [11] F. Gelbard, J.W. Fitzgerald, and W.A. Hoppel. A one-dimensional sectional model to simulate multicomponent aerosol dynamics in the marine boundary layer: 3. Numerical methods and comparisons with exact solutions. *Journal of Geophysical Research: Atmospheres*, 103(D13):16119–16132, 1998.

- [12] E.M.A. Frederix, M. Stanic, A.K. Kuczaj, M. Nordlund, and B.J. Geurts. Extension of the compressible PISO algorithm to single-species aerosol formation and transport. *International Journal of Multiphase Flow*, 74:184–194, 2015.
- [13] R.I. Issa, B. Ahmadi-Befrui, K.R. Beshay, and A.D. Gosman. Solution of the implicitly discretised reacting flow equations by operator-splitting. *Journal of Computational Physics*, 93(2):388–410, 1991.
- [14] C.M. Rhie and W.L. Chow. Numerical study of the turbulent flow past an airfoil with trailing edge separation. *AIAA Journal*, 21(11):1525–1532, 1983.
- [15] R.I. Issa. Solution of the implicitly discretised fluid flow equations by operator-splitting. *Journal of Computational Physics*, 62(1):40–65, 1986.
- [16] R.I. Issa, A.D. Gosman, and A.P. Watkins. The computation of compressible and incompressible recirculating flows by a non-iterative implicit scheme. *Journal of Computational Physics*, 62(1):66–82, 1986.
- [17] N.W. Bressloff. A parallel pressure implicit splitting of operators algorithm applied to flows at all speeds. *International Journal for Numerical Methods in Fluids*, 36(5):497–518, 2001.
- [18] I. E. Barton. Comparison of SIMPLE- and PISO-type algorithms for transient flows. *International Journal for Numerical Methods in Fluids*, 26(4):459–483, 1998.
- [19] A. Wanik and U. Schnell. Some remarks on the PISO and SIMPLE algorithms for steady turbulent flow problems. *Computers & Fluids*, 17(4):555–570, 1989.
- [20] C. M. Xisto, J. C. Páscoa, P. J. Oliveira, and D. A. Nicolini. A hybrid pressure-density-based algorithm for the euler equations at all mach number regimes. *International Journal for Numerical Methods in Fluids*, 70(8):961–976, 2012.
- [21] R. Payri, S. Ruiz, J. Gimeno, and P. Martí-Aldaraví. Verification of a new CFD compressible segregated and multi-phase solver with different flux updates-equations sequences. *Applied Mathematical Modelling*, 39(2):851–861, 2015.
- [22] D. M. Wang, A. P. Watkins, and R. S. Cant. Three-dimensional diesel engine combustion simulation with a modified EPISO procedure. *Numerical Heat Transfer, Part A: Applications*, 24(3):249–272, 1993.
- [23] D.M. Wang and A.P. Watkins. Numerical modeling of diesel spray wall impaction phenomena. *International Journal of Heat and Fluid Flow*, 14(3):301–312, 1993.
- [24] W.K. Chow and N.K. Fong. Application of field modelling technique to simulate interaction of sprinkler and fire-induced smoke layer. *Combustion Science and Technology*, 89(1–4):101–151, 1993.

- [25] K.W. Morton and D.F. Mayers. *Numerical Solution of Partial Differential Equations*. Cambridge University Press, 2005.
- [26] E.M.A. Frederix, M. Stanic, A.K. Kuczaj, M. Nordlund, and B.J. Geurts. Characteristics-based sectional modeling of aerosol nucleation and condensation. *Journal of Computational Physics*, 326:499–515, 2016.
- [27] F. Gelbard and J. H. Seinfeld. Numerical solution of the dynamic equation for particulate systems. *Journal of Computational Physics*, 28(3):357–375, 1978.
- [28] T. H. Tsang and A. Rao. Comparison of different numerical schemes for condensational growth of aerosols. *Aerosol Science and Technology*, 9(3):271–277, 1988.
- [29] S. Rigopoulos and A.G. Jones. Finite-element scheme for solution of the dynamic population balance equation. *AIChE Journal*, 49(5):1127–1139, 2003.
- [30] A. Sandu and C. Borden. A framework for the numerical treatment of aerosol dynamics. *Applied Numerical Mathematics*, 45(4):475–497, 2003.
- [31] M. Cui, K. Fu, D. Liang, Y. Cheng, and W. Wang. Numerical analysis of the second-order characteristic FEM for nonlinear aerosol dynamic equations. *Journal of Computational and Applied Mathematics*, 261:48–61, 2014.
- [32] X. Kwauk and P.G. Debenedetti. Mathematical modeling of aerosol formation by rapid expansion of supercritical solutions in a converging nozzle. *Journal of Aerosol Science*, 24(4):445–469, 1993.
- [33] S.E. Pratsinis. Simultaneous nucleation, condensation, and coagulation in aerosol reactors. *Journal of Colloid and Interface Science*, 124(2):416–427, 1988.
- [34] E.R. Whitby and P.H. McMurry. Modal aerosol dynamics modeling. *Aerosol Science and Technology*, 27(6):673–688, 1997.
- [35] M. Wilck and F. Stratmann. A 2-D multicomponent modal aerosol model and its application to laminar flow reactors. *Journal of Aerosol Science*, 28(6):959–972, 1997.
- [36] D.P. Brown, E.I. Kauppinen, J.K. Jokiniemi, S.G. Rubin, and P. Biswas. A method of moments based CFD model for polydisperse aerosol flows with strong interphase mass and heat transfer. *Computers & Fluids*, 35(7):762–780, 2006.
- [37] R. McGraw. Description of aerosol dynamics by the quadrature method of moments. *Aerosol Science and Technology*, 27(2):255–265, 1997.

- [38] D.L. Wright, R. McGraw, and D.E. Rosner. Bivariate extension of the quadrature method of moments for modeling simultaneous coagulation and sintering of particle populations. *Journal of Colloid and Interface Science*, 236(2):242–251, 2001.
- [39] R. McGraw and D.L. Wright. Chemically resolved aerosol dynamics for internal mixtures by the quadrature method of moments. *Journal of Aerosol Science*, 34 (2):189–209, 2003.
- [40] D.L. Marchisio, R.D. Vigil, and R.O. Fox. Implementation of the quadrature method of moments in CFD codes for aggregation-breakage problems. *Chemical Engineering Science*, 58(15):3337–3351, 2003.
- [41] R. Fan, D.L. Marchisio, and R.O. Fox. Application of the direct quadrature method of moments to polydisperse gas–solid fluidized beds. *Powder Technology*, 139(1):7–20, 2004.
- [42] R. Fox, F. Laurent, and M. Massot. Numerical simulation of spray coalescence in an eulerian framework : direct quadrature method of moments and multi-fluid method. *Journal of Computational Physics*, 227(6):3058–3088, 2008.
- [43] M. Massot, F. Laurent, D. Kah, and S. De Chaisemartin. A robust moment method for evaluation of the disappearance rate of evaporating sprays. *SIAM Journal on Applied Mathematics*, 70(8):3203–3234, 2010.
- [44] A. Alshaarawi and F. Bisetti. The effect of mixing rates on the formation and growth of condensation aerosols in a model stagnation flow. *Journal of Aerosol Science*, 81:34–46, 2015.
- [45] D. Mitrakos, E. Hinis, and C. Housiadis. Sectional modeling of aerosol dynamics in multi-dimensional flows. *Aerosol Science and Technology*, 41(12):1076–1088, 2007.
- [46] J. Pyykön. Modelling studies for high temperature aerosol formation in laminar flow reactors. *Journal of Aerosol Science*, 1001(28):S325–S326, 1997.
- [47] Y.P. Kim and J.H. Seinfeld. Simulation of multicomponent aerosol condensation by the moving sectional method. *Journal of Colloid and Interface Science*, 135(1): 185–199, 1990.
- [48] F. Laurent and M. Massot. Multi-fluid modelling of laminar polydisperse spray flames: origin, assumptions and comparison of sectional and sampling methods. *Combustion Theory and Modelling*, 5(4):537–572, 2001.
- [49] S.H. Park and S.N. Rogak. A novel fixed-sectional model for the formation and growth of aerosol agglomerates. *Journal of Aerosol Science*, 35(11):1385–1404, 2004.

- [50] S. Kumar and D. Ramkrishna. On the solution of population balance equations by discretization-II. A moving pivot technique. *Chemical Engineering Science*, 51(8):1333–1342, 1996.
- [51] M.M. Attarakih, C Drumm, and H Bart. Solution of the population balance equation using the sectional quadrature method of moments (SQMOM). *Chemical Engineering Science*, 64(4):742–752, 2009.
- [52] S. Kumar and D. Ramkrishna. On the solution of population balance equations by discretization-III. Nucleation, growth and aggregation of particles. *Chemical Engineering Science*, 52(24):4659–4679, 1997.
- [53] P. Marchal, R. David, J.P. Klein, and J. Villermaux. Crystallization and precipitation engineering-I. An efficient method for solving population balance in crystallization with agglomeration. *Chemical Engineering Science*, 43(1):59–67, 1988.
- [54] M.J. Hounslow, R.L. Ryall, and V.R. Marshall. A discretized population balance for nucleation, growth, and aggregation. *AIChE Journal*, 34(11):1821–1832, 1988.
- [55] R. David, J. Villermaux, P. Marchal, and J.P. Klein. Crystallization and precipitation engineering-IV. Kinetic model of adipic acid crystallization. *Chemical Engineering Science*, 46(4):1129–1136, 1991.
- [56] E.X. Berry. Cloud droplet growth by collection. *Journal of the Atmospheric Sciences*, 24(6):688–701, 1967.
- [57] C. Winkelmann, A.K. Kuczaj, M. Nordlund, and B.J. Geurts. Simulation of aerosol formation due to rapid cooling of multispecies vapors. *Journal of Engineering Mathematics*, Submitted.
- [58] R.C. Reid, J.M. Prausnitz, and T.K. Sherwood. *The Properties of Gases and Liquids*. McGraw-Hill: New York, 1977.
- [59] E.M.A. Frederix, M. Stanic, A.K. Kuczaj, M. Nordlund, A.E.P. Veldman, and B.J. Geurts. Application of the characteristics-based sectional method to spatially varying aerosol formation and transport. *Journal of Aerosol Science*, Submitted.
- [60] E. Erturk, T. C. Corke, and C. Gökcöl. Numerical solutions of 2-D steady incompressible driven cavity flow at high Reynolds numbers. *International Journal for Numerical Methods in Fluids*, 48(7):747–774, 2005.
- [61] U. Ghia, K.N. Ghia, and C.T. Shin. High-Re solutions for incompressible flow using the Navier-Stokes equations and a multigrid method. *Journal of Computational Physics*, 48(3):387–411, 1982.

- [62] K.W. Lee and H. Chen. Coagulation rate of polydisperse particles. *Aerosol Science and Technology*, 3(3):327–334, 1984.
- [63] D. Thorne and J. Adamson. A review of in vitro cigarette smoke exposure systems. *Experimental and Toxicologic Pathology*, 65:1183–1193, 2013.
- [64] J. Adamson, D. Thorne, G. Errington, W. Fields, X. Li, R. Payne, T. Krebs, A. Dalrymple, K. Fowler, D. Dillon, F. Xie, and C. Meredith. An inter-machine comparison of tobacco smoke particle deposition in vitro from six independent smoke exposure systems. *Toxicology in Vitro*, 7:1320–1328, 2014.
- [65] S. Majeed, S. Frentzel, S. Wagner, D. Kuehn, P. Leroy, P.A. Guy, A. Knorr, J. Hoeng, and M.C. Peitsch. Characterization of the Vitrocell® 24/48 in vitro aerosol exposure system using mainstream cigarette smoke. *Chemistry Central Journal*, 8(62), 2014.
- [66] A.K. Kuczaj, M. Nordlund, S. Jayaraju, E. Komen, T. Krebs, M. Peitsch, and J. Hoeng. Aerosol flow in the Vitrocell® 24/48 exposure system: flow mixing and aerosol coalescence. *Applied In Vitro Toxicology*, 2015, submitted.
- [67] H.V. Nguyen, K. Okuyama, T. Mimura, Y. Kousaka, R.C. Flagan, and J.H. Seinfeld. Homogeneous and heterogeneous nucleation in a laminar flow aerosol generator. *Journal of Colloid and Interface Science*, 119(2):491–504, 1987.
- [68] E.M.A. Frederix, A.K. Kuczaj, M. Nordlund, A.E.P. Veldman, and B.J. Geurts. Prediction of non-isokinetic sampling with a sectional drift flux model. *Computers & Fluids*, Submitted.
- [69] M.R. Maxey and J.J. Riley. Equation of motion for a small rigid sphere in a nonuniform flow. *Physics of Fluids*, 26(4):883–889, 1983.
- [70] J. Fernandez De La Mora and D.E. Rosner. Effects of inertia on the diffusional deposition of small particles to spheres and cylinders at low Reynolds numbers. *Journal of Fluid Mechanics*, 125:379–395, 1982.
- [71] M. Manninen, V. Taivassalo, and S. Kallio. *On the mixture model for multiphase flow*. VTT Publications 288, Technical Research Center of Finland, 1996.
- [72] J. Ferry and S. Balachandar. A fast Eulerian method for disperse two-phase flow. *International Journal of Multiphase Flow*, 27(7):1199–1226, 7 2001.
- [73] J. Xi and P. Worth Longest. Numerical predictions of submicrometer aerosol deposition in the nasal cavity using a novel drift flux approach. *International Journal of Heat and Mass Transfer*, 51(23–24):5562–5577, 2008.
- [74] M. Pilou, S. Tsangaris, P. Neofytou, C. Housiadas, and Y. Drossinos. Inertial particle deposition in a 90° laminar flow bend: an Eulerian fluid particle approach. *Aerosol Science and Technology*, 45(11):1376–1387, 2011.

- [75] M. Pilou, V. Antonopoulos, E. Makris, P. Neofytou, S. Tsangaris, and C. Housiadas. A fully Eulerian approach to particle inertial deposition in a physiologically realistic bifurcation. *Applied Mathematical Modelling*, 37(8):5591–5605, 2013.
- [76] L. Grdon and D. Orlicki. Deposition of inhaled aerosol particles in a generation of the tracheobronchial tree. *Journal of Aerosol Science*, 21(1):3–19, 1990.
- [77] E. Makris, M. Pilou, P. Neofytou, S. Tsangaris, and C. Housiadas. Particle transport and deposition under high-frequency oscillatory ventilation and normal breathing. *Aerosol Science and Technology*, 48(2):150–162, 02 2014.
- [78] P. Worth Longest and M.J. Oldham. Numerical and experimental deposition of fine respiratory aerosols: Development of a two-phase drift flux model with near-wall velocity corrections. *Journal of Aerosol Science*, 39(1):48–70, 2008.
- [79] S.P. Belyaev and L.M. Levin. Investigation of aerosol aspiration by photographing particle tracks under flash illumination. *Journal of Aerosol Science*, 3(2): 127–140, 3 1972.
- [80] S.P. Belyaev and L.M. Levin. Techniques for collection of representative aerosol samples. *Journal of Aerosol Science*, 5(4):325–338, 8 1974.
- [81] D.C. Stevens. Review of aspiration coefficients of thin-walled sampling nozzles. *Journal of Aerosol Science*, 17(4):729–743, 1986.
- [82] D.J. Rader and V.A. Marple. A study of the effects of anisokinetic sampling. *Aerosol Science and Technology*, 8(3):283–299, 1988.
- [83] S. Li and D.A. Lundgren. Aerosol aspiration efficiency of blunt and thin-walled samplers at different wind orientations. *Aerosol Science and Technology*, 36(3): 342–350, 2002.
- [84] S. Paik and J.H. Vincent. Aspiration efficiency for thin-walled nozzles facing the wind and for very high velocity ratios. *Journal of Aerosol Science*, 33(5):705–720, 2002.
- [85] B.Y.H. Liu, Z.Q. Zhang, and T.H. Kuehn. A numerical study of inertial errors in anisokinetic sampling. *Journal of Aerosol Science*, 20(3):367–380, 1989.
- [86] S.J. Dunnett. A numerical study of the aspiration efficiency of a thin-walled sampler facing the wind for high velocity ratios. *Journal of Aerosol Science*, 36(1): 111–122, 2005.
- [87] A.K. Gil’fanov, S.K. Zaripov, and D.V. Maklakov. Calculation of particle concentration in the problem of aerosol aspiration into a thin-walled tube. *Fluid Dynamics*, 44(6):873–881, 2009.

- [88] S.K. Zaripov, A.K. Gil'fanov, and D.V. Maklakov. Numerical study of thin-walled sampler performance for aerosols in low windspeed environments. *Aerosol Science and Technology*, 44(2):152–160, 2010.
- [89] J.E. Brockmann. *Aerosol Measurement: principles, techniques, and applications*, chapter Aerosol transport in sampling lines and inlets. John Wiley & Sons, Inc., 3<sup>rd</sup> edition, 2011.
- [90] V. Armenio and V. Fiorotto. The importance of the forces acting on particles in turbulent flows. *Physics of Fluids*, 13(8):2437–2440, 2001.
- [91] R. Clift, J.R. Grace, and M.E. Weber. *Bubbles, Drops and Particles*. Academic Press, 1978.
- [92] A. Harten. High resolution schemes for hyperbolic conservation laws. *Journal of Computational Physics*, 49(3):357–393, 1983.
- [93] D. Mark, J.H. Vincent, H. Gibson, and W.A. Witherspoon. Applications of closely graded powders of fused alumina as test dusts for aerosol studies. *Journal of Aerosol Science*, 16(2):125–131, 1985.
- [94] P.L. Roe. Characteristic-based schemes for the Euler equations. *Annual Review of Fluid Mechanics*, 18(1):337–365, 1986.
- [95] B. van Leer. Towards the ultimate conservative difference scheme. V. A second-order sequel to Godunov's method. *Journal of Computational Physics*, 32(1):101–136, 1979.
- [96] E.M.A. Frederix, M. Nordlund, A.K. Kuczaj, A.E.P. Veldman, and B.J. Geurts. Eulerian modeling of inertial and diffusional aerosol deposition in bent pipes. *Computers & Fluids*, Submitted.
- [97] J. Heyder, J. Gebhart, G. Rudolf, C.F. Schiller, and W. Stahlhofen. Deposition of particles in the human respiratory tract in the size range 0.005–15  $\mu\text{m}$ . *Journal of Aerosol Science*, 17(5):811–825, 1986.
- [98] C. Mitsakou, C. Helmis, and C. Housiadis. Eulerian modelling of lung deposition with sectional representation of aerosol dynamics. *Journal of Aerosol Science*, 36(1):75–94, 2005.
- [99] P. Worth Longest and L.T. Holbrook. In silico models of aerosol delivery to the respiratory tract —development and applications. *Advanced Drug Delivery Reviews*, 64(4):296–311, 2012.
- [100] D. Gupta and M.H. Peters. A brownian dynamics simulation of aerosol deposition onto spherical collectors. *Journal of Colloid and Interface Science*, 104(2):375–389, 1985.

- [101] Y. Zhang, W.H. Finlay, and E.A. Matida. Particle deposition measurements and numerical simulation in a highly idealized mouth–throat. *Journal of Aerosol Science*, 35(7):789–803, 7 2004.
- [102] Y. S. Cheng and C. S. Wang. Motion of particles in bends of circular pipes. *Atmospheric Environment* (1967), 15(3):301–306, 1981.
- [103] R. I. Crane and R. L. Evans. Inertial deposition of particles in a bent pipe. *Journal of Aerosol Science*, 8(3):161–170, 6 1977.
- [104] C. Tsai and D.Y.H. Pui. Numerical study of particle deposition in bends of a circular cross-section-laminar flow regime. *Aerosol Science and Technology*, 12(4): 813–831, 01 1990.
- [105] K. Sun, L. Lu, and H. Jiang. A computational investigation of particle distribution and deposition in a 90 degree bend incorporating a particle–wall model. *Building and Environment*, 46(6):1251–1262, 6 2011.
- [106] S.R. Wilson, Y. Liu, E.A. Matida, and M.R. Johnson. Aerosol deposition measurements as a function of reynolds number for turbulent flow in a ninety-degree pipe bend. *Aerosol Science and Technology*, 45(3):364–375, 02 2011.
- [107] P. Zhang, R.M. Roberts, and A. Bénard. Computational guidelines and an empirical model for particle deposition in curved pipes using an Eulerian-Lagrangian approach. *Journal of Aerosol Science*, 53:1–20, 11 2012.
- [108] M. Breuer, H.T. Baytekin, and E.A. Matida. Prediction of aerosol deposition in bends using LES and an efficient Lagrangian tracking method. *Journal of Aerosol Science*, 37(11):1407–1428, 2006.
- [109] P. Armand, D. Boulaud, M. Pourprix, and J. Vendel. Two-fluid modeling of aerosol transport in laminar and turbulent flows. *Journal of Aerosol Science*, 29 (8):961–983, 1998.
- [110] K. Mohanarangam, Z.F. Tian, and J.Y. Tu. Numerical simulation of turbulent gas–particle flow in a 90° bend: Eulerian–Eulerian approach. *Computers & Chemical Engineering*, 32(3):561–571, 2008.
- [111] P. Zhang, R.M. Roberts, and A. Bénard. Numerical simulation of turbulent mist flows with liquid film formation in curved pipes using an Eulerian–Eulerian method. *Journal of Fluids Engineering*, 135(9), 2013.
- [112] J. Lin, Z. Yin, P. Lin, M. Yu, and X. Ku. Distribution and penetration efficiency of nanoparticles between 8–550 nm in pipe bends under laminar and turbulent flow conditions. *International Journal of Heat and Mass Transfer*, 85:61–70, 6 2015.

- [113] E.S. Vasquez, K.B. Walters, and D.K. Walters. Analysis of particle transport and deposition of micron-sized particles in a 90 degree bend using a two-fluid Eulerian–Eulerian approach. *Aerosol Science and Technology*, 49(9):692–704, 09 2015.
- [114] D.Y.H. Pui, F. Romay-Novas, and B.Y.H. Liu. Experimental study of particle deposition in bends of circular cross section. *Aerosol Science and Technology*, 7(3): 301–315, 1987.
- [115] K. Sun and L. Lu. Particle flow behavior of distribution and deposition throughout 90 degree bends: Analysis of influencing factors. *Journal of Aerosol Science*, 65:26–41, 11 2013.
- [116] J. Xi and P. Worth Longest. Transport and deposition of micro-aerosols in realistic and simplified models of the oral airway. *Annals of Biomedical Engineering*, 35(4):560–581, 2007.
- [117] D.B. Ingham. Diffusion of aerosols from a stream flowing through a cylindrical tube. *Journal of Aerosol Science*, 6(2):125–132, 1975.
- [118] E.M.A. Frederix, M. Nordlund, A.K. Kuczaj, M. Belka, F. Lizal, J. Jedelsky, J. Elcner, M. Jicha, and B.J. Geurts. Size-dependent aerosol deposition in a model of the upper human airways. *Journal of Aerosol Science*, Submitted.
- [119] W. Hofmann. Modelling inhaled particle deposition in the human lung – a review. *Journal of Aerosol Science*, 42(10):693–724, 2011.
- [120] A.S. Wexler and S.S. Park. Size-dependent deposition of particles in the human lung at steady-state breathing. *Journal of Aerosol Science*, 39:266–276, 2008.
- [121] Z. Li, C. Kleinstreuer, and Z. Zhang. Particle deposition in the human tracheo-bronchial airways due to transient inspiratory flow patterns. *Journal of Aerosol Science*, 38:625—644, 2007.
- [122] M. Alzahrany and A. Banerjee. Aerosolized drug delivery in patient-specific lung model during invasive high frequency oscillatory ventilation. *Journal of Aerosol Science*, 81:1–20, 2015.
- [123] R. Mead-Hunter, A.J.C. King, A.N. Larcombe, and B.J. Mullins. The influence of moving walls on respiratory aerosol deposition modelling. *Journal of Aerosol Science*, 64:48–59, 2013.
- [124] Z. Zhang, C. Kleinstreuer, and C.S. Kim. Cyclic micron-size particle inhalation and deposition in a triple bifurcation lung airway model. *Journal of Aerosol Science*, 33:257–281, 2002.

- [125] A. Moskal and L. Gradon. Temporary and spatial deposition of aerosol particles in the upper human airways during breathing cycle. *Journal of Aerosol Science*, 33:1525–1539, 2002.
- [126] Z. Zhang, C. Kleinstreuer, and S. Hyun. Size-change and deposition of conventional and composite cigarette smoke particles during inhalation in a subject-specific airway model. *Journal of Aerosol Science*, 46:34—52, 2012.
- [127] Z. Zhang, C.S. Kim, and C. Kleinstreuer. Water vapor transport and its effects on the deposition of hygroscopic droplets in a human upper airway model. *Aerosol Science and Technology*, 40:1–16, 2006.
- [128] P. Worth Longest and J. Xi. Effectiveness of direct lagrangian tracking models for simulating nanoparticle deposition in the upper airways. *Aerosol Science and Technology*, 41(4):380–397, 2007.
- [129] A.R. Lambert, P.T. O’shaughnessy, M.H. Tawhai, E.A. Hoffman, and C. Lin. Regional deposition of particles in an image-based airway model: Large-eddy simulation and left-right lung ventilation asymmetry. *Aerosol Science and Technology*, 45:11–25, 2011.
- [130] Z. Zhang, C. Kleinstreuer, and C.S. Kim. Comparison of analytical and CFD models with regard to micron particle deposition in a human 16-generation tracheobronchial airway model. *Journal of Aerosol Science*, 40:16–28, 2009.
- [131] B. Ma, V. Ruwet, P. Corieri, R. Theunissen, M. Riethmuller, and Ch. Darquenne. CFD simulation and experimental validation of fluid flow and particle transport in a model of alveolated airways. *Journal of Aerosol Science*, 40:403–414, 2009.
- [132] F. Krause, A. Wenk, Ch. Lacor, W.G. Kreyling, W. Moeller, and S. Verbanck. Numerical and experimental study on the deposition of nanoparticles in an extrathoracic oral airway model. *Journal of Aerosol Science*, 57:131–143, 2013.
- [133] L.T. Holbrook and P. Worth Longest. Validating CFD predictions of highly localized aerosol deposition in airway models: In vitro data and effects of surface properties. *Journal of Aerosol Science*, 59:6–21, 2013.
- [134] Y. Feng and C. Kleinstreuer. Micron-particle transport, interactions and deposition in triple lung-airway bifurcations using a novel modeling approach. *Journal of Aerosol Science*, 71:1–15, 2014.
- [135] J. Xi and P.W. Longest. Characterization of submicrometer aerosol deposition in extrathoracic airways during nasal exhalation. *Aerosol Science and Technology*, 43:808–827, 2009.

- [136] P. Worth Longest and M.J. Oldham. Mutual enhancements of CFD modeling and experimental data: A case study of 1- $\mu\text{m}$  particle deposition in a branching airway model. *Inhalation Toxicology*, 18:761–771, 2006.
- [137] Z. Zhang, C. Kleinstreuer, C.S. Kim, and Y.S. Cheng. Vaporizing microdroplet inhalation, transport, and deposition in a human upper airway model. *Aerosol Science and Technology*, 38:36–49, 2004.
- [138] S.K. Varghese and S. Gangamma. Particle deposition in human respiratory system: Deposition of concentrated hygroscopic aerosols. *Inhalation Toxicology*, 21(7):619–630, 2009.
- [139] J.D. Schroeter, B. Asgharian, O.T. Price, J.S. Kimbell, L. Kromidas, and M. Singal. Simulation of the phase change and deposition of inhaled semi-volatile liquid droplets in the nasal passages of rats and humans. *Journal of Aerosol Science*, 95 (15–29), 2016.
- [140] N. Khajeh-Hosseini-Dalasm and P. Worth Longest. Deposition of particles in the alveolar airways: Inhalation and breath-hold with pharmaceutical aerosols. *Journal of Aerosol Science*, 79:15–30, 2015.
- [141] Y. Feng, C. Kleinstreuer, N. Castro, and A. Rostami. Computational transport, phase change and deposition analysis of inhaled multicomponent droplet—vapor mixtures in an idealized human upper lung model. *Journal of Aerosol Science*, 96:96–123, 2016.
- [142] M. Nordlund, M. Belka, A.K. Kuczaj, F. Lizal, J. Jedelsky, J. Elcner, M. Jicha, Y. Sauser, S. Le Bouhellec, S. Cosandey, S. Majeed, G. Vuillaume, M.C. Peitsch, and J. Hoeng. Aerosol particle deposition measurements in a realistic cast of the human upper respiratory tract. *Aerosol Science & Technology*, Submitted.
- [143] F. Lizal, M. Belka, J. Adam, J. Jedelsky, and M. Jicha. A method for in vitro regional aerosol deposition measurement in a model of the human tracheo-bronchial tree by the positron emission tomography. *Proceedings of the Institution of Mechanical Engineers, Part H: Journal of Engineering in Medicine*, 2015.
- [144] A. Schmidt, S. Zidowitz, A. Kriete, T. Denhard, S. Krass, and H. Peitgen. A digital reference model of the human bronchial tree. *Computerized Medical Imaging and Graphics*, 28(4):203–211, 2004.
- [145] Y.S. Cheng, Y. Zhou, and B. Chen. Particle deposition in a cast of human oral airways. *Aerosol Science & Technology*, 31(4):286–300, 1999.
- [146] J. Elcner, F. Lizal, J. Jedelsky, M. Jicha, and M. Chovancova. Numerical investigation of inspiratory airflow in a realistic model of the human tracheobronchial airways and a comparison with experimental results. *Biomechanics and modeling in mechanobiology*, 15(2):447–469, 2016.

- [147] A.K. Kuczaj, E.M.J. Komen, and M.S. Loginov. Large Eddy Simulation study of turbulent mixing in a T-junction. *Nuclear Engineering and Design*, 240:2116–2122, 2010.
- [148] S. Elghobashi. On predicting particle-laden turbulent flows. *Applied Scientific Research*, 52(4):309–329, 1994.



## SUMMARY

Aerosols are all around us in many shapes and forms such as clouds, dust, fog or haze. We interact with them daily, often as a means to transport material, e.g., a fuel spray inside a combustion engine or delivery of drugs with a nebulizer. Aerosols are generally defined as suspensions of small particles or droplets in gases. Although aerosols often appear as continuous substances, distinguishing between a particulate and gas phase which constitute this apparent unity assists in understanding aerosol dynamics.

This thesis aims at answering the question: can we model the aerosol dynamics? In answering this question tools should be developed to assist us. First, however, we identify the mechanisms which constitute aerosol dynamics. We distinguish between two types of aerosol dynamics: aerosol evolution and aerosol transport. The first type governs the changes in the properties of an aerosol without the necessity of macroscopic physical motion, and includes mechanisms such as droplet nucleation, droplet condensation or evaporation and droplet coagulation or break-up. The second type governs all changes to an aerosol where droplet transport is involved, such as inertial drift, diffusion and deposition.

In order to capture the dominant aerosol mechanisms by mathematical models, a suitable framework is developed in which these mechanisms may be embedded. In this framework it is key to properly account for the polydispersity of the particulate phase, as most aerosol mechanisms are droplet size-dependent. Most frameworks, within the context of computational fluid dynamics, are either Lagrangian or Eulerian. In the Lagrangian framework each particle, or a particle representing many other particles, is tracked. Although this method is conceptually straight-forward and captures polydispersity intrinsically, it is often computationally expensive. In this thesis we develop an Eulerian aerosol framework instead, in which the particulate phase is treated from a continuous point of view. A key feature of our Eulerian formulation is that it is sectional, allowing to model a polydisperse aerosol without laying constraints or making assumptions on the shape of the size distribution. A second key element of the model is that it is internally mixed; the droplets chemical composition is locally independent of droplet size. This reduces the complexity of the model significantly in order to retain computational feasibility. Finally, the general Eulerian sectional aerosol model is embedded inside the compressible PISO algorithm, for finding a time-accurate solution to the set of coupled transport equations, including

droplet number concentrations, mass concentrations, momentum and energy.

The developed PISO algorithm stands at the heart of all further modeling presented. First, aerosol evolution mechanisms are studied. The ‘characteristics-based sectional method’ is developed to capture condensational growth and nucleation, exploiting the method of characteristics. The method is shown to preserve a pre-specified number of moments of the droplet size distribution. Moreover, the method avoids a severe numerical time step restriction and can be readily extended to spatially inhomogeneous settings. This extension is extensively discussed with reference to aerosol formation in lid-driven cavity flow and aerosol formation inside a double mixing-tee chamber, also demonstrating the computational feasibility of the method.

In terms of aerosol transport dynamics a consistent method is derived to capture aerosol droplet drift. Generally, the trajectories of relatively large droplets tend to deviate from carrier gas streamlines. This introduces a drift of droplets with respect to the carrier gas, and can lead to ‘aerosol aspiration’, i.e., a mechanism in which aerosol concentrations locally increase due to an additional influx of drifting droplets. The model is validated against experimental data of aerosol sampler aspiration, and generally good agreement is found. Special emphasis is placed on the consistent description of aerosol drift inside the model and its numerical counterpart, meaning that two internal consistency relations are respected by construction. Within this consistent formulation droplet diffusion is also introduced. Both drift and diffusion may lead to a non-zero droplet motion at walls, driving deposition of droplets. The problem of both drift and diffusion-driven deposition is studied inside a bent pipe geometry and good agreement is found with literature for both the diffusional and inertial regime.

Finally, the Eulerian aerosol model is applied to simulate aerosol deposition inside the upper human airways. This allows to validate the model in a realistically complex setting, as experimental data is available of regional deposition inside a lung cast of the upper human respiratory tract. We find good agreement in terms of regional deposition for a monodisperse aerosol. To illustrate the computational feasibility as well as the capability of the method, polydisperse aerosol deposition for a large size range from nanometer to micrometer is studied in terms of local deposition patterns as well as regional deposition data as function of the lung generation.

In summary, this thesis explores the Eulerian approach in the mathematical modeling of aerosol dynamics and presents accurate predictions for a range of relevant flows involving aerosols. The Eulerian approach offers a reliable, useful and affordable computational tool in many applications, such as aerosol nucleation in a turbulent mixing chamber, predicting aerosol aspiration inside aerosol samplers and determining droplet size-dependent deposition patterns inside complex geometries.

## SAMENVATTING

Aerosolen bevinden zich overal om ons heen in verschillende vormen, zoals wolken, stof, mist of nevel. We hebben dagelijks met ze te maken, vaak om materiaal te transporteren, e.g., een brandstofspray in een verbrandingsmotor of het innemen van een medicijn met een verstuiver. De algemene definitie van een aerosol is een suspensie van kleine deeltjes of druppels in een gas. Ondanks dat aerosolen vaak als continue substanties op ons overkomen (zoals bijvoorbeeld een wolk) is het zinvol om onderscheid te maken tussen de deeltjes- en gasfase van het aerosol.

Dit proefschrift poogt de vraag te beantwoorden: kan aerosol dynamica gemonsterd worden? Bij het beantwoorden van deze vraag dienen gereedschappen ontwikkeld te worden die ons hierin helpen. Eerst identificeren we de relevante aerosol dynamica mechanismen. We onderscheiden twee types: aerosol evolutie en aerosol transport. Het eerste type aerosol dynamica omvat veranderingen in de eigenschappen van een aerosol zonder dat daar macroscopisch fysisch transport voor nodig is, zoals nucleatie, condensatie en verdamping en druppelsamensmelting of -opsplitsing. Het tweede type aerosol dynamica omvat veranderingen waarbij druppeltransport noodzakelijk is, zoals druppeldrift, diffusie en depositie.

Om de dominante aerosolmechanismen te vangen in wiskundige modellen moet een geschikt raamwerk ontwikkeld worden waarin deze mechanismen opgenomen kunnen worden. In dit raamwerk is het cruciaal dat het polydisperse karakter van de druppels meegenomen wordt, aangezien de meeste mechanismen druppelgrootte-afhankelijk zijn. In het kader van CFD (computational fluid dynamics) kunnen de meeste wiskundige modellen gekwalificeerd worden als Lagrangiaans of Euleriaans. In het Lagrangiaanse raamwerk wordt elk deeltje, of een 'effectief' deeltje dat andere deeltjes vertegenwoordigt, gevuld. Ondanks dat deze aanpak conceptueel aantrekkelijk is en het polydisperse karakter van een aerosol intrinsiek vangt, is de methode vaak rekenkundig duur. In dit proefschrift ontwikkelen we in plaats daarvan een Euleriaans raamwerk, waarin de deeltjesfase vanuit een continue benadering beschreven wordt. Een cruciaal onderdeel is dat onze Euleriaanse aanpak 'sectioonel' is. Dit is een methode die de mogelijkheid geeft om polydisperse aerosolen te modelleren zonder een beperking te leggen op, of een aanname te maken over de vorm van de druppelgrootteverdeling. Een tweede sleutelement van het model is de 'intern gemengde aanname'; de chemische compositie van de druppels is lokaal onafhankelijk van de druppelgrootte. Dit reduceert de complexiteit van het model

aanmerkelijk en bewaakt daardoor de rekenkundige haalbaarheid van de totale aanpak. Uiteindelijk wordt het Euleriaanse raamwerk verankerd in het compressibele PISO algoritme waarmee een tijdsnauwkeurige oplossing gevonden kan worden van de set gekoppelde transportvergelijkingen voor druppelnummerconcentraties, massaconcentraties, momentum en energie.

Het ontwikkelde PISO algoritme staat aan de basis van alle modellen die vervolgens gepresenteerd worden. Eerst wordt aerosol evolutie beschouwd. Een methode wordt ontwikkeld waarmee druppelgroei door condensatie en druppelnucleatie beschreven wordt door gebruik te maken van de methode van karakteristieken. De verkregen methode kan een aantal momenten van de druppelgrootteverdeling exact bewaren. Daarnaast wordt de methode vrij van een strenge tijdstaprestrictie en kan gemakkelijk uitgebreid worden naar ruimtelijk inhomogene situaties. Deze uitbreiding wordt uitvoerig beschouwd in de context van aerosol evolutie in een caviteit en in een dubbele T-vormige mengkamer. Dit toont ook de rekenkundige haalbaarheid aan van de methode in een realistische setting.

Voor aerosol transport is een consistente methode ontwikkeld voor de beschrijving van druppeldrift. Algemeen gesproken hebben de stromingsbanen van relatief grote deeltjes de neiging af te wijken van de stromingsbanen van het dragende gas. Dit geeft drift ten opzichte van het dragende gas, en kan zelfs leiden tot aerosol aspiratie, i.e., het effect waarbij aerosolconcentraties lokaal stijgen door een toegenomen stroom van wegdrivende druppels. Het model wordt gevalideerd met experimentele data waarmee een goede overeenkomst gevonden wordt. De nadruk wordt gelegd op de consistente beschrijving van aerosoltransport in het model en in zijn numerieke tegenhanger. Dit betekent dat twee interne consistentierelaties ten alle tijden expliciet gerespecteerd worden. In dit consistente raamwerk wordt ook druppeldiffusie beschouwd. Zowel drift als diffusie kunnen leiden tot een druppelstroom aan wanden. Dit leidt tot druppeldepositie. Het probleem van zowel drift- als diffusie-gedreven depositie wordt bestudeerd in een gebogen pijp en goede overeenkomst met de literatuur wordt gevonden.

Tot slot wordt het Euleriaanse aerosolmodel toegepast om aerosol depositie te simuleren in de bovenste luchtwegen van een mens. Aangezien er experimentele data beschikbaar is voor regionale depositie van een fysiek longmodel biedt ons dit de mogelijkheid om ons model te valideren in een realistische complexe setting. We vinden goede overeenkomst tussen onze voorspellingen en experimentele data voor een monodispers aerosol. Om de rekenkundige haalbaarheid van de methode te illustreren bestuderen we ook polydisperse aerosoldepositiepatronen in de long voor druppels met een grootte variërend van een nanometer tot meer dan een micrometer.

Dit proefschrift verkent de Euleriaanse aanpak in het wiskundig modelleren van aerosoldynamica en presenteert nauwkeurige voorspellingen voor een scala aan relevante aerosolstromingen. De Euleriaanse aanpak biedt voor veel toepassingen een betrouwbaar, nuttig en betaalbaar rekenhulpmiddel, bijvoorbeeld in het geval van druppelnucleatie in een turbulente T-vormige mengkamer, in het geval van

het voorspellen van aspiratie in een aerosol meetinstrument of in het bepalen van druppelgrootte-afhankelijke depositiepatronen in complexe geometrieën.



## ABOUT THE AUTHOR

Edo Frederix was born on August 6, 1986, in Ubachsberg, the Netherlands. After he graduated from the Bernardinus College in Heerlen (2005), he moved to Eindhoven where he started his studies in Mechanical Engineering at the Eindhoven University of Technology. Quickly, Edo developed an interest in fluid dynamics and numerical modeling, which resulted in a final bachelor project titled “VINSAX: an axisymmetric viscous model of a deforming bubble” (2009) under supervision of Prof. Cees van der Geld followed by an internship at the Johns Hopkins University in Baltimore, MD, USA (2011) under supervision of Prof. Charles Meneveau and Prof. Hans Kuerten, during which a Matlab library was developed for the interaction with a public turbulence database.

Edo successfully completed his master with a research project titled “DNS of particle-laden turbulent pipe flow” (2012) under supervision of Hans Kuerten. It was Hans who pointed Edo in the direction of Twente, where, on November 1, 2012, Edo started his Ph.D. project under supervision of Prof. Bernard Geurts in the group of Multiscale Modeling and Simulation in the department of Applied Mathematics at the University of Twente.

In his project, Edo worked on the development of Eulerian methods in the mathematical modeling of aerosols. His work was part of an already existing collaboration between the University of Twente and Philip Morris International (PMI), which led to a unique and close interaction with Dr. Arkadiusz Kuczaj and Dr. Markus Nordlund from PMI, through whom Edo’s work became directly applicable and relevant to industry. During his Ph.D., Edo was handed the opportunity to present his work in many locations, as well as to work for an extended amount of time at PMI’s facilities in Switzerland. Edo complimented his main research activity of modeling aerosols with the development of numerical algorithms for porous flows in close collaboration with Dr. Milos Stanic and with the development and maintenance of a small high-performance computing system.

In his spare time Edo likes to do many sports (football, squash, running and hiking) and works for his small company offering tailor-made IT products.



## LIST OF PUBLICATIONS

### REFEREED JOURNALS

1. Yu, H., Kanov, K., Perlman, E., Graham, J., Frederix, E.M.A., Burns, R., Szalay, A., Eyink, G. and Meneveau, C. **Studying Lagrangian dynamics of turbulence using on-demand fluid particle tracking in a public turbulence database** *Journal of Turbulence* 13 (2012): N12.
2. Frederix, E.M.A., Stanic, M., Kuczaj, A.K., Nordlund, M. and Geurts, B.J. **Extension of the compressible PISO algorithm to single-species aerosol formation and transport.** *International Journal of Multiphase Flow* 74 (2015): 184-194.
3. Nordlund, M., Stanic, M., Kuczaj, A.K., Frederix, E.M.A. and Geurts, B. J. **Improved PISO algorithms for modeling density varying flow in conjugate fluidporous domains.** *Journal of Computational Physics* 306 (2016): 199–215.
4. Stanic, M., Nordlund, M., Frederix, E.M.A., Kuczaj, A.K. and Geurts, B. J. **Evaluation of oscillation-free fluid-porous interface treatments for segregated finite volume flow solvers.** *Computers & Fluids* 131 (2016): 169–179.
5. Frederix, E.M.A., Stanic, M., Kuczaj, A.K., Nordlund, M. and Geurts, B.J. **Characteristics-based sectional modeling of aerosol nucleation and condensation.** *Journal of Computational Physics* 326 (2016): 499-515.
6. Frederix, E.M.A., Stanic, M., Kuczaj, A.K., Nordlund, M., Veldman, A.E.P. and Geurts, B.J. **Application of the characteristics-based sectional method to spatially varying aerosol formation and transport.** *Journal of Aerosol Science*, submitted (2015).
7. Frederix, E.M.A., Kuczaj, A.K., Nordlund, M., Veldman, A.E.P. and Geurts, B.J. **Prediction of non-isokinetic sampling with a sectional drift flux model.** *Computers & Fluids*, submitted (2016).
8. Frederix, E.M.A., Kuczaj, A.K., Nordlund, M., Veldman, A.E.P. and Geurts, B.J. **Eulerian modeling of inertial and diffusional aerosol deposition in bent pipes.** *Computers & Fluids*, submitted (2016).
9. Frederix, E.M.A., Kuczaj, A.K., Nordlund, M., Belka, M., Lizal, F., Jedelsky, J., Elcner, J., Jicha, M. and Geurts, B.J. **Simulation of size-dependent aerosol deposition in a realistic model of the upper human airways.** *Journal of Aerosol Science*, submitted (2016).

## CONFERENCE PROCEEDINGS

1. Frederix, E.M.A., Kuczaj, A.K., Nordlund, M., Winkelman, C. and Geurts, B.J. **An OpenFOAM-based tool for computational modeling of aerosol nucleation and transport.** *Nucleation and Atmospheric Aerosols: 19th International Conference* (Jun. 2013), Fort Collins, CO, USA.
2. Frederix, E.M.A., Kuczaj, A.K., Nordlund, M., Winkelman, C. and Geurts, B.J. **Computational modeling of aerosol formation and evolution using OpenFOAM.** *European Aerosol Conference* (Sep. 2013), Prague, Czech Republic.
3. Frederix, E.M.A., Kuczaj, A.K., Nordlund, M. and Geurts, B.J. **Aerosol nucleation and condensation simulation using PISO and MUSCL with solution-adaptive grid refinement.** *International Conference on Numerical Multiphase Flow* (Jun 2014), Darmstadt, Germany.
4. Frederix, E.M.A., Kuczaj, A.K., Nordlund, M. and Geurts, B.J. **Capturing aerosol droplet nucleation and condensation bursts using PISO and TVD schemes.** *6th European Conference on Computational Fluid Dynamics* (Jul. 2014): 3462-3472, Barcelona, Spain.
5. Frederix, E.M.A., Kuczaj, A.K., Nordlund, M., Stanic, M. and Geurts, B.J. **Characteristics-based sectional modeling of aerosol nucleation, condensation and transport.** *67th Annual Meeting of the APS Division of Fluid Dynamics* (Nov. 2014), San Francisco, CA, USA.
6. Frederix, E.M.A., Kuczaj, A.K., Nordlund, M. and Geurts, B.J. **Sectional model for aerosol formation in cooled lid-driven cavity flow.** *European Aerosol Conference* (Sep. 2015), Milan, Italy.
7. Frederix, E.M.A., Kuczaj, A.K., Nordlund, M. and Geurts, B.J. **Prediction of aerosol sampling efficiency using a sectional droplet drift flux model.** *International Conference on Multiphase Flow* (May 2016), Florence, Italy.
8. Frederix, E.M.A., Kuczaj, A.K., Nordlund, M. and Geurts, B.J. **Sectional Eulerian modeling of aerosol drift, diffusion and deposition.** *European Congress on Computational Methods in Applied Sciences and Engineering* (Jun. 2016), Crete, Greece.
9. Frederix, E.M.A., Kuczaj, A.K., Nordlund, M. and Geurts, B.J. **Aerosol dynamics in the upper airways.** *Burgers Symposium* (Jun. 2016), Lunteren, The Netherlands.
10. Frederix, E.M.A., Kuczaj, A.K., Nordlund, M. and Geurts, B.J. **Eulerian modeling of polydisperse aerosol deposition in a realistic cast of the human upper respiratory tract.** *European Aerosol Conference* (Sep. 2016), Tours, France.
11. Frederix, E.M.A., Kuczaj, A.K., Nordlund, M. and Geurts, B.J. **A validated sectional aerosol model applied to deposition in the human upper airways.** *American Aerosol Association for Aerosol Research Annual Conference* (Oct. 2016), Portland, OR, USA.



## **Eulerian modeling of aerosol dynamics**

We explore the feasibility and applicability of the Eulerian approach in the mathematical modeling of aerosol dynamics including droplet nucleation, condensation, drift, diffusion and deposition. Both the methodology as well as a number of illustrating applications are contained, establishing the accuracy of the Eulerian aerosol model. Results are presented of aerosol formation inside a turbulent mixing-tee, aerosol aggregation inside an aerosol sampler and size dependent aerosol deposition inside a realistic cast of the human upper airways. Through these applications, as well as via a rigorous validation of the presented models and methods against experimental data, this thesis demonstrates the relevance of the Eulerian approach for accurately and efficiently modeling aerosol dynamics.